SANDIA REPORT

SAND2015-6612
Unclassified Unlimited Release
Printed August 2015

Fukushima Daiichi Unit 1 Uncertainty Analysis – Exploration of Core Melt Progression Uncertain Parameters – Volume II

M.R. Denman, D.M. Brooks

Prepared by
Sandia National Laboratories
Albuquerque, New Mexico 87185 and Livermore, California 94550

Sandia National Laboratories is a multi-program laboratory managed and operated by Sandia Corporation, a wholly owned subsidiary of Lockheed Martin Corporation, for the U.S. Department of Energy's National Nuclear Security Administration under contract DE-AC04-94AL85000.

Issued by Sandia National Laboratories, operated for the United States Department of Energy by Sandia Corporation.

Available to DOE and DOE contractors from
U.S. Department of Energy
Office of Scientific and Technical Information
P.O. Box 62
Oak Ridge, TN 37831

Telephone: (865) 576-8401
Facsimile: (865) 576-5728
E-Mail: reports@adonis.osti.gov
Online ordering: http://www.osti.gov/bridge

Available to the public from
U.S. Department of Commerce
National Technical Information Service
5285 Port Royal Rd.
Springfield, VA 22161

Telephone: (800) 553-6847
Facsimile: (703) 605-6900
E-Mail: orders@ntis.fedworld.gov
Online order: http://www.ntis.gov/help/ordermethods.asp?loc=7-4-0#online

SAND2015-6612
Unclassified, Unlimited Release
Printed August 2015

Fukushima Daiichi Unit 1 Uncertainty Analysis – Exploration of Core Melt Progression Uncertain Parameters – Volume II

Matthew Denman, Dusty Brooks

P.O. Box 5800
Albuquerque, New Mexico 87185-MS0748

Abstract

Sandia National Laboratories (SNL) has conducted an uncertainty analysis (UA) on the Fukushima Daiichi unit (1F1) accident progression with the MELCOR code. Volume I of the 1F1 UA discusses the physical modeling details and time history results of the UA. Volume II of the 1F1 UA discusses the statistical viewpoint. The model used was developed for a previous accident reconstruction investigation jointly sponsored by the US Department of Energy (DOE) and Nuclear Regulatory Commission (NRC). The goal of this work was to perform a focused evaluation of uncertainty in core damage progression behavior and its effect on key figures-of-merit (e.g., hydrogen production, fraction of intact fuel, vessel lower head failure) and in doing so assess the applicability of traditional sensitivity analysis techniques.

The following insights were gained from this analysis:

1. The 1F1 UA shows that, with current modeling techniques, water injection at 15 hours would likely have been expected to successfully cool the rubbilized reactor core without failure of the lower vessel head. While lower head failure was not ruled out by our simulated results, lower head failure was only predicted in approximately 40% of the MELCOR simulations. All simulations that resulted in lower head failure before 15 hours predict that most of the reactor core is no longer intact in the core region.
2. Discrete events (e.g., valve chatter, core material relocation) reduce the stability of severe accident system model outputs, and can produce output variability on the same order as the epistemic uncertainties. This behavior makes direct comparisons of results (e.g., tradeoff studies) difficult to defend without a characterization of the uncertainty or variability in predicted results. Only inputs which can exhibit enough influence on output figures-of-merit to rise above the stability limitations of severe accident modeling can be isolated through sensitivity analysis alone. In this analysis molten Zircaloy breakthrough temperature, fuel collapse criteria, and radial solid debris relocation time constant were inputs that were found to meet this criterion. It should be noted that common LWR severe accident codes exhibit this behavior to some degree.

ACKNOWLEDGEMENTS

The authors would like to acknowledge the U.S. Department of Energy's Office of Nuclear Energy for providing the funding which supported this work.

The authors would like to thank Sandia Management for their review and guidance during this project.

The authors would also like to thank Jeff Cardoni for supplying decay heat SCALE calculations for 1F1, 1F2, and 1F3, and Randall Gauntt for his efforts to ensure that the report contents were presented in a balanced manner.

The authors would also like to thank Donald Kalinich for conducting the MELCOR simulations for the 1F1 UA.

CONTENTS

FIGURES

TABLES

ACRONYMS

1F1	Fukushima Daiichi Unit 1
1F2	Fukushima Daiichi Unit 2
1F3	Fukushima Daiichi Unit 3
ADS	automatic depressurization system
ANS	American Nuclear Society
BAF	bottom of active fuel
BMLE	Beta Maximum Likelihood Estimate
BWR	boiling water reactor
CDF	Cumulative Distribution Function
CRD	control rod drive
CRDHS	control rod drive hydraulic system
CRGT	control rod guide tube
CST	condensate storage tank
CV	control volume
CVH	Control Volume Hydrodynamics (package)
DC	direct current
DCH	Decay Heat
DOE	Department of Energy
DF	Damage Fraction
DTRA	Defense Threat Reduction Agency
D/W	drywell
EDG	emergency diesel generator
EoS	End of Simulation (start of firewater injection at 15 hours)
EPRI	Electric Power Research Institute
FDI	Fuel Dispersal Interactions (package)
FoM	Figures of Merit
FSAR	Final Safety Analysis Report
GBD	Generalized Binomial Distribution
HPCI	high-pressure coolant injection system
IAEA	International Atomic Energy Agency
IC	isolation condenser
INL	Idaho National Laboratory
INPO	Institute of Nuclear Power Operators
JST	Japanese Standard time

LPCS	low-pressure core sprays
MC	Monte Carlo
MCCI	molten core concrete interaction
MELCOR	not an acronym
MLE	Maximum Likelihood Estimate
MOX	mixed oxide
MSIV	main steam-line isolation valve
MSL	main steam line
MZBT	Molten Zircaloy Breakthrough Temperature
NARAC	National Atmospheric Release Advisory Center
NPSH	net positive suction head
NRC	Nuclear Regulatory Commission
ORNL	Oak Ridge National Laboratory
P1	Small Input Sample Perturbation {Samples from Uniform($\mathbf{X}_{13}$*0.995, $\mathbf{X}_{13}$*1.005)}
P2	dt_{max} Perturbation {Samples from LogUniform(0.01s, 0.1s)}
P3	Flow path Shuffle {Random numbering order for flow paths}
PBF	Prompt Burst Facility (test reactor at INL)
PCV	primary containment vessel (drywell and wetwell)
PCT	peak cladding temperature
PWR	pressurized water reactor
RCIC	reactor core isolation cooling system
RCS	reactor coolant system
RHR	residual heat removal system
RN	Radionuclide (package)
RPV	reactor pressure vessel
RSDR	Radial Solid Debris Relocation Time Constant
SBO	station blackout
SCALE	Standardized Computer Analyses for Licensing Evaluation
S/C	suppression chamber (i.e., wetwell)
SFP	spent fuel pool
SNL	Sandia National Laboratories
SOARCA	State of the Art Reactor Consequence Analysis
SRV	safety relief valve
SRV1	SRV with the lowest opening pressure set-point (the SRV that opens first)
TAF	top of active fuel
TaT	Effective Fuel Failure Temperature
TEPCO	Tokyo Electric Power Company
TMI	Three Mile Island

WW	wetwel

EXECUTIVE SUMMARY

Volume II of the Fukushima Daiichi Unit 1 (1F1) Uncertainty Analysis (UA) provides the statistical background for the MELCOR simulations explored in Volume I of the 1F1 UA. Key insights from Volume II of the 1F1 are presented in this executive summary.

General Insights

As shown in the Visual Statistical Inspection portion of the Executive Summary, the 1F1 UA shows that, with current modeling techniques, water injection at 15 hours would likely have been expected to successfully quench the rubbilized reactor core without failure of the lower vessel head. While lower head failure was not ruled out by our simulated results, lower head failure was only predicted in approximately 40% of the MELCOR simulations. All simulations that resulted in lower head failure before 15 hours predict that most of the fuel rods (i.e., >98%) are no longer intact in the core region.

Both the degree of core degradation and likelihood of lower-head failure were relatively independent of oxidation throughout the accident sequence. The levels of oxidation, as estimated by cumulative hydrogen production, early in the accident sequences (e.g., at the time of first fuel collapse) neither correlated positively nor negatively with the cumulative levels of oxidation at 15 hours (i.e., the end of the simulation). Furthermore, the cumulative oxidation before the time of lower head failure did not correspond to the timing of lower head failure. While slower core degradation, as measured by the intact fuel mass fraction at the time of key bifurcation events throughout core degradation, corresponded to less oxidation at the end of the simulation, the level of cumulative oxidation at the time of the key event neither corresponded to the degree of oxidation before the event nor the timing of the event.

Of the inputs considered, only a few input parameters examined in this analysis are both consistently statistically significant in regressions and appear in reliable, predictive regression models. These parameters include the temperature at which molten Zircaloy breaks through the structural zirconium di-oxide shell, the fuel collapse criteria, and the radial solid debris relocation time constant.

Convergence

Examination of event timing (e.g., time at first fuel collapse or time of lower plenum dryout) convergence shows fairly stable median estimates between the replicate samples. Outlier impact on the median is evident at 100 samples, especially for the conditional lower head failure timings which only converge over a subset (approximately 35) of the original 100 samples per replicate. Additionally, the replicate derived from the uniform input distributions shows a small but noticeable deviation (i.e., on the order a few percent) from the informed distribution replicate results (Replicates 1-3).

Visual Statistical Inspection

When conducting a statistical analysis of a large systems code, key insights can be derived from a rudimentary examination of figures of merit. Simple scatter plots relating sampled decay heat, fuel collapse criteria, and molten Zircaloy breakthrough temperature demonstrate clearly

distinguishable trends with hydrogen production at select times throughout the accident. Figure E-1 presents linear trends in both hydrogen production at lower plenum dryout, shown as the gray line on Figure E-1, and the timing of lower plenum dryout, shown via the color scale to the right of the figure, as a function of the sampled Zircaloy breakthrough temperature.

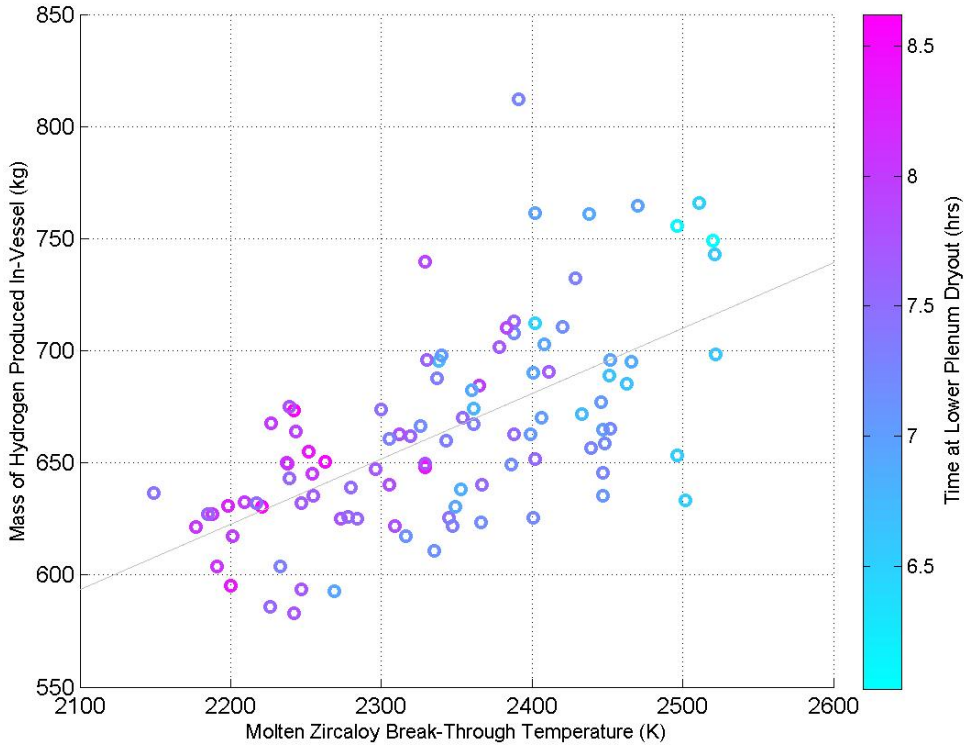

Figure E.1 – Molten Zircaloy Breakthrough Temperature Scatterplot for Cumulative Hydrogen Production at Lower Plenum Dryout for Replicate 1.

The distribution of the timing of events (e.g., main steam line failure or lower core plate failure) can be difficult to discern given only time histories as presented in the 1F1 UA Volume I and reproduced in this report in Appendix A. Cumulative Distribution Functions (CDFs) provide the analyst with another way to visualize the output data and provide key insights regarding accident progression not visible in traditional time histories. For example, from the CDFs in Figure E.2, the timing of steam line failure and first fuel collapse are predicted to be intermingled events (i.e., some simulations experience main steam line failure before first fuel failure and others switch the timing of these events). This insight potentially allows the analyst to partition the analysis into multiple subsets which may allow for more informative analyses.

Figure E.2 highlights that, while the timing of first control rod failure and first channel box failure are nearly co-incident, the hydrogen produced by the first channel box failure is over twice the hydrogen produced at first control rod failure. This divergence in CDF results is due to the rapid oxidation reaction occurring in the accident during this time period.

The CDFs in Figure E.2 also clearly show that while experts believe that the 1F1 lower head failed before water injection occurred at 15 hours [ES.1, ES.2], the 1F1 UA results predict only a

35% chance of lower head failure given current SNL MELCOR calculations. The range of hydrogen generated before both lower head failure and the end of the simulation (i.e., 15 hours) are the same. This means that the simulations that produce the most amount of hydrogen and those that produce the least amount of hydrogen both resulted in lower head failure, and the CDFs show no noticeable differentiating trends between two event timings. These insights suggest that failure of the lower head in MELCOR appears to be independent of the amount of hydrogen, and thus oxidation energy, produced in the MELCOR simulation.

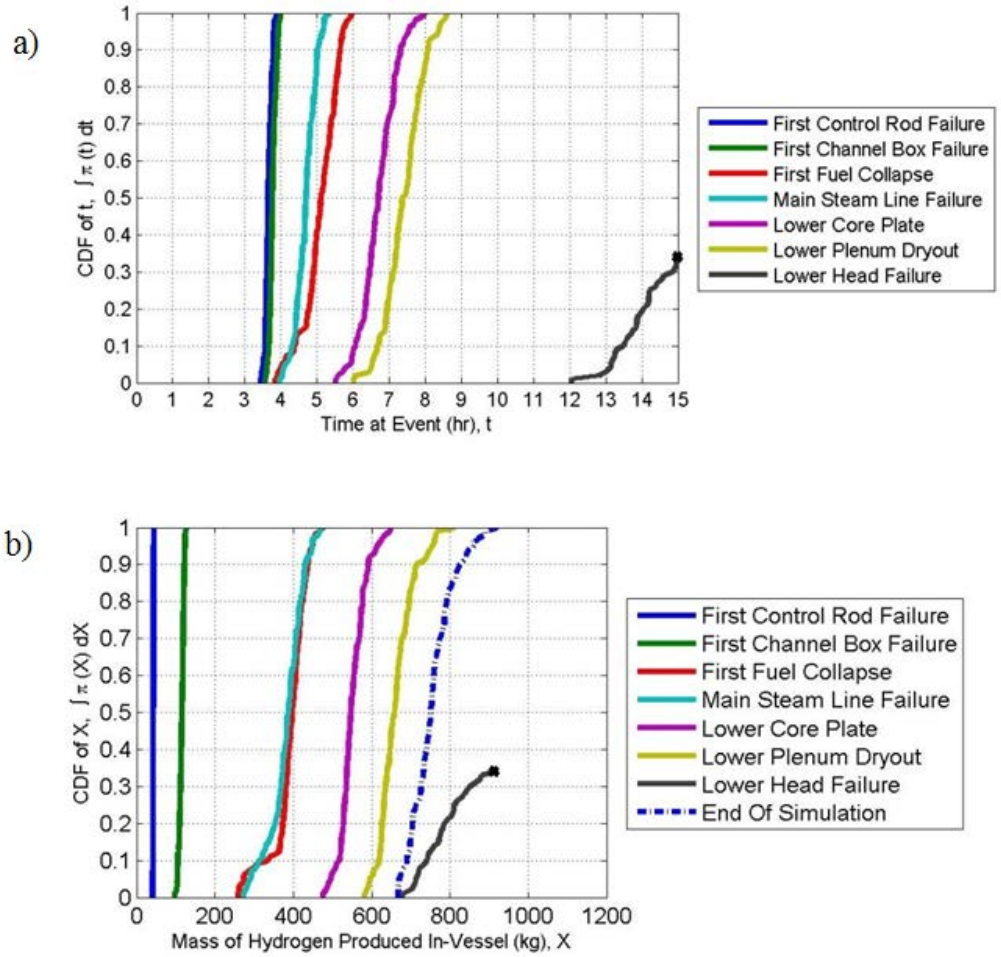

Figure E.2 – Cumulative Distributions for Replicate 1 Event Timings and Corresponding Cumulative Hydrogen Production Before the Event Occurrence

Automated Dynamic Regressions

Severe accident progression involves complicated, non-linear phenomena. Thus, conducting regressions only at the end of the accident may fail to detect important driving phenomena during the actual accident progression. The 1F1 UA performed regressions for cumulative hydrogen production, intact fuel fraction, and mass of material ejected from the lower head to produce meta-models of the output variability at the occurrence of eight cliff edge events during the 1F1 accident. The meta-models were created using an automated stepwise algorithm, incorporating both linear and interaction dependencies, for both the original and rank transformed MELCOR outputs. An example regression table for the rank transformed

cumulative hydrogen data is shown in Table E.1. The beta values in the table represent the relative impact of the regressed trend for the input parameter defined in the table row and blank entries represent variables that were not regressed. Many input parameters, e.g., effective fuel failure temperature and decay heat, have impacts whose influences rise and fall with the progression of the accident.

As seen in Table E.1, only a select few input parameters, such as molten Zircaloy breakthrough temperature, were consistently resolved throughout key event timing. It was consistently noticed that event timings during core degradation were more easily regressed, although this insight may be reflective of the relative system stabilization once material has relocated to the lower head and most of the water has left the vessel.

When assessing the usefulness of the regression results, three key insights became apparent. First, mass of material ejected from the lower head was not a feasible regression output due to the relatively small number of samples available for regression (i.e., 35% of the simulations predicted lower head failure). Second, the fraction of intact fuel occurs in quantized segments on the basis of the core nodalization. This discrete/discontinuous parameter violates some regression assumptions, thus the outputs must be scrutinized with care. Third, scatterplots were identified as an important tool to use in conjunction with regression model summaries for understanding and validating the regression results.

Regression Validation

Regressions are a useful tool when parsing through statistical outputs of large system codes; outputs of such analyses can become so large that systematic visual inspections of the output data can become impractical. The variability present in the MELCOR stability results (Table E.2 and E.3) stemming from the repeated discrete and non-linear events involved in system level severe accident simulations highlight why care must be taken to ensure that regression results are reflective of physical effects. Analyses of individual disparate sequences, as conducted in Volume I of the 1F1 UA, show the potential for nearly identical initial conditions to produce results that can provide the illusion of a significant trend. Therefore, a simple manual validation of physical effects suggested in the regression model is ineffective and subject to bias.

Thus, Volume II of the 1F1 UA tested a subset of the regressions, trained on data from a given replicate at a given event on a given physical parameter, on corresponding data from the other replicates. It was consistently shown that regressions fit to the training data that have higher R^2 values did not produce regression models that were predictive when evaluated on new testing data. It was also shown that rank transformation of the training data lessened, but did not remove, the tendency of stepwise regressions to produce non-predictive meta-models that fit inherent variability instead of, or in addition to, physical trends. See Table E.2 and E.3 for comparisons between the R^2 of the regressions on the training data (shaded blue) and the predictive effectiveness of that regression on new test data.

Specific insights from Table E.2 and E.3 include:

- The rank transformation of the output data for the replicate sampled from uniform distributions (RepU) allows for either: 1) the stepwise regression algorithm to produce a more predictive meta-model of output variability or 2) the transformation of the distribution of output data variability into a predictable arrangement.

Table E.1 – Mass of In-Vessel Hydrogen Produced, Beginning of Simulation Until Event, Rank Transformed Data

	First Control Rod Failure	First Channel Box	First Fuel Failure	Main Steam Line	Lower Core Plate	Lower Plenum Dry-out	Lower Head Failure	End of Simulation
R^2 / R^2_{adj} / F-stat vs. Const. / pval	.26 / .24 / 16.7 / 0	.05 / .04 / 5.02 / .027	.23 / .21 / 9.78 / 0	.42 / .38 / 11 / 0	.53 / .5 / 21.1 / 0	.52 / .5 / 25.8 / 0	.4 / .37 / 10.5 / .0003	.17 / .16 / 10.1 / .0001
Intercept	0.84	0.62	0.54	0.104	0.24	0.28	0.08	0.40
Time Constants for Radial (solid) Debris Relocation (s) [1]				$\beta_i = 0.174$ $\beta_{1,4} = -0.871$	$\beta_i = -0.189$			
Time Constants for Radial (liquid) Debris Relocation (s)								
dT|dz Model, Time Constant for Averaging Flows (s)		$\beta_i = -0.227$						
dT|dz Model, Characteristic Coupling Time (s)								
dT|dz Model, Relative Weight of Historical Flow (s)								
Molten Zircaloy Break-Through Temperature (K) [2]				$\beta_i = -0.867$ $\beta_{2,3} = 1.082$	$\beta_i = 0.545$	$\beta_i = 0.669$	$\beta_i = 0.467$	$\beta_i = 0.373$
Molten Cladding (pool) Drainage Rate (kg/(m*s)) [3]			$\beta_i = -0.222$	$\beta_i = -0.727$ $\beta_{2,3} = 1.082$				
Fraction of Strain at Which Lower Head Failure Occurs								
Scaling Factor for Candling Heat Transfer Coefficients								
Fraction of Un-oxidized Cladding Thickness Initiating T. M. Weakening (m)							$\beta_i = 0.363$	
Debris Quenching Heat Transfer Coefficient to Pool (W/(m*m*K)) [4]				$\beta_i = 0.238$ $\beta_{1,4} = -0.871$	$\beta_i = -0.187$	$\beta_i = -0.52$ $\beta_{4,5} = 0.632$		$\beta_i = -0.185$
Debris Falling Velocity (m/s)	$\beta_i = -0.199$							
Minimum Debris Porosity								
Time At Temperature - Effective Failure Temperature (K) [5]			$\beta_i = 0.4$		$\beta_i = 0.513$	$\beta_i = -0.039$ $\beta_{4,5} = 0.632$		
Decay Heat Integrated to 10 hours (J)	$\beta_i = -0.46715$		$\beta_i = -0.234$		$\beta_i = -0.151$			

Note: This table is included in the executive summary for illustrative purposes only. β_i represents the regression coefficient for the variable associated with the row of the cells and $\beta_{1,4}$ represents the regression with coefficient for the terms with [1] and [4] in the first column (i.e., Time Constant for Solid Debris Relocation Debris Quenching Heat Transfer Coefficient to Pool respectively). For additional explanation of how to interpret the results in this table, please see Section 6.1 Interpreting Regression Dependency Tables in the main report.

- Replicate 1 (Rep1) produced the highest R^2 for the training data but performed with the poorest predictive merit when the Rep1 meta-model was applied to testing data from Rep2, Rep3 and RepU.
- Combining Rep1 with Rep2 did not produce a more predictive regression meta-model than regressions trained with Rep2 data alone. Rep1 may include significant outliers which distort the stepwise regression results.

Table E.2 – Comparison of Predictive Ability of Linear Regressions, with Interaction Terms, for Cumulative Hydrogen Production at the Time of Lower Plenum Dryout

	Rep1	*Rep2*	*Rep3*	*RepU*	*Rep12*
Rep1	0.48	0.30	0.31	0.01	0.41
Rep2	0.27	0.40	0.40	0.23	0.41
Rep3	0.30	0.34	0.34	0.19	0.29
RepU	0.26	0.37	0.36	0.45	0.36
$\overline{R^2_{pred}}$	0.27	0.34	0.36	0.14	0.32
R^2_{adj}	0.46	0.39	0.33	0.43	0.40

Table E.3 – Comparison of Predictive Ability of Rank Regressions for Cumulative Hydrogen Production at the Time of Lower Plenum Dryout

	Rep1	*Rep2*	*Rep3*	*RepU*	*Rep12*
Rep1	0.52	0.40	0.36	0.37	0.44
Rep2	0.24	0.38	0.36	0.34	0.44
Rep3	0.31	0.34	0.38	0.30	0.30
RepU	0.25	0.39	0.39	0.41	0.35
$\overline{R^2_{pred}}$	0.27	0.37	0.37	0.34	0.32
R^2_{adj}	0.50	0.37	0.36	0.40	0.43

Though regression model assumptions are difficult to validate, the extent to which the assumptions are violated affects the likelihood that the model will produce a reliable explanation of system variance. A meta-model that violates the assumptions of the regression technique employed can still provide insight, but inference based upon the model should be done with care.

MELCOR Stability

A stability analysis was also performed on the 1F1 UA MELCOR deck. Figure E.3 plots the spread of cumulative hydrogen production as a function of maximum time step defined in the input deck. The scatter is weighted toward a maximum time step of 0.01 since a log-uniform distribution was sampled for this stability study. The timing of lower plenum dryout is represented by the color bar on the right side of the plot. As can be seen by Figure E.3, neither the event timing, which can vary by approximately 1 hour, nor the cumulative amount of

hydrogen produced before lower plenum dryout, which can vary by over 225 kg, are shown to be a strong function of maximum time step. It should also be noted that a constant variability in output can be experienced over both small and large ranges of selected maximum time step. Thus, MELCOR stability can be estimated over a smaller range of maximum time steps which may prevent computational resources from being wasted without the need to execute the code with very small time steps (i.e. less than 0.01 to 0.05), thereby precluding excessive CPU time.

Additionally, the impact of MELCOR stability on event timing was assessed and compared to the timing variability computed by the full 1F1 UA, using Figure E.4. Core degradation variability due to MELCOR stability was smaller for the three perturbation studies [i.e., sub-figures b), c) and d)]; the span timing of first fuel collapse and lower core plate failure occurred over 2 and 3 hours respectively for Replicate 1 of the full UA [i.e, sub-figure a)]. These events were compressed into an approximately one hour time window for the perturbation studies. The separation of the span of late phased event timings is more closely aligned between the 1F1 UA and perturbation results. Thus, it is extremely important to assess the impacts of code stability when informing late-phased accident management with system codes.

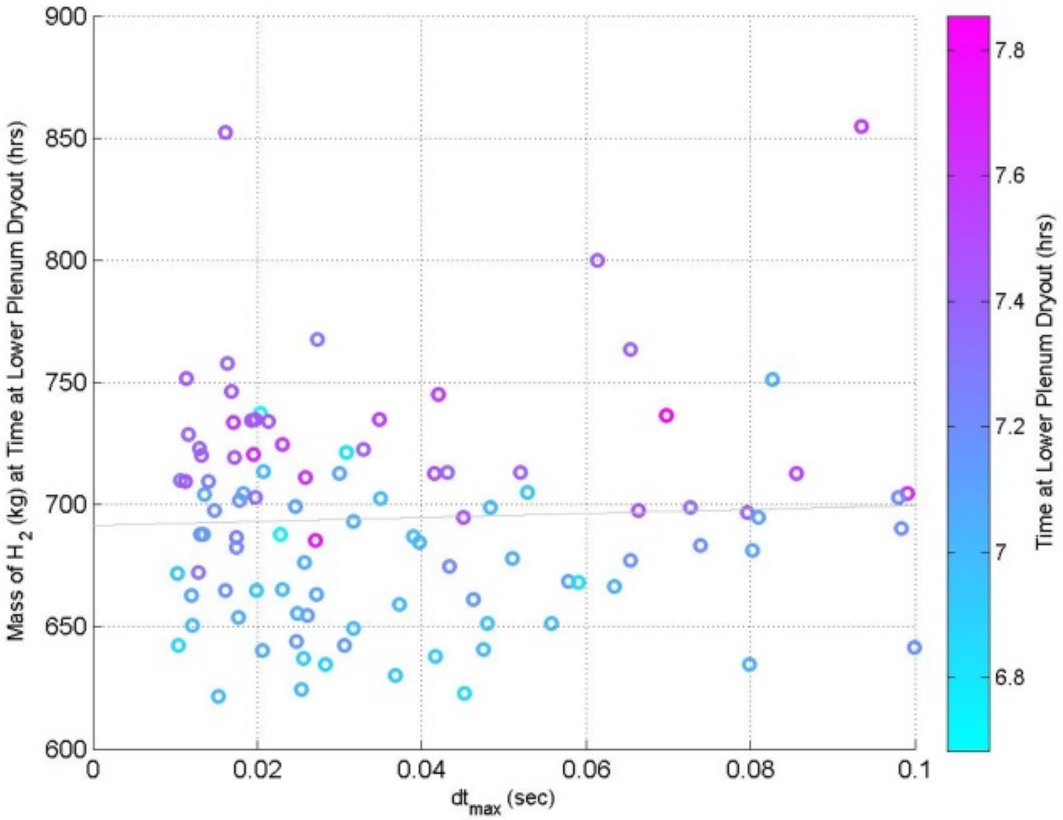

Figure E.3 – Variability of Cumulative Hydrogen Production at the Time of Lower Plenum Dryout, and the Timing of Lower Plenum Dryout, as a function of Maximum Allowable Time-Step

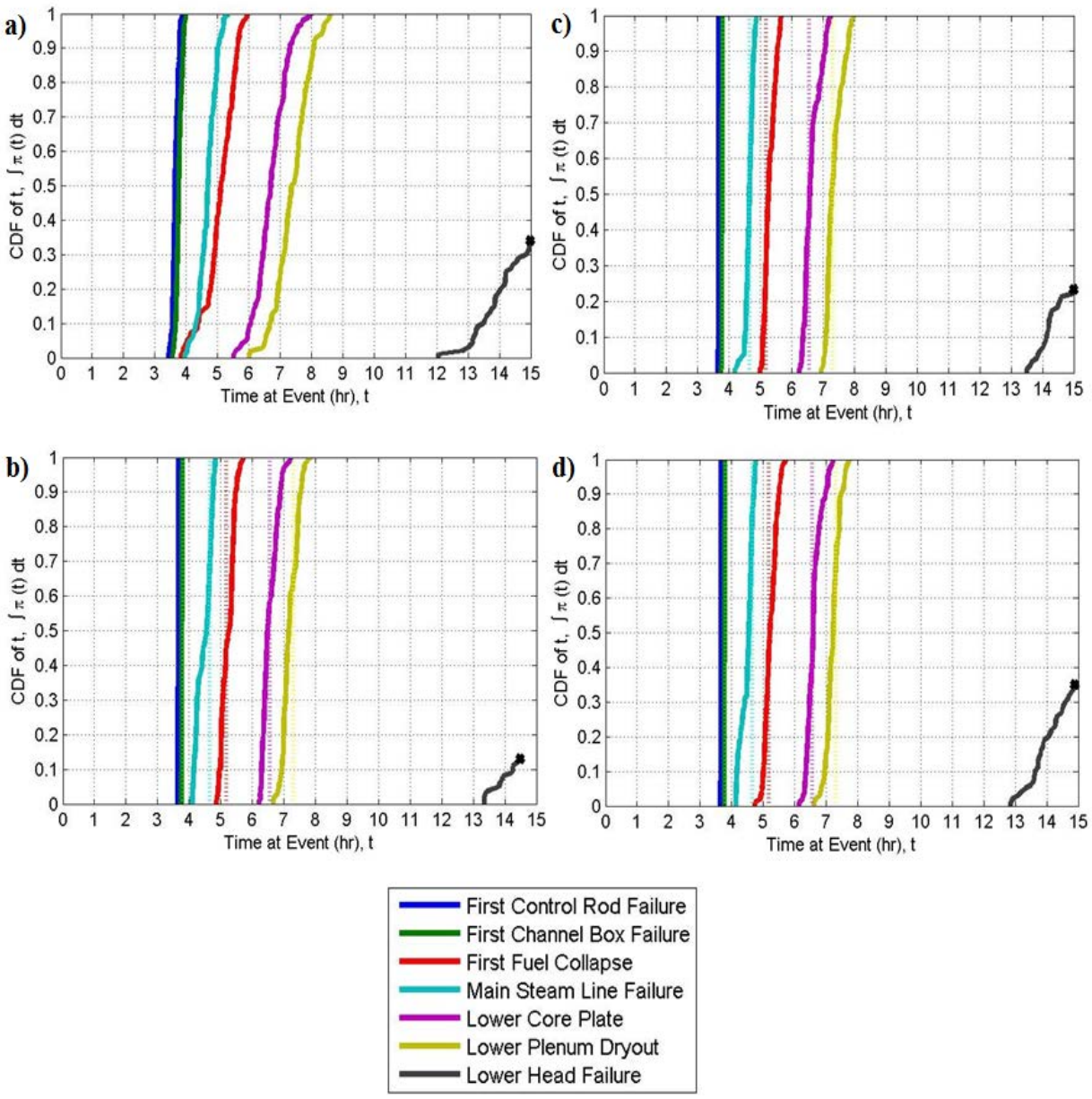

Figure E.4 – Event Timing CDFs for a) Replicate 1, b) Small Input Perturbation, c) Maximum Time Step Perturbation, d) Flow Path Shuffle Perturbation

References

ES.1 R.O. Gauntt, et al., SAND2012-6173, "Fukushima Daiichi Accident Study (Status as of April 2012)," SNL, Albuquerque, NM, 2012.

ES.2 TEPCO, "MAAP Code-based Analysis of the Development of the Events at the Fukushima Daiichi Nuclear Power Station," http://www.tepco.co.jp/en/nu/fukushima-np/images/handouts_120312_04-e.pdf (2012).

1 INTRODUCTION

1.1 Background

Sandia National Laboratories (SNL) conducted uncertainty analyses (UA) with a MELCOR [1.1] representation of the 1F1 reactor. This representation was previously developed for an accident reconstruction investigation jointly sponsored by the U.S. Department of Energy (DOE) and Nuclear Regulatory Commission (NRC) [1.2]. However, this study only examined a handful of inputs and boundary conditions, and the predictions yielded fair agreement with plant data and release estimates. Further MELCOR Fukushima simulation efforts [1.3][1.4][1.5] proceeded at SNL in a similar fashion–that is, only analyzing a few simulations–and these simulations resulted in better agreement with plant data and release estimates.

The severe accidents at Fukushima Daiichi units involve high levels of uncertainty in accident progression and consequence, as evidenced by the numerous international accident analyses that all predict various degrees of plant damage and radioactivity releases [1.2][1.7][1.8][1.9] [1.10][1.11]. Because each analysis employs different plant nodalizations, physics models (if different codes are used), and boundary conditions, every analysis predicts unique accident progressions with varying degrees of agreement with data. Inevitably, the inherent uncertainty and complexity of severe accidents forces analysts to adjust inputs and boundary conditions in order to "match" data. The SNL Fukushima UA project intends to improve upon these previous forensic analysis methods by taking a more methodical approach to severe accident uncertainty.

A thorough forensic understanding of these complicated accidents entails rigorous uncertainty analyses. More than two years after the accidents, many events and operator actions remain unknown. Moreover, key severe accident phenomena are not fully understood; thus some current computational models involve high degrees of uncertainty. Uncertainty analyses are required to gain a better understanding of the Fukushima accidents because these accidents are of critical importance to the future of nuclear safety and the use of nuclear power. These analyses also provide an opportunity for validation of severe accident codes, which build confidence in the codes and in the guidance derived from their results with respect to reactor decommissioning and severe accident management.

1.2 Purpose and Relationship to 1F1 UA

Volume I of this report series discusses the MELCOR model used for the 1F1 UA and provides a deterministic examination of the variability in the 1F1 MELCOR output due to Monte Carlo sampling of input parameter distributions. Volume I also conducted perturbation studies to determine the robustness of the output distribution to: 1) small changes in input parameters, 2) changes in dt_{max}, and 3) changes in the order in which flow path information is read by MELCOR.

Volume II of this report series discusses the input parameter uncertainties sampled in the 1F1 UA and convergence of the output distribution, and examines various methods that can be used to parse results from an UA. It is hypothesized that statistical techniques, such as traditional regression techniques, can help sort through the large volume of output data produced by an uncertainty analysis and possibly provide key insights into accident progression that would otherwise be difficult to isolate.

1.3 Document Outline

This report is comprised of 9 chapters. There contents are as follows:

1. Introduction – Provides a high level background regarding the purpose of this report.
2. Definition of Uncertain Input Parameters – Defines the uncertain parameters which were sampled for the time histories in Volume I and the subsequent statistical analyses in Volume II.
3. Treatment of Output Uncertainties – Provides a high level description of how output uncertainties will be treated throughout the report. This is an extremely important section if the review of the regression chapters is to be understood.
4. Convergence of Timing Figures of Merit (FoMs) – Demonstrates the degree of convergence reached by the various replicates used in the 1F1 UA.
5. Visual Inspection of the MELCOR Statistical Outputs – Examines the UA outputs through visual statistical tools such as scatterplots and Cumulative Distribution Functions (CDFs).
6. Automated Regression Analyses – Regressions were conducted using an automated stepwise algorithm, incorporating both linear and two-way interaction dependencies, for both the original and rank transformed MELCOR outputs.
7. Regression Validation – Applies the regressions calculated within each replicate to data from other replicates to validate the regressed terms.
8. MELCOR Output Stability – Examines the degree of output stability achieved in the 1F1 UA by examining the output variability due to small input perturbations, changes in maximum allowable time step, and rearrangement of flow path order in the MELCOR input.
9. Summary and Conclusions – Reviews what was learned from the 1F1 UA.

1.4 References

[1.1] R.O. Gauntt, et al., NUREG/CR-6119, "MELCOR Computer Code Manuals, Vol. 2: Reference Manuals, Version 1.8.6 (Vol. 2, Rev. 3)," Sandia National Laboratories, Albuquerque, NM, 2005.

[1.2] R.O. Gauntt, et al., SAND2012-6173, "Fukushima Daiichi Accident Study (Status as of April 2012)," SNL, Albuquerque, NM, 2012

[1.3] R.O. Gauntt, D.A. Kalinich, et al., "MELCOR Simulations of the Severe Accident at the Fukushima 1F1 Reactor," Proceedings of 2012 ANS Winter Meeting & Nuclear Technology Expo, San Diego, CA, November 11-15 (2012).

[1.4] J. Phillips, J.N. Cardoni, et al., "MELCOR Simulations of the Severe Accident at the Fukushima 1F2 Reactor," Proceedings of 2012 ANS Winter Meeting & Nuclear Technology Expo, San Diego, CA, November 11-15 (2012).

[1.5] J.N. Cardoni, R.O. Gauntt, et al., "MELCOR Simulations of the Severe Accident at the Fukushima 1F3 Reactor," Proceedings of 2012 ANS Winter Meeting & Nuclear Technology Expo, San Diego, CA, November 11-15 (2012).

[1.6] D. Luxat and J. Gabor "Fukushima Technical Evaluation: Phase 1– MAAP5 Analysis," EPRI Final Report 1025750, Palo Alto, CA, April (2012).

[1.7] M. Braun and G. Urzua, “MELCOR 1.8.6 Analysis of the Core Degradation in the Fukushima Daiichi Power Plant,” Severe Accident Research Program and MELCOR Code Assessment Program (MCAP2011), Bethesda, MD, September 20-23 (2011).

[1.8] TEPCO, “MAAP Code-based Analysis of the Development of the Events at the Fukushima Daiichi Nuclear Power Station,” http://www.tepco.co.jp/en/nu/fukushima-np/images/handouts_120312_04-e.pdf (2012).

[1.9] H. Hoshi, et al., “Severe Accident Analyses of Fukushima-Daiichi Units 1 to 3,” Proceedings of 2012 Fukushima Ministerial Conference on Nuclear Safety, Fukushima Prefecture, Japan, December 15-17 (2012).

[1.10] K. Robb, et al., “Fukushima Daiichi Unit 3 MELCOR Investigation,” Proceedings of 2012 ANS Winter Meeting & Nuclear Technology Expo, San Diego, CA, November 11-15 (2012).

[1.11] M. Pellegrini, et al., “Analysis of Accident Progression of Fukushima Dai-ichi with SAMPSON Code—(3) Unit 3,” Proceedings of 2012 ANS Winter Meeting & Nuclear Technology Expo, San Diego, CA, November 11-15 (2012).

[1.12] D. Kalinich, R. Schmidt, “Fukushima Daiichi Unit 1 Uncertainty Analysis – Exploration of Core Melt Progression Uncertain Parameters – Volume I,” Sandia National Laboratories, Draft Report, Albuquerque NM (Draft).

2 DEFINITION OF UNCERTAIN INPUT PARAMETERS

Chapter 2 describes the input and output uncertainty treatment for the 1F1 uncertainty analysis. Section 2.1 outlines the formulation of point estimate parameters which were appropriated nearly identically from both previous and ongoing uncertainty studies [2.1][2.2]. Chapter 2.2 describes epistemic uncertainties which were modified significantly from pre-existing MELCOR UA. Sections 2.3 and 2.4 briefly describe the treatment of additional aleatory uncertainties, or lack thereof, and the major differences between the 1F1 UA and the Peach Bottom Mark I UA.

2.1 Point Estimate Distributions for Input Uncertainties

The uncertainty analysis presented in this report leverages uncertainty characterizations from previous MELCOR studies [2.1][2.2][2.3]. Table 2.1 presents the point estimates of uncertain parameters treated in this analysis.

Table 2.1 presents epistemic uncertainty distributions that accomplish two goals:

1. Represent the current understanding of physical parameter values or the effective impact of input approximations (e.g., the disabled eutectics sub-model within MELCOR) and
2. Exploration of the impact of purely numerical inputs within MELCOR (e.g., numerical smoothing coefficients).

Except for the tabular uncertainty distributions for decay heat (Section 2.2.2) and fuel rod time at temperature relationships (Section 2.2.3), the epistemic uncertainties are cast as a beta fit of either the original Peach Bottom distributions or updates of the Peach Bottom distributions for ongoing MELCOR UA work. Beta distributions were utilized for two reasons:

1. Beta distributions are defined in the MELCOR Uncertainty Engine [2.5] and
2. Beta distributions are flexible, thus they are able to mimic the shape of most common distributions while being bounded between two values.

While beta distributions are typically bounded between zero and one, they can be shifted and renormalized to characterize any continuous range of potential values. This is shown in Equation (2-1), where LB is the lower bound, UB is the upper bound, k is the normalization constant for the beta distribution, α and β are shape parameters, and X is the uncertain variable.

$$Beta(X|LB,UB,\alpha,\beta) = LB + \frac{1}{k}\left\{\frac{(X-UB)}{UB-LB}\right\}^{\alpha-1}\left\{\frac{(X-UB)}{UB-LB}\right\}^{\beta-1} \quad (2\text{-}1)$$

The Fukushima UA recasts all of the uncertain parameters in beta distributions either by matching the median and mode of the original distribution to the beta distribution or by moment matching via the Beta Maximum Likelihood Estimates (BMLE). For most distributions, the mean and mode of the original distribution were matched to the mean and mode of the beta distribution. This approach was selected over the BMLE approach because the BMLE approach does not preserve the mode of the initial distribution. Many of the transformed distributions were originally cast as triangular distributions, where the mode, not the mean, value was defined. Thus, transformations that disregard the mode were not desired. The BMLE approach was used to transform the log-uniform distribution for the debris fall velocity because the quality of the mean/mode beta fit was poor.

Table 2.1 – List of Epistemic Uncertain Parameters

Parameter	Nomenclature	Uniform Distribution	Shifted Beta Distribution (Mode/Mean)	Shifted Beta Distribution (BMLE)	Source
Time constants for radial (solid) debris relocation	SC1020_1	LB = 180 s UB = 720 s	LB = 180 s UB = 720 s α = 1.33 β = 1.67	LB = 180 s UB = 720 s α = 2.08 β = 2.56	[2.2]
Time constants for radial (liquid) debris relocation	SC1020_2	LB = 30 s UB = 120 s	LB = 30 s UB = 120 s α = 1.33 β = 1.67	LB = 30 s UB = 120 s α = 2.08 β = 2.59	[2.2]
d*T*/dz sub-model, time constant for averaging flows	SC1030_2	LB = 0.09 s UB = 0.11 s	LB = 0.09 s UB = 0.11 s α = 1.1 β = 1.1	LB = 0.09 s UB = 0.11 s α = 1 β = 1	Assumed
d*T*/dz model, characteristic time for coupling d*T*/dz temperatures to average CVH volume temperature when d*T*/dz model is active	SC1030_4	LB = 8 s UB = 12 s	LB = 8 s UB = 12 s α = 1.1 β = 1.1	LB = 8 s UB = 12 s α = 1 β = 1	Assumed
d*T*/dz model, maximum relative weight of old flow in smoothing algorithm involving time constant for averaging flows	SC1030_5	LB = 0.5 s UB = 0.7 s	LB = 0.5 s UB = 0.7 s α = 1.1 β = 1.1	LB = 0.5 s UB = 0.7 s α = 1 β = 1	Assumed
Molten Zircaloy break-through temperature	SC1131_2	LB = 2100 K UB = 2540 K	LB = 2100 K UB = 2540 K α = 2.77 β = 2.33	LB = 2100 K UB = 2540 K α = 2.58 β = 2.05	Section 2.2.1
Molten cladding (pool) drainage rate	SC1141_2	LB = 0.1 kg/m-s UB = 2.0 kg/m-s	LB = 0.1 kg/m-s UB = 2.0 kg/m-s α = 1.11111 β = 1.8889	LB = 0.1 kg/m-s UB = 2.0 kg/m-s α = 1.24 β = 2.26	[2.2]
Fraction of strain at which lower head failure occurs	SC1601_4	LB = 0.16 UB = 0.20	LB = 0.16 UB = 0.20 α = 1.1 β = 1.1	LB = 0.16 UB = 0.20 α = 1 β = 1	Assumed

Table 2.1 – List of Epistemic Uncertain Parameters, Cont.

Parameter	Nomenclature	Uniform Distribution	Shifted Beta Distribution (Mode/Mean)	Shifted Beta Distribution (BMLE)	Source
Fraction of un-oxidized cladding thickness at which thermal-mechanical weakening of oxidized cladding begins	cor_rod_2	LB = 0.0005 m UB = 0.0015 m	LB = 0.0005 m UB = 0.0015 m α = 1.1 β = 1.1	LB = 0.0005 m UB = 0.0015 m α = 1 β = 1	Assumed
Scaling factor for candling heat transfer coefficients	cor_cht_hfzrXX	LB = 0.9 UB = 1.1	LB = 0.9 UB = 1.1 α = 1.1 β = 1.1	LB = 0.9 UB = 1.1 α = 1 β = 1	Assumed
Debris falling velocity	cor_lp_4	log-uniform dist. LB = 0.01 m/s UB = 1.0 m/s	LB = 0.01 m/s UB = 1.0 m/s α = 0.0587 β = 0.4763	LB = 0.01 m/s UB = 1.0 m/s α = 0.85 β = 1.14	[2.2]
Minimum debris porosity (Lipinski dryout model); SC1244(1) Min. porosity used in flow blockage Ergun pressure drop equation; SC4413(5) Min. hydrodynamic volume fraction; SC4414(1) Minimum porosity to be used in calculating the flow resistance in the flow blockage model; SC1505(1) Minimum porosity to be used in calculating the area for heat transfer to fluid; SC1505(2)[1]	minpordp	LB = 0.01 UB = 0.2	LB = 0.01 UB = 0.2 α = 1.1 β = 1.1	LB = 0.01 UB = 0.2 α = 1 β = 1	Assumed
Fuel rod time-at-temperature relationship	TaT	(1)[2]	(1)	(1)	Section 2.2.3
Time dependent core decay heat	dch	(2)	(2)	(2)	Section 2.2.2

[1] Minimum debris porosity is defined in many locations of the MELCOR input. For consistency, the same distribution and subsequent sampled values are applied to each sensitivity coefficient.

[2] Fuel rod time-at-temperature and time dependent decay heat are tabular uncertain variables, not point estimates. See the appropriate section for more information regarding the characterization of these variables.

The distributions that were initially defined as uniform distributions are still uniform distributions under either the mean/mode or the BMLE transformation (i.e., the shape parameters $\alpha = 1$ and $\beta = 1$ correspond to a uniform distribution). Uniform distributions are typically used when the upper and lower bounds of the parameter can be estimated, but no maximum likelihood can be ascertained. It should be noted that while not initially defined by the analysis, uniform distributions both impart a mean and standard deviation and imply significant likelihood to the tails of the parameter distribution. In these cases, the authors used expert judgment to reassign the shape parameters from $\alpha = 1$ and $\beta = 1$ to $\alpha = 1.1$ and $\beta = 1.1$ to de-emphasize the tails of the uniform distributions.

2.2 Development of Select Epistemic Uncertainties

This section describes the epistemic distributions used in the Fukushima UA that deviate significantly from previous SNL MELCOR-UA research. The parameters described in this section are significantly modified from those previous studies and thus the approaches taken to modify these parameters are documented in this section.

2.2.1 Molten Zirconium Breakthrough Temperature

As the fuel temperature rises, the cladding undergoes many chemical and structural transitions. As modeled in MELCOR using best practices [2.9], once the temperature reaches 1073K the fuel rod cladding ruptures and releases fission products from the fuel-cladding gap. As the temperature increases (starting as low as 1100 K) the steam rapidly oxidizes the cladding, forming a ZrO_2 shell. Above 2100 K, the zirconium the does not fully oxidize forms an α-phase ZrO fluid, which is held up by the ZrO_2 shell. The ZrO also migrates through the fuel pellet cracks and forms a $(U,Zr)O_{2-x}$ mixture through slow dissolution of the irradiated UO_2 fuel. The thickness of the ZrO_2 is primarily a function of:

- Steam supply of oxygen to the α-ZrO, thus increasing the ZrO_2 shell thickness,
- Oxygenation of the α-ZrO from the ZrO2 shell, thus decreasing the shell thickness[3], and
- Cladding temperatures, which heavily influence reaction rates (i.e., higher temperature => faster reactions)

It should be noted that the α-ZrO can also extract oxygen from the UO_2 pellet. Schematic representations of the process approximated by the molten Zircaloy breakthrough temperature (*MZBT*) can be seen in Figure 2.1 and Figure 2.2. When Zircaloy-melt breaks through the ZrO_2 shell, it also removes some dissolved uranium and fission products and stops the heat generation from the zirconium oxidation reaction. This dissolution process is simulated in the SOARCA study by assuming 0.2 kg of UO_2 is dissolved for every 1 kg of Zirconium melt generated by the candling process.[4]

[3] Does not occur below 2273 K [2.6]

[4] A more mechanistic approach to determining dissolved UO_2 content could be taken by the eutectics model, if this model did not lead to code instabilities.

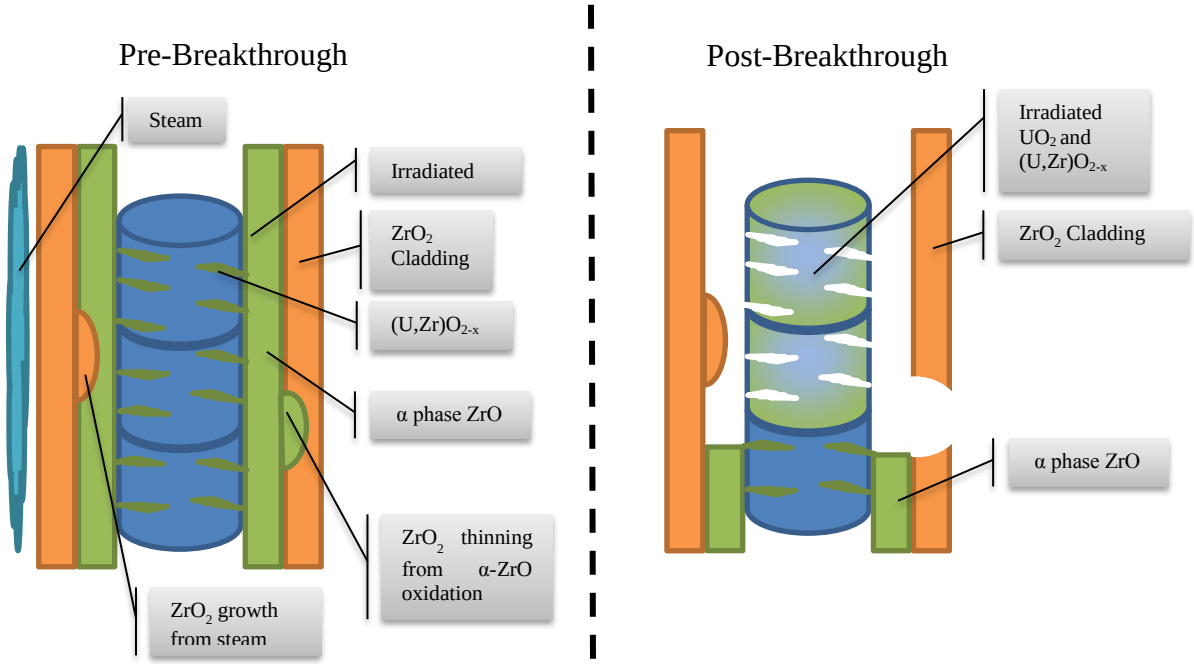

Figure 2.1 – Schematic of Zircaloy Melt Breakthrough (Not to Scale)

Using structural models of the oxide shell, it has been shown [2.6] that high temperature failure (a.k.a. flowering) of the ZrO_2 shell can occur through two primary failure modes:

1. Oxide shell grows too thick under intermediate rate temperature ramps in Kelvin (K) per second (s) $\left\{\sim 3\frac{K}{s} < \frac{dT}{dt} < \sim 6\frac{K}{s}\right\}$ and the surface stress exceeds the flexural limits. The stress causes cracks in the ZrO_2 shell, which are filled with melt. The melt then oxidizes, causing more cracks. Eventually, the oxide shell expands to the point that the incompressible melt applies enough internal pressure to rupture the oxide shell.[5] Results of simulations with the code S/Q [2.6] have been conducted and the simulation results are presented as Figure 2.3 and Figure 2.4.
2. Oxide shell erodes and is too thin under rapid temperature ramps to contain the melt $\left\{\frac{dT}{dt} > \sim 6\frac{K}{s}\right\}$. Thinning of the oxide shell is caused by internal erosion by the melt. This failure mode can be seen in Figure 2.5.
3. The last possibility is that the oxide shell completely oxidizes the melt. This is predicted to occur under extremely slow temperature ramps $\{\frac{dT}{dt} < \sim 3\frac{K}{s}\}$.

[5] Small variations in pellet diameter can dramatically change the predicted failure temperature.

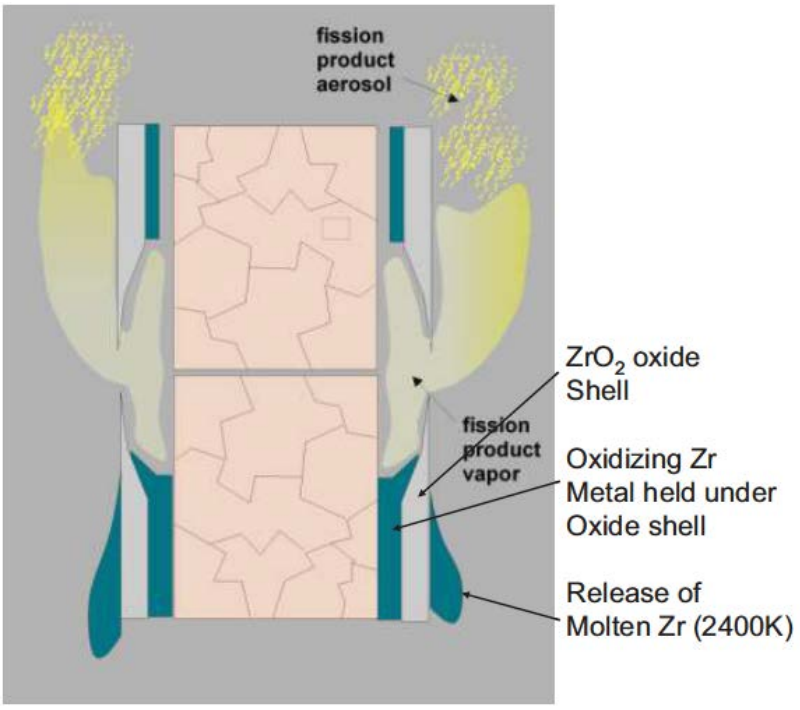

Figure 2.2 – Depiction of Molten Zirconium Breakthrough (Figure 4-7, [2.7])

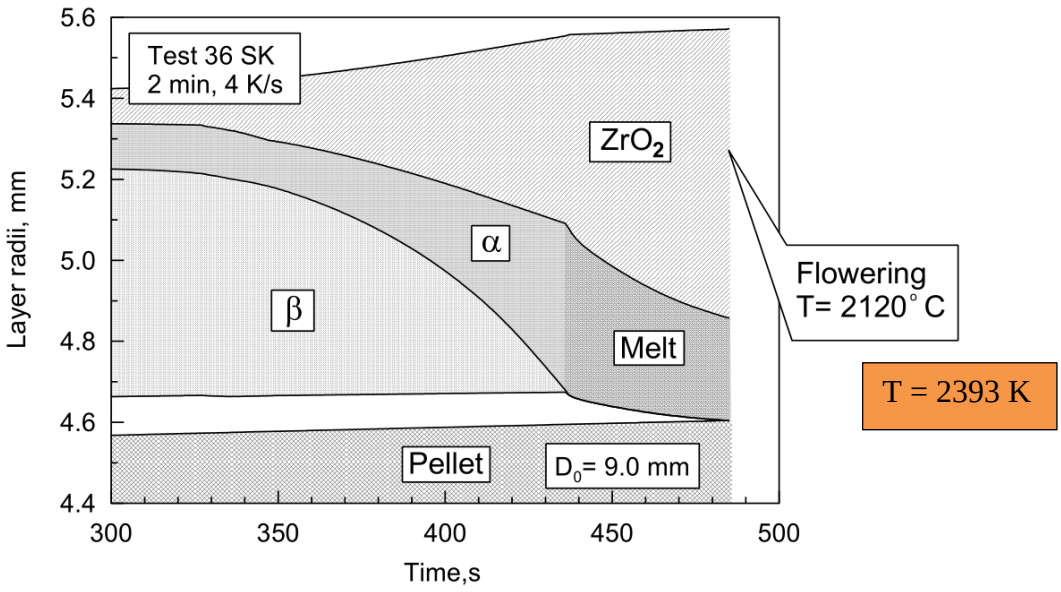

Figure 2.3 – Flowering Failure of ZrO_2 Shell at a Heat-Up Rate of 4K/s with Pellet Diameter of 9.0 mm (Figure 14, [2.6])

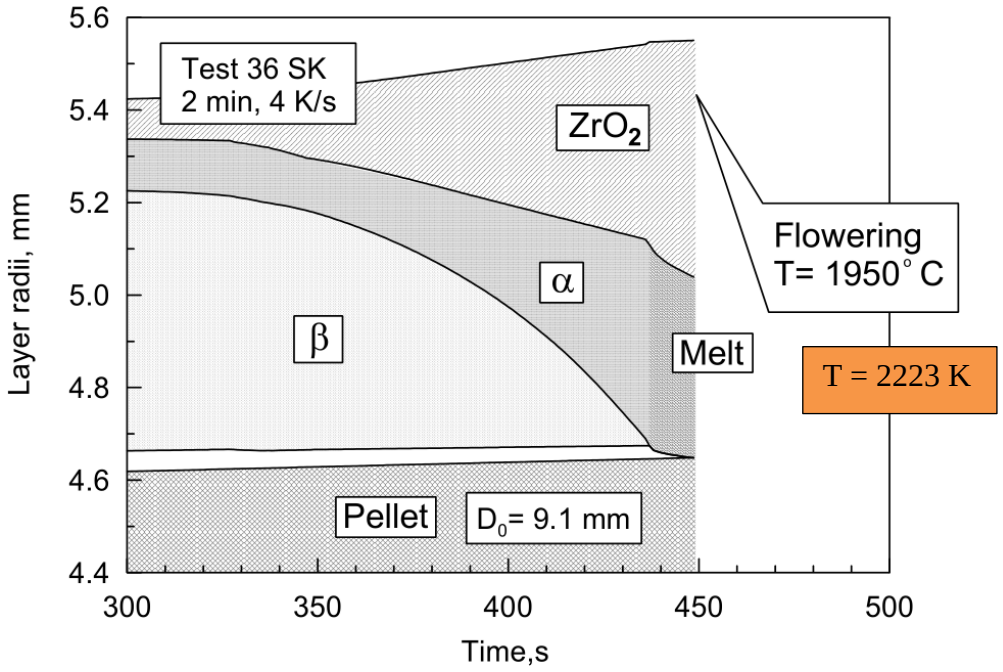

Figure 2.4 - Flowering Failure of ZrO_2 Shell at a Heat-Up Rate of 4K/s with Pellet Diameter of 9.1 mm (Figure 16, [2.6])

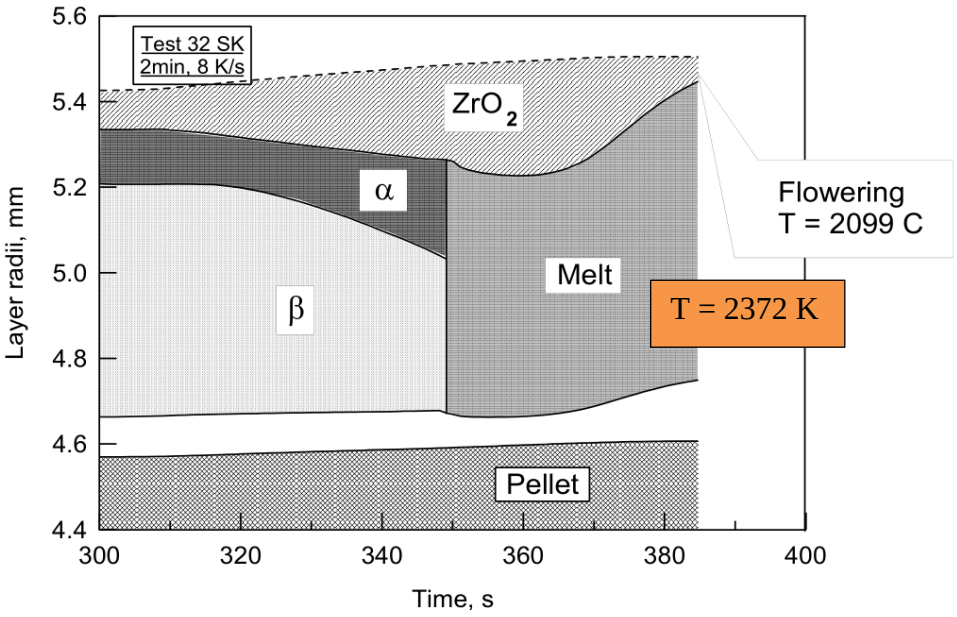

Figure 2.5 - Flowering Failure of ZrO_2 Shell at a Heat-Up Rate of 8 K/s (Figure 15, [2.6])

The epistemic uncertainty for the *MZBT* was previously characterized by a triangular distribution because only three points (a lower bound, a most likely value, and an upper bound) are available [2.1]. The lower bound is defined as the Zircaloy melting temperature of 2100 K. The upper value of 2540 K was selected in the hydrogen uncertainty study [2.1] based on qualitative consideration of α-ZrO phase diagram and observations/analyses of the PHEBUS experiments

[2.9]. The mode is 2400 K, the value used in the deterministic SOARCA analysis and the default MELCOR value [2.4]. The selection of a triangle distribution suggests that a most probable value for the uncertain parameter is the MELCOR recommended value (mode), with decreasing likelihood for values away from the most probable.

Subsequent to the current analysis, reference [2.10] was considered to improve the uncertainty distribution for *MZBT*. Figure 2.3 - Figure 2.5 show the results of high temperature fuel/cladding simulations and predicted two failure modes: (#1) erosion of the shell and (#2) rapid expansion of the shell which is subsequently stressed by unoxidized melt. Two simulations were conducted for the later failure mode to show variability due to pellet diameter uncertainties. During the updating process, the two failure modes were assigned equal weight (i.e., without knowledge of the transient conditions, it is assumed that failure modes #1 and #2 are equally likely to occur) and the two simulation results for failure mode #1 were assigned equal weight. The new data and their associated weights can be seen in Table 2.2. These weights will be used in equation (2-10) to create the new epistemic *MZBT* uncertainty distribution.

Table 2.2 – Molten Zircaloy Breakthrough Temperature Estimates from S/Q Simulations

Failure Mode	*Figure #*	*MZBT Temperature*	*Weight*
#1-Surface stress exceeds the flexural limits.	Figure 2.3	2393 K	0.5
#1-Surface stress exceeds the flexural limits.	Figure 2.4	2223 K	0.5
#2- Oxide shell erodes and is too thin	Figure 2.5	2372 K	1

During the 1F1 UA, it is believed that the triangular distribution prescribed too much certainty on the MELCOR default value for *MZBT*, given the limited information available. In order to move the information density away from the MELCOR default and toward the tails of the distribution, the Fukushima UA study converted the triangular distribution into a beta distribution which preserved the mode and mean of the triangular distribution. A BMLE transformation, which preserves the mean and the standard deviation of the original distribution, simultaneously shifts the mode away from the default MELCOR value and increases the confidence in that new mode.

The epistemic *MZBT* distribution found in Table 2.1 was created by combining the original epistemic uncertainty distribution defined above with the simulation data in Table 2.2 using Bayesian updating. Details regarding the Bayesian updating process can be found below, although many readers may wish to skip ahead to Section 2.2.2.

The Bayesian updating process evaluates the likelihood of the simulation data against the prior understanding of potential breakthrough temperatures. The prior distribution is represented by a mean/mode beta transformation from the triangular distribution. The likelihood function takes the form of a Generalized Binomial Distribution (GBD) to allow for incorporation of the non-integer weighted data [2.11]. The posterior distribution then takes the form of the beta distribution because the binomial and beta distributions are conjugate distributions, which can be found in Table 9.1 of [2.12]. A detailed description of the updating process follows:

Step 1: Define the Prior Distribution.

The 1F1 UA uses a shifted Beta distribution with lower bound (*LB*) of 2100K, upper bound (*UB*) of 2540 K, and the shape parameters α = 5.58 and β = 6.42. These shape parameters were chosen to preserve the mean and the mode of the Peach Bottom UA prior distribution.

$$\pi(Temp) = Beta(Temp|LB, UB, \alpha, \beta) \tag{2-2}$$

Step 2: Define the Likelihood Function

The likelihood function selected to examine the likelihood of the prior distribution given the new evidence is a GBD. The binomial distribution is defined as:

$$L(k, n|p) = \left(\frac{n!}{k!(n-k)!}\right) p^k 1 - p^{n-k} \tag{2-3}$$

where there is evidence of *k* events happening in n trials with probability *p*. Written in this form, the evidence must be provided in integer values. For the *MZBT* temperature, the evidence is a temperature value, or a fractional value between the upper bound and the lower bound. This will be explained later, but is mentioned here to specify that the likelihood function must be modified to account for non-integer values. It has been shown in [2.11] and using [2.13] that the gamma function can be substituted for factorials while allowing for non-integer values through the definition of the gamma function presented in equation (2-4).

$$x! = \Gamma(x + 1) \tag{2-4}$$

Thus, equation (2-3) can be transformed into the GBD in (2-5):

$$L(k, n|p) = \left(\frac{\Gamma(n+1)}{\Gamma(k+1)\Gamma(n-k+1)}\right) p^k 1 - p^{n-k}. \tag{2-5}$$

Using (2-5), it is now possible to use the GBD to evaluate positive non integer evidence. Here is an example to demonstrate constancy with the binomial distribution. Imagine that a system exists with two parallel primary components. The system works per design 8 out of 10 times, each component failing once on different tests. Though this system met success criteria (one out of two in operation), a risk analysis may wish to treat each failure as a partial failure. Thus, each failure may be treated a ½ a failure in the binomial distribution.

Ultimately, the factorial and/or gamma terms will factor out in the Bayesian updating process and thus the transformation is only academic.

Step 3: Transform the Evidence to be consistent with the Likelihood Function

The binomial and beta distributions (or at least MATLAB's formulations of these distributions) bound the random variable between zero and one. Thus, the *MZBT* temperature must be transformed to fall between zero and one. The transformation of the i^{th} piece of evidence E^i is defined in (2-6):

$$p^i = \frac{E^i - LB}{UB - LB}. \tag{2-6}$$

Step 4: Conduct the Updating With Unequally Weighted Likelihood Functions

Nominally, the Bayesian updating process would treat all evidence equally. The general equation for Bayesian updating can be seen in Equation (2-7):

$$\pi(Temp|E) = \frac{1}{c} L(E|Temp) * \pi(Temp) \quad (2\text{-}7)$$

where c is a normalizing constant and E the collection of evidence used in the updating process (i.e., k and n above). If each piece of evidence is considered separately, (2-7) becomes (2-8):

$$\pi(Temp|E) = \frac{1}{c} \pi(Temp) \prod_{i=1}^{N} \{L(E_i|Temp)\}, \quad (2\text{-}8)$$

where $\prod_{i=1}^{N} \{L(E_i|Temp)\}$ is the product of likelihood functions for each piece of evidence. Equation (2-8) can be generalized further to incorporate unequal weighting of evidence by raising each likelihood function to the power of its weight. This ensures that the weights are additive in the product likelihood function:

$$\pi(Temp|E) = \frac{1}{c} \pi(Temp) \prod_{i=1}^{N} \{L(E_i|Temp)\}^{w_i}. \quad (2\text{-}9)$$

Figure 2.6 and Figure 2.7 show the Fukushima *MZBT* distributions.

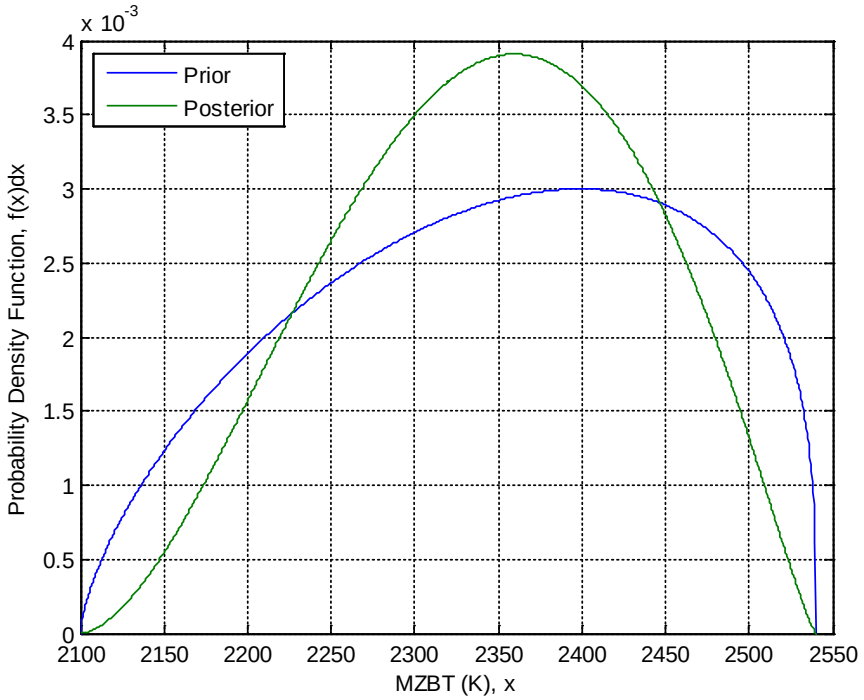

Figure 2.6 – Fukushima *MZBT* Uncertainty PDFs: Blue = Prior Density Function, Green = Updated Density Function.

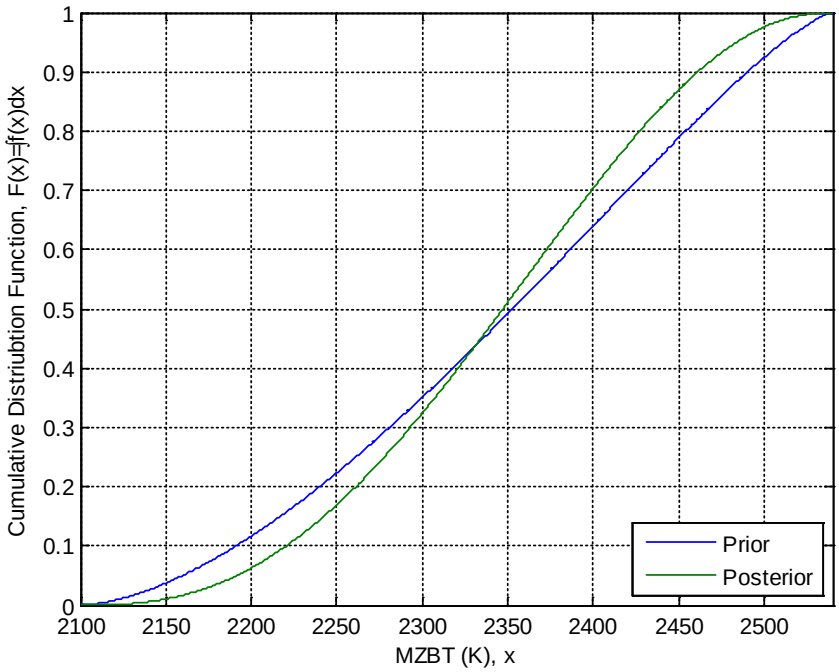

Figure 2.7 – Fukushima *MZBT* Uncertainty CDFs. Blue = Prior Density Function, Green = Updated Distribution.

2.2.2 Decay Heat

Decay heat is the initial driving force for most accidents in nuclear power plants. It is the dominant energy source for severe accidents of shutdown LWRs, such as the 1F1 station blackout accident sequence. Given this, uncertainties in the radionuclide inventories and decay data lead to uncertainties in the time-dependent production of decay heat.

For the Fukushima uncertainty analyses, it is impractical to characterize the epistemic uncertainties associated with the buildup and decay of radionuclides. Fortunately, it is feasible to run SCALE [2.14] calculations to determine best estimate values of the following three parameters:

- Time-dependent decay heat reduction,
- Power fraction amongst fissile isotopes at reactor scram, and
- Radionuclide inventories.

The first two outputs can be used to supplant the nominal decay heat estimates in ANS-5.1, thus allowing SNL to combine the ANS-5.1 [2.16] time-dependent decay heat uncertainties on primary fissile nuclides with the SCALE best estimate curves [2.15].

ANS-5.1 provides conservative time dependent decay heat curves for four nuclides (i.e., U-235, U-238, Pu-239, and Pu-241) on a per-fission basis along with a 1-sigma uncertainty estimate for each of the four nuclides in tabular form with 79 entries starting at 1 second after shutdown and ending at $1x10^{13}$ seconds ($3.2x10^{5}$ years) after shutdown. This analysis truncates the ANS data at $1x10^{6}$ seconds, thus only including the first 37 entries for each nuclide table. Thus, this method

will sample the decay heat for each isotope 37 times per simulation. From literature [2.17][6], a correlation coefficient of 0.8 was selected. A large correlation was desired because hotter-than-expected parent nuclides likely lead to hotter-than-expected daughter nuclides, not significantly cooler daughter nuclides.

ANS-5.1 breaks decay heat estimates into short-term and long-term irradiation components. These components are then combined to produce burn-up specific decay heat estimates. While the short term and long term variability in decay heat estimates are important to the base decay heat curve (which this analysis replaces with a SCALE calculation), the time dependent 1-sigma uncertainty estimates were comparable. Thus, for simplicity only the long-term irradiation 1-sigma values were utilized to determine the relative decay heat variability around the base case SCALE simulation estimates.

The first stage of sampling was conducted for the time dependent decay energy release for each of the four isotopes using the multivariate normal distribution with the covariance matrix derived from the time dependent 1-sigma estimates and the correlation coefficient of 0.8. The horse-tail results of this analysis can be seen in Figure 2.8. These results are independent of any light water reactor type or time in cycle calculation. As can be seen from the figure, uncertainties in decay heat are dominated by fissioning of U-238 and Pu-241.

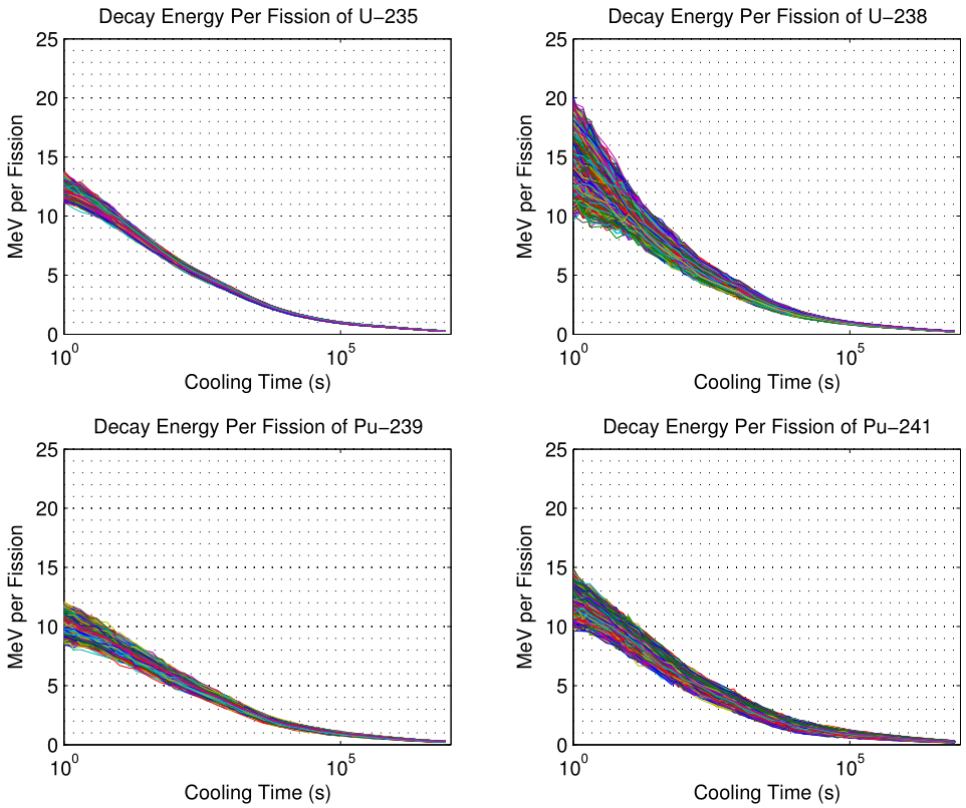

Figure 2.8 – Decay Energy Uncertainty for each of the Four Isotopes in ANS-5.1.

[6] This reference is dated 1979 and only examined U-235 decay heat. A more current reference including additional data for U-235 and any data from U-238, Pu-239, and Pu-241 would improve the accuracy of this methodology.

Next, the isotopic decay heats for each sample were multiplied by the best estimate power fractions provided by SCALE and summed to give the total MeV/fission for the time at cycle (or the unit in the case of Fukushima). The MeV per fission curves for reactor configuration *k* can be calculated with equation (2-10), where the time dependent vectors $E_k^i(t)$ or $E_j^i(t)$ are i^{th} the MeV per fission curve for configuration k (time at cycle and/or unit number) and *j* is the isotopic index number. The power fractions (F_j^k**)** from SCALE can be found in Table 2.3.

$$E_k^i(t) = \sum_{j=1}^{4} F_j^k E_j^i(t) \tag{2-10}$$

Table 2.3 – Fukushima Unit 1, 2, and 3 Isotopic Power Fractions

Nuclide	*1F1*	*1F2*	*1F3*
U-235	0.48	0.56	0.55
U-238	0.070	0.065	0.067
Pu-239	0.37	0.32	0.32
Pu-241	0.074	0.053	0.063

Once the time dependent samples of $E_k^i(t)$ are computed, they can be normalized by the power fraction averaged ANS 5.1 point estimate curves for the four isotopes, $E_j(t)$. The normalized decay heat curves $\boldsymbol{E_k^i(t)}$ are:

$$\boldsymbol{E_k^i(t)} = \frac{E_k^i(t)}{\sum_{j=1}^{4} F_j^k E_j(t)}. \tag{2-11}$$

Then these normalized decay heat curves $\boldsymbol{E_k^i(t)}$ can be multiplied by the SCALE computed decay heat curves for each reactor configuration $P_k(t)$ at each point (i.e., the notation $.*$ is used instead of traditional vector multiplication) in time to obtain:

$$P_k^i(t) = P_k(t) .* \boldsymbol{E_k^i(t)}, \tag{2-12}$$

where $P_k^i(t)$ is the i^{th} realization of the decay heat curve for reactor configuration *k*.

The decay heat curves for 1F1, 1F2, and 1F3 (of which the 1F1 UA only utilizes the 1F1 decay heat curves) can be seen in Figure 2.9, Figure 2.10, and Figure 2.11. Each curve, $P_k^i(t)$, is equally likely and the database of $P_k^i(t)$ curves are sampled without replacement with equal weighting.

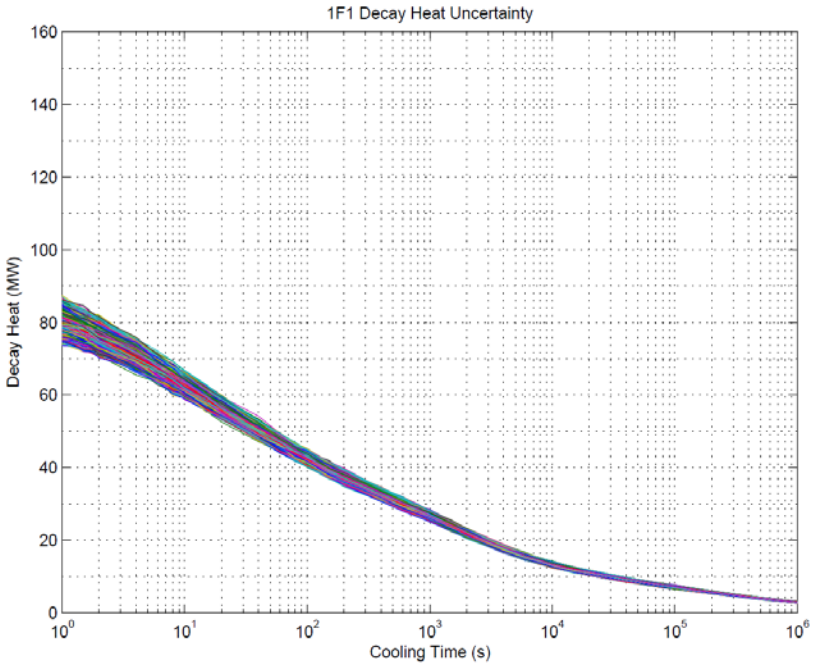

Figure 2.9 – Fukushima 1F1 Decay Heat Curve Horsetails.

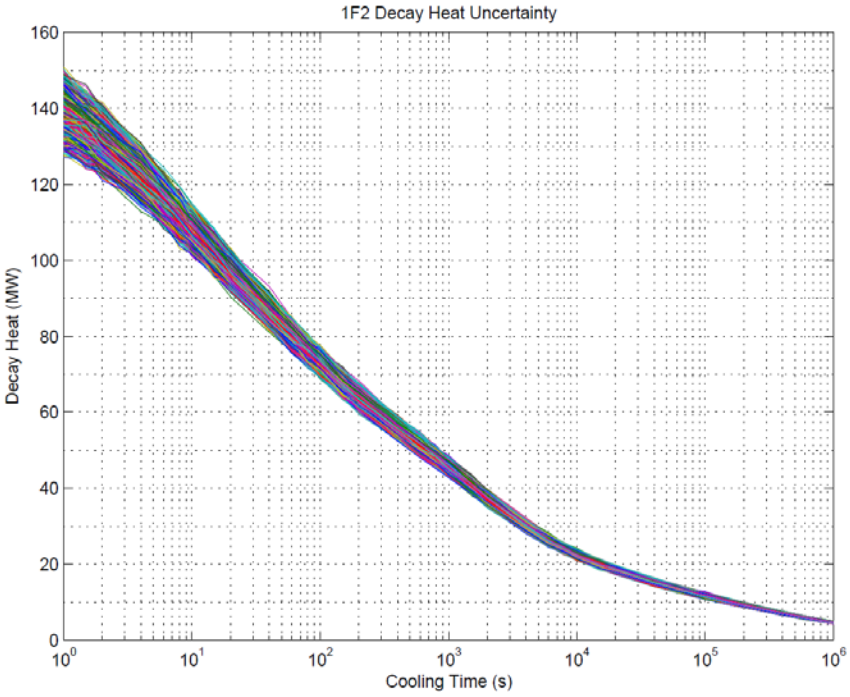

Figure 2.10 - Fukushima 1F2 Decay Heat Curve Horsetails.

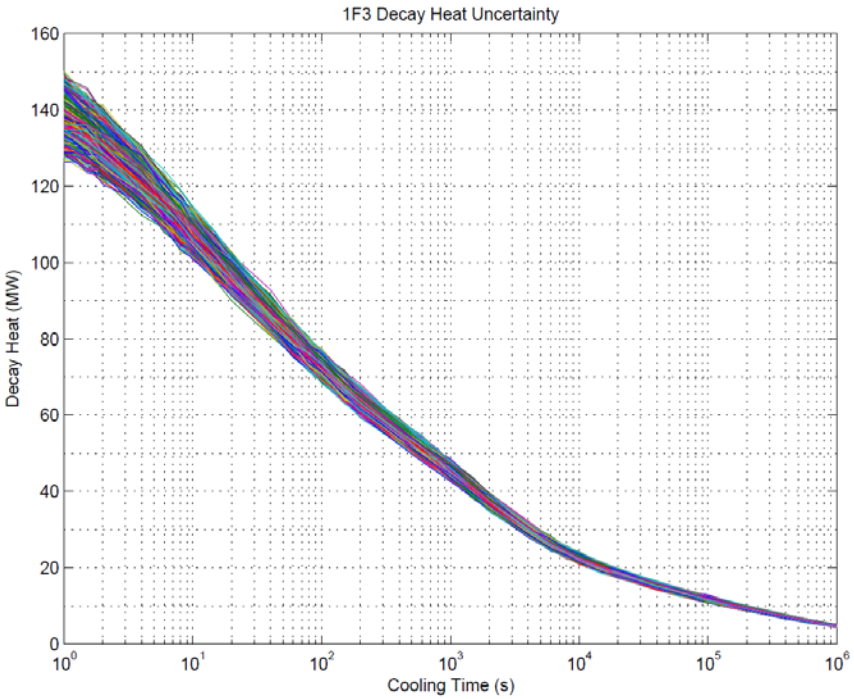

Figure 2.11 - Fukushima 1F3 Decay Heat Curve Horsetails.

2.2.3 Time at Temperature

The current 1F1 MELCOR representation lacks detailed mechanistic models for evaluating fuel mechanical response to the effects of cladding oxidation, material interactions (i.e., eutectic formation), Zircaloy melting, fuel swelling, and other processes that occur at very high temperatures.[7] In lieu of detailed models, a simple temperature-based criterion is used to define the threshold beyond which normal ("intact") fuel rod geometry can no longer be maintained, and the core materials at a particular location collapse into particulate debris. The temperature-based criterion reflects physico-chemical processes that affect fuel rod integrity. Using a composite of information, such as from the PHEBUS studies [2.9], four data points were log-linearly interpolated to create the rod collapse criteria used in the SOARCA study. This time-at-temperature criterion was introduced in an attempt to avoid non-physical cliff-edge effects that are observed during a calculation when fuel temperatures are predicted to hover just below a failure temperature for extended periods. However, the code still models local rod collapse due to high temperature as a discrete and near-instantaneous (over one time step) event at each core cell.

[7] One MELCOR fuel rod collapse parameter which may or may not be used is the COR_CCT record that specifies the minimum unoxidized metal thickness that can support intact rod geometry (once metal thickness drops below the threshold vale in the local COR cell, the rods are instantly converted to particulate debris). From the MELCOR COR reference manual: "It is possible for a fuel rod to be hot but unoxidized, either as a result of heating in an inert environment or following total loss of ZrO_2 through candling involving secondary transport or eutectics. As currently coded, such a rod will be converted to particulate debris when the remaining metal thickness falls below the user-specified minimum value" (on COR_CCT).

The *TaT* is a time-at-temperature structural representation of the remaining lifetime of the fuel rod system. Thus, the *TaT* is an integral damage model, where rubblization of the core region is predicted when the damage fraction (DF)[8] equals one. The DF is defined by Equation (2-13) where, Δt_i is the width of the i^{th} time step and $L_i(T)$ is the lifetime value during the i^{th} time step (fresh material is expected to fail at temperature *T* for the lifetime *L(T)*, and *T* is the temperature in Kelvin).

$$DF = \sum_{i=1}^{N} \frac{\Delta t_i}{L_i(T)} \tag{2-13}$$

The purpose of this function is to ensure realism in the simulation by ensuring high temperature failure pathways exist even if failure threshold values are not exceeded. The original SOARCA version of the *TaT* was developed to force rubblization of the fuel rod between 2500K and 2700K to provide consistency with the PHEBUS experiments [2.9].

The original SOARCA version of the *TaT* curve has three distinct regions. The first region shows a rapid decrease in lifetime, from effectively infinite (in severe accident time scales) to 10 hours near the melting point of zirconium. The lifetime then drops from 10 hours at 2100K to 1 hour at 2500K. At this point, the PHEBUS experiments demonstrated that eutectic effects start to weaken the structural integrity of the fuel assembly. Thus, the lifetime of the fuel assembly decreases rapidly after 2500K, down to 1 minute at 2700K.

TaT is only one of three parameters which can cause the fuel rod to rubblize. The other two parameters are:

- Melting of either the fuel or oxide shell, and
- Collapse of the core support structure.

A distribution of *TaT* curves was developed using the Bayesian updating process described in the subsections below by combining insights from previous uncertainty analyses with the time temperature profiles prior to fuel collapse from the VERCORS tests [2.10] (see Figure 2.12). It is assumed that the Arrhenius equation is an acceptable first order model to determine the expected lifetime at a given temperature. Thus, the damage model is defined as in Equation (2-14):

$$\frac{1}{L(T)} = A * exp(BT) \ , D(t) = \sum \left(\frac{1}{L(T)} * \Delta t \right) \tag{2-14}$$

[8] Also referred to as a cumulative damage fraction, but this parameter will be referred to as a DF in this report to avoid confusion with the cumulative distribution function (CDF).

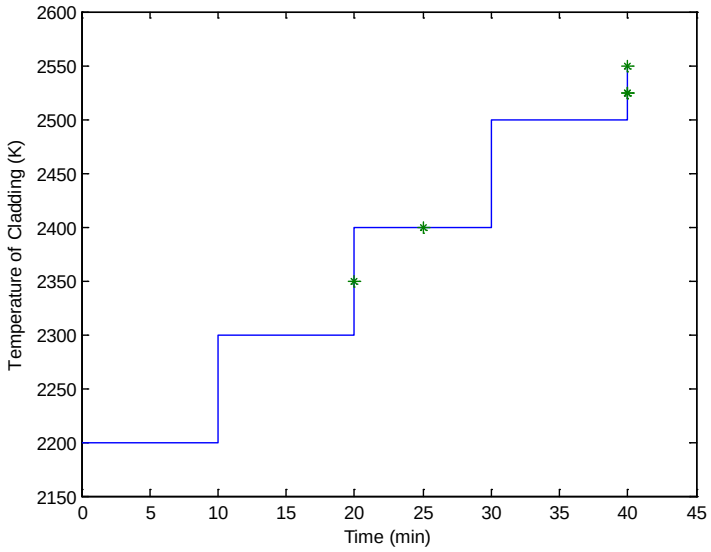

Figure 2.12 - Time at Temperature Histories From the VERCORS Experiments [2.10]. All tests underwent identical temperature ramps, stars indicate fuel collapse times.

2.2.3.1 Defining the Likelihood Function

Due to a combination of experimental variability and model inadequacy, no one combination of *A* and *B* in Equation (2-14) will result in each VERCORS experiment predicting failure when damage equals 1.0. Thus, a lognormal likelihood function was utilized to determine the probability that a given combination of A and B describes the VERCORS data. The lognormal distribution was chosen in part due to the exponential dependency between lifetime and temperature, but other likelihood distributions may be more appropriate and should be examined in future work. The likelihood function is defined in Equation (2-15), where *E* is evidence, or the collection of predicted damage fractions from a given combination of *A* and *B* at the fuel collapse time (D_1 ,D_2 ,…,D_N), and σ is the standard deviation of the log transformation of the damage fractions. Because the desired mean corresponds to a damage fraction of 1.0, which is defined as 0.0 under log transformation, no μ term appears in the likelihood function.

$$L(E|A,B,\sigma,M) = \prod_{i=1}^{N}\left[\frac{1}{D_i * \sigma * \sqrt{2\pi}} * \exp\left(-\frac{\ln(D_i)}{2\sigma^2}\right)\right] \quad (2\text{-}15)$$

2.2.3.2 Defining the Prior Distributions

The damage fraction model used in the 1F1 MELCOR representation uses one aleatory and two epistemic parameters to determine the likelihood of fuel collapse from the VERCORS data. Each of these parameters needs prior distributions to describe the state of knowledge before the Bayesian updating process. The prior distribution for the aleatory component of uncertainty, $\pi(\sigma)$, describes the likelihood of experimental variability associated with a given DF that would allow fuel collapse through inherent experimental randomness. Then the prior joint epistemic uncertainty, $\pi(A,B)$, will be developed to describe the best state of knowledge in fuel collapse that a given combination of the shape parameters *A* and *B* in Equation (2-14) will result in when predicted by the damage fraction model.

The prior distribution of, or the understanding of the potential values for, the lognormal distribution's aleatory term σ was extracted from the raw VERCORS data and the original piecewise SOARCA *TaT* curve [2.7]. It is desirable to fully separate prior distributions from the evidence, but in this case the expected distribution of potential model variance was difficult to ascertain without looking at the data; the utilization of a non-Arrhenius *TaT* curve reduces the potential for self-reinforcing information feedback. First, the SOARCA *TaT* curve was used to calculate the damage fraction at failure time for each VERCORS experiment. The distribution of failure DFs can be seen in Figure 2.13, with a MLE of σ of 0.59 and a 95% confidence interval of [0.37 to 1.45]. This information was used to develop the prior distribution of σ, or $\pi(\sigma|M^*, E^*)$, where M^* is the SOARCA *TaT* curve and E^* is the collection of VERCORS DFs at failure.

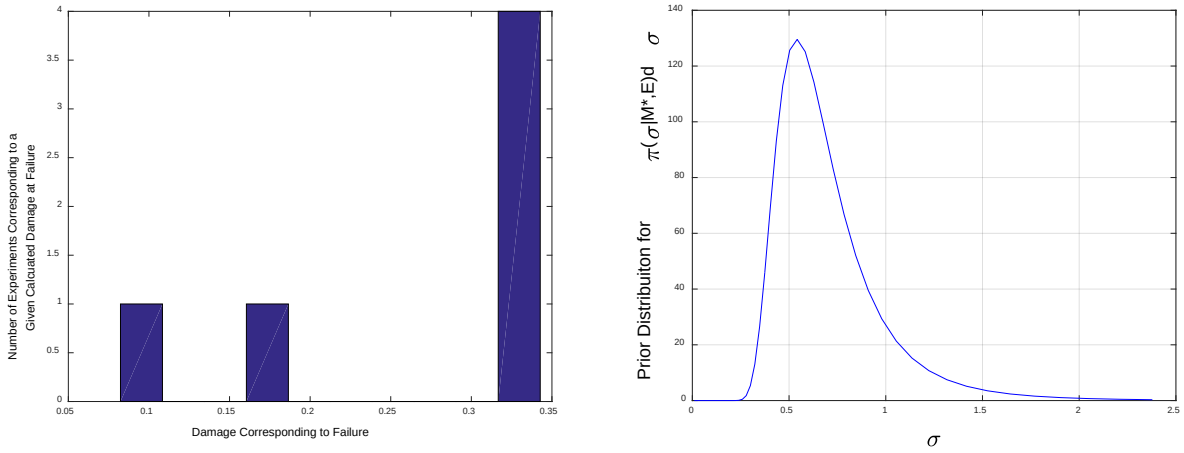

Figure 2.13 – Histogram of Damage Fractions Corresponding to Failure Using the SOARCA DF Model and Corresponding Prior Distribution of σ. Count are experimental failures from the VERCORS tests, with 6 tests in total.

The initial likelihoods of the shape parameters A and B were extracted from assessments from the Peach Bottom UA [2.2] and expert elicitation from the VERCORS failure temperatures (excluding the time at temperature information). These shape parameters were evaluated though Arrhenius fits of independent Monte Carlo samples from two distributions: one which varied over fuel lifetime at 2100K taken from the Peach Bottom UA and the other which varied the temperature corresponding to one minute of fuel lifetime at that temperature taken from expert elicitation. These two distributions are defined in Equation (2-16), where T is temperature, L(T) is lifetime at a given temperature, *EF* is the Error Factor of the lognormal distribution ($\frac{\lambda_{95}}{\lambda_{05}}$). SurryUA implies that unpublished work from the Surry UA was leveraged and Experts implies that expert elicitation was leveraged.

$$\begin{aligned} \pi(L(T)|T = 2hrs, SurryUA) &= LogNormal(\ln(T), EF = 10) \\ \pi(T|L(T) = 1min, Experts) &= Normal(\mu = 2479K, \sigma = 89K) \end{aligned} \tag{2-16}$$

It should not be surprising that this methodology creates a correlation between *A* and *B*. Thus, a linear relationship was developed between *B* and the natural log of *A* so that *B* can be treated as an independent variable and *A* can be treated as a conditional distribution. The linear relationship and conditional distribution are defined in Equation (2-17). The marginal prior of *B*|*M*, the

conditional prior of *A*|*B*,*M*, and the joint prior $\pi(A, B\,|M)dAdB$ can be seen in Figure 2.14. The joint prior is calculated as a product of the marginal and conditional prior.

$$\mu_{\ln(A)}(B) = -3 * B - 2295 + \epsilon$$
$$\pi(ln(A)\,|B) = N(\,ln(A)\,\big|\,\mu_{ln(A)}(B)\;,(\sigma\,\big|\,\epsilon), M) \tag{2-17}$$

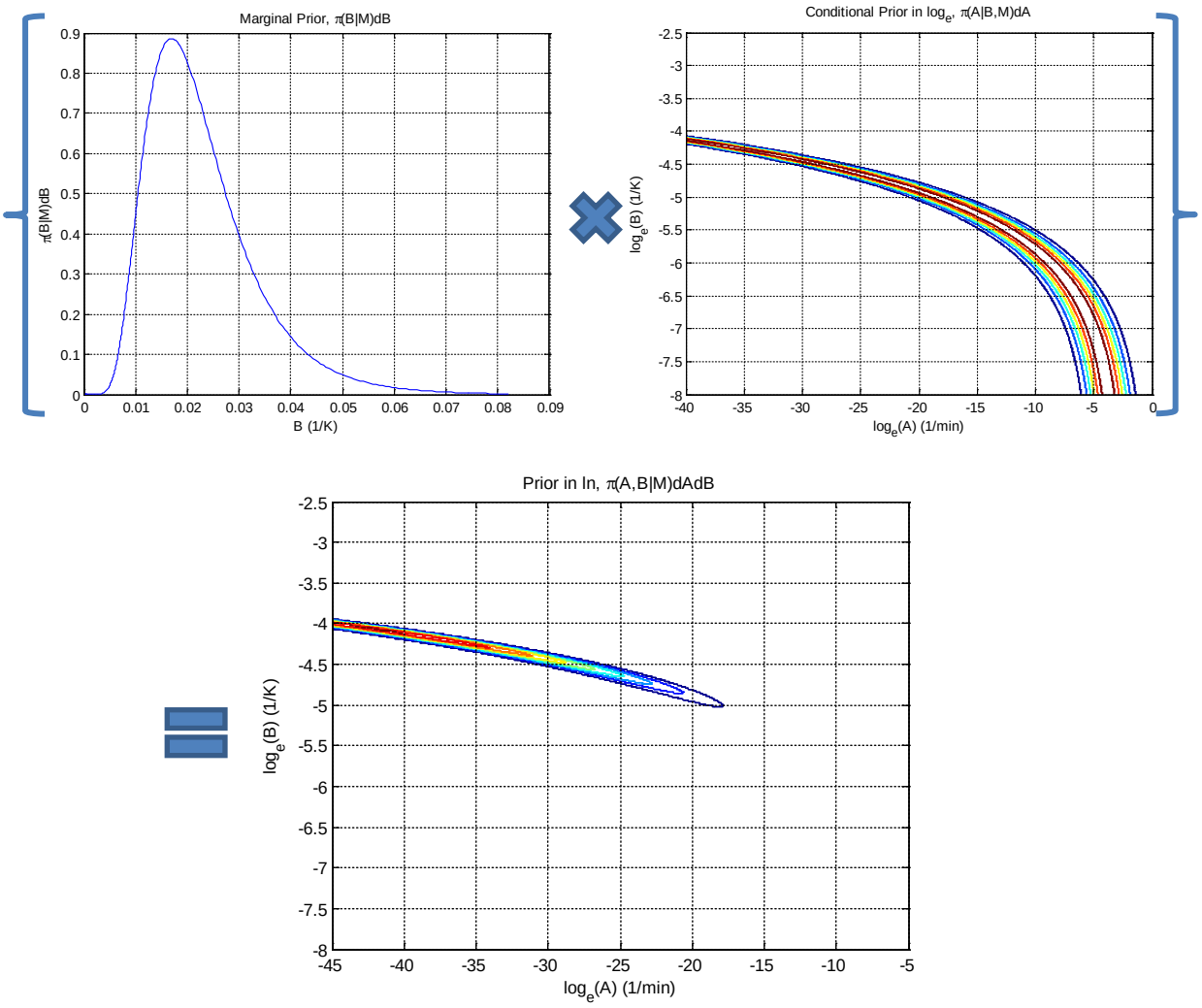

Figure 2.14 – Marginal Prior Distribution for B|M, Contour plot Conditional Prior Distribution for A|B,M, and Joint Prior Distribution $\pi(A, B|M)dAdB$

The full joint prior distribution, $\pi(A, B, \sigma\,|M, M^*, E^*)dAdBd\sigma$, is calculated via the multiplication rule found in Equation (2-18).

$$\begin{aligned}\pi(A, B, \sigma|M)dAdBd\sigma &= \pi(A, B|M)dAdB * \pi(\sigma|M^*, E^*)d\sigma \\ &= \pi(A|B, M)dA * \pi(B|M)dB * \pi(\sigma|M^*, E^*)d\sigma\end{aligned} \tag{2-18}$$

2.2.3.3 Calculating the Posterior Distribution

Once the prior distribution and likelihood functions are defined, Bayes Theorem [Equation (2-19)] is then applied to combine the prior judgment of the likelihood of *A*, *B*, and σ values with

the experimental information from the VERCORS failure temperatures to produce a new understanding of the probability of A, B, σ sets. With enough information, the product term in the likelihood function $L(E|A,B,\sigma,M)$ defined in Equation (2-15) outweighs the prior distribution. Without a preponderance of new information, the prior distribution outweighs the likelihood function and the state of knowledge does not substantially change. In this way, Bayesian methods can be used to protect analyses from misinterpreting small samples of information.

$$\pi(A,B,\sigma|E,M)dAdBd\sigma = \frac{L(E|A,B,\sigma,M) * \pi(A,B,\sigma|M)dAdBd\sigma}{\int L(E|A,B,\sigma\ ,M) * \pi(A,B,\sigma|M)dAdBd\sigma} \qquad (2\text{-}19)$$

Because MELCOR always assumes fuel collapse at DF = 1.0, the σ term, while important to include during the Bayesian updating process, is not important to the final MELCOR calculations and is thus integrated out of the final analysis. Therefore, the subsequent figures presented in this report were created after performing the integration over all possible values of σ as seen in Equation (2-20).

$$\pi(A,B|E,M)dAdB = \int_0^\infty \pi(A,B,\sigma|E,M)dAdBd\sigma \qquad (2\text{-}20)$$

By discretizing A, B, and σ, the numerator of Equation (2-19) can be calculated numerically for millions of combinations of A, B, and σ. These combinations can then be numerically integrated over to solve for the normalization constant in the dominator of Equation (2-19). Contour plots of the prior, likelihood, and posterior functions, all three averaged over $\pi(\sigma)d\sigma$, can be seen in Figure 2.15 and Figure 2.16.

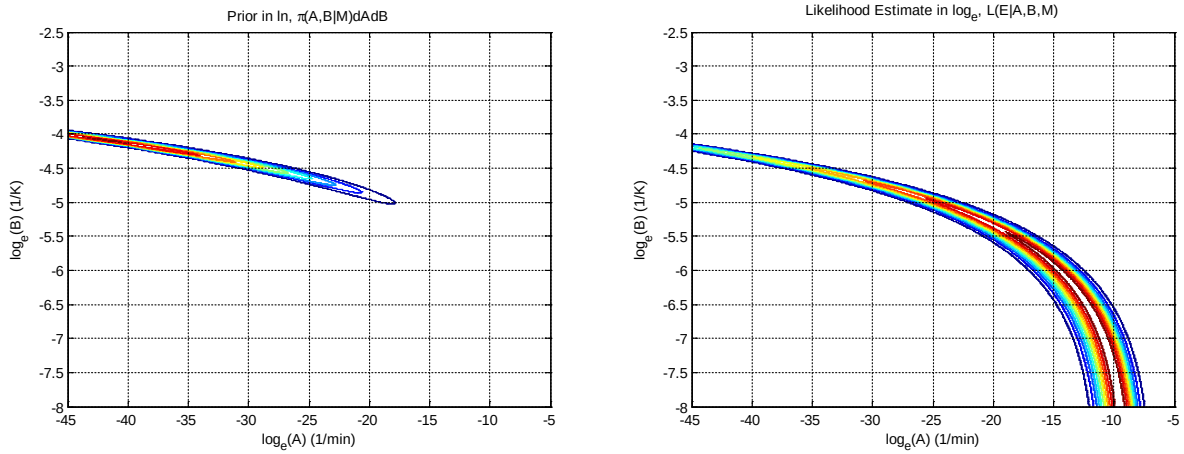

Figure 2.15 – Prior and Likelihood Contour Plots

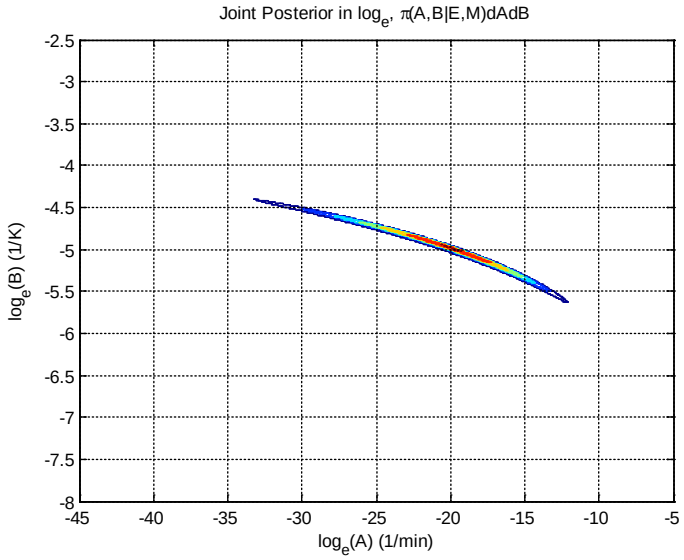

Figure 2.16 – Posterior Distribution

A 3-D view of the joint posterior distribution, $\pi(A, B \mid E, M)dAdB$, can be seen in Figure 2.17. The posterior joint distribution resulting from the Bayesian updating process described herein is referred to as the SharkFin distribution due to the fin-like shape of the probability density function in Figure 2.17. This distribution is sampled to select (*A*, *B*) pairs to define SharkFin *TaT* curves for the 1F1 UA. The distribution of SharkFin *TaT* curves overlaid on top of the original SOARCA curve can be seen in Figure 2.18.

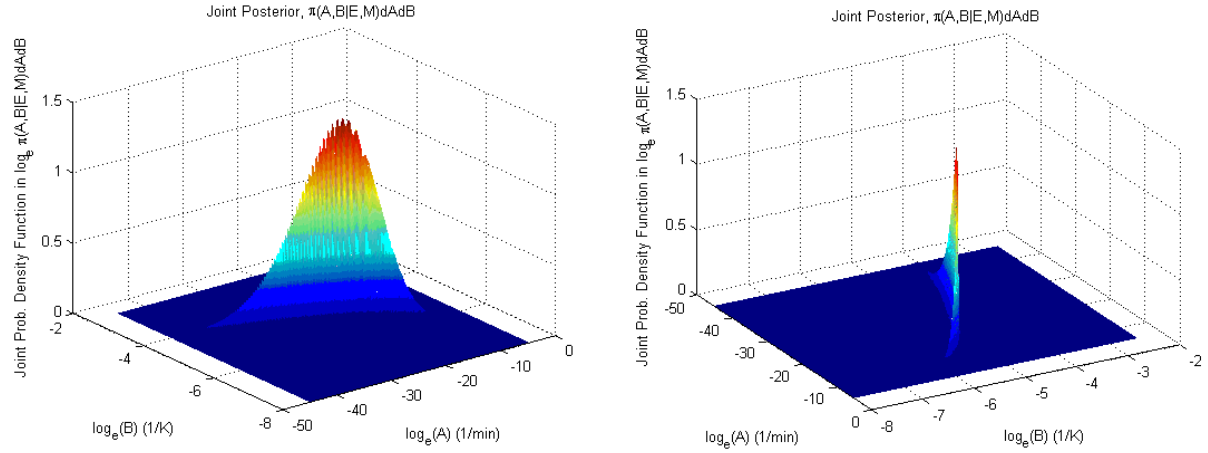

Figure 2.17– Plot of the Joint Posterior Distribution, $\boldsymbol{\pi(A, B \mid E, M)dAdB}$.

For use in follow-on studies, the median *TaT* curve is:

$$\frac{1}{L_{50^{th}}(T)\{sec\}} = 2.16x10^{-11} * exp(7x10^{-3} * T) \qquad (2\text{-}21)$$

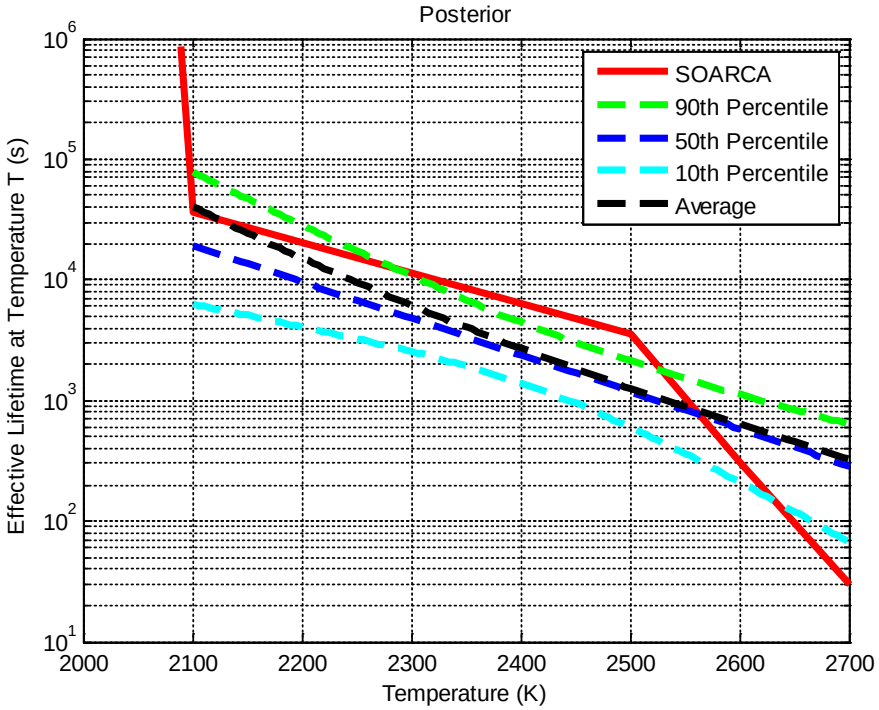

Figure 2.18 – Posterior Statistical Representation of Shark-Fin Failure Curves Overlaid on the SOARCA [2.7] Time at Temperature Failure Curve.

2.3 Aleatory Uncertainties

No additional explicit aleatory uncertainties were included in this analysis because the focus was on exploring the impact of core degradation uncertainties. In MELCOR, most of the core degradation parameters that can be sampled are either purely epistemic or an inseparable mixture of epistemic and aleatory uncertainties.

2.4 SOARCA Peach Bottom Uncertainties Not Included in This Report

The Fukushima UA only explores core degradation phenomena and does not extend to containment performance and offsite releases. The Fukushima UA also does not address sequence uncertainties, which may be handled in follow-up analyses. The neglect of sequence uncertainties facilitates a concentrated analysis of the uncertainties involved in modeling core degradation and in-vessel accident phenomena using MELCOR.

2.5 References

[2.1] R.O. Gauntt, N. Bixler, and K.C. Wagner, An Uncertainty Analysis of the Hydrogen Source Term for a Station Blackout Accident in Sequoyah Using MELCOR 1.8.5, Sandia

National Laboratories, SAND2014-2210, Sandia National Laboratories, Albuquerque, NM, 2003.

[2.2] U.S. Nuclear Regulatory Commission, State-of-the-Art Reactor Consequence Analyses Project: Uncertainty Analysis of Unmitigated Long-Term Station Blackout of the Peach Bottom Atomic Power Station-Draft Report, NUREG/CR-7155, SAND2012-10702P, Washington, DC, 2012.

[2.3] K. M. Groth, M. R. Denman, J. N. Cardoni, T. A. Wheeler, Proof of Principle Framework for Developing Dynamic Risk-Informed Severe Accident Management Guidelines, SAND2013-8324, Sandia National Laboratories, Albuquerque NM, September 2013.

[2.4] R.O. Gauntt, et al., MELCOR Computer Code Manuals, Vol. 2: Reference Manuals, Version 1.8.6 (Vol. 2, Rev. 3)," U.S. Nuclear Regulatory Commission, NUREG/CR-6119, Washington, D.C., 2005.

[2.5] J. Renoylds, MELCOR Uncertainty Engine User Manual, Sandia National Laboratories, 2014.

[2.6] P. Hofmann et al., ZrO_2 Dissolution by Molten Zircaloy and Cladding Oxide Shell Failure. New Experimental Results and Modeling, Wissenschaftliche Berechte, INV-CIT(98)-P026, Dezember 1999.

[2.7] U.S. Nuclear Regulatory Commission, State-of-the-Art Reactor Consequence Analyses (SOARCA) Report, NUREG-1935,Washington, DC, 2012.

[2.8] T.J. Haste et al., In-Vessel Core Degradation in LWR Severe Accidents, European Commission, EUR16695EN, 1996.

[2.9] M.S. Veshchunov, A.V. Boldyrev, K. Muller, Study on Bundle Degradation and Molten Pool Formation in the PHEBUS Experiments, IBRAE Nuclear Safety Institute Russian Academy of Sciences, NSI-SARR-185-2004, December 2004.

[2.10] Y. Pontillon, et al., “Lessons learnt from VERCORS tests. Study of the active role played by UO2–ZrO2–FP interactions on irradiated fuel collapse temperature,” *Journal of Nuclear Materials*, 344, 265–273, 2005.

[2.11] G. Apostolakis & A. Mosleh, “Expert Opinion and Statistical Evidence: An Application to Reactor Core Melt Frequency”, *Nuclear Science and Technology, 70*, 135-149, 1979.

[2.12] A.H-S. Ang and W. H. Tang, Probability Concepts in Engineering, 2nd Ed., John Wiley & Sons, Inc., pg. 366-367, March 2006.

[2.13] MATLAB version 2014a, Natick, Massachusetts: The MathWorks Inc., 2010.

[2.14] B.J. Ade, NUREG/CR-7041, SCALE/TRITON Primer: A Primer for Light Water Reactor Lattice Physics Calculations, ORNL/TM-2011/21, Oak Ridge National Laboratory, Oak Ridge, TN, 2012.

[2.15] J. Cardoni, Radionuclide Inventory and Decay Heat Quantification Methodology for Severe Accident Simulations, SAND2014-17667, Sandia National Labs, Albuquerque NM, September 2014.

[2.16] American National Standard for Decay Heat Power in Light Water Reactors, ANSI/ANS-5.1-2005, American Nuclear Society, 2005.

[2.17] G.K. Schenter and F. Schmittroth, “Beta and Gamma Decay Heat Evaluation for the Thermal Fission of ^{235}U,” *Nuclear Cross Sections for Technology: Proceedings of the International Conference*, **594**, Knoxville, TN, 1979.

3 TREATMENT OF OUTPUT UNCERTAINTIES

Chapter 3 describes the output uncertainty treatment for the 1F1 uncertainty analysis. Once the uncertain parameters have been propagated through the 1F1 MELCOR representation, various statistical checks and evaluations can be employed to interrogate the output. This section reviews the convergence testing, scatter plot, and regression methodologies employed on the output data for Fukushima 1F1.

In its most general sense, Monte Carlo is simply a technique to evaluate integrals via random sampling of input parameter distributions. Often, but not always, these methods are used when the integrals are difficult to solve analytically or even numerically. For the 1F1 calculations, the integral is:

$$\overline{y} = \int f(\boldsymbol{X}|\boldsymbol{Z}) * \pi(\boldsymbol{X})\mathrm{d}\boldsymbol{X}$$

where $f(\boldsymbol{X}|\boldsymbol{Z})$ is the MELCOR output as a function of the uncertain vector of inputs **X**, with the epistemic uncertainties of all input variables contained in the matrix $\boldsymbol{X}$ defined by $\pi(\boldsymbol{X})\mathrm{d}\boldsymbol{X}$, and given the assumed certain inputs, $\boldsymbol{Z}$. The number of assumed certain inputs, $\boldsymbol{Z}$, is greater than the number of uncertain inputs, $\boldsymbol{X}$, by orders of magnitude.

3.1 Convergence Testing

Due to the non-linear nature of MELCOR calculations and the large number of uncertain parameters evaluated in this analysis, a full evaluation of the equation above would likely involve tens to hundreds of thousands of samples from $\pi(\boldsymbol{X})\mathrm{d}\boldsymbol{X}$. This degree of analysis was impractical for the 1F1 UA. Instead, this analysis focuses on resolving the median value (i.e. the 50th percentile) of the distribution of $f(\boldsymbol{X}|\boldsymbol{Z}) * \pi(\boldsymbol{X})\mathrm{d}\boldsymbol{X}$.

Because the 50th percentile is less sensitive to tail effects the median can often stabilize with only a few tens of Monte Carlo samples. In general, statistical convergence is similar to numerical convergence, in that the residuals (or the difference between the current estimate and the next estimate) are chosen to suit the needs of the analysis. A licensing or regulatory support calculation might require reduced sampling related uncertainty around the median than an exploratory calculation, such as this UA. As convergence criteria, the authors saw that the median often did not shift more than $0.5\frac{\%}{Sample}$ for the last 20% of the samples (e.g., if a replicate has one hundred realizations, no single realization between realizations eighty through one hundred should move the median estimate of the FoM by more than 0.5%). This criterion was deemed adequately stable for the sensitivity analysis.

Three graphical convergence tests were conducted on each sample. These tests were:

1. 1→N convergence of the 33rd, 50th, 67th percentiles. This examination was proposed to examine the degree to which the centroid of the distribution has converged and to determine if the outputs were symmetric or non-symmetric, not to demonstrate convergence of non-median values.
2. 1→N convergence of the bootstrap (i.e., resampled with replacement) median of a sample of MELCOR output FoMs.

3. Histograms of medians from a bootstrapped 80% of the Monte Carlo simulations with replacement. Ideally this histogram should consist of values with a margin of error appropriate for the analysis (the medians should have a standard error of less than 5%).

Due to the numerical methods and non-linearity, including cliff-edge affects in MELCOR, it is recognized that a best estimate input simulation does not correlate with any given output figure of merit (e.g. mean, median, mode). It should be emphasized that the intent of this UA is not to completely characterize the tails or the mean of the output distribution. Instead a representative percentile (i.e. median) is desired to represent the output.

3.2 Scatter Plots

Scatter plots of select output variables were examined to find visual trends in the data. Analytical techniques are extremely powerful tools for automated trend detection, but they can only detect what the analyst asks them to detect. Scatterplots can help an analyst ask the correct questions through subsequent analytical techniques and can be an important verification step to determine if an analytical technique is functioning properly.

3.3 Regression

Before stepwise linear regression is discussed, it is important to emphasize the purpose of the meta-models produced in the 1F1 UA. One approach to evaluating the capability of a regression to explain population variability is to use the regression to predict variability in new samples of data. Thus the data is broken into two sets (referred to in this report as a training set and a testing set). A predictive regression analysis is typically fit to the training set and then applied to the testing set to determine the predictive accuracy of the meta-model. It is extremely important that the testing and training set be divided randomly to prevent user bias in the evaluation process.

The regression analysis for the 1F1 UA is not conducted to produce a reduced order predictive relationship. Instead, this UA utilizes regression as a tool to determine which variables have higher (e.g. first) order effects on the FoM. While this approach is applied to the entire sample, the trends within the samples should be validated against other samples to ensure that potentially noisy system response does not introduce linear behaviors in the sample which are not indicative of the population.

Stepwise linear regression analysis was used to identify potential first order (i.e. linear) relationships between sampled inputs and FoM. Using matrix algebra to solve for linear regression parameters [3.1], the MELCOR output, $\mathrm{F}\begin{pmatrix}\overrightarrow{x_1}\\ \overrightarrow{x_2}\\ \vdots\\ \overrightarrow{x_N}\end{pmatrix}$, for a vector of uncertain inputs, $\overrightarrow{x_1}$, can be linearly approximated by:

$$\mathrm{F}\begin{pmatrix}\overrightarrow{x_1}\\ \overrightarrow{x_2}\\ \vdots\\ \overrightarrow{x_N}\end{pmatrix} \cong \mathbf{Y} = \mathbf{B}\,\mathbf{X} \cong \widehat{\boldsymbol{\beta}}\,\boldsymbol{X} + \in \qquad (3\text{-}1)$$

Where **Y** is the output vector, **B** is the actual vector of input coefficients, $\widehat{\boldsymbol{\beta}}$ is the inferred vector of input coefficients, and **X** is the set of input vectors with first and second order interactions between input variables. For the regressions conducted in this report, **Y** is the MELCOR output

vector of size n, where n is the sample size. The input matrix can potentially be as large as a *n* by 120 matrix consisting of first order, interaction, and quadratic behaviors of the input variables. **X**, **Y,** and $\widehat{\boldsymbol{\beta}}$ are shown in Equation (3-2).

$$\boldsymbol{Y} = \begin{bmatrix} y_1 \\ \vdots \\ y_n \end{bmatrix}, \boldsymbol{B} = \begin{bmatrix} B_1 \\ \vdots \\ B_n \end{bmatrix},$$
$$\boldsymbol{X} = \begin{bmatrix} X_{1,1} & \cdots & X_{1,15} & X_{1,1}^2 & X_{1,1}X_{1,2} & \cdots & X_{1,15}^2 \\ \vdots & \ddots & \vdots & & \vdots & \ddots & \vdots \\ X_{n,1} & \cdots & X_{n,15} & X_{15,1}^2 & X_{15,1}X_{15,2} & \cdots & X_{n,15}^2 \end{bmatrix} \tag{3-2}$$

From Equation (3-1), $\widehat{\boldsymbol{\beta}}$ can be solved for using Equation (3-3):

$$\widehat{\boldsymbol{\beta}} = (\boldsymbol{X}'\boldsymbol{X})^{-1}\boldsymbol{X}'\boldsymbol{Y} \tag{3-3}$$

Taking the variance of each side of Equation (3-3), it can be shown that the variance of the $\widehat{\boldsymbol{\beta}}$ vector can be computed as in (3-4)

$$Var(\widehat{\boldsymbol{\beta}}) = Var((\boldsymbol{X}'\boldsymbol{X})^{-1}\boldsymbol{X}'\boldsymbol{Y}) = \sigma^2(\boldsymbol{X}'\boldsymbol{X})^{-1} \tag{3-4}$$

where σ^2 is defined as the standard error of the population, which is approximated based on the sample (size n) by S^2 in (3-5). The number of degrees of freedom (or columns in the input matrix $\boldsymbol{X}$) is defined as k (i.e. dependent variables) + 1 (i.e., the constant).

$$\sigma^2 \cong S^2 = \frac{SSE}{n-k-1} \tag{3-5}$$

SSE, defined in (3-6), is the sum of the square of the errors and is defined by S_{yy} defined in (3-7), a measure of the variability in components of the MELCOR output vector, **Y** and SSR defined in (3-8), a measure of variability in the components of the regression output vector, $\widehat{\boldsymbol{Y}}$, to the MELCOR output.

$$SSE = S_{yy} - SSR \tag{3-6}$$

$$S_{yy} = \frac{(n\sum_{i=1}^{n} y_i^2 - (\sum_{i=1}^{n} y_i)^2)}{n} \tag{3-7}$$

$$SRR = \sum_{i=1}^{n} \hat{y_i}^2 - \frac{(\sum_{i=1}^{n} y_i)^2}{n} \tag{3-8}$$

Because statistical variability can cause regression techniques to identify false trends and dependencies, only terms which can estimate that a coefficient is ($\widehat{\boldsymbol{\beta}}_{\boldsymbol{i}}$) is not zero with high probability (typically greater than 5%), are included in a regression model. A pictorial example can be seen in Figure 3.1. It should be noted that confidence interval calculations for regression coefficients are dependent on additional statistical assumptions regarding the distribution of residuals which are likely violated in this analysis.

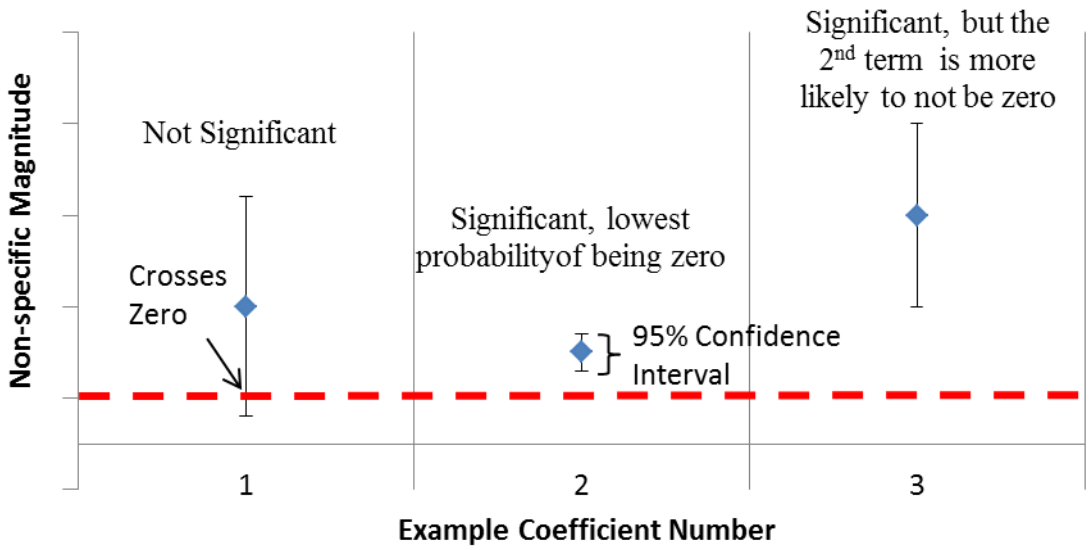

Figure 3.1. Graphical Example of Statistically Significant Coefficients [3.2]

A stepwise regression model is constructed as follows:

1. The average FoM output is used as the constant (A) term in the regression model with no other dependent terms.
2. Every dependent coefficient (B_{Xi}) is evaluated for addition to the meta-model. The coefficient with the lowest probability of being zero is added to the meta-model, so long as the probability of that term being zero is lower than 0.05. When a new term is added, the residuals (X-$X_{predicted}$) are readjusted to incorporate the predictive capability of the new model.
3. Step 2 is repeated with linear (X_i) and interaction (X_iX_j) terms until no additional terms have a probability of being zero that is less than 0.05.
4. The model is pruned by removing terms with dependent coefficients whose probability of being zero has risen above 0.1. Every time a term is added to a meta-model, the uncertainties of all other coefficients change as the meta-model estimates change. The uncertainties can either grow or shrink, and if the probability of being zero grows too large (>10%) they are removed from the analysis.
5. Steps 3 and 4 are repeated until no additional terms can be included or removed.

Statistical meta-model checks using R^2, R^2_{adj}, and the F statistic were conducted for each stepwise regression.

R^2 is the ratio between the variance explained by the model and the variance within the original data and is calculated in (3-9).

$$R^2 = \frac{SSR}{S_{yy}} = \frac{\sum_i(\hat{y}_i - \bar{y})}{\sum_i(y_i - \bar{y})} \tag{3-9}$$

One concern with using R^2 as the sole metric for determining the goodness-of-fit of a regression model is that if the number of terms in a regression model approaches the sample size, R^2 will

approach unity. Thus, it is common to adjust R^2 to penalize the goodness-of-fit measure for adding new terms. This R^2_{adj} is defined in equation (3-9).

$$R^2_{adj} = R^2 - (1 - R^2) * \frac{n-1}{n-k-1} \tag{3-10}$$

Finally, the F statistic is used to examine the following hypotheses: Is a simpler model more appropriate than the current model? The F-statistic is a two parameter statistic which requires:

- The population size,
- The degrees of freedom in the current meta-model,
- The degrees of freedom in the reduced meta-model, and
- SSE computed for both the current and the reduced meta-models.

The hypothesis test used in the 1F1 UA analysis answers the question: Is a constant model more appropriate than the regression model? Thus, the F-statistic is calculated as:

$$F_{Stat_{k,\ n-k-1}} = \frac{\frac{SSE_{constant} - SSE_{regression}}{k}}{\frac{SSE_{regression}}{n-k}} \tag{3-11}$$

After calculating the F statistic, the F distribution can be used to determine the probability that a constant meta-model is more appropriate than the regression model.

The stepwise regressions used to derive the desired FoMs were automated using the linear stepwise regression functionality (i.e., stepwiselm) found within MATLAB [2.13].

3.3.1 Model Summary Tables

The stepwise regression function used in MATLAB to perform all of the linear regressions begins by assuming that a constant model is appropriate. Then, the parameters are added and removed systematically from the model based on p-values obtained from the F-test described in section 3.3; parameters with a p-value greater than 0.05 were excluded from the regressions [2.13] and included in subsequent models unless their p-value exceeded 0.1. The final results of the stepwise regression procedure are presented in model summary tables in sections 6.2 and 6.3.

Each summary table (e.g. Table 6.2) lists coefficient estimates (**Estimate**), standard error estimates (**SE)**, and the t-statistic (**tStat**) with corresponding p-value (**pValue**) from the t-test for each parameter included in the model. In this context, the t-test was used to test the hypothesis that the regression coefficient for the predictor variable is zero given the current model. Thus, a p-value below 0.05 for a parameter indicates that within the current model, we have confidence that the regression coefficient for that parameter is non-zero. Similarly, a p-value above 0.1 indicates that we have less than 10% confidence that the regression coefficient for that parameter is non-zero. Hence, the p-values in the summary tables do not rank of the importance of the variables, but rather justify their inclusion in the model.

3.3.2 Regression Validation

The purpose of the regression analysis is not always to describe all of the variance in the system; indeed that objective may be difficult regardless of statistical technique. Instead, the purpose of these regression analyses is to identify which parameters have high impacts on physical FoM

when compared to nominal MELCOR precision. Put another way, MELCOR's results may have a high enough level of inherent variability that regression results can be skewed and/or representative of inherent variability rather than meaningful trends.

Thus the best regression is not necessarily the regression with the highest r^2 when fit to the sampled training data. The square of the regression coefficient can be defined as the fraction of response variance explained by the regression model [3.3]:

$$R^2 \cong r^2 = 1 - \frac{s_{Y|M}^2}{s_Y^2} \tag{3-12}$$

In equation (3-12), R^2 is the same R^2 as defined in equation (3-9), $s_{Y|M}^2$ is the variance of the Y output data given the output meta-model M, and s_Y^2 is the variance of the Y output data. s_Y^2 is defined in equation (3-10). For a regression fit, $s_{Y|M}^2$ is defined in equation (3-11), where the minus k term unbiased the estimate to account for the loss of degrees of freedom in the data as a result of the regression fit. s_Y^2 and $s_{Y|M}^2$ for the sample used to train the regression model are defined in equations (3-13) and (3-14).

$$s_Y^2 = \frac{1}{n-1}\sum_{i=1}^{n}(y_i - \bar{y})^2 \tag{3-13}$$

$$s_{Y|M}^2 = \frac{1}{n-k-1}\sum_{i=1}^{n}\left(y_i - y_{i|M}\right)^2 \tag{3-14}$$

In these formulations, k is the number of regressed terms in the meta-model, the -1 in the denominator is due to a loss of one degree of freedom involved in calculating the constant term (which equals the average output value $\bar{y}$ in the absence of a regression model), y_i is the i^{th} MELCOR output and $y_{i|M}$ is the i^{th} regression model prediction.

When a regression is fit to one sample and then applied to another sample, statistical estimates are no longer biased due to the loss of degrees of freedom. Thus, equation in (3-14) can be simplified to:

$$s_{Y|M}^2 = \frac{1}{n}\sum_{i=1}^{n}\left(y_i - y_{i|M}\right)^2 \tag{3-15}$$

Now we have two fit estimates, one for the training data (3-16) and one for the predicted data (3-17).

$$R_{training}^2 = 1 - \frac{\frac{1}{n-k-1}\sum_{i=1}^{n}\left(y_i - y_{i|M}\right)^2}{\frac{1}{n-1}\sum_{i=1}^{n}(y_i - \bar{y})^2} \tag{3-16}$$

$$r_{predict}^2 = 1 - \frac{\frac{1}{n}\sum_{i=1}^{n}\left(y_i - y_{i|M}\right)^2}{\frac{1}{n-1}\sum_{i=1}^{n}(y_i - \bar{y})^2} \tag{3-17}$$

Given these two relationships, analysts now have the ability to compare relative predictive and training merit as a fraction of explained initial variance in a sample. Due to the formulation of $R^2_{predict}$, if the predictive meta-model produces a higher variance than the raw data, negative values are possible.

3.4 Important Notes for Interpreting Regression Analyses

This section provides:

1. A key for decoding which variables were regressed within a model summary table,
2. A description of how the tabular variables decay heat and time at temperature were condensed into point estimates for the regression analysis, and
3. An explanation for interpreting MATLAB's regression formulations

3.4.1 Input Variable Decoder Ring

Each regression uses a unique identifier to represent an input variable. The decoder ring abbreviations and definitions are provided in Table 3.1.

Table 3.1 – Regression Input Variable Abbreviation

Abbreviation	*Definition*
'RSDR'	Time Constants for Radial (solid) Debris Relocation (s)
'RLDR'	Time Constants for Radial (liquid) Debris Relocation (s)
'dTdz_TCAF'	dT|dz Model, Time Constant for Averaging Flows (s)
'dTdz_CVH'	dT|dz Model, Characteristic Coupling Time (s)
'dTdz_Smooth'	dT|dz Model, Relative Weight of Historical Flow (s)
'MZBT'	Molten Zircaloy Break-Through Temperature (K)
'MCDR'	Molten Cladding (pool) Drainage Rate (kg/(m*s))
'FSLHF'	Fraction of Strain at Which Lower Head Failure Occurs
'SFCHTC'	Scaling Factor for Candling Heat Transfer Coefficients
'DebrisHT'	Debris Quenching Heat Transfer Coefficient to Pool (W/(m^2*K))
'DFV'	Debris Falling Velocity (m/s)
'minPorosity'	Minimum Debris Porosity (unit-less)
'TaT'	Time At Temperature - Effective Failure Temperature (K)
'DCH'	Decay Heat Integrated to 10 hours (J)

3.4.2 Tabular Variable Representation for DCH and TaT

Functional inputs (often represented in MELCOR by table lookups) cannot be directly included into the **X** vector defined in Equation (3-2). Thus, the tabular functions must be represented by point estimates. Ideally, these estimates should have some relation to the physical FoM being

regressed. For example, if hydrogen production at the time of first fuel failure is being regressed, it would make sense for the decay heat to be representative of that event timing. Thus, the analyst may choose to integrate decay heat from the beginning of the accident until the time of first fuel failure, which itself is an uncertain event. This approach can be undesirable because of the challenges involved with implementation and the potential for unintended correlation with other parameters which also drive the timing of the event.

A simpler approach is to define a predetermined scenario independent of the accident being analyzed. The point estimate for each sampled table is then approximated by analyzing the table against the independent scenario. The benefit of this approach is that the representative value is independent of any other uncertain parameter sampled in the 1F1 UA. This simpler approach was adopted for the 1F1 UA.

3.4.2.1 Time at Temperature (*TaT*)

The time at temperature (*TaT*) curves, defined in Section 2.2.3, were derived from the VERCORS experiments. Damage is accrued as a function of temperature using Equation (2-14). To approximate the temperature ramp that would be experienced in the 1F1 calculations, the fuel was assumed to begin accruing damage at 2100K while experiencing a 10K/min temperature ramp with one minute time steps. When the cumulative damage equaled one, the fuel temperature at that time was selected to be representative of the time at temperature curve. The distribution of *TaT* effective failure temperatures can be seen in Figure 3.2.

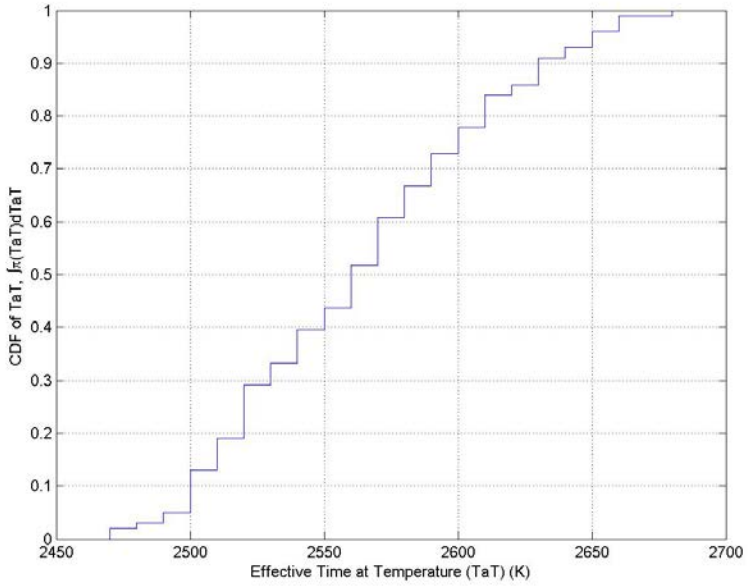

Figure 3.2 – Empirical CDF of Effective Time at Temperature Values

3.4.2.2 Decay Heat

Instead of fixing the decay heat value for subsequent regressions to a given event within the 1F1 accident progression, the decay heat curve was integrated out to ten hours for all timing and physical FoMs. Decay heat was integrated to ten hours because most of the impacts of decay heat on core degradation in the emergency core water injection time-horizon have been

experienced by this time. The selection of ten hours also ensured that all timing FoMs were bounded by the decay heat estimate, with the exception of lower head failure. The empirical CDFs of the integrated *DCH* values are presented in Figure 3.3.

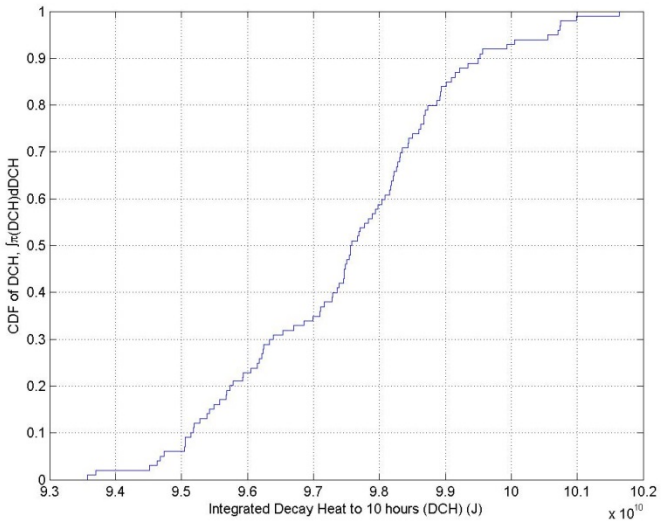

Figure 3.3 – Empirical CDF of Effective Integrated Decay Heat Load from 0 to 10 hours

3.4.3 Interpretation of MATLAB regression Equations

The regression equations produced by MATLAB can be counterintuitive at first glance; this section is intended to provide a primer to help the reader interpret the MATLAB regression equation.

An example MATLAB regression output is:

y ~ 1 + X1 + X2*X3

First, the reader should note that MATLAB does not include a placeholder for the regression coefficients. Thus, in matrix form, MATLAB is essentially providing Equation (3-18) and omitting the $\widehat{\boldsymbol{\beta}}$ vector.

$$\boldsymbol{Y} \sim \boldsymbol{X} \tag{3-18}$$

Thus, the 1 in the MATLAB output is not implying the constant is one. Instead, MATLAB is implying that the constant is 1 times $\widehat{\beta_0}$ which can be found in the associated model summary table.

Second, MATLAB cannot include an interaction term into a regression without including the independent terms as well, regardless of statistical significance. Thus, *X2*X3* actually represents *X2+X3+*(*X2* times *X3*). In the model summary table, the coefficient for *X2* times *X3* is represented by *X2:X3*.

Thus, the example MATLAB regression output could be more intuitively understood as:

$$y = \beta_0 + \beta_1 X_1 + \beta_2 X_2 + \beta_3 X_3 + \beta_{23} X_2 X_3$$

3.5 References

[3.1] J.S. Milton and J.C. Arnold, Introduction to Probability and Statistics - 4th Edition, Mc Graw Hill, 2002.

[3.2] M.R. Denman, Probabilistic Transient Analysis of Fuel Choices for Sodium Fast Reactors, Ph.D. Thesis, Massachusetts Institute of Technology, Cambridge MA, June 2011.

[3.3] A.H-S. Ang and W. H. Tang, **Probability Concepts in Engineering**, 2nd Ed., John Wiley & Sons, Inc., pg. 309, March 2006.

4 CONVERGENCE OF TIMING FOMS

Section 4 examines the statistical convergence of Replicate 1 for various timing FoMs. Similar tests are conducted for all three Replicates and all three perturbations, although for brevity these results are not presented in this report.

This section examines the degree of convergence of the median estimate of the timing FoMs:

1. First Control Rod Failure,
2. First Channel Box Failure,
3. First Fuel Failure,
4. Main Steam Line Failure,
5. Lower Core Plate Failure, and
6. Lower Plenum Dryout.

In general, these timing FoMs occur in order, although first fuel failure can, and often does, occur after main steam line failure. Physical FoMs (i.e., material ejected from the lower head, hydrogen produced, and intact fuel mass) are examined at these timing FoMs (and the end of simulation) and not at fixed points in time. The convergence testing presented in this report focuses on the convergence of the median for the timing FoMs. All physical FoMs were examined during the post-processing of the UA but were not reproduced in this report for brevity. In addition, only convergence results for Replicate 1 are presented in this report, although the other replicates were examined and also converged.

Convergence of the timing FoMs are presented using three different methods. Section 4.1 examines the convergence the 31.4^{th}, 50^{th}, and 68.6^{th} percentiles of the timing FoMs as a function of as the number of realizations originally sampled. Section 4.2 uses a bootstrap resampling approach to examine the order dependency of the median convergence as a function of sample number. Finally, Section 4.3 uses the bootstrap subsampling approach to produce histograms of potential median estimates using only 80% of the sampled data.

4.1 Distribution Convergence as a Function of Sample Size

Figure 4.1 through Figure 4.7 show the convergence of the 31.4^{th}, 50^{th}, and 68.6^{th} quantiles ($q_{0.314}$, $q_{0.5}$, and $q_{0.686}$) of the timing FoMs as a function of realization numbers as originally sampled for Replicates 1, 2, 3 and the Uniform Replicate. These quantiles ($q_{0.314}$, $q_{0.5}$, and $q_{0.686}$) were chosen to be one standard deviation in either direction of the median. While convergence of the 50^{th} percentile was the primary concern to the authors, the other two quantiles were arbitrarily selected to demonstrate the convergence, or lack thereof, of the bulk of the remaining distribution.

The desired convergence criterion is that the median should stabilize to within 5% of the median within 80% of the sample size, or at the 80 realization marker for all but Figure 4.7. It should be noted that every timing FoM meets this convergence criteria, although the median timing of lower plenum dryout wanders more than other timing events. This wandering may be due to bifurcation in the intact fuel fraction at lower plenum dryout discussed in Section 5.4.

Figure 4.7, or the conditional timing of lower head failure, only has 35 realizations because only 35% of the Replicate 1 realizations led to lower head failure within 15 minutes.

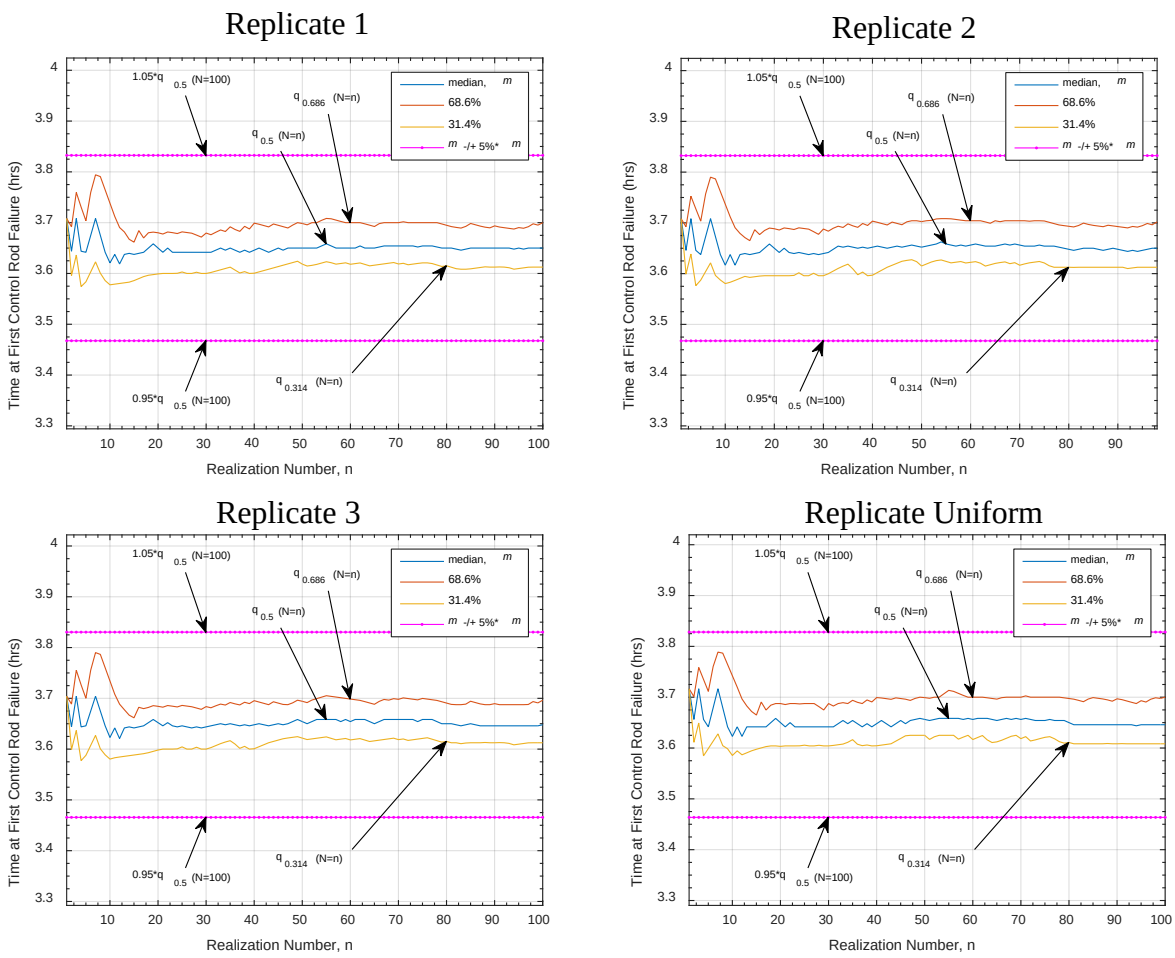

Figure 4.1 - Convergence the 31.4th, 50th, and 68.6th Percentiles of the Timing of First Control Rod Failure FoM as a Function of Realization Number

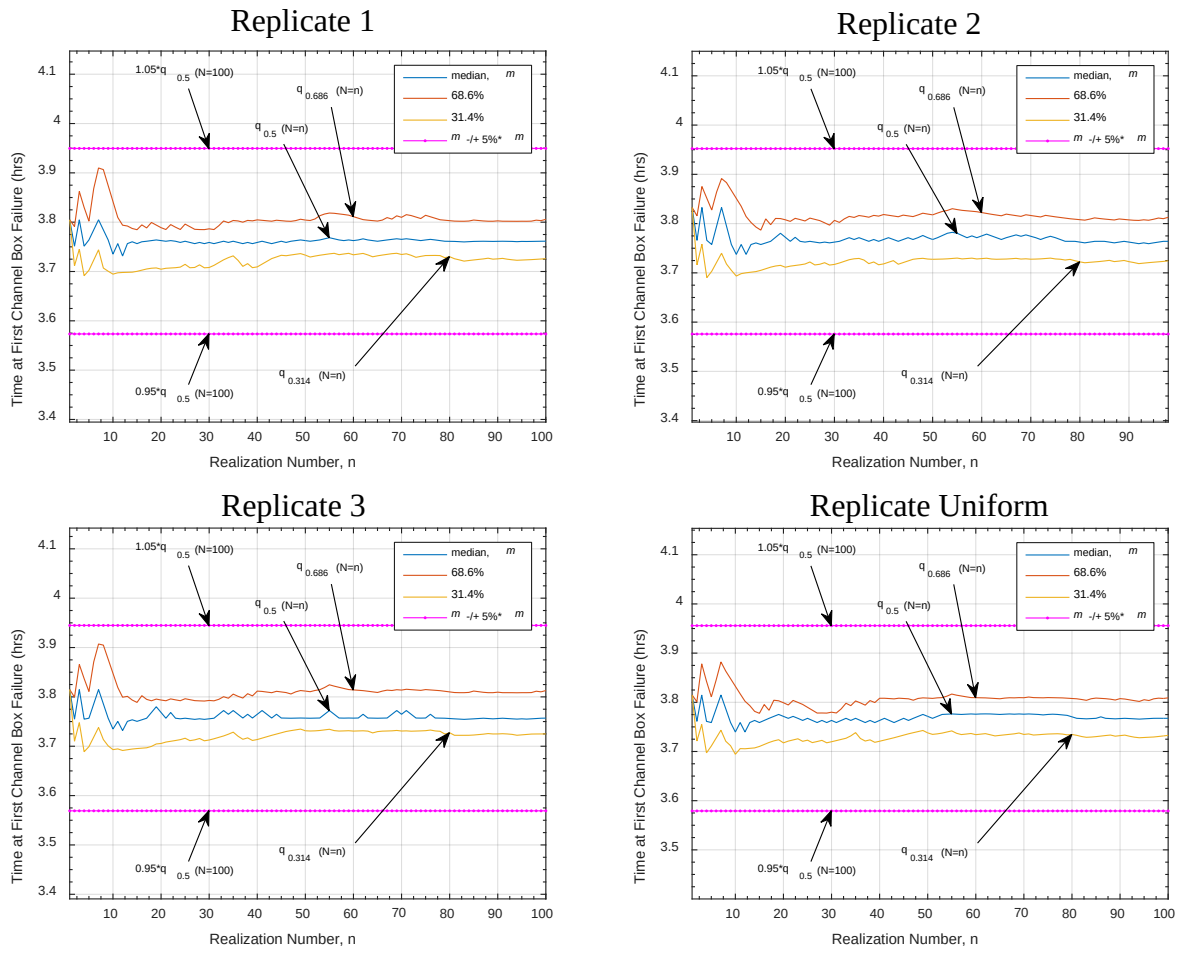

Figure 4.2 - Convergence the 31.4th, 50th, and 68.6th Percentiles of the Timing of First Channel Box Failure FoM as a Function of Realization Number

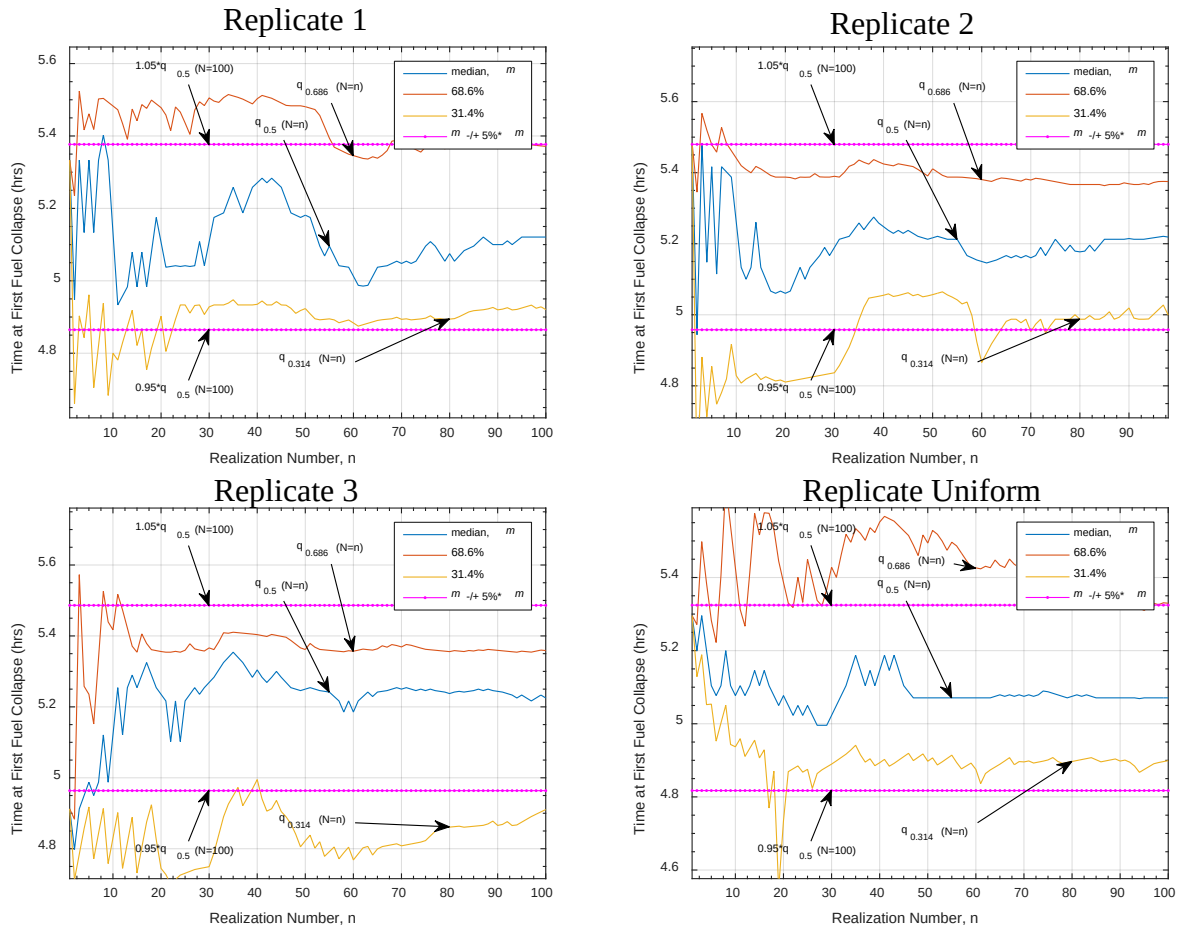

Figure 4.3 - Convergence the 31.4th, 50th, and 68.6th Percentiles of the Timing of First Fuel Failure FoM as a Function of Realization Number

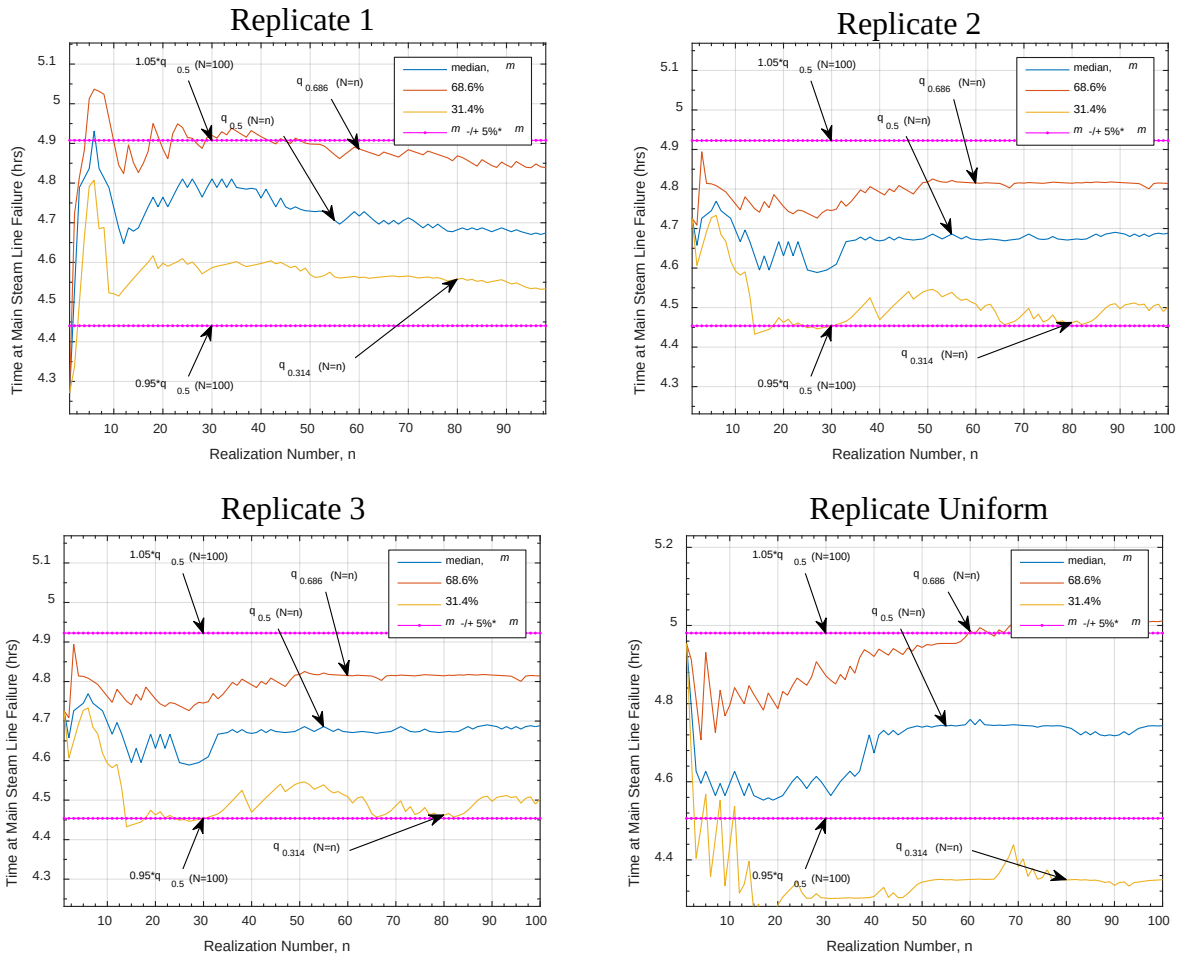

Figure 4.4 - Convergence the 31.4th, 50th, and 68.6th Percentiles of the Timing of Main Steam Line Failure FoM as a Function of Realization Numbers as Originally Sampled

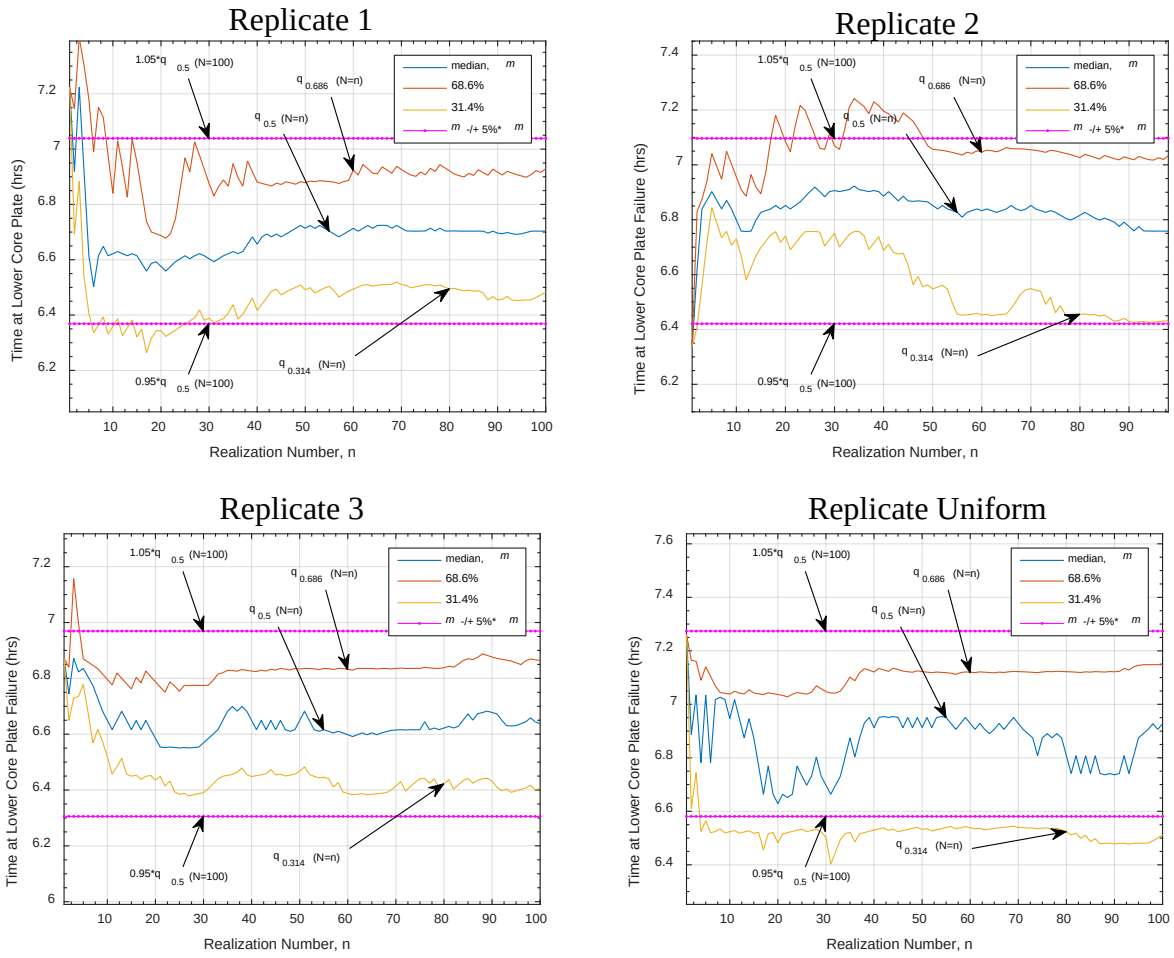

Figure 4.5 - Convergence the 31.4th, 50th, and 68.6th Percentiles of the Timing of Lower Core Plate Failure FoM as a Function of Realization Numbers as Originally Sampled

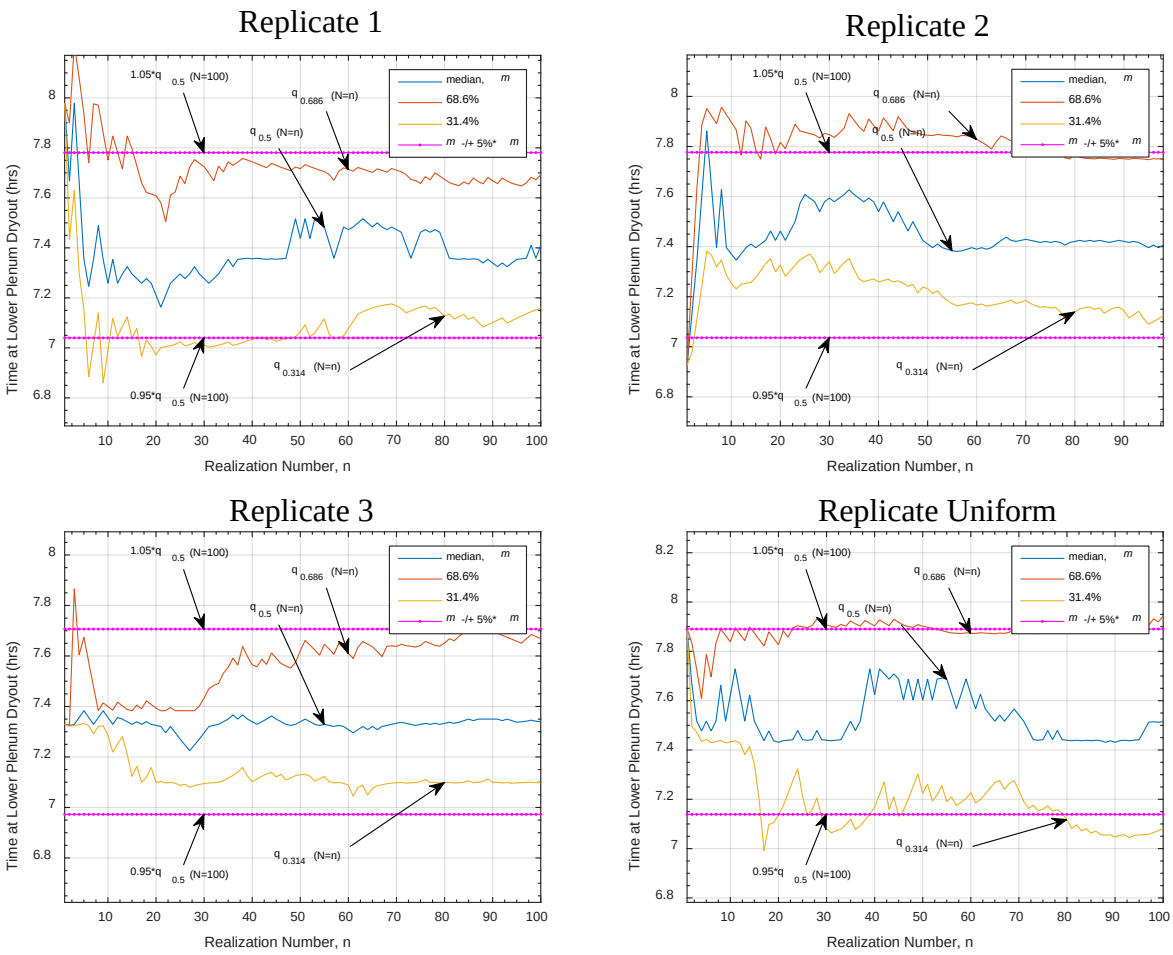

Figure 4.6 - Convergence the 31.4th, 50th, and 68.6th Percentiles of the Timing of Lower Plenum Dryout FoM as a Function of Realization Numbers as Originally Sampled

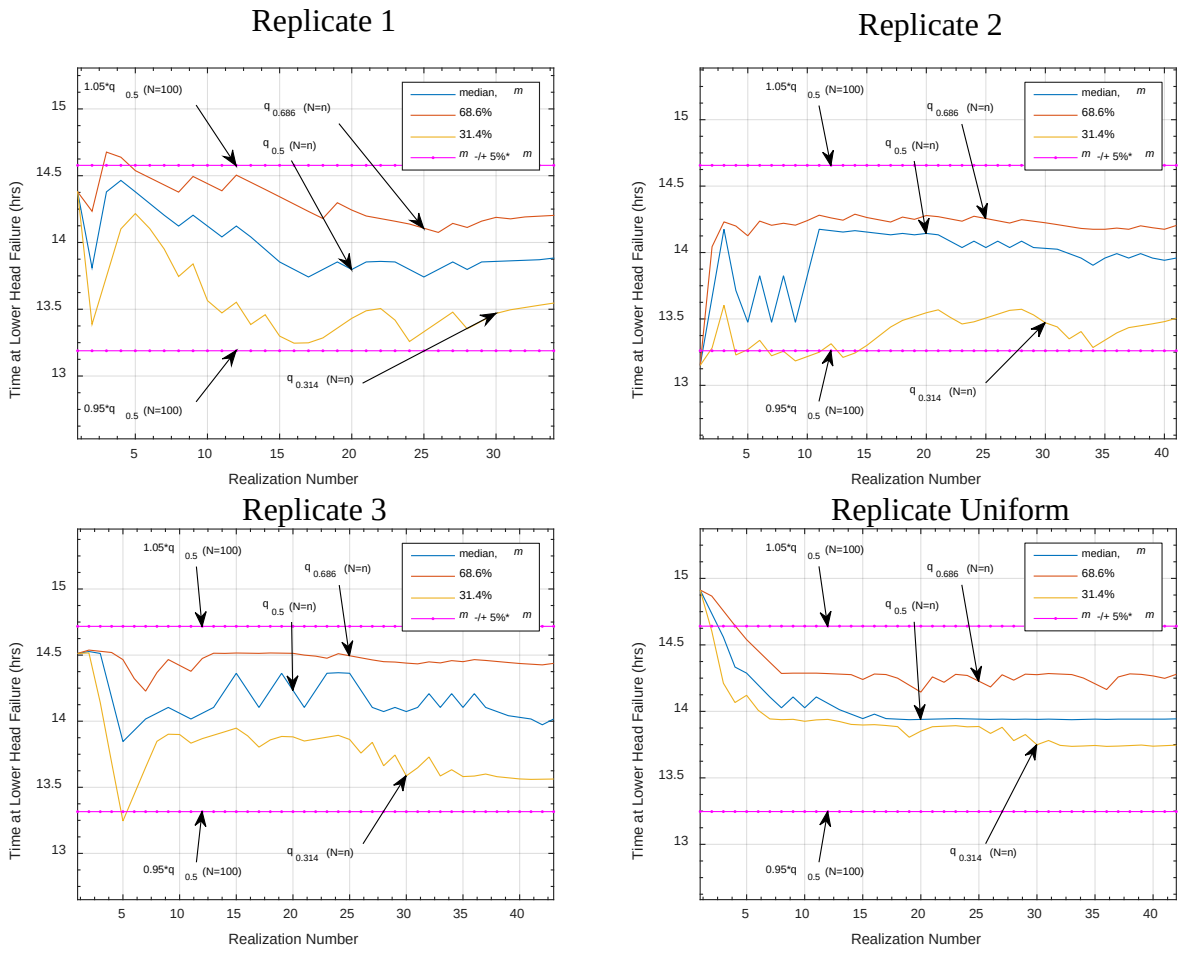

Figure 4.7- Convergence the 31.4th, 50th, and 68.6th Percentiles of the Conditional Timing of Lower Head Failure FoM as a Function of Realization Numbers as Originally Sampled

4.2 Bootstrapped Distribution Convergence as a Function of Sample Size

While Section 4.1 examined the convergence of the median as a function of the original sample order, Section 4.2 explores the effect that order has on the convergence of the median. Figure 4.8 through Figure 4.14 were developed by taking the 100 original sample data points and resampling the entire set with replacement 1,000 times to generate 1000 samples of 100 data points. The new 1,000x100 matrix, as pictured below, was then examined to find the row with maximum, median and minimum timing FoMs as a function of resampled realization number.

Table 4.1 - An example 1000 by 100 matrix, in which each row contains one sample of 100 data.

$$\begin{bmatrix} n_{1,1} & n_{1,2} & \cdots & n_{1,n} & \cdots & n_{1,100} \\ n_{2,1} & n_{2,2} & \cdots & n_{2,n} & \cdots & n_{2,100} \\ \vdots & \vdots & \vdots & \vdots & \vdots & \vdots \\ n_{1000,1} & n_{1000,2} & \cdots & n_{1000,n} & \cdots & n_{1000,100} \end{bmatrix}$$

In this way, the authors could determine if the median value is dominated by a subset of sampled values or if convergence is approximately order independent. In general, median timing FoMs converged to within 5% of the final estimated median after ~40% of the samples regardless of order.

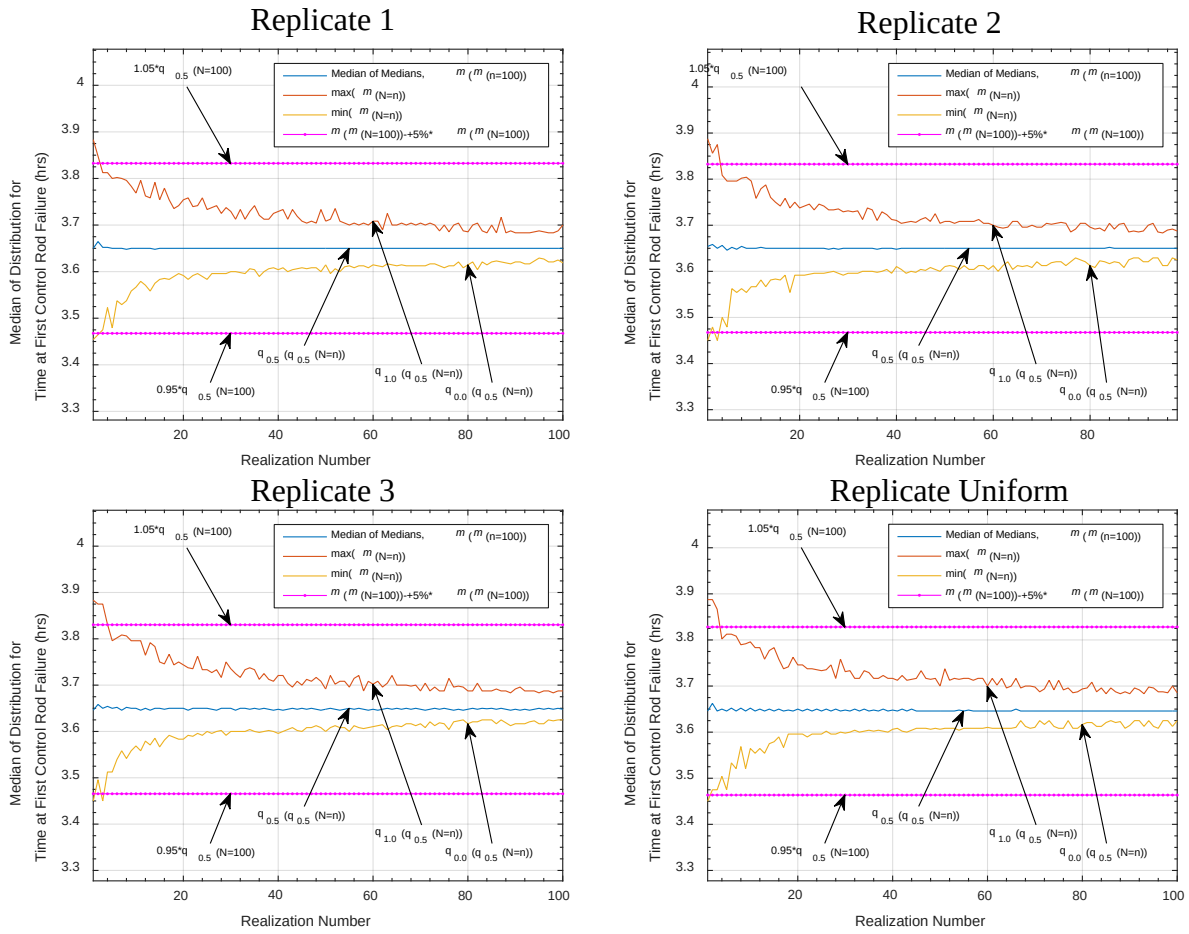

Figure 4.8 – Bootstrap Resampled Convergence of the Median of the Timing of First Control Rod Failure FOM as a Function of Realization Numbers for Replicate 1.

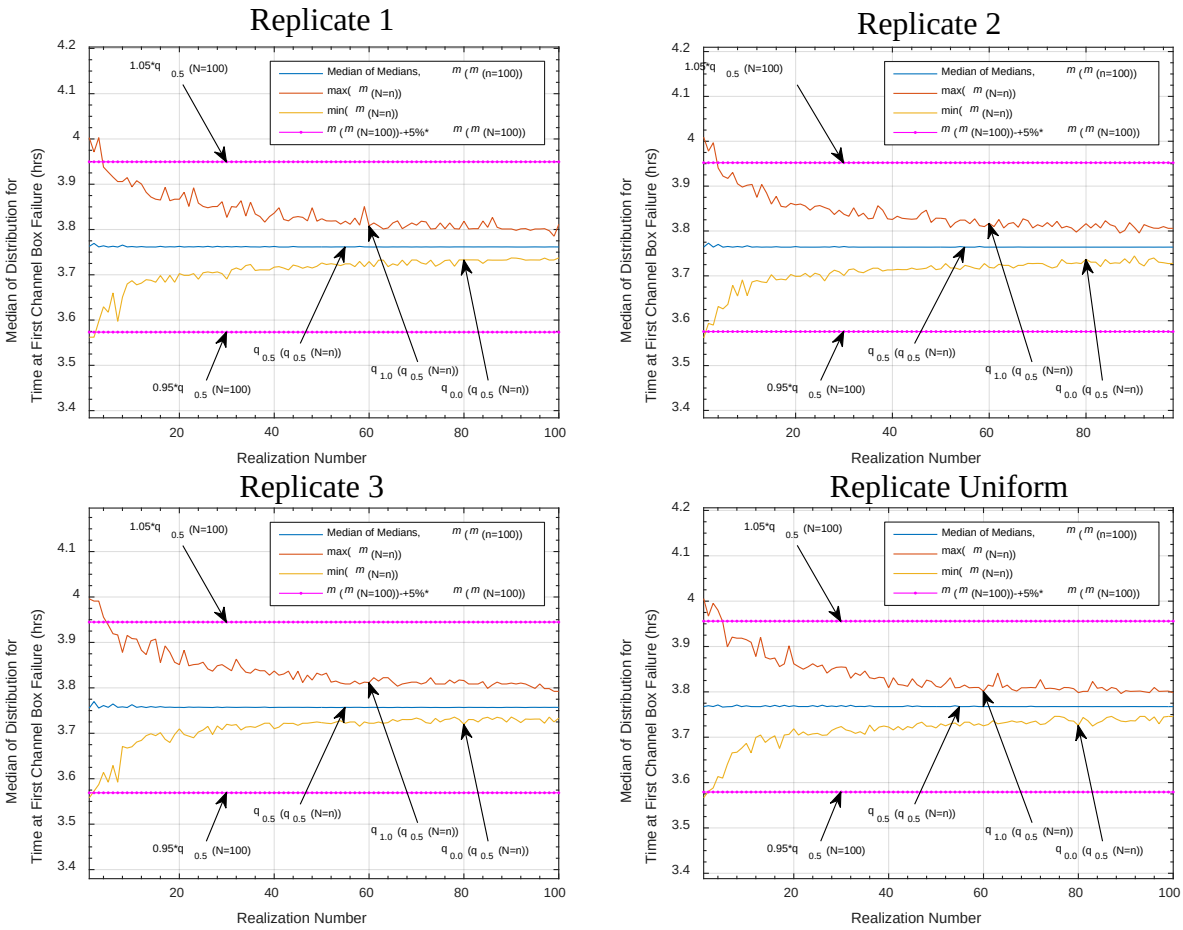

Figure 4.9 – Bootstrap Resampled Convergence of the Median of the Timing of First Channel Box Failure FOM as a Function of Realization Number

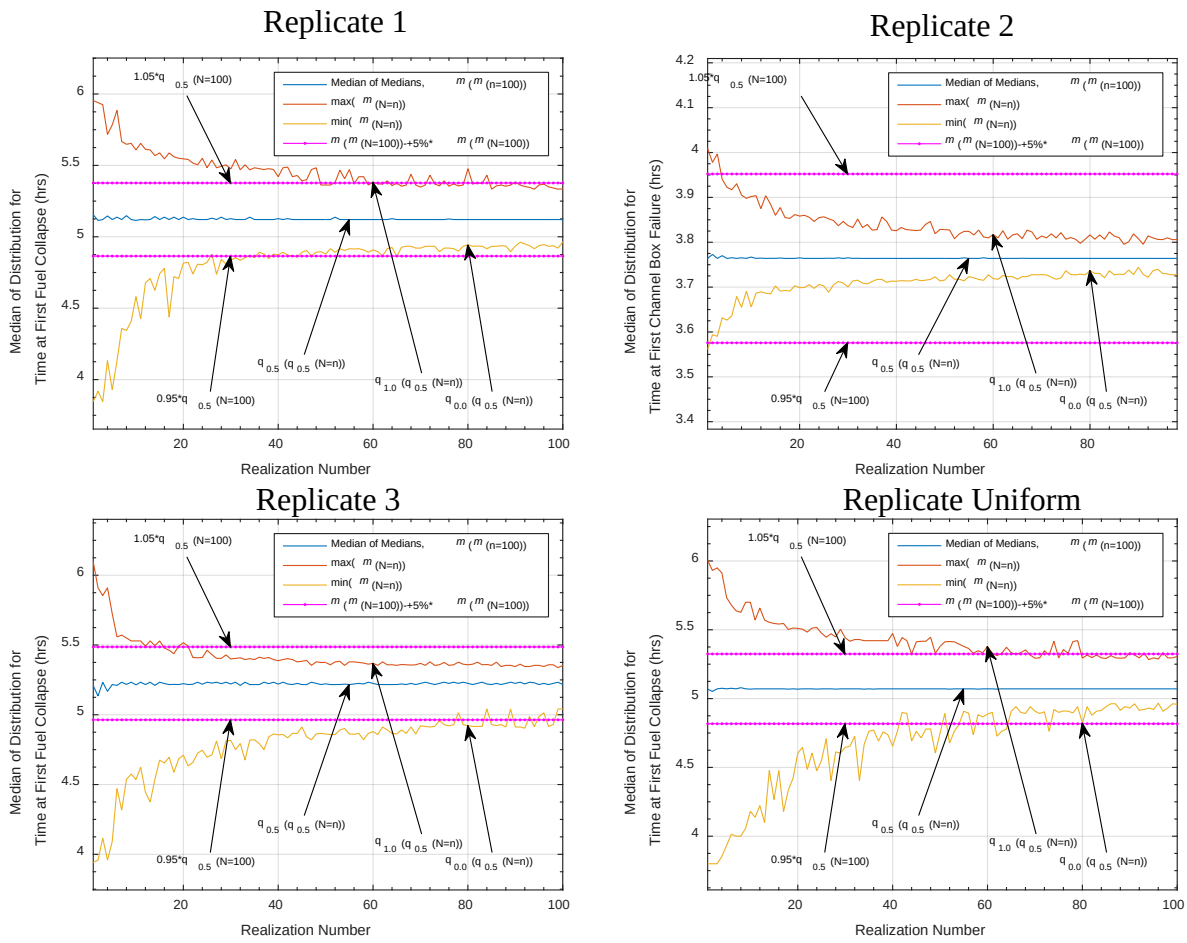

Figure 4.10 – Bootstrap Resampled Convergence of the Median of the Timing of First Fuel Failure FOM as a Function of Realization Number

Note that the Replicate 2 converges the median of the timing of first channel box failure quickly while Replicate 3 has a harder time converging the median within the first 100 resamples. All replicates converge the time of first fuel collapse to an acceptable degree (i.e., within 5%).

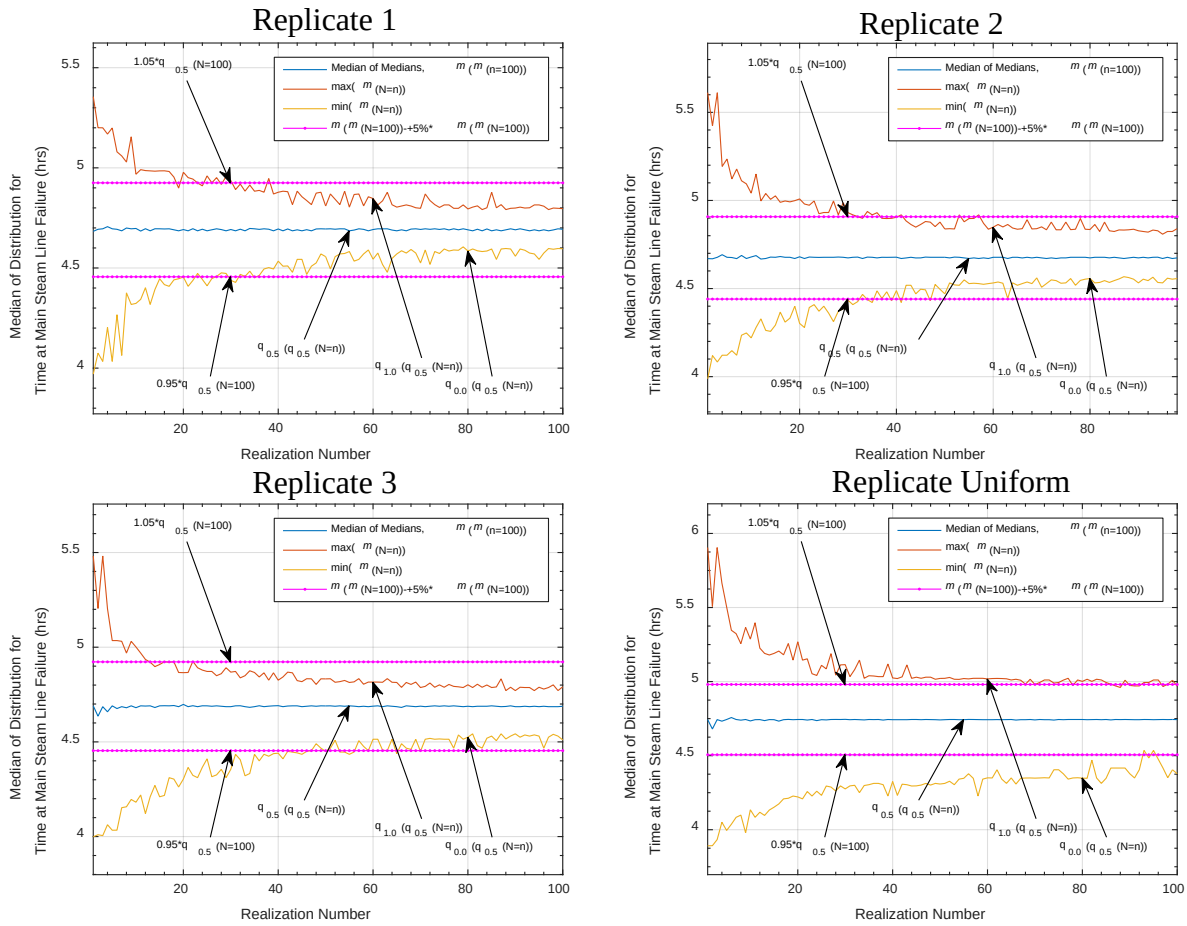

Figure 4.11 – Bootstrap Resampled Convergence of the Median of the Timing of Main Steam Line Failure FOM as a Function of Realization Number

Note that the replicate which used the uniform distribution experiences a slightly slower convergence of the median of lower plenum dryout timing than the informed Replicates (1-3). The medians for replicates 1-3 converge the time of main steam line failure to an acceptable degree (i.e., within 5%), while the median for the replicate uniform does not acceptably converge. This lack of acceptable convergence may indicate that the number of realizations was not sufficient to reliably calculate the median. Thus, statistics calculated using only the replicate uniform data may not accurately represent the true behavior of the data.

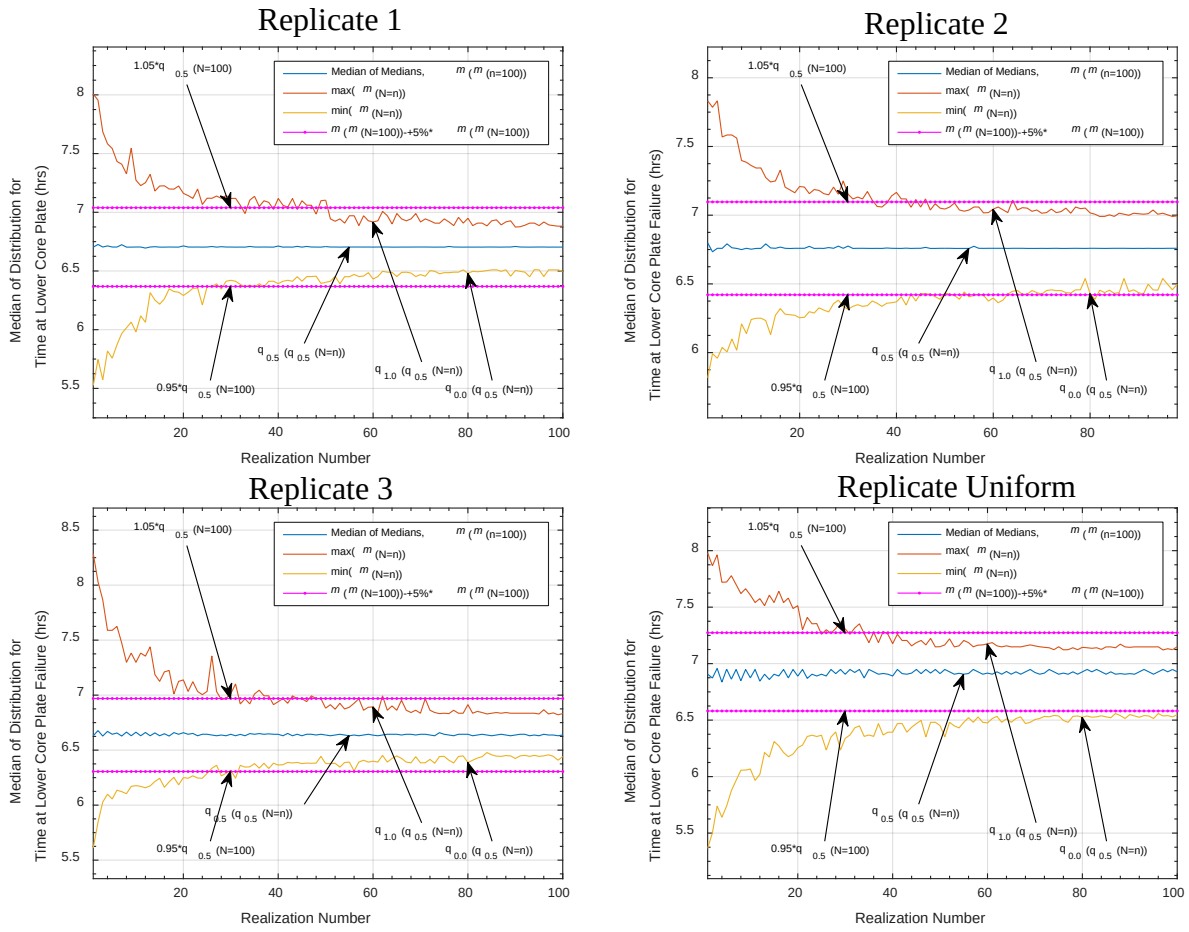

Figure 4.12 – Bootstrap Resampled Convergence of the Median of the Timing of Lower Plenum Dryout FOM as a Function of Realization Number

The medians for replicates 1-3 converge the time of lower core plate failure to an acceptable degree (i.e., within 5%), while the median for the replicate uniform does not acceptably converge.

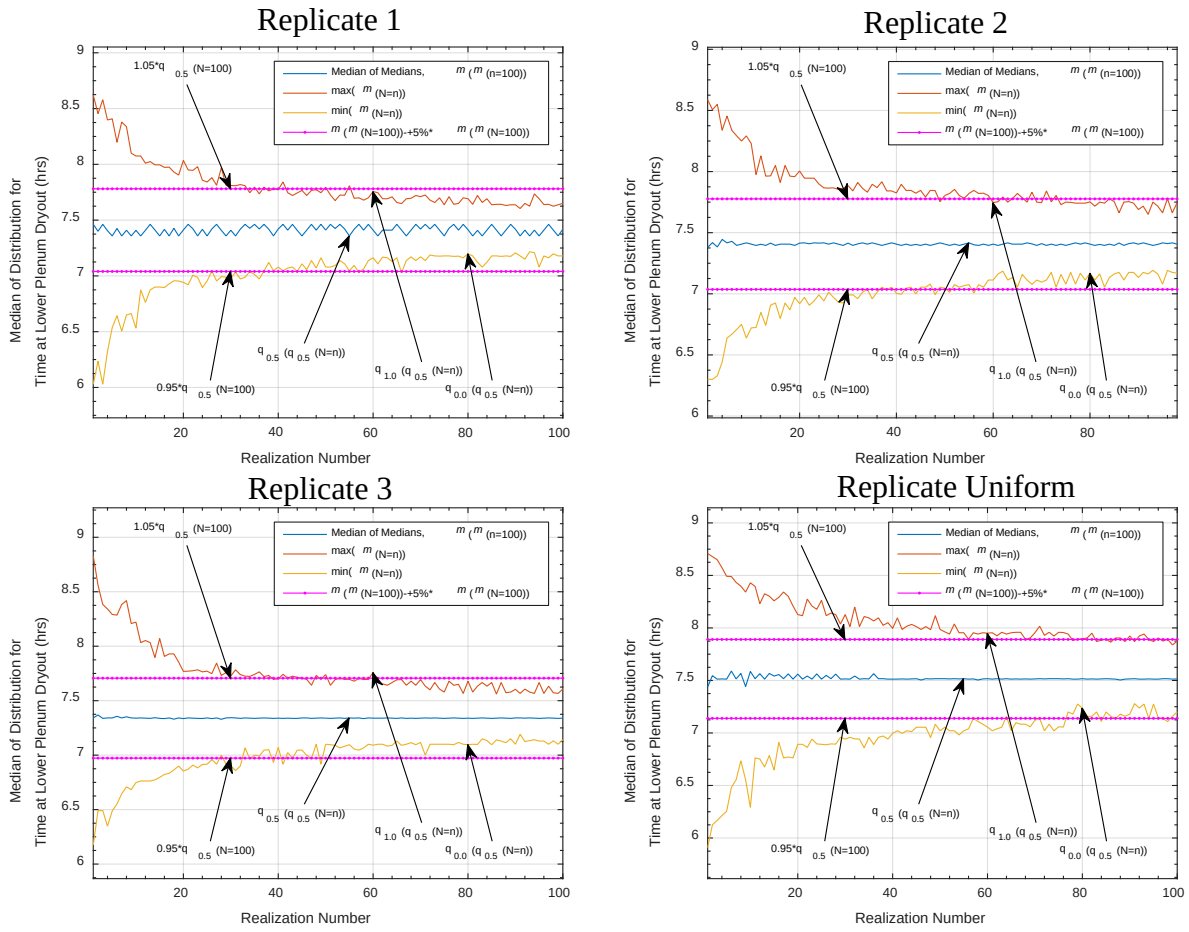

Figure 4.13 – Bootstrap Resampled Convergence of the Median of the Timing of Lower Core Plate Failure FOM as a Function of Realization Number

The medians for replicates 1-3 converge the time of lower plenum dryout to an acceptable degree (i.e., within 5%), while the median for the replicate uniform does not acceptably converge.

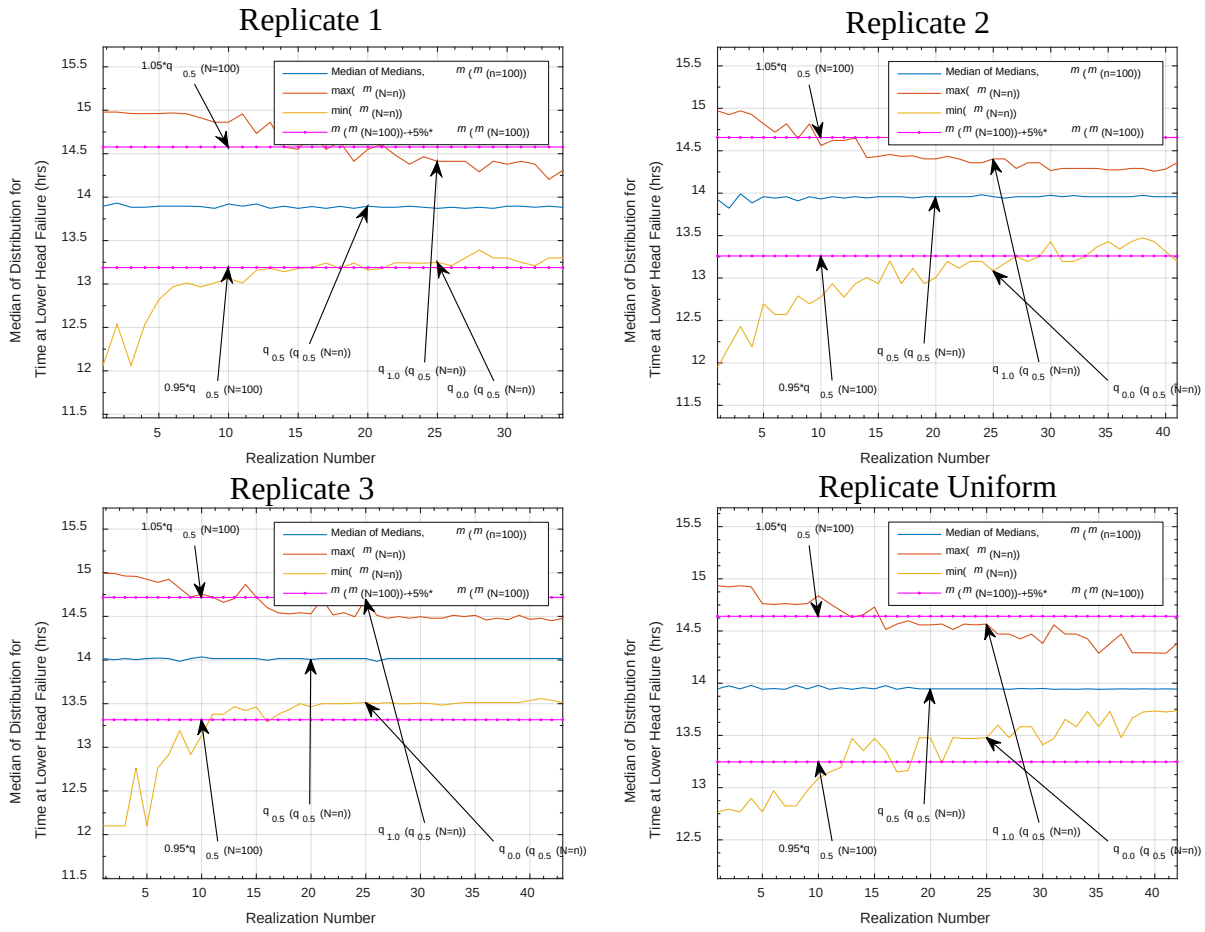

Figure 4.14 – Bootstrap Resampled Convergence of the Median of the Conditional Timing of Lower Head Failure FOM as a Function of Realization Numbers

4.3 Bootstrapped Histograms of Sampled Medians

Sections 4.1 and 4.2 focused on the convergence of the median as a function of realization number. This section will elaborate on the shape of the distribution of potential medians that could have arisen from the original sample. To examine this question, the bootstrapped samples from 4.2 were used and the medians were obtained for each of the 1000 samples of size 80 (i.e. see sample matrix in figure with $n = 80$). These bootstrapped medians where then used to create histograms of potential median estimates, as seen in Figure 4.15 through Figure 4.21.

Multimodal behavior, as evidenced in the timing of main steam line failure (Figure 4.18) and lower plenum dryout (Figure 4.20), are likely caused by discontinuities in the FoM near the 50th percentile. It should be noted that the replicate sampled from uniform input distributions exhibits a higher tendency of multimodal and/or flat output timing distributions.

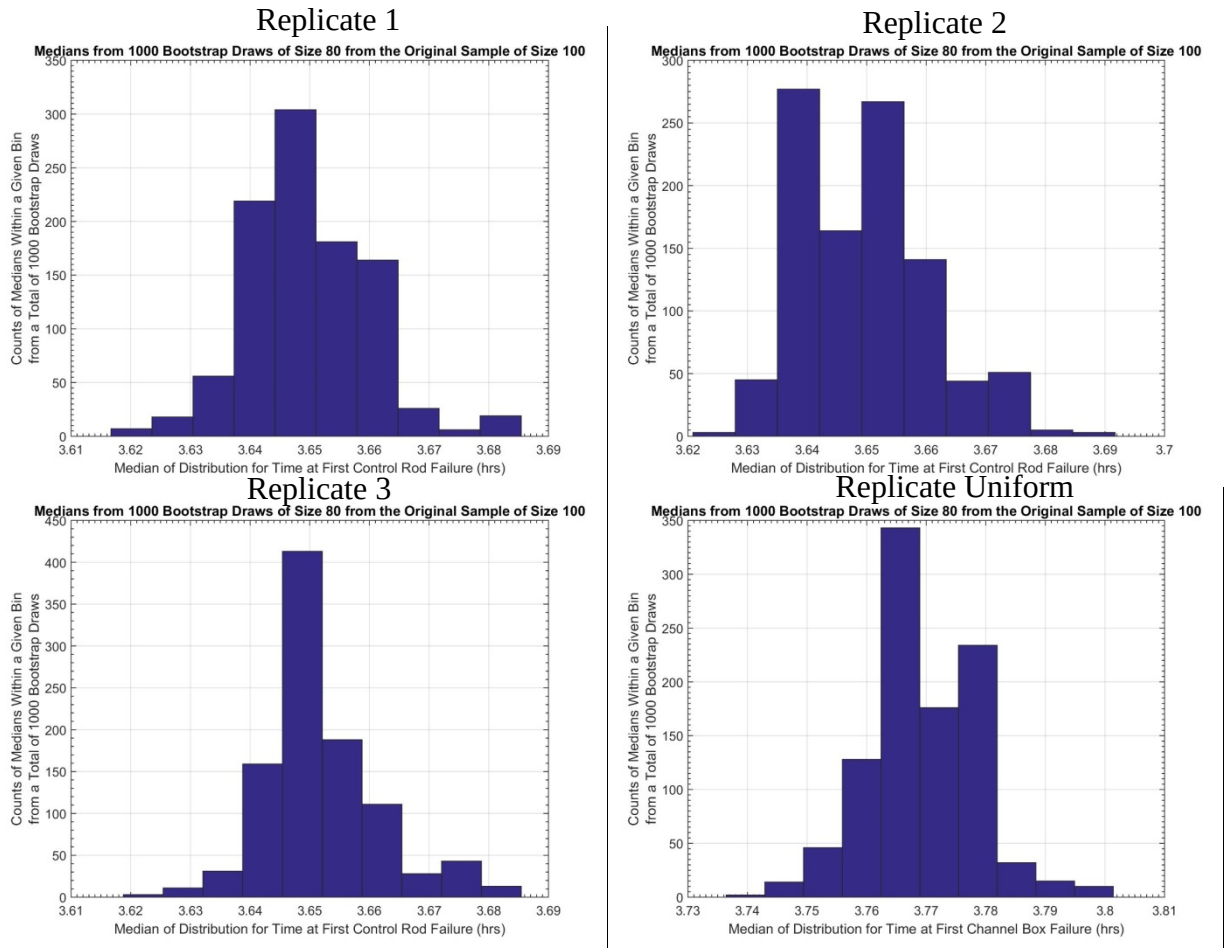

Figure 4.15 – Histogram of Bootstrapped Medians for First Control Rod Failure for Replicate 1.

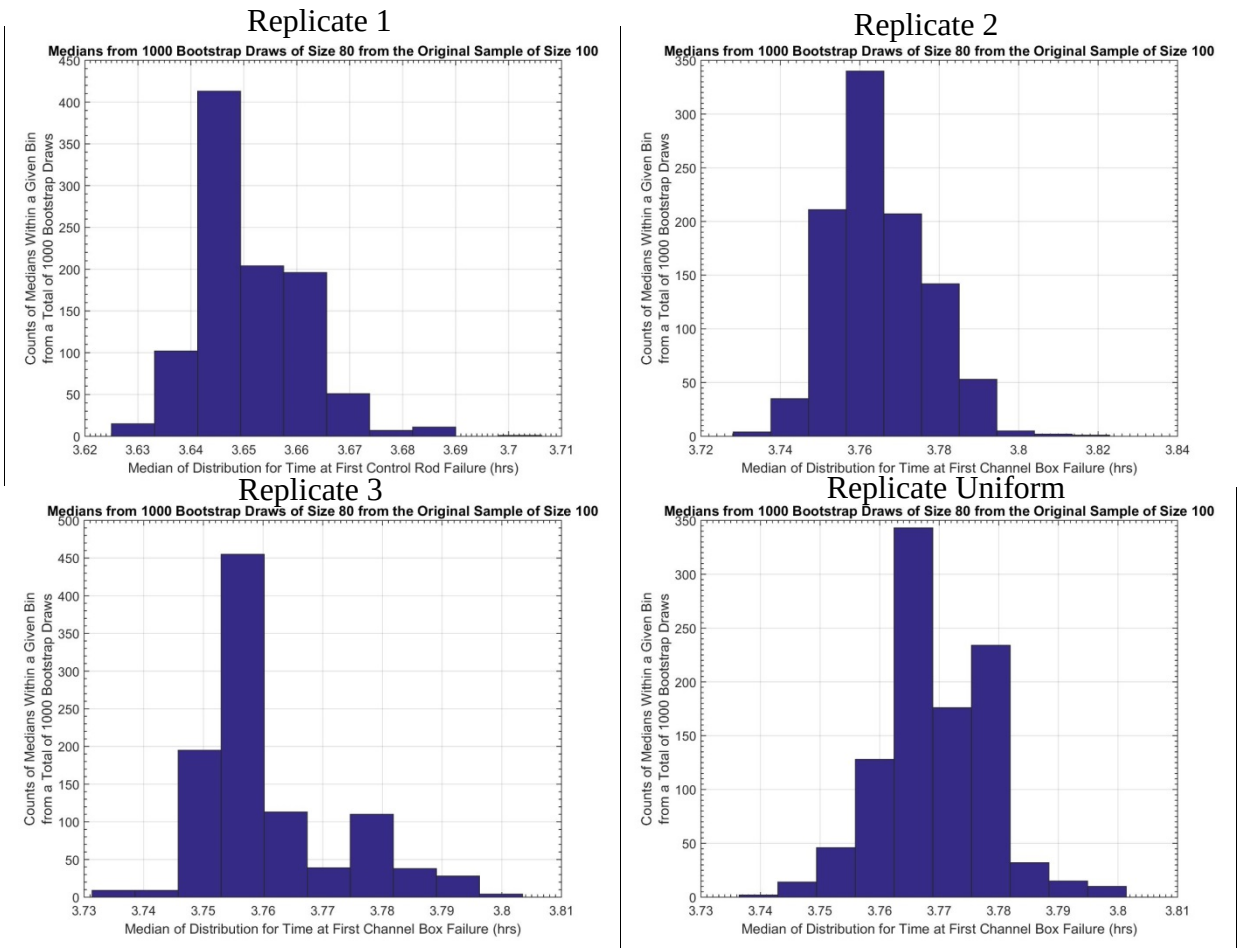

Figure 4.16 – Histogram of Bootstrapped Medians for First Channel Box Failure

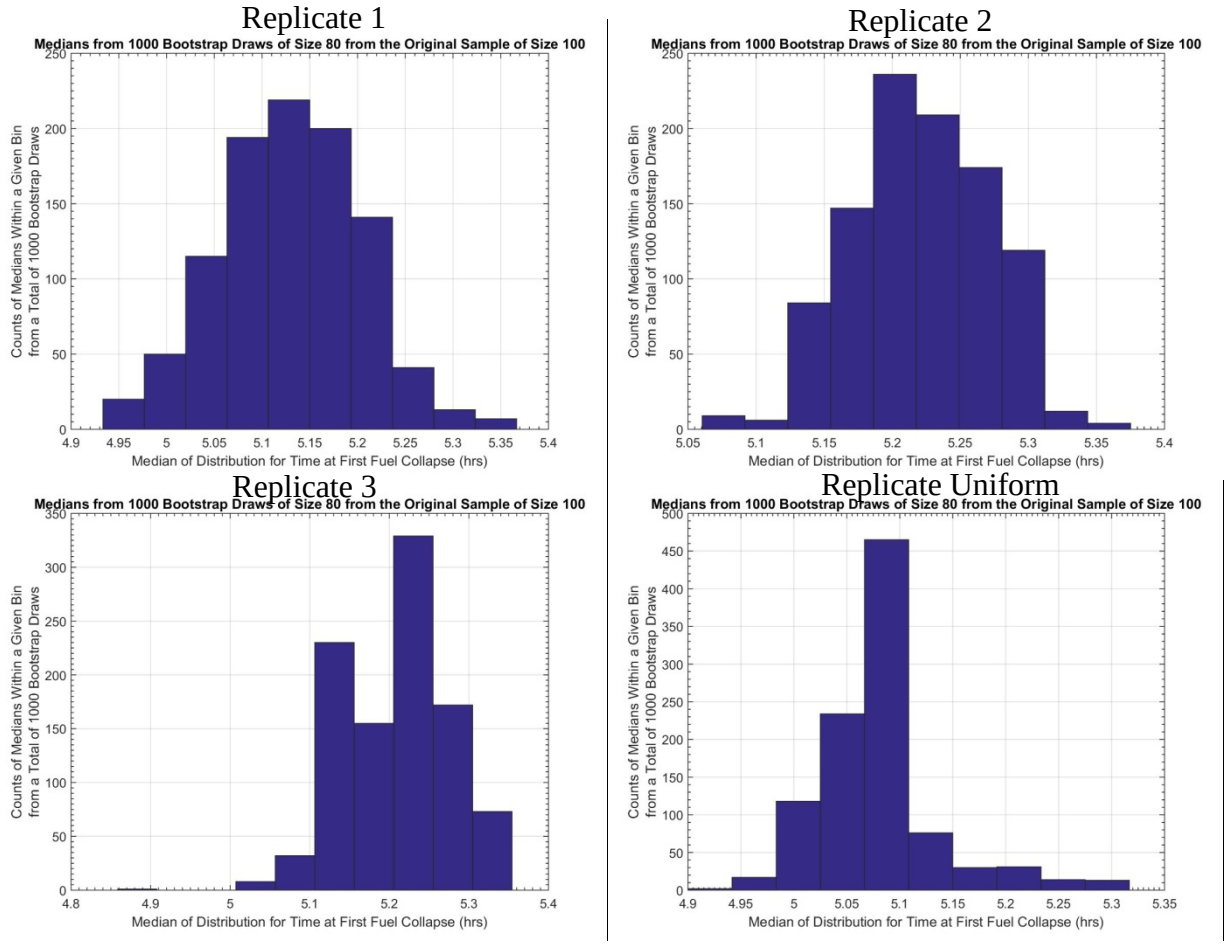

Figure 4.17 – Histogram of Bootstrapped Medians for First Fuel Failure (Collapse)

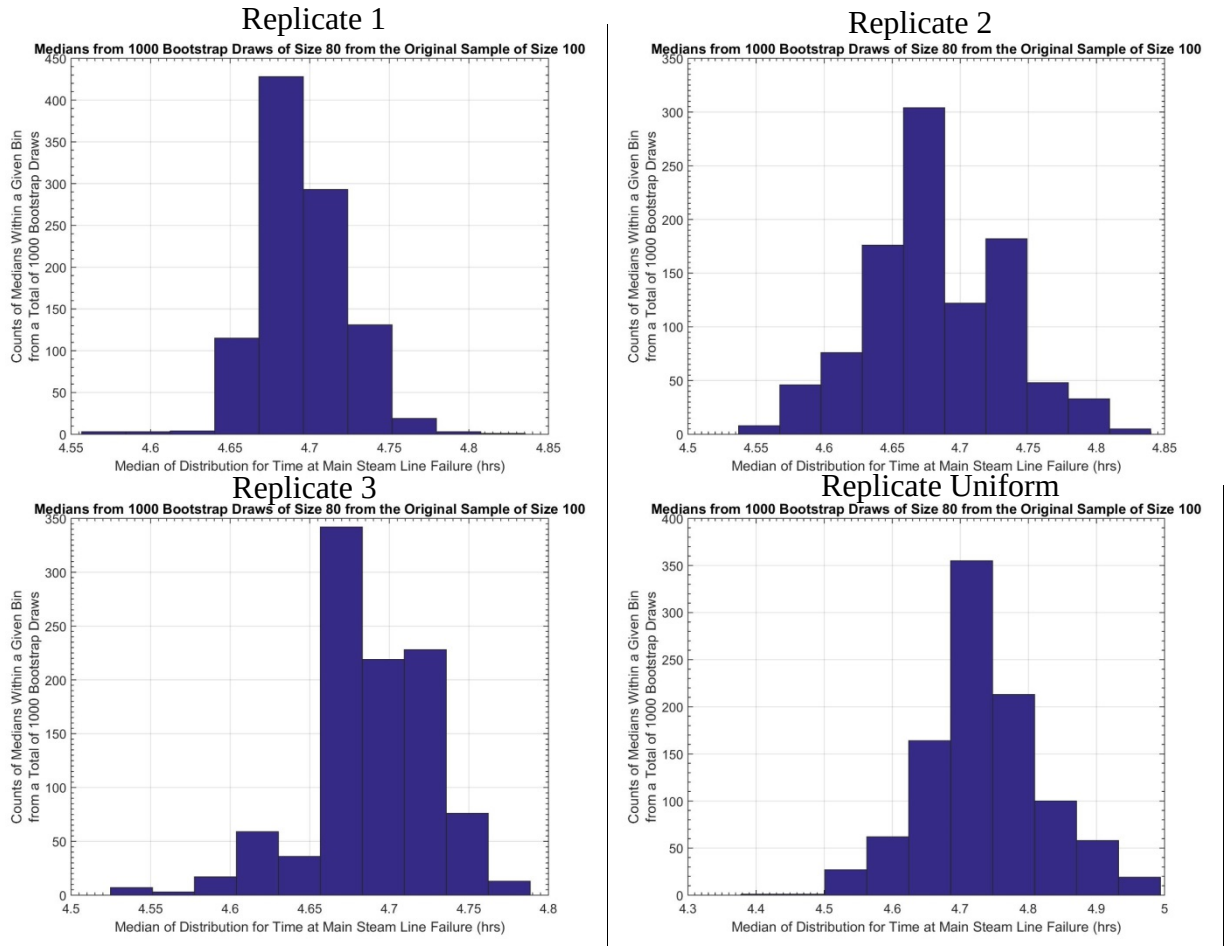

Figure 4.18 – Histogram of Bootstrapped Medians for Main Steam Line Failure

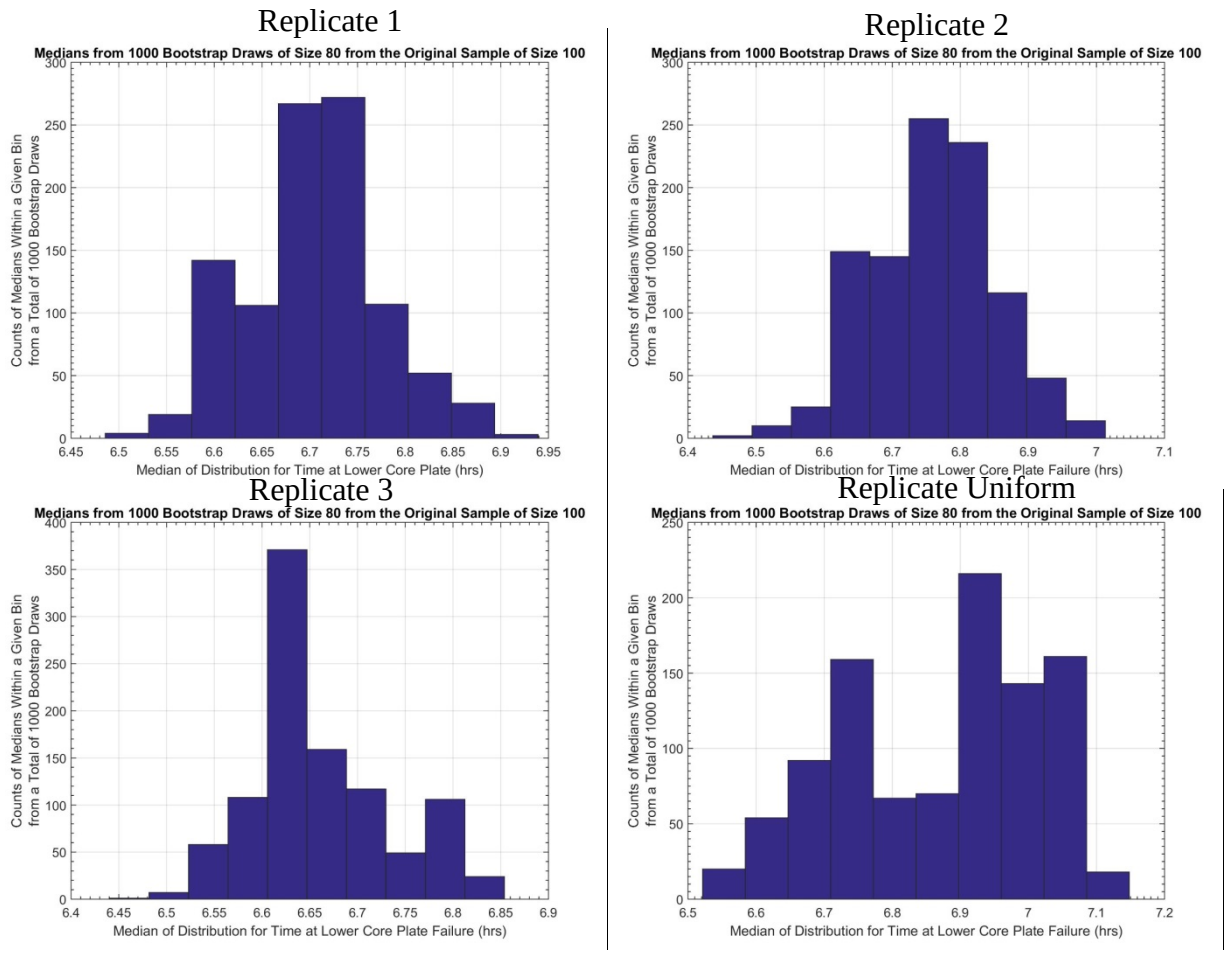

Figure 4.19 – Histogram of Bootstrapped Medians for Lower Core Plate Failure

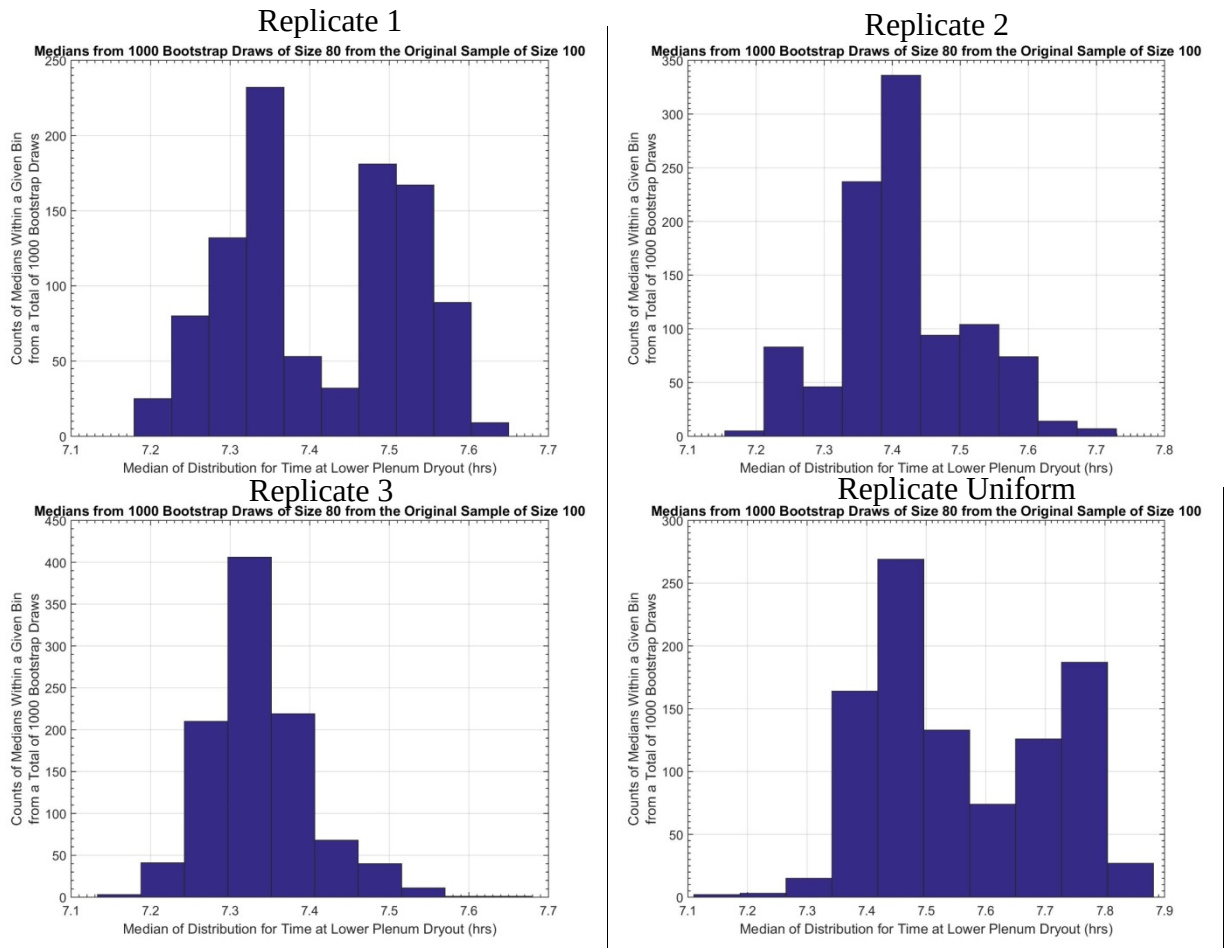

Figure 4.20 – Histogram of Bootstrapped Medians for Lower Plenum Dryout

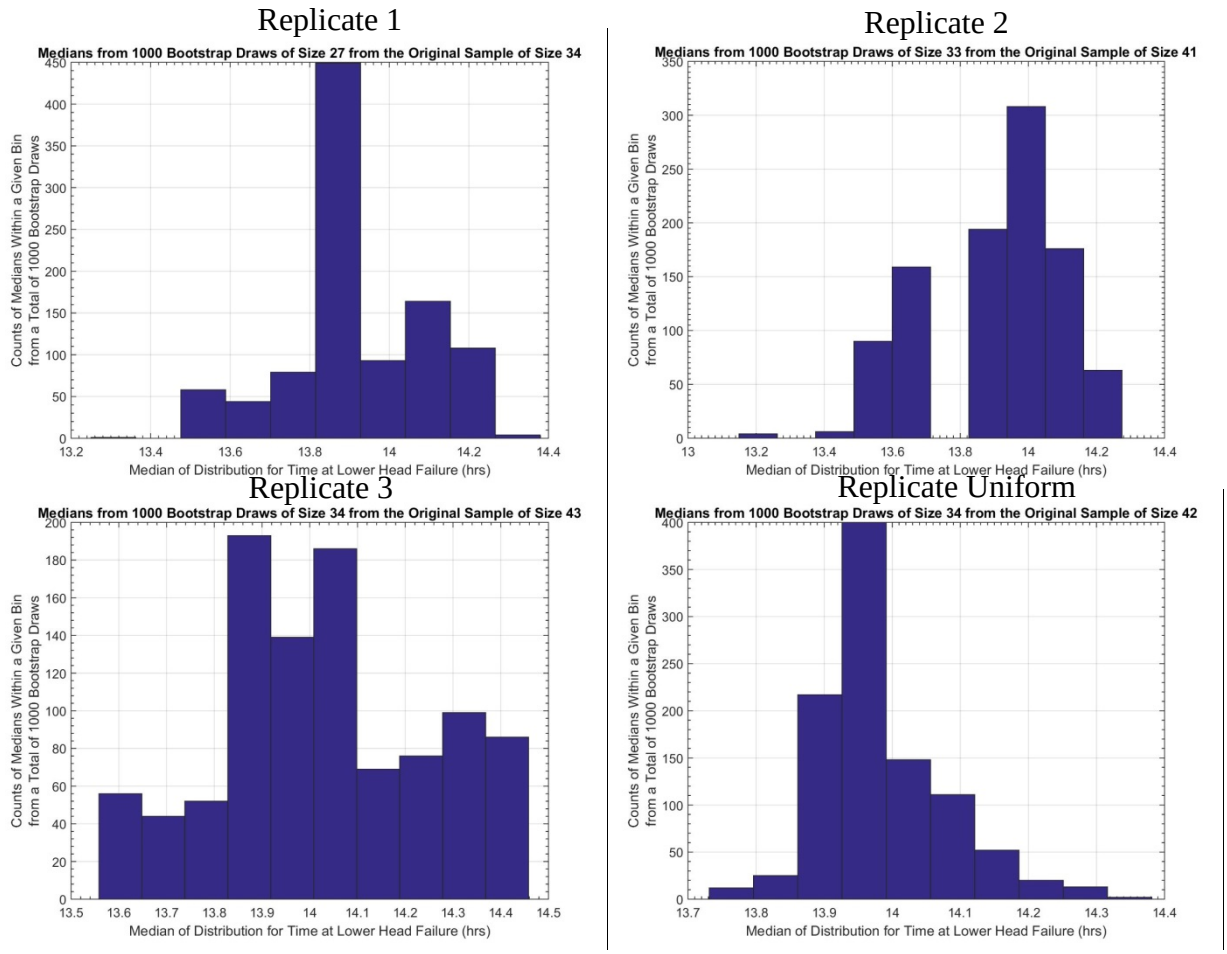

Figure 4.21 – Histogram of Bootstrapped Medians for Lower Head Failure

4.4 Insights from Convergence Examinations

Examination of timing FoM convergence shows fairly stable median estimates between the replicate samples. Outlier impact on the median is still evident at 100 samples, especially for the conditional lower head failure timing FoM which converges on a subset of the original 100 samples. The replicate derived from the uniform input distributions shows a small but noticeable deviation from the informed distribution Replicate (1-3) results.

5 VISUAL INSPECTION OF THE MELCOR STATISTICAL OUTPUTS

Chapter 5 uses visual statistical interrogation techniques to deduce high level insights regarding the 1F1 accident progression. The first three sections of chapter 5 examine a subset of scatter plots to determine if any trends are visible in the raw data. Section 5.1 examines scatter plots of select input variables against hydrogen production FoMs. Section 5.2 examines scatter plots of physical FoMs at timing FoMs to end of simulation FoMs to produce a first order examination of potential time dependent correlations within the FoMs. Finally, Section 5.3 examines the time progression of timing FoMs during the accident.

Section 5.4 examines cumulative distributions of timing figures of merit with their accompanying hydrogen generation and intact fuel mass cumulative distributions. These distributions can be useful when interpreting how figures of merit change over the transient and provide new perspective to physical FoM when compared to the time histories Appendix A.

5.1 Scatter Plots of Inputs FoM and Output FoM at Select Timing FoMs

A cursory examination of independent variable scatterplots was made to identify obvious trends which may inform subsequent sensitivity analyses. Three parameters exhibited notable trends:

1. molten Zircaloy breakthrough temperature,
2. effective time at temperature for fuel failure, and
3. decay heat.

5.1.1 Molten Zircaloy Break-Through Temperature

Subjectively, the molten Zircaloy breakthrough temperature parameter provides the clearest trends to hydrogen production as a function of uncertain input. Figure 5.1, 6.23, and Figure 5.2 show a fairly linear influence of the breakthrough temperature on hydrogen production at main steam line failure, lower core plate failure, and lower plenum dryout.

Interestingly, the trend reverses from a negative trend at main steam line failure to a positive trend at lower plenum dryout and lower core plate failure. While the trend of hydrogen production reverses, the trend of event timing, shown as a 3rd dimensional color axis on the scatterplot, consistently shows that higher breakthrough temperatures correspond to earlier failure times for subsequent events. One potential explanation for this trend is that holding up material for a longer period of time in the hotter regions of the core accelerates subsequent failures when relocation finally occurs.

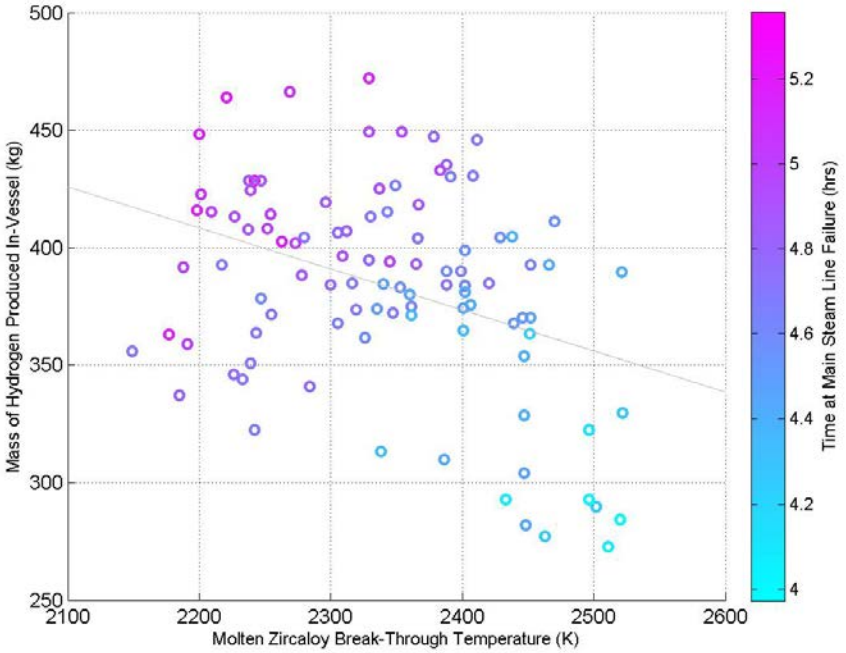

Figure 5.1 – Molten Zircaloy Breakthrough Temperature Scatterplot for Cumulative Hydrogen Production at Main Steam Line Failure for Replicate 1.

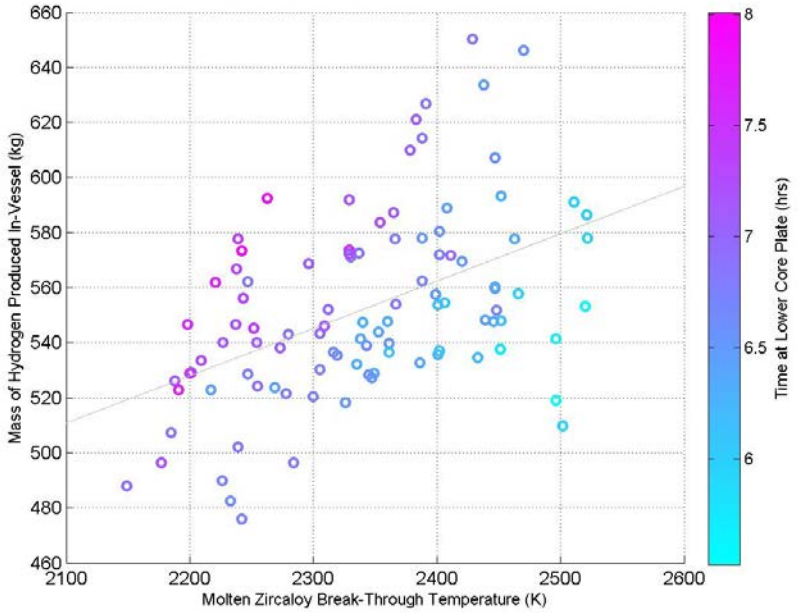

Figure 5.2 – Molten Zircaloy Breakthrough Temperature Scatterplot for Cumulative Hydrogen Production at Lower Core Plate Failure for Replicate 1.

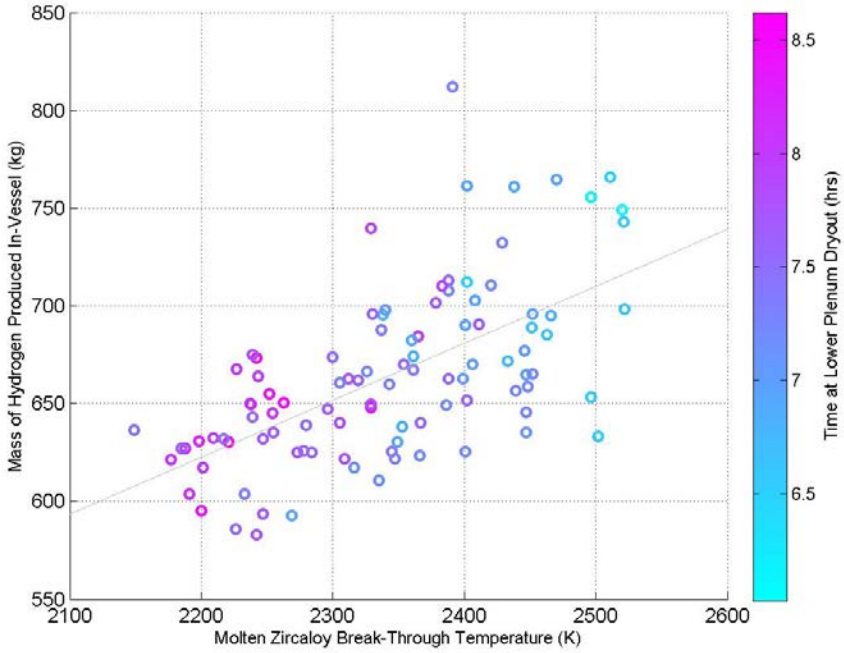

Figure 5.3 – Molten Zircaloy Breakthrough Temperature Scatterplot for Cumulative Hydrogen Production at Lower Plenum Dryout for Replicate 1.

5.1.2 Time at Temperature

The effective temperature at fuel collapse is more complex than the breakthrough temperature described in the previous section. The effective time at temperature relationships were ascribed to a discrete failure temperature estimate via a surrogate temperature transient as described in Section 3.4.2.1.

In Figure 5.4, the collapse temperature does not appear to have a significant positive trend for in-vessel hydrogen produced, save for a cluster of outlier points near 2500K. This cluster of low hydrogen production samples, all failing before 4.5 hours and producing less than 325kg of H_2, suggests that the data is split into two regimes: one set of simulations where hydrogen has effectively plateaued, due to the cooling impacts following main steam line failure (RPV depressurization and the subsequent temporary steam cooling), and thus is invariant to failure temperature, and one set where hydrogen is rapidly generated and thus early failure temperatures correspond to lower hydrogen production.

Figure 5.5 illustrates this relationship further by adding an axis for time differential between main steam line failure and first fuel failure. As can be seen, before main steam line failure, hydrogen produced before fuel failure is scattered from low to high hydrogen production values. Once main steam line failure occurs additional hydrogen production tends to decrease dramatically[9], as can be seen by the milder relationship between the difference of main steam line failure and first fuel failure and hydrogen production in Figure 5.5. At this point, the

[9] One theory for stabilization of the cumulative hydrogen production after main steam line failure is that the fuel is cooled during blowdown. The fuel must then reheat to resume significant hydrogen production.

cumulative hydrogen generation is negatively correlated to conditional additional time to first fuel collapse, potentially due to the lower cumulative damage prior to main steam line failure. This impact with main steam line failure is even more visible with intact fuel mass (see Figure 5.6).

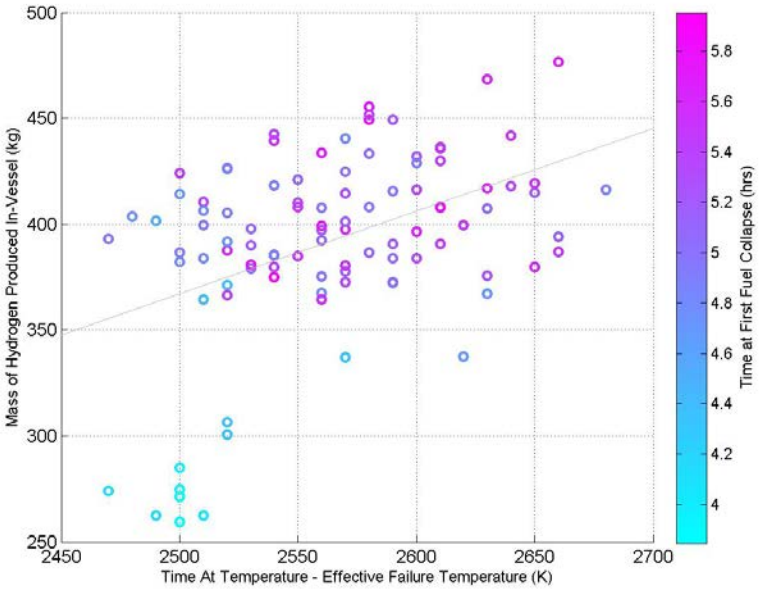

Figure 5.4 – Effective Temperature of Fuel Failure Scatterplot for Cumulative Hydrogen Production at First Fuel Failure for Replicate 1.

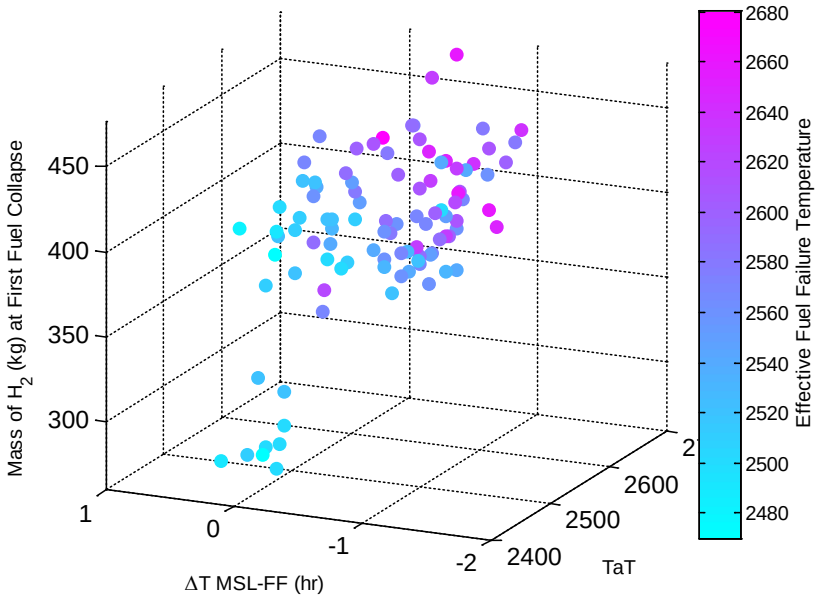

Figure 5.5 – Effective Temperature of Fuel Failure (*TaT*) Scatterplot at Main Steam Line Failure with Time Differential (ΔT) Between the Time of Main Steam Line Failure (T_{MSL}) and First Fuel Failure (T_{FF}) vs Intact Fuel Fraction ($\Delta T = T_{MSL} - T_{FF}$) for Replicate 1.

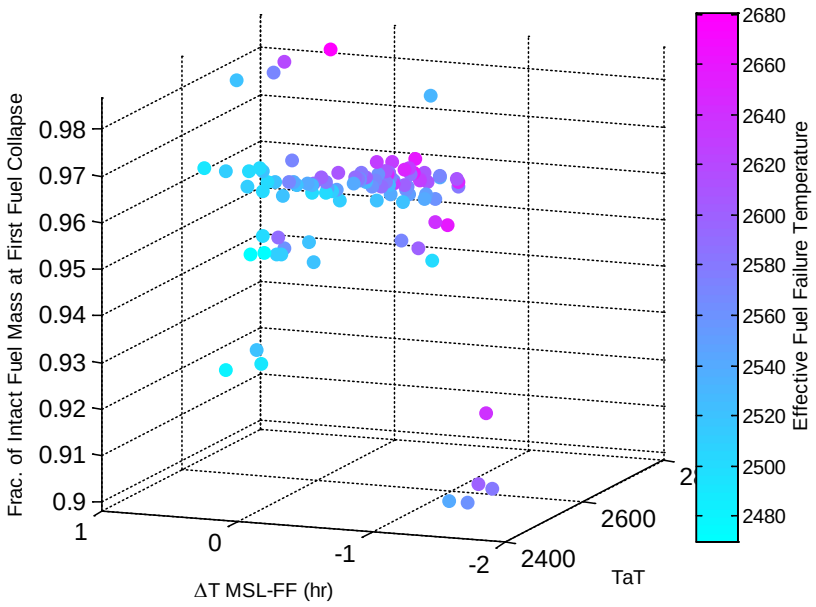

Figure 5.6– Effective Temperature of Fuel Failure (*TaT*, in °C) Scatterplot at First Fuel Failure with Time Differential (ΔT) Between the Time of Main Steam Line Failure (T_{MSL}) and First Fuel Failure (T_{FF}) vs Intact Fuel Fraction ($\Delta T = T_{MSL} - T_{FF}$) for Replicate 1.

Figure 5.7 shows a noisy, but positive, relationship between effective fuel failure temperature and hydrogen produced before lower core plate failure.

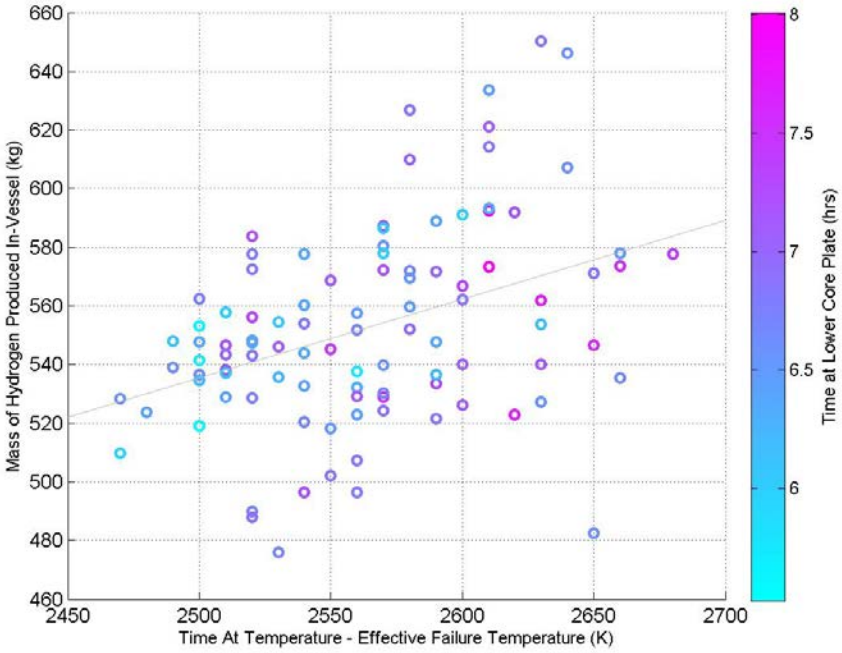

Figure 5.7 – Effective Temperature of Fuel Failure Scatterplot with Cumulative Hydrogen Production at Lower Core Plate Failure for Replicate 1.

5.1.3 Decay Heat

The effect of decay heat was only easily visible during the first two failure times, first channel box failure and first control rod failure. During these timing FoMs, it is evident that higher decay heat leads to earlier event timings, which seems to roughly correlate to lower hydrogen production at the time. The scatter plots for hydrogen production at first control rod and first channel box failure can be seen in Figure 5.8 and Figure 5.9.

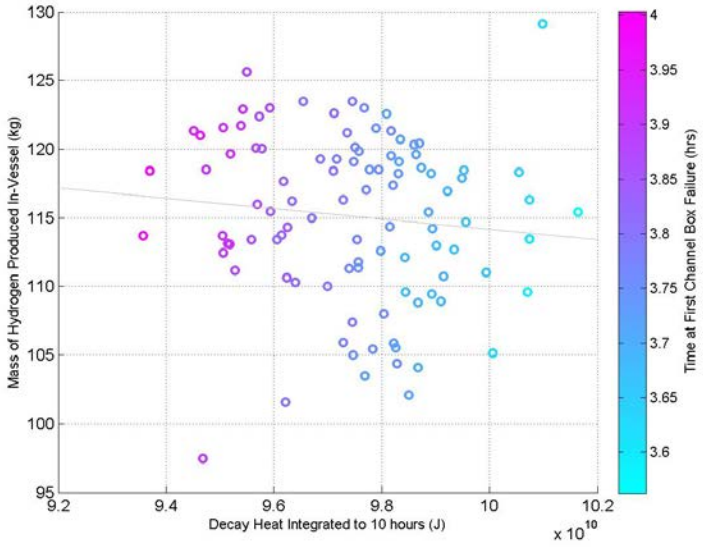

Figure 5.8 – 10 Hour Integrated Decay Heat Scatterplot at First Channel Box Failure for Replicate 1.

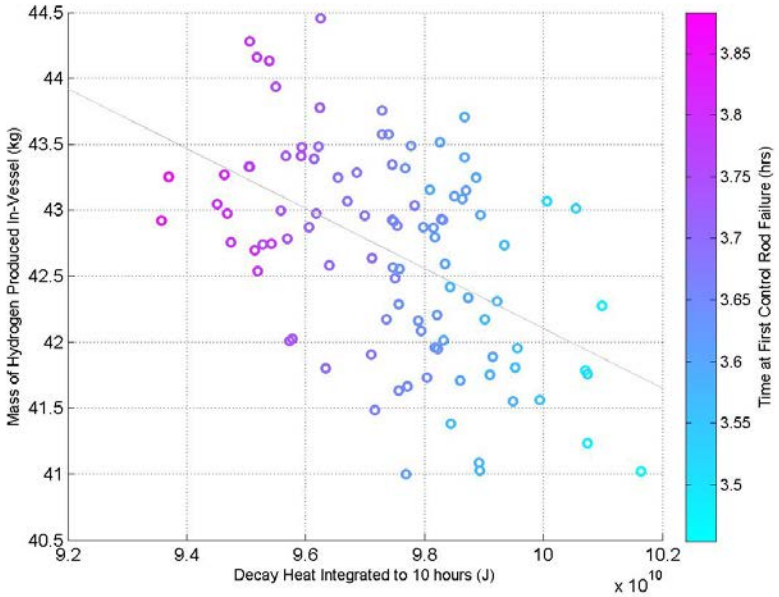

Figure 5.9 – 10 Hour Integrated Decay Heat Scatterplot at First Control Rod Failure for Replicate 1.

5.2 Scatter Plots H_2 generated at a Timing FoM and H_2 at the End of Simulation

This section examines the evolution of cumulative hydrogen production scatter, from major timing FoMs to the end of simulation.

From Figure 5.10, there is no discernable relationship between H_2 generation at first fuel collapse and H_2 generation at the end of the simulation. The bifurcation at lower fuel collapse times was due to the main steam line failing later than first fuel failure for a portion of the simulations. Because main steam line failure and first fuel failure overlap, Figure 5.11 is essentially Figure 5.10 with hydrogen production values before main steam line failure shifted to higher values to account for additional hydrogen production between fuel failure and main steam line failure.

By the time of lower plenum dryout, the major discrete events during core degradation have occurred and hydrogen production has stabilized because most of the liquid water available for oxidation reactions has been boiled and transported away from the core/lower plenum regions of the RPV. Thus, Figure 5.12 shows a correlation structure start to form between timing FoMs and the end of simulation.

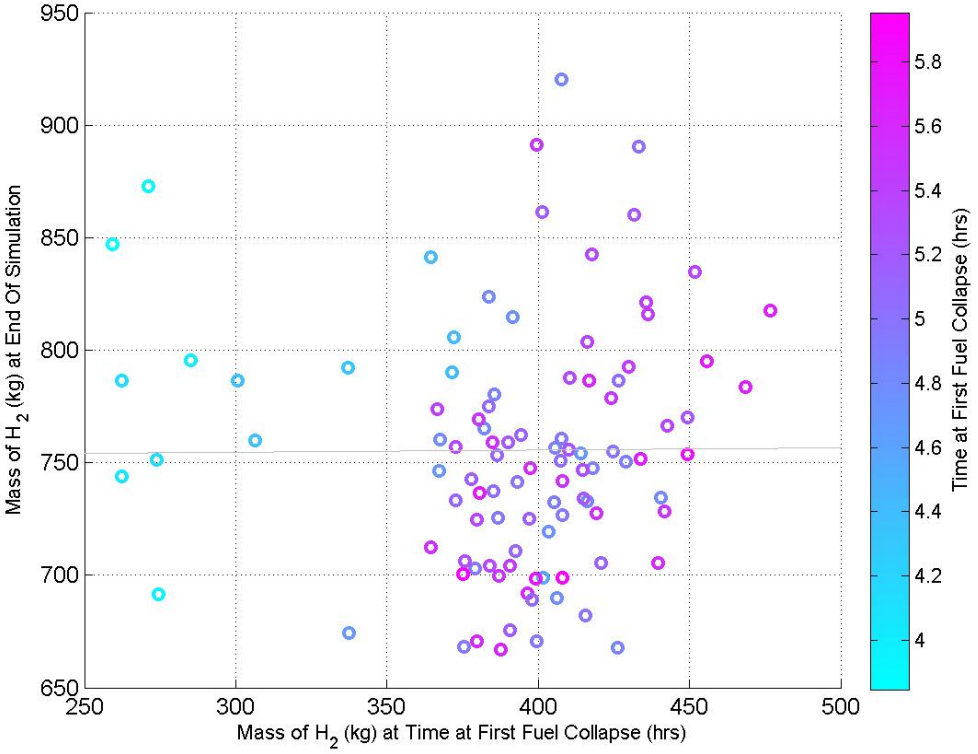

Figure 5.10 – Hydrogen at First Fuel Failure vs Hydrogen at End of Simulation for Replicate 1.

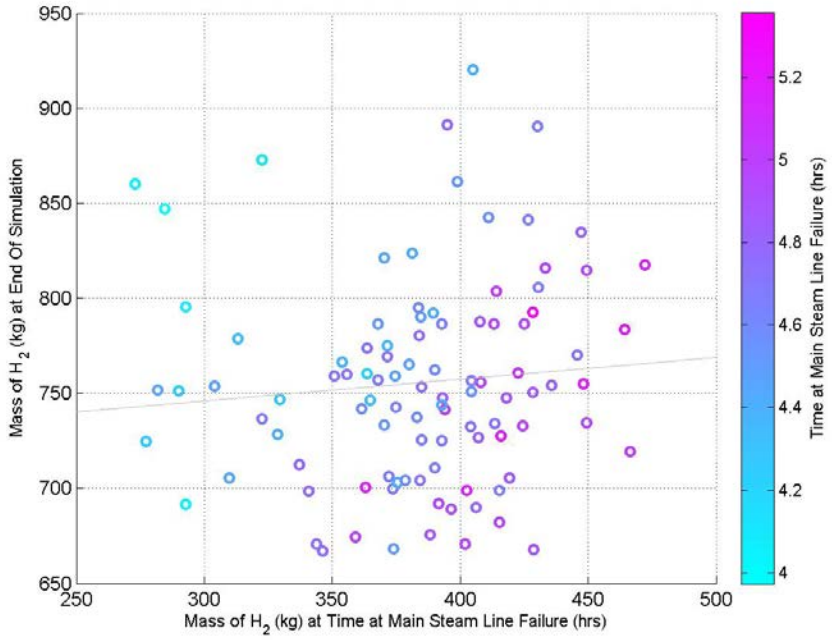

Figure 5.11 – Hydrogen at Main Steam Line Failure vs Hydrogen at End of Simulation for Replicate 1.

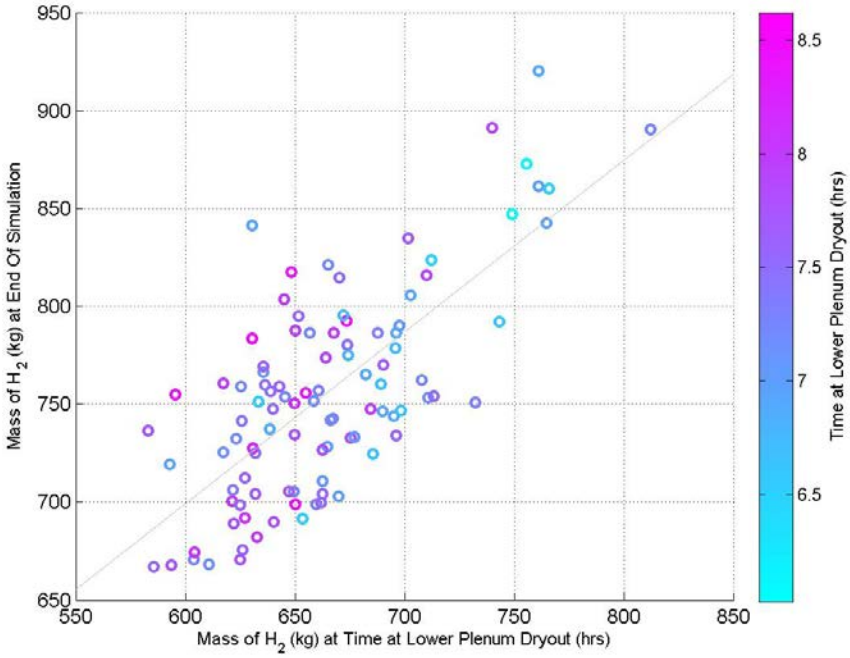

Figure 5.12 – Hydrogen at Lower Plenum Dryout vs Hydrogen at End of Simulation for Replicate 1.

5.3 Scatter Plots of Time Progression of Hydrogen Production Between Timing FoMs

As shown in Section 5.1.2, some physical FoMs can only be explained in the context of timing between events. Thus, it behooves the analyst to examine the variability in the timing of FoMs. The event couplings were examined both in terms of the absolute timing of the events and the conditional timing of events for the following events:

1. first fuel failure versus lower plenum dryout (Figure 5.13) and
2. lower plenum dryout versus lower head failure (Figure 5.14)

A positive correlation exists between the time of first fuel failure and lower plenum dryout, but a negative correlation exists between first fuel collapse and the time it takes to move from first fuel collapse to lower plenum dryout. One interpretation of this plot is that lower plenum dryout is accelerated by later fuel collapse because later fuel collapse has hotter material and more time for decay heat to accumulate in the system. It should be noted from the color axis of the plot, that higher hydrogen levels at a given time tend to both relate to earlier first fuel failures and reduce the conditional time of lower plenum dryout at a given first fuel collapse time.

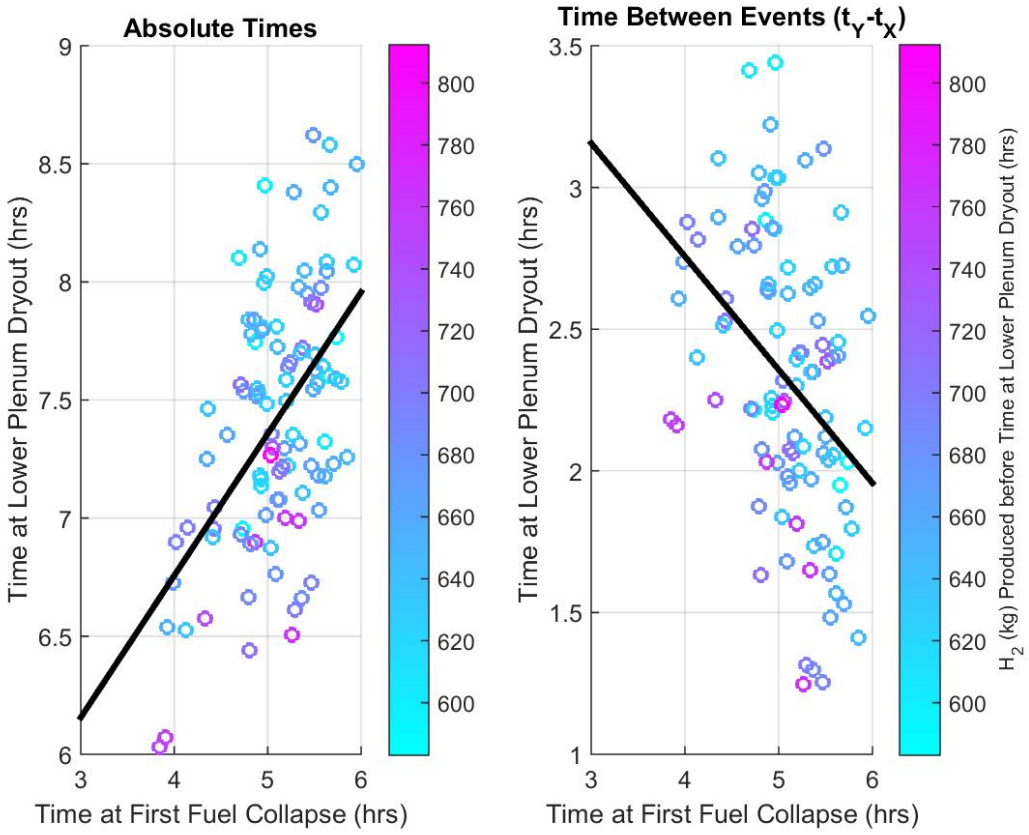

Figure 5.13 – Timing of First Fuel Collapse vs Lower Plenum Dryout for Replicate 1.

Figure 5.14 shows the time at lower plenum dryout versus lower head failure conditional on that simulation yielding lower head failure before 15 hours. Again, a positive correlation between

event times relative to the beginning of the accident transforms into a negative conditional correlation when the time of the first event is subtracted from the time of the second event. Hydrogen production levels, a surrogate for oxidation energy generated, seem to have little to no effect on the timing or prevalence of lower head failure.

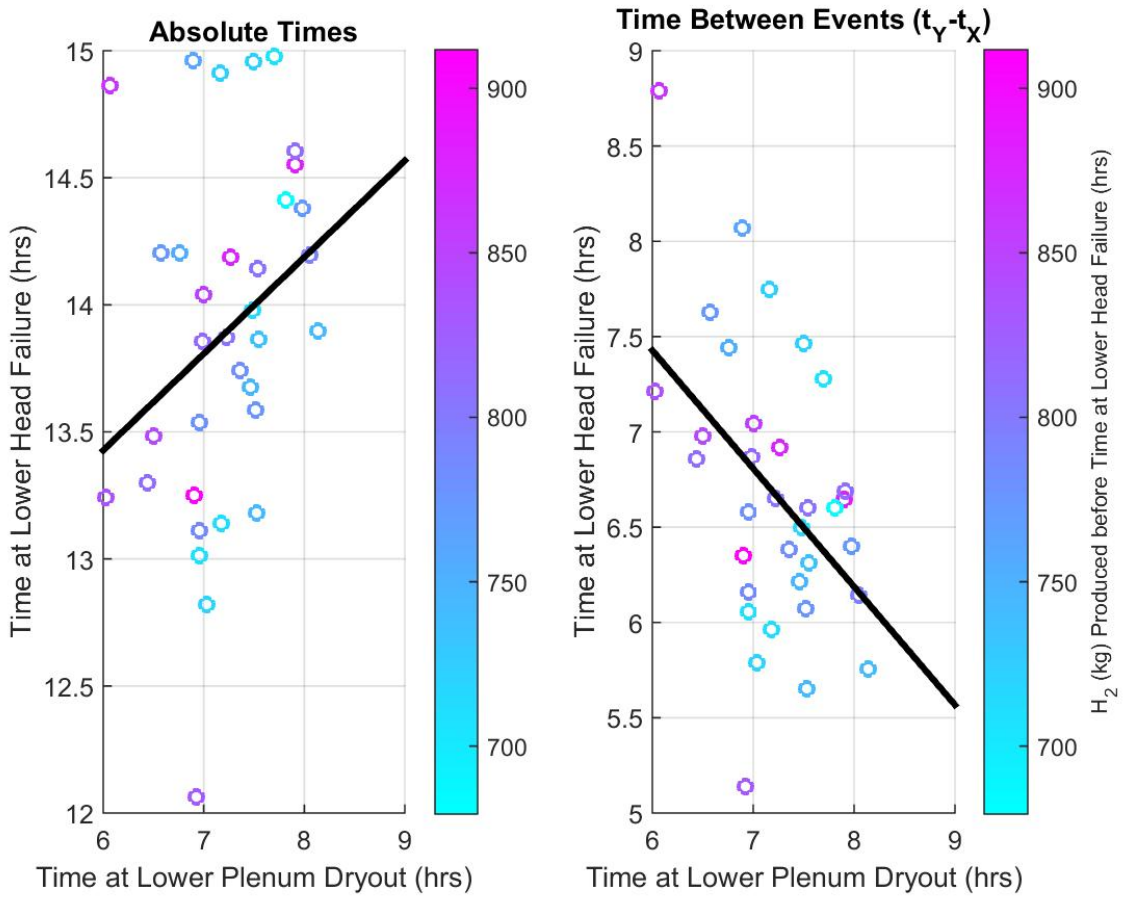

Figure 5.14 – Timing of Lower Plenum Dryout vs Lower Head Failure for Replicate 1.

5.4 Cumulative Distribution Functions

In addition to scatterplots, cumulative distributions can be useful for interpreting uncertainty results. From Equation (5-1), the cumulative distribution function (CDF or $F(\cdot)$)of an uncertain parameter is defined as the integral of the probability density function, $\pi(X')\mathrm{d}X'$, from negative infinity to the value X. Because one of the values in $\pi(X')\mathrm{d}X'$ must be the "real" value, and by the definition of probability distributions, the integral from $-\infty$ to ∞ must equal unity.

$$CDF = F(X) = \int_{-\infty}^{X} \pi(X')\mathrm{d}X' \tag{5-1}$$

Figure 5.15 and Figure 5.16 show the cumulative distribution event timing (on top of the figure) and either for cumulative hydrogen production or intact fuel mass (on the bottom of the figure), respectively. A CDF was generated for each physical FoM for each timing FoM. By potting each CDF on a single FoM axis, the distribution of outcomes of the FoM is visible throughout

the accident. It should be noted that CDFs for lower head failure were not plotted as a conditional distribution and thus these CDFs do not reach a value of one within the plot.

Figure 5.15 shows the CDFs associated with hydrogen production. Regressions associated with these CDFs can be found in Table 6.3. The decrease and subsequent rapid increase of the CDF slope for the main steam line failure and first fuel failure for both event timing and hydrogen generation near a CDF value of 0.1 is due to the relative timing of main steam line and first fuel failure discussed previously. These effects seem to dilute as the accident sequence progresses. From the lower head failure and end of simulation CDFs for hydrogen generation, the range of the CDFs span the same hydrogen levels even though not all simulations led to lower head failure. Thus, hydrogen generation (and hence oxidation energy produced) is not the primary driving force for lower head failure.

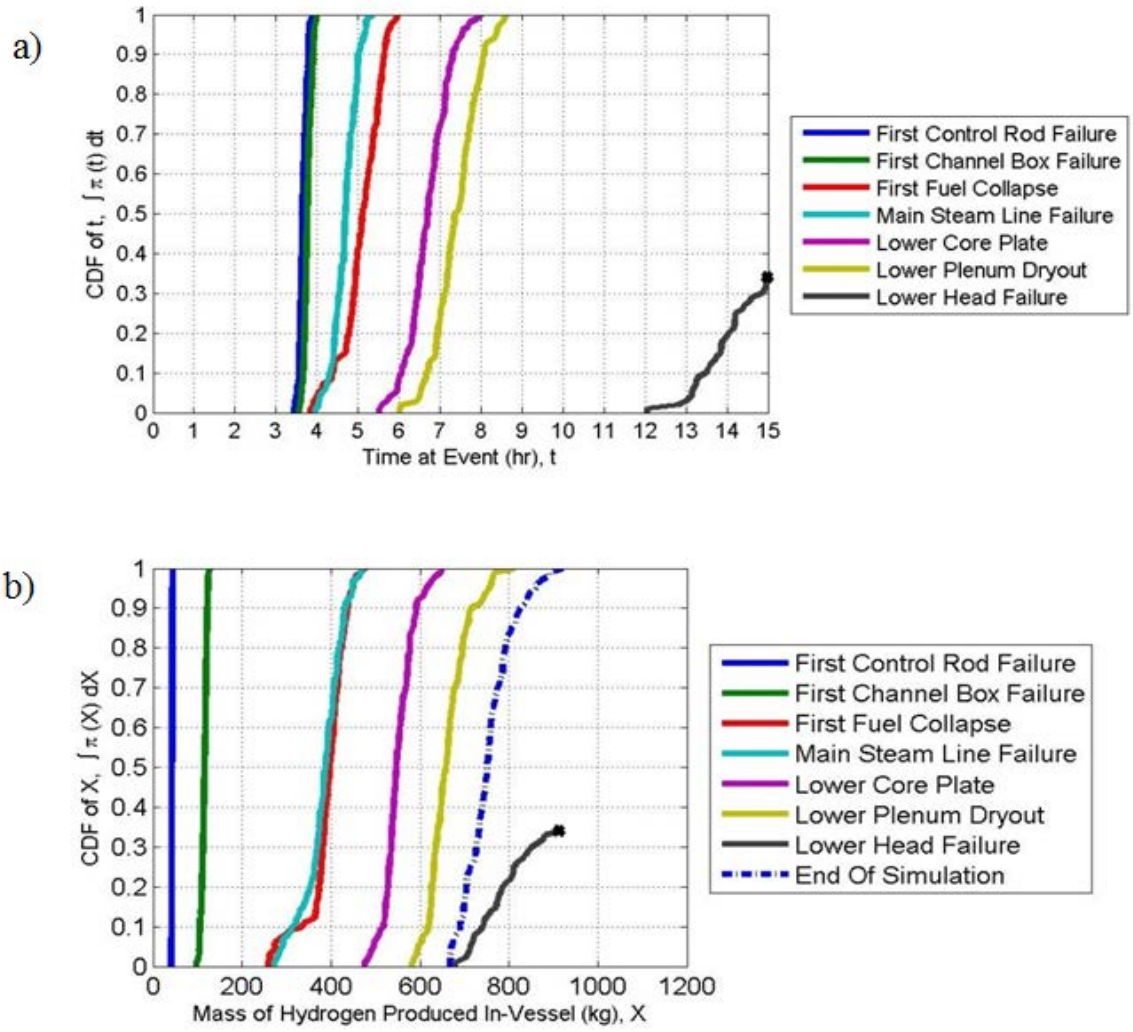

Figure 5.15 – Cumulative Distributions for Replicate 1 FoM Timings and Corresponding Hydrogen Production

Figure 5.16 b) shows the CDFs associated with the fraction of intact fuel mass. As can be seen from the main steam line curve, approximately 15% of Replicate 1 simulations resulted in a significant (~>5%) loss of intact fuel before the main steam line failed. That fraction can drop to below 63% of fuel remaining intact by the time main steam line fails. The lower core plate failure, lower plenum dryout, and end of simulation CDFs all experience dramatic bifurcations in the intact fuel fractions, which may be the result of ring collapse only being predicted in a fraction of the Replicate 1 simulations. An entire MELCOR COR ring can collapse when the stub tubes and supporting CRD-columns yield due to high temperature stress and/or melting. When lower support is lost, MELCOR assumes that all intact material above the failure elevation instantly transforms to particulate debris and relocates.

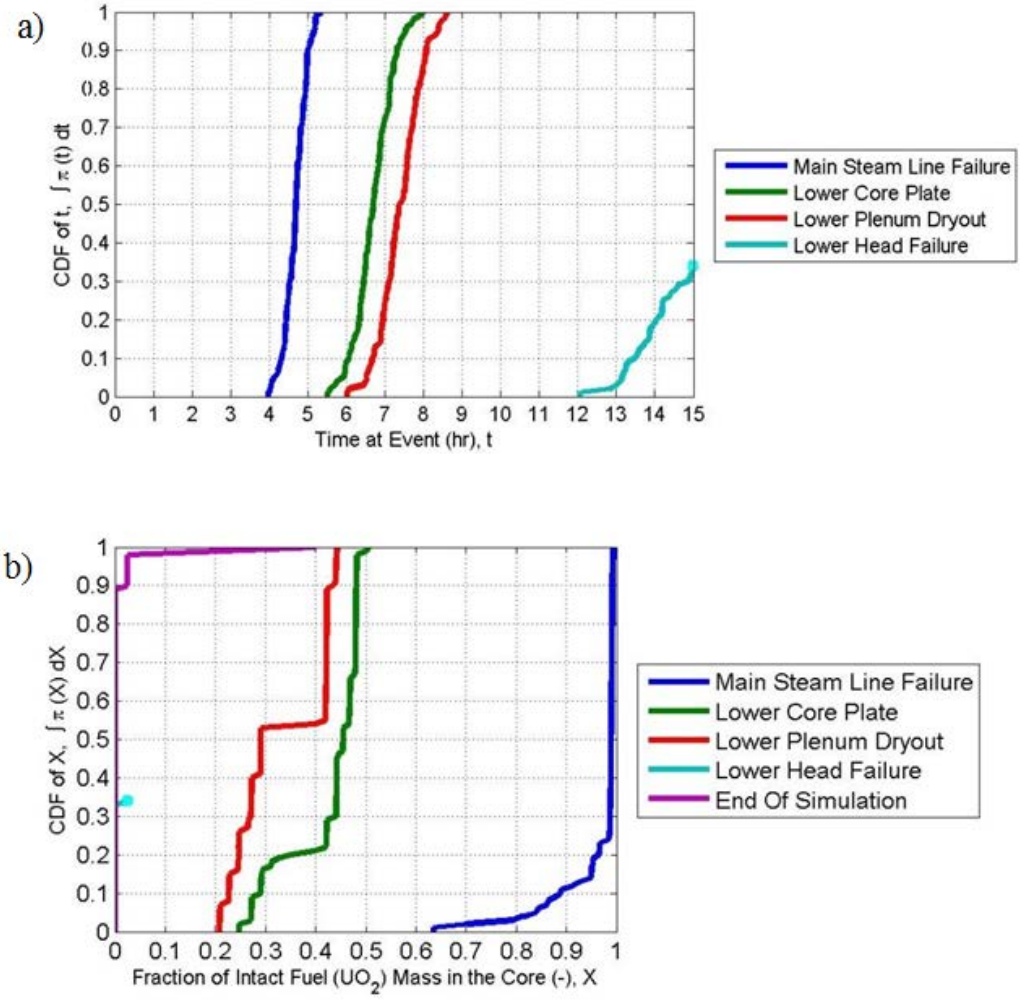

Figure 5.16 – Cumulative Distributions for Replicate 1 FoM Timings and Corresponding Intact Fuel Mass

5.5 Summary of Insights from a Visual Inspection of the MELCOR Statistical Outputs

Key insights from the automated regression analysis are summarized below:

- While experts believe that the 1F1 lower head failed before water injection occurred at 15 hours, the 1F1 UA results show that there is only a 40% chance of that outcome given the current state of 1F1 severe accident representations in MELCOR.
- For the simulations that experienced lower head failure, almost all of the fuel was transitioned to particulate debris and is not expected to be held up in the core region.
- The timing of steam line failure and fuel collapse are predicted to be intermingled events, which complicates the early phase core degradation analysis.
- Decay heat, fuel collapse criteria (*TaT*), and molten Zircaloy breakthrough temperature have clearly distinguishable trends with hydrogen production at select times throughout the accident.

6 AUTOMATED REGRESSION ANALYSIS

Chapter 6 presents the results of the Replicate 1 regression analysis for each combination of the physical and timing FoM. Regressions are conducted for both of the untransformed and the rank transformed data. A representative timing regression from Replicate 1 physical FoM is selected, then corresponding regressions are taken from Replicates 2-3 and Replicate U. Each of these 4 regressions is then applied to the other 3 samples to evaluate the predictive merit of the regression fits.

This chapter reviews the results from a series of regression analyses. These analyses were applied to three physical FoMs, at various timing FoMs, for the 1F1 accident progression results from Replicate 1. Utilizing regression analysis, first order influences may be inferred from the samples of the population of potential MELCOR output results. When interpreting regression results, it is important to remember that a regression model can only regress influences for which it is preconditioned. Section 5.1 and 5.4 did not produce obvious transformations in the FoMs and/or input variables to facilitate linear regressions. Thus, without additional transformations to the input/output data, the only influences which can be inferred using a stepwise regression process are:

- Linear influences in an input parameter, e.g. $\Delta Y = \beta_i \Delta X_i$, and
- Interaction influences between input parameters, e.g. $\Delta Y = \beta_{ji} \Delta X_i X_j$.

Other regression techniques both can and have been employed to infer input influences on output behavior [6.1]. For the 1F1 analysis, the authors are concerned that due to the high variability of core degradation-influenced MELCOR outputs, regressions may be susceptible to fitting inherent variability instead of or in addition to the physical trends derived from input variability. Thus, only simple linear regressions are employed across various event times to determine if trends hold throughout the accident and then these regressions are validated across multiple samples to determine if either the regression results are applicable to the entire population of 1F1 MELCOR outputs or simply to fitting inherent variability within a given sample.

Section 6.2 outlines the regression results from the untransformed input and output MELCOR FoM data. A series of dependency tables are presented for each physical FoM. In these dependency tables, each column summarizes the magnitude of the influence of the physical FoMs at each of the timing FoMs and each row represents the input variable attributed to that influence. Multiple dependency tables are presented for each physical FoM to infer changes in the influencing input variables between timing FoMs.

Section 6.3 repeats the efforts in 6.2 except that the X and Y variables are rank transformed. This potentially allows for non-monatomic effects to be linearized and thus detected in the linear regression analysis.

Chapter 7 takes three raw and three rank regressions from Sections 6.2 and 6.3 and compares them across the three replicate samples and the uniform sample in order to gauge predictive merit to the population of potential 1F1 MELCOR simulations. Additionally, Replicates 1 and 2 were combined and regressed and the resulting regressions were applied to the sample data in Replicate 3 and the uniform sample to determine if a larger training sample size would produce better predictive regressions.

6.1 Interpreting Regression Dependency Tables

This section describes the methodology used for conducting regressions on the raw (i.e. untransformed) input and output MELCOR data at each timing FoM. As a reminder, the timing FoMs we selected because they mark the addition of new discrete events in the core degradation process:

1. First Control Rod Failure,
2. First Channel Box Failure,
3. First Fuel Failure,
4. Main Steam Line Failure,
5. Lower Core Plate Failure,
6. Lower Plenum Dryout,
7. Lower Head Failure,
8. End of Simulation.

Three physical FoMs are examined:

- Mass of Material Ejected from the Lower Head,
- Cumulative In Vessel Hydrogen Production, and
- Intact Fuel Mass in the Core.

As many as 36 raw regressions were conducted for each physical FoM. Practicality prevents the authors from systematically discussing each regression, thus dependency tables were created to summarize the key results from each regression. After the dependency tables are presented, select model summary tables are provided to allow the reader to more completely understand the results of the regression analysis.

An example dependency table is shown in Figure 6.1. This table is illustrative and has been shrunk to fit on a portrait page. The table can be read as follows:

1. The first row defines the timing FoM in which the regression in a given column is conducted. For example, the column within the blue dashed box defines the regression for a physical FoM (e.g. cumulative in-vessel hydrogen production) at the timing FoM defined by the first cell in the column (i.e., lower core plate failure).
2. The second row provides R^2, R^2_{adj}, F-statistic and the probability that a constant model is more appropriate derived from the F-statistic. These measures are defined in Section 3.3. On a basic level, a regression is a better fit to the data if it has a high R^2 value and a lower F-statistic based probability.
3. Rows 3 through 18 will indicate if the variable in the first cell of that row was found in the regression. For example, the row with the orange dashed border defines all of the timing FoMs which regressed molten Zircaloy breakthrough temperature as having a linear influence on the physical FoM. If a parameter was not identified in a regression, it was not included in the dependency table and the cell is left blank. Thus, blank cells are included to emphasize the lack of evidence for significant influence of parameters at different timing FoMs.

	1st Control Rod Failure	1st Channel Box	1st Fuel Failure	Main Steam Line	Lower Core Plate	Lower Plenum Dry-out	Lower Head Failure	End of Simulation
R^2 / R^2_{adj} / F-stat vs. Const./ p-val	.28 / .26 / 18.7 / 0	.06 / .05 / 5.9 / 0.017	.26 / .24 / 11.3 / 0	.33 / .31 / 11.9 / 0	.58 / .55 / 21.1 / 0	.485 / .463 / 22.3 / 0	.66 / .6 / 10.7 / 0	.194 / .177 / 11.7 / 0
Intercept	65 kg	144 kg	155 kg	757 kg	8288 kg	158.44 kg	-126.73 kg	242.09 kg
Time Constants for Radial (solid) Debris Relocation (s) [1] RSDR				[33, 81, 128] [-184, -117, -48][4] [-56, -36, -15]	[-34, -22, -9]		[35, 84, 132]	
Time Constants for Radial (liquid) Debris Relocation (s) RLDR								
dT/dz Model, Time Constant for Averaging Flows (s) dTdz_TCAF		[-32, -29,-26]						
dT/dz Model, Characteristic Coupling Time (s) dTdz_CVH								
dT/dz Model, Relative Weight of Historical Flow (s) dTdz_Smooth								
Molten Zircaloy Break-Through Temperature (K) [2] MZBT			[-217, -202, -185]	[-470, -437,-400]	[-9221, -8570, -7857] [8248, 8996, 9679][6] [391, 426, 459]	[665, 725, 780]	[632, 689, 742]	[491, 535, 576]
Molten Cladding (pool) Drainage Rate (kg/(m*s)) MCDR								
Fraction of Strain at Which Lower Head Failure Occurs FSLHF					[73, 83, 91]			
Scaling Factor for Candling Heat Transfer Coefficients SFCHTC								
Fraction of Un-oxidized Cladding Thickness Initiating T. M. Weakening (m)[3] MechWeak							[97, 177, 282] [-151, -95, -52][5] [45, 82, 131	
Debris Quenching Heat Transfer Coefficient to Pool (W/(m*m*K)) [4] DebrisHT				[9, 95, 162] [-200, -117, -11][1] [-38, -22, -2]		[-1314, -772, -74] [73, 757, 1290][6] [-25, -14, -1]		[-37, -22, -2]
Debris Falling Velocity (m/s)[5] DFV	[-0.511, -0.187, -0.007]						[2, 62, 169] [-258, -95, -4][3] [-89, -33, -1]	
Minimum Debris Porosity minPorosity					[-19, -10, -1]			
Time At Temperature - Effective Failure Temperature (K)[6] TaT			[887, 919, 962]		[-8597, -8212, -7924] [8680, 8996, 9418][2] [756, 784, 821]	[-215, -205, -198] [731, 757, 793][4] [533, 552, 578]		
Decay Heat Integrated to 10 hours (J) DCH	[-23, -22, -21]		[-502, -482, -462]					

Figure 6.1 – Example Dependency Table

The numbers contained in a given box provide a measure of the impact of that variable on the regression. The columns in the **X** matrix consist of variables which can vary by orders of magnitude (e.g. decay heat is often on the order of 10^{10} J while unoxidized cladding thickness until thermal mechanical weakening is on the order of 0.001), thus the beta values also vary over orders of magnitudes to convert the input parameter to the regressed changes in Y. As a result, beta values cannot be compared directly.

Instead of only providing β_i, the product of $X_i\beta_i$ is the FoM within the regression output which allows the effect of one variable, X_i, to be compared to the effect of another variable, X_j, on the output FoM, Y. For notational simplicity, define the estimate for the minimum value of X_i taken over all samples as $X_{i_{(1)}}$. Similarly define the estimates for the median value of X_i and the maximum value of X_i by $X_{i_{(n/2)}}$ and $X_{i_{(n)}}$ respectively. Since β_i may be either positive or negative, the product $X_{i_{(n)}}\beta_i$ will estimate the maximum effect when β_i is positive, but will estimate the minimum effect when β_i is negative. Thus, the minimum and maximum are taken after multiplication by β_i. Because the range of X_i varies from parameter to parameter, the impact of the direct influence from the variable is reported in Equation (6-1).

(6-1)

$$[\Delta Y_{\min}, \Delta Y_{median}, \Delta Y_{\max}] | X_i \sim \left[\min\left\{\hat{\beta}_i X_{i_{(1)}}, \hat{\beta}_i X_{i_{(n)}}\right\}, X_{i_{(n/2)}}, \max\left\{\hat{\beta}_i X_{i_{(1)}}, \hat{\beta}_i X_{i_{(n)}}\right\}\right]$$

Thus, as highlighted by the blue cloud in Figure 6.1, the time at temperature parameter can increase hydrogen production at the time of first fuel failure anywhere from 887 to 962 kg of H_2, with half the samples estimating hydrogen production over or under 919 kg of H_2. This high

positive causal relationship is balanced by the presence of negative decay heat and molten Zircaloy breakthrough temperature influences in the same column. In summary, this regression is implying that higher fuel failure temperatures correlates with additional H_2 at first fuel failure for the sample of 1F1 MELCOR simulations regressed, while higher molten Zircaloy breakthrough temperatures and decay heat levels may lower H_2 produced at time of fuel failure.

Important: Regression insights are correlative, not necessarily causal, and are comingled with the timing of the event. For example, reduced H_2 at fuel failure with higher decay heat may be caused by higher decay heat collapsing fuel earlier, thus reducing the available time to produce hydrogen. Thus, higher decay heat levels should not be interpreted to produce less H_2 during a severe accident.

When interaction effects are fit to the meta-model, explaining the parameter influence becomes more complex. The three parameter vector described in Equation (6-1) is still used to describe direct effects of the parameter and is the first vector in an interaction cell within the dependency table. Below the direct effect vector lays the interaction vector. It includes the interaction coefficient, the median of the interaction term, and the three parameter X vector used in (6-1). This interaction vector is defined in Equation (6-2).

$$[\Delta Y_{\min}, \Delta Y_{median}, \Delta Y_{\max}] | X_i X_{j_{(n/2)}} \sim \left[\min\left(\hat{\beta}_{i,j}\, X_{j_{(n/2)}} \left[X_{i_{(1)}}, X_{i_{(n/2)}}, X_{i_{(n)}}\right]\right), \right.$$
$$\left. \text{median}\left(\hat{\beta}_{i,j}\, X_{j_{(n/2)}} \left[X_{i_{(1)}}, X_{i_{(n/2)}}, X_{i_{(n)}}\right]\right), \max\left(\hat{\beta}_{i,j}\, X_{j_{(n/2)}} \left[X_{i_{(1)}}, X_{i_{(n/2)}}, X_{i_{(n)}}\right]\right)\right] \quad (6\text{-}2)$$

Obviously, the influence on the FoM of X_i is a combination of the direct and interaction effects. Thus, a third vector is included to approximate the full impact of X_i in the regression. This third vector, the sum of the previous two, is defined in Equation (6-3). All interaction terms have a color coded numerical indicator to identify the interacting variable.

$$\begin{aligned}[\Delta Y_{\min}, \Delta Y_{median}, \Delta Y_{\max}] | X_i, X_i X_{median,j} \sim \; & \left[\min\left(\hat{\beta}_{i,j}\, X_{j_{(n/2)}} \left[X_{i_{(1)}}, X_{i_{(n/2)}}, X_{i_{(n)}}\right]\right.\right. \\ & + \hat{\beta}_i \left[X_{i_{(1)}}, X_{i_{(n/2)}}, X_{i_{(n)}}\right]\Big), \text{median}\left(\hat{\beta}_{i,j}\, X_{j_{\left(\frac{n}{2}\right)}} \left[X_{i_{(1)}}, X_{i_{\left(\frac{n}{2}\right)}}, X_{i_{(n)}}\right]\right. \\ & + \hat{\beta}_i \left[X_{i_{(1)}}, X_{i_{(n/2)}}, X_{i_{(n)}}\right]\Big), \max\left(\hat{\beta}_{i,j}\, X_{j_{\left(\frac{n}{2}\right)}} \left[X_{i_{(1)}}, X_{i_{\left(\frac{n}{2}\right)}}, X_{i_{(n)}}\right]\right. \\ & \left.\left. + \hat{\beta}_i \left[X_{i_{(1)}}, X_{i_{(n/2)}}, X_{i_{(n)}}\right]\right)\right] \end{aligned} \quad (6\text{-}3)$$

Only the most relevant model summary tables are provided, as including every model summary table for the regressions in the dependency tables is not practical.

6.2 Raw Regressions

This section presents the dependency tables for regressions conducted on the original MELCOR data from Replicate 1. First, the regressions for material ejected from the lower head conditional on lower head failure are presented. Next, the in-vessel hydrogen production regressions are presented. Finally, the fraction of intact fuel mass regressions are presented.

6.2.1 Material Ejected from the Lower Head Conditional on Lower Head Failure

This section provides the dependency and summary tables for the physical FoM – material ejected from the lower head. The dependency table which displays FoM values from the beginning of simulation can be seen in Table 6.1. Material cannot eject from the lower head until lower head fails, and once failure occurs there is a near instantaneous relocation of a fraction of the material held up in the lower head to the drywell. A moderate fraction (~ 52%) of the sample variance of debris relocation at the time of lower head failure can be explained with a regression involving the:

- Characteristic couple time of the *dT/dz* model,
- Debris quenching heat transfer coefficient, and
- Debris falling velocity.

Table 6.1 – Mass of Material Ejected from the Lower Head Conditional on Lower Head Failure, Beginning of Simulation Until t_{FOM}, Raw Data

	Lower Head Failure	**End of Simulation**
R^2 / R^2_{adj} / F-stat vs. Const./ p-val	.56 / .516 / 12.7 / 0	N/A
Intercept	1998.7 kg	44930 kg
Time Constants for Radial (solid) Debris Relocation (s) RSDR		
Time Constants for Radial (liquid) Debris Relocation (s) RLDR		
dT|dz Model, Time Constant for Averaging Flows (s)		
dT|dz Model, Characteristic Coupling Time (s) dTdz_TCAF	[66450, 81748, 99124]	
dT|dz Model, Relative Weight of Historical Flow (s) dTdz_CVH		
Molten Zircaloy Break-Through Temperature (K) MZBT		
Molten Cladding (pool) Drainage Rate (kg/(m*s)) MCDR		
Fraction of Strain at Which Lower Head Failure Occurs MSLHF		
Scaling Factor for Candling Heat Transfer Coefficients SFCHTC		
Fraction of Un-oxidized Cladding Thickness Initiating T. M. Weakening (m) MechWeak		
Debris Quenching Heat Transfer Coefficient to Pool (W/(m*m*K)) DebrisHT	[-51758, -30396, -2910]	
Debris Falling Velocity (m/s) DFV	[482, 12511, 34129]	
Minimum Debris Porosity minPorosity		
Time At Temperature - Effective Failure Temperature (K) TaT		
Decay Heat Integrated to 10 hours (J) DCH		

Note: Blank cells denote that the parameter was not regressed at the timing FoM.

While prior physical intuition is difficult to extract for *dT/dz* model parameters, it is logical that debris heat transfer coefficients, which likely influence the timing of vessel head failure, and debris falling velocity, which likely effects how much of the rubbilized core material makes its way to the lower head before failure, are likely influencing parameters of the mass of material ejected from the lower head at the time of lower head failure.

No statistically significant regression results could be obtained for the end of simulation (i.e. 15 hours after the start of the transient). This finding strengthens the hypothesis that correlations may be easier to find at key bifurcation points in an accident progression than at set times.

The model summary table for the regression of mass of material ejected from the lower head at the time of lower head failure can be seen in Table 6.2. The scatterplots of these variables are shown in Figure 6.2.

Table 6.2 – Model summary Table for Mass of Material Ejected from the Lower Head at the Time of Lower Head Failure

Event	*Parameters*	*Estimate*	*SE*	*tStat*	*pValue*
Lower Head Failure [n=34, f=3]	Intercept	1998.7	29340	0.068	0.95
	dTdz_CVH	8274	2682	3.09	0.004
	DebrisHT	-27	5.6	-4.78	0.00004
	DFV	34160	12331	2.77	0.0095
Note: see dependency table for regression fit statistics					

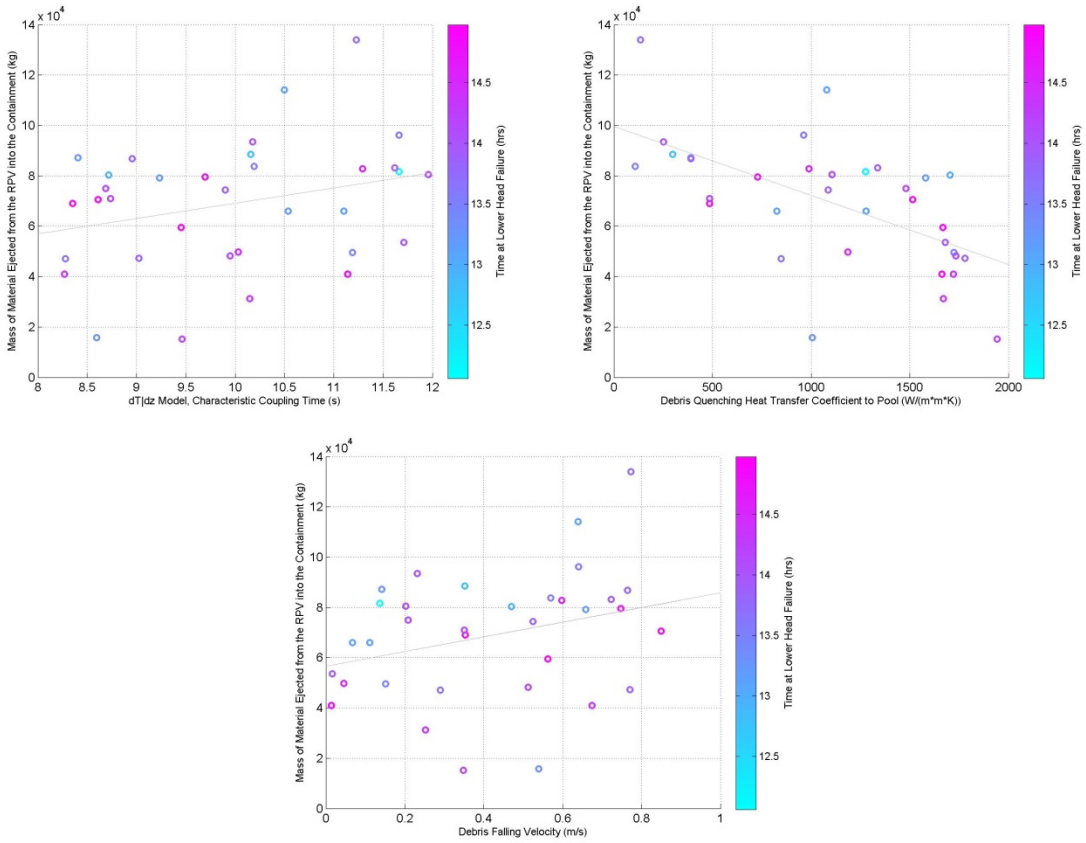

Figure 6.2 – Scatter Plots of the Three Regressed Variables of Mass of Material Ejected From the Lower Head from Replicate 1.

6.2.2 In-Vessel Hydrogen Production

Unlike mass of material ejected from the lower head, hydrogen production begins before every timing FoM, thus a full dependency table is needed to examine the regressions for every timing FoM. This table is presented in Table 6.3.

The first trend to be discussed from the dependency Table 6.3 is the evolution of fit qualities to the Replicate 1 sample. With the exceptions of first channel box failure, lower plenum dryout, and end of simulation, R^2 and R^2_{adj} increase as the accident progresses and the amount of hydrogen produced starts to stabilize. From Figure 5.15 b), this behavior is expected as the spread of H_2 produced starts to stabilize after first fuel failure. The timing of lower head failure extends through end of simulations, causing a bifurcation in hydrogen production between simulations which experienced lower head failure and simulations that did not experience lower head failure. Thus, the end of simulation fit for H_2 production is poor. Additionally, the timing FoMs do not comprise a comprehensive list of discrete events which occur during core degradation. Discrete events, e.g. failure of core sections or rings, can and do occur throughout the distribution of core degradation timing FoMs. These discrete events can dramatically reduce the ability of a linear regression to resolve potential dependencies.

The second noticeable trend is with *MZBT*. This is the only parameter within the Replicate 1 sample that was included in every stage throughout the accident sequence in which the parameter could potentially have a physical impact on hydrogen generation. It would have been

disconcerting if this parameter was included for control rod and channel box failure since *MZBT* would first occur after channel box failure. At first fuel failure and main steam line failure, whose timing distributions are essentially coincident from Figure 5.15 b), a negative trend[10] was regressed between *MZBT* and hydrogen production, suggesting a suppressive effect at higher sampled *MZBT*. By the time of lower core plate failure, this trend reversed and a positive correlation was established between *MZBT* and hydrogen production for all remaining timing FoMs.

A number of the interaction effects[11], resolved also seem physical. For the main steam line failure, a negative correlation was resolved for the interaction between *RSDR* and *DebrisHT*, both parameters which would affect debris behavior in the core. At the time of lower core plate failure, a positive correlation was resolved for the interaction between *TaT* and *MZBT*, both parameters effecting how long hot material is held up in the core region, a trend which is clearly visible in Figure 6.3. Interaction effects were also observed for lower plenum dryout and lower core plate failure, but the physical justification for those interactions is less clear.

The three input variables *RSDR*, *DebrisHT*, and *TaT* are regressed at three separate times throughout the accident progression. No other variables, except *MZBT*, were regressed at more timing FoMs. It is also notable that both variables *TaT* and *DCH*, approximated as described in Section 6.4.1.2, were regressed.

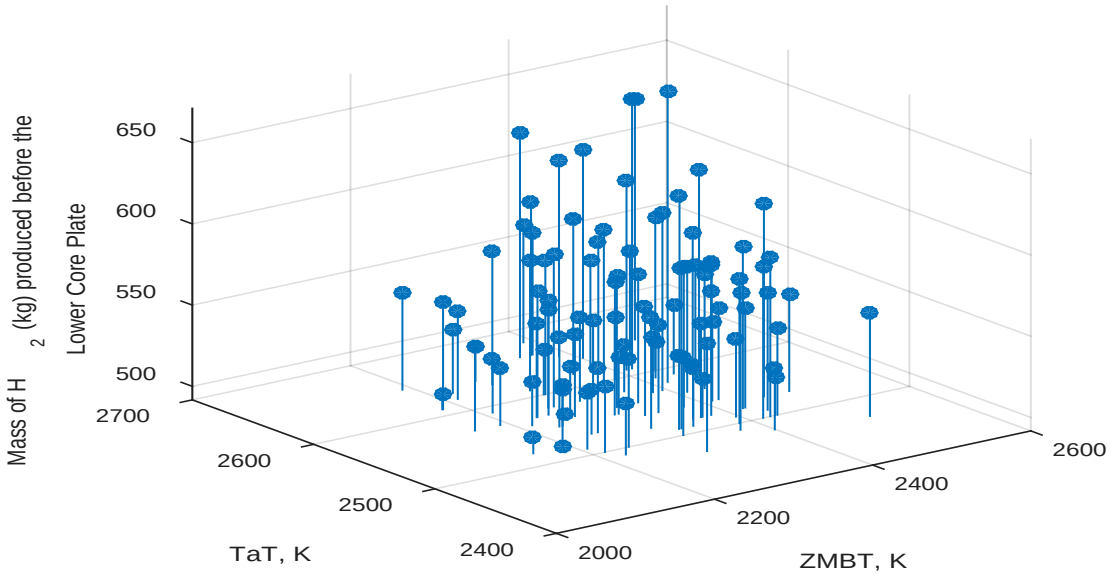

Figure 6.3 – Linear Interaction Between Effective Fuel Failure Temperature (K) {*TaT*} and Molten Zircaloy Melt Breakthrough Temperature (K) {*MZBT*} at the Time of Lower Core Plate Failure for Cumulative Hydrogen Production.

[10] The sign of the regressed trend is shown by the sign of the regression coefficients provided in the dependency tables.

[11] Interaction effects are conjoint influence on the output FoM. These effects are provided in the dependency tables as described in Section 6.4.1.

Table 6.3 – Mass of In-Vessel Hydrogen Produced, Beginning of Simulation Until t_{FOM}, Raw Data

	First Control Rod Failure	First Channel Box	First Fuel Failure	Main Steam Line	Lower Core Plate	Lower Plenum Dry-out	Lower Head Failure	End of Simulation
R^2 / R^2_{adj} / F-stat vs. Const./ p-val	.28 / .26 / 18.7 / 0	.06 / .05 / 5.9 / 0.017	.26 / .24 / 11.3 / 0	.33 / .31 / 11.9 / 0	.58 / .55 / 21.1 / 0	.485 / .463 / 22.3 / 0	.66 / .6 / 10.7 / 0	.194 / .177 / 11.7 / 0
Intercept	65 kg	144 kg	155 kg	757 kg	8288 kg	158.44 kg	-126.73 kg	242.09 kg
Time Constants for Radial (solid) Debris Relocation (s) [1] RSDR				[33, 81, 128] [-184, -117, -48][4] [-56, -36, -15]	[-34, -22,-9]		[35, 84, 132]	
Time Constants for Radial (liquid) Debris Relocation (s) RLDR								
dT|dz Model, Time Constant for Averaging Flows (s) dTdz_TCAF		[-32, -29,-26]						
dT|dz Model, Characteristic Coupling Time (s) dTdz_CVH								
dT|dz Model, Relative Weight of Historical Flow (s) dTdz_Smooth								
Molten Zircaloy Break-Through Temperature (K) [2] MZBT			[-217, -202, -185]	[-470, -437,-400]	[-9221, -8570, -7857] [8248, 8996, 9679][6] [391, 426, 459]	[665, 725, 780]	[632, 689, 742]	[491, 535, 576]
Molten Cladding (pool) Drainage Rate (kg/(m*s)) MCDR								
Fraction of Strain at Which Lower Head Failure Occurs FSLHF					[73, 83, 91]			
Scaling Factor for Candling Heat Transfer Coefficients SFCHTC								
Fraction of Un-oxidized Cladding Thickness Initiating T. M. Weakening (m)[3] MechWeak							[97, 177, 282] [-151, -95, -52][5] [45, 82, 131	
Debris Quenching Heat Transfer Coefficient to Pool (W/(m*m*K)) [4] DebrisHT				[9, 95, 162] [-200, -117, -11][1] [-38, -22, -2]		[-1314, -772, -74] [73, 757, 1290][6] [-25, -14, -1]		[-37, -22, -2]
Debris Falling Velocity (m/s)[5] DFV	[-0.511, -0.187, -0.007]						[2, 62, 169] [-258, -95, -4][3] [-89, -33, -1]	
Minimum Debris Porosity minPorosity					[-19, -10, -1]			
Time At Temperature - Effective Failure Temperature (K)[6] TaT			[887, 919, 962]		[-8597, -8212, -7924] [8680, 8996, 9418][2] [756, 784, 821]	[-215, -205, -198] [731, 757, 793][4] [533, 552, 578]		
Decay Heat Integrated to 10 hours (J) DCH	[-23, -22, -21]		[-502, -482, -462]					

In order to promote additional clarity regarding the regression results presented in the hydrogen dependency table, model summary tables at first fuel failure, lower core plate failure, and lower head failure are shown in Table 6.4, Table 6.5, and

Table 6.6.

Table 6.4 – Model Summary Table for Hydrogen Produced Before First Fuel Failure

Event	Parameters	Estimate	SE	tStat	pValue
First Fuel Failure *[n=100]*	*Intercept*	155	330.7	0.47	0.64
	MZBT	-0.09	0.042	-2.03	0.05
	TaT	0.36	0.08	4.49	0.00002
	DCH	-5e-09	2e-09	-2.14	0.04
Note: see dependency Table 6.4 for regression fit statistics					

Table 6.5 – Model Summary Table for Hydrogen Produced Before Lower Core Plate Failure

Event	Parameters	Estimate	SE	tStat	pValue
Lower Core Plate *[n=100]*	*Intercept*	*8288*	*3048*	*2.72*	*0.008*
	RSDR	*-0.05*	*0.018*	*-2.79*	*0.006*
	MZBT	*-3.66*	*1.3*	*-2.81*	*0.006*
	FSLHF	*453.8*	*203.7*	*2.23*	*0.028*
	minPorosity	*-94.4*	*42.6*	*-2.22*	*0.029*
	TaT	*-3.2*	*1.2*	*-2.69*	*0.008*
	MZBT:TaT	*0.0014*	*0.0005*	*2.95*	*0.004*
Note: see dependency Table 6.4 for regression fit statistics					

Table 6.6 – Model Summary Table for Hydrogen Produced Before Lower Head Failure

Event	Parameters	Estimate	SE	tStat	pValue
Lower Head Failure *[n=34]*	*Intercept*	-127	167	-0.76	0.455
	RSDR	0.19	0.055	3.48	0.002
	MZBT	0.29	0.07	4.18	0.0003
	MechWeak	0.00002	44456	4.24	0.0002
	DFV	169.07	87.5	1.93	0.064
	MechWeak:DFV	-0.00003	93175	-2.95	0.006
Note: see dependency Table 6.4 for regression fit statistics					

6.2.3 *Fraction of Intact Fuel Mass*

The dependency table for intact fuel mass is Table 6.7. No regressions were conducted before fuel failure because, nominally, all fuel is intact before the first fuel failure. In general, the regressions for intact fuel mass explain less of the variance than was seen with hydrogen production in Table 6.3. The finding that intact fuel mass is less susceptible to linear regression than hydrogen generation is not surprising when examining the cumulative distribution functions for hydrogen production and intact fuel mass found in Figure 5.15 b) and Figure 5.16 b), respectively. The discontinuous nature of Figure 5.16 arises from the core nodalization scheme employed in the 1F1 MELCOR deck and thus inhibits the effectiveness of linear regression techniques.

Even with these limitations, some valuable trends are noticeable. The interaction term between *TaT* and *MZBT* found in the hydrogen production regressions is still noticeable for intact fuel mass, although based on Figure 6.5 this interaction may be less significant. These two parameters are the primary parameters identified throughout the accident progression, with the exception of decay heat's contribution to driving first fuel failure.

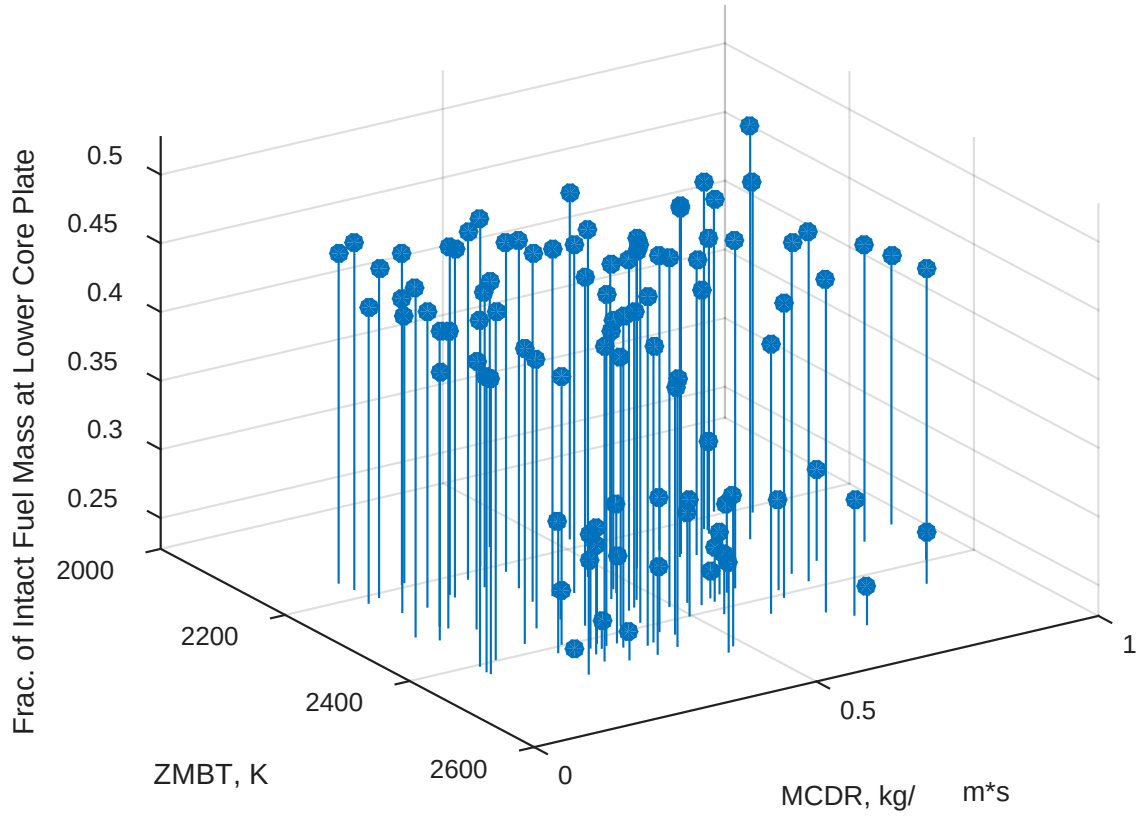

Figure 6.4 – Linear Interaction Effective Temperature of Fuel Failure (K) and Molten Zircaloy Breakthrough Temperature (K) {*MZBT*} at the Time of Lower Core Plate Failure for Fraction of Intact Fuel Mass.

Table 6.7 – Fraction of Intact Fuel Mass, Beginning of Simulation Until t_{FOM}, Raw Data

	First Fuel Failure	Main Steam Line	Lower Core Plate	Lower Plenum Dry-out	Lower Head Failure	End of Simulation
R^2 / R^2_{adj} / F-stat vs. Const./ p-val	.12 / .102 / 6.62 / .002	.185 / .176 / 22.2 / 0	.307 / .286 / 14.2 / 0	.182 / .165 / 10.8 / 0	N/A	.238 / .215 / 10 / 0
Intercept	0.8415 kg	-0.36111 kg	16.947 kg	0.23813 kg	0.00074 kg	-0.12205 kg
Time Constants for Radial (solid) Debris Relocation (s) RSLD						
Time Constants for Radial (liquid) Debris Relocation (s) RLDR						
dT|dz Model, Time Constant for Averaging Flows (s) dTdz_TCAF						
dT|dz Model, Characteristic Coupling Time (s) dTdz_CVH						
dT|dz Model, Relative Weight of Historical Flow (s) dTdz_Smooth						
Molten Zircaloy Break-Through Temperature (K) [1] MZBT	[-0.1005, -0.1097, -0.11979]		[-19, -18, -16] [16, 17, 18] **[4]** [-0.79. -0.74, -0.68]	[-0.84, -0.78, -0.72]		
Molten Cladding (pool) Drainage Rate (kg/(m*s)) MCDR						
Fraction of Strain at Which Lower Head Failure Occurs FSLHF						
Scaling Factor for Candling Heat Transfer Coefficients SFCHTC						
Fraction of Un-oxidized Cladding Thickness Initiating T. M. Weakening (m) [2] MechWeak						[0.08, 0.15, 0.24] [-0.192, -0.12, -0.066] **[3]** [0.016, 0.029, 0.046]
Debris Quenching Heat Transfer Coefficient to Pool (W/(m*m*K)) [3] DebrisHT						[0.01, 0.1, 0.17] [-0.2, -0.12, -0.01] **[2]** [-0.035, -0.021, -0.002]
Debris Falling Velocity (m/s) DFV						
Minimum Debris Porosity minPorosity						
Time At Temperature - Effective Failure Temperature (K) [4] TaT		[1.28, 1.33, 1.39]	[-17, -16, -15] [16, 17, 18] [1] [1.14, 1.18, 1.24]	[0.85, 0.88, 0.92]		
Decay Heat Integrated to 10 hours (J) DCH	[0.219, 0.228, 0.238]					

In order to promote additional clarity regarding the regression results presented in the fractional intact fuel mass dependency table, model summary tables at lower core plate failure, lower plenum dryout, and end of simulation are shown in Table 6.9, Table 6.9, and Table 6.10.

Table 6.8 – Model Summary Table for Intact Fuel Mass Fraction at Lower Core Plate Failure

Event	Parameters	Estimate	SE	tStat	pValue
Lower Core Plate *[n=100]*	*Intercept*	17	8.3	2.038	0.044
	MZBT	-0.008	0.004	-2.13	0.036
	TaT	-0.006	0.003	-1.9	0.06
	MZBT:TaT	3e-06	1e-06	2.04	0.0437
Note: see dependency table for regression fit statistics					

Table 6.9 – Model Summary Table for Intact Fuel Mass Fraction at Lower Plenum Dryout

Event	***Parameters***	***Estimate***	***SE***	***tStat***	***pValue***
Lower Plenum Dryout [n=100]	Intercept	0.24	0.49	0.48	0.629
	MZBT	-0.0003	0.00009	-3.83	0.0002
	TaT	0.0003	0.0002	2.09	0.039
Note: see dependency table for regression fit statistics					

Table 6.10 – Model Summary Table for Intact Fuel Mass Fraction at End of Simulation

Event	Parameters	Estimate	SE	tStat	pValue
End of Simulation *[n=100]*	*Intercept*	-0.12	0.03	-3.71	0.0003
	MechWeak	158	32.91	4.81	5e-06
	DebrisHT	0.00009	0.00003	3.35	0.001
	MechWeak:DebrisHT	-0.11	0.027	-4.23	0.00005
Note: see dependency table for regression fit statistics					

6.3 Rank Regressions

The rank regressions are similar to the raw regressions conducted in Section 6.4.2, except that the inputs and the outputs are rank transformed before the linear regressions are conducted. A rank transformation takes the variable being transformed and assigns an integer value corresponding to the "rank" of that component.[12] Thus, the observation with the highest value is

[12] Aside: Rank transformation are commonly used in sports to rank the production of players. For example, on Nov. 10th, 2014, the rank transformation of passing yard in the National Football League was: 1. Andrew Luck (3085

assigned rank 1, the second largest observation is assigned rank 2 and so on. When two or more observations have the same value, they are all assigned the mean of their ranks. Thus, the total number of distinct ranks in the transformed data is the number of distinct values in the original data, which may be less than the sample size n. If only one data point attains the largest observed value, the first rank will be 1. However, if multiple data points attain the largest observed value then the first rank will be greater than 1. Similarly, if every observation is unique (i.e. there are no ties in the data), then the smallest observation will have rank *n*. Otherwise, the smallest observation will have a rank less than *n*. Hence, for the example rank transformation shown in Equation (6-4), *i* and *j* are integers less than *n* and greater than or equal to 1, and *n* is the length of the vector **Y**, accounting for the possible occurrence of ties in the data.

$$Rank(\boldsymbol{Y}) = Rank\left(\begin{bmatrix} y_1 \\ \vdots \\ y_n \end{bmatrix}\right) = \begin{bmatrix} i \\ \vdots \\ j \end{bmatrix}, where\ 1 \leq\ i, j \leq\ \ n \tag{6-4}$$

The rank transformation of variables equally spaces out the components within a vector by non-dimensional spaces of one. Thus all vectors, no matter how small or large the range they cover, will be spaced between one and *n* (i.e., the number of Monte Carlo simulations run for the sample). With the range of all *X* and *Y* variables equal to each other and the median equaling $^{n}/_{2}$ by definition, the regression coefficients produced can be directly compared to each other without the need to transform a ΔY vector as was done in Equations (6-1) and (6-3). The potential challenge with conducting a rank transformation blindly is that the rank transformation process may introduce trends that do not exist, or alternatively miss linear trends which are harder to detect under a rank transformation. Thus, it is important to take the rank regression results and examine them in an untransformed state to determine the true impact of the regressed trend.

One additional transformation was conducted on the rank transformed data in order to allow the regressions to be applied to samples of different sizes than the training data size. This transformation involves dividing each value in the rank transformed vector by the maximum rank. This normalizes the values in the *X* and *Y* column vectors to the interval $(0,1]$.

6.3.1 Material Ejected from the Lower Head Conditional on Lower Head Failure

The dependency table for the rank regressions of mass of material ejected from the lower head only regressed to two timing FoMs: lower head failure and end of simulation. In addition to examining the trends highlighted in the rank regression dependency table (see Table 6.11), it is informative to compare these trends to those highlighted in the raw regressions dependency table (see Table 6.1).

As both of the rank and raw regressions were performed upon the same sample (e.g. Replicate 1), the variables indicated in each timing FoM regression should be similar. An examination of both dependency tables reveals generally higher fit estimates for later timing FoMs. The rank regressions fit the mass ejected from the lower head at timing FoM data set slightly better, with the rank regression even resolving an interaction effect for the end of simulation. It should be

---

yards), 2. Ben Roethlisberger (3063 yards), 3. Peyton Manning (2912 yards), 4. Drew Brees (2816 yards), 5. Matt Ryan (2525 yards). Source: www.rotoworld.com.

noted that while the rank regression resolved more of the variance than the raw regression resolved, no additional parameters were included in the rank regression.

Table 6.11 – Mass of Material Ejected from the Lower Head Conditional on Lower Head Failure, Beginning of Simulation Until t_{FOM}, Rank Data

	Lower Head Failure	**End of Simulation**
R^2 / R^2_{adj} / F-stat vs. Const./ p-val	.62 / .58 / 16.4 / 0	.16 / .14 / 6.18 / .0007
Intercept	0.46	0.027
Time Constants for Radial (solid) Debris Relocation (s) *RSDR*		
Time Constants for Radial (liquid) Debris Relocation (s) *RLDR*		
dT|dz Model, Time Constant for Averaging Flows (s) *dTdz_TCAF*		
dT|dz Model, Characteristic Coupling Time (s) **dTdz_CVH**	$\beta_i = 0.378$	
dT|dz Model, Relative Weight of Historical Flow (s) *dTdz_Smooth*		
Molten Zircaloy Break-Through Temperature (K) *MZBT*		
*Molten Cladding (pool) Drainage Rate (kg/(m*s))* *MCDR*		
Fraction of Strain at Which Lower Head Failure Occurs *FSLHF*		
Scaling Factor for Candling Heat Transfer Coefficients *SFCHTC*		
Fraction of Un-oxidized Cladding Thickness Initiating T. M. Weakening (m) *MechWeak*		
Debris Quenching Heat Transfer Coefficient to Pool (W/(m*m*K)) **DebrisHT**	$\beta_i = -0.612$	
Debris Falling Velocity (m/s) **DFV**	$\beta_i = 0.326$	
Minimum Debris Porosity [1] **minPorosity**		$\beta_i = 0.631$ $\beta_{1,2} = -0.846$
Time At Temperature - Effective Failure Temperature (K) [2] **TaT**		$\beta_i = 0.115$ $\beta_{1,2} = -0.846$
Decay Heat Integrated to 10 hours (J) *DCH*		

Note: Blank cells denote that the parameter was not regressed at the timing FoM.

In order to promote additional clarity regarding the regression results presented in the mass of material ejected dependency table, a model summary table at lower head failure is shown in Table 6.12.

Table 6.12 – Model Summary Table for Mass of Material Ejected From the Lower Head at Lower Head Failure

Event	Parameters	Estimate	SE	tStat	pValue
Lower Head Failure *[n=34]*	*Intercept*	0.463	0.121	3.82	0.0006
	dTdz_CVH	0.378	0.114	3.31	0.002
	DebrisHT	-0.612	0.113	-5.41	7e-06
	DFV	0.326	0.117	2.8	0.009
Note: see dependency table for regression fit statistics					

6.3.2 In-Vessel Hydrogen Production

The dependency table for the rank regressions of hydrogen production covers every timing FoM. In addition to examining the trends highlighted in the rank regression dependency table (see Table 6.13), it is informative to compare these trends to those highlighted in the raw regressions dependency table (see Table 6.3).

As both of the rank and raw regressions stem from the same sample (i.e., Replicate 1), the relative suitability of the regression for each timing FoM should be similar. Indeed, an examination of both dependency tables reveals generally higher fit estimates for later timing FoMs. The rank regressions fit the hydrogen production at timing FoM data sets slightly better, with the exception of main steam line failure and lower plenum dryout. Rank regressions fit the sample data significantly better for lower head failure, likely due to the small number of samples associated with this conditional timing FoM (i.e., 34 out of 100 simulations lead to lower head failure and thus were available for regression).

MZBT still shows the most suitability for regression amongst sampled parameters, having high regression coefficients from main steam line failure to end of simulation. Interestingly, *MZBT* was not resolved for the timing of first fuel failure as was the case for the raw regression. At main steam line failure, an interaction effect was identified between *MZBT* and *MCDR*, an interaction which was not seen in the raw regression. This trend can be seen in the raw data shown in Figure 6.5, but a fraction of high *MZBT* samples indicate low hydrogen production.

Table 6.13 – Mass of In-Vessel Hydrogen Produced, Beginning of Simulation Until t_{FOM}, Rank Data

	First Control Rod Failure	First Channel Box	First Fuel Failure	Main Steam Line	Lower Core Plate	Lower Plenum Dry-out	Lower Head Failure	End of Simulation
R^2 / R^2_{adj} / F-stat vs. Const. / pval	.26 / .24 / 16.7 / 0	.05 / .04 / 5.02 / .027	.23 / .21 / 9.78 / 0	.42 / .38 / 11 / 0	.53 / .5 / 21.1 / 0	.52 / .5 / 25.8 / 0	.4 / .37 / 10.5 / .0003	.17 / .16 / 10.1 / .0001
Intercept	0.84	0.62	0.54	0.104	0.24	0.28	0.08	0.40
Time Constants for Radial (solid) Debris Relocation (s) [1] RSDR				$\beta_i = 0.174$ $\beta_{1,4} = -0.871$	$\beta_i = -0.189$			
Time Constants for Radial (liquid) Debris Relocation (s) RLDR								
dT|dz Model, Time Constant for Averaging Flows (s) dTdz_TCAF		$\beta_i = -0.227$						
dT|dz Model, Characteristic Coupling Time (s) dTdz_CVH								
dT|dz Model, Relative Weight of Historical Flow (s) dTdz_Smooth								
Molten Zircaloy Break-Through Temperature (K) [2] MTBT				$\beta_i = -0.867$ $\beta_{2,3} = 1.082$	$\beta_i = 0.545$	$\beta_i = 0.669$	$\beta_i = 0.467$	$\beta_i = 0.373$
Molten Cladding (pool) Drainage Rate (kg/(m*s)) [3] MCDR			$\beta_i = -0.222$	$\beta_i = -0.727$ $\beta_{2,3} = 1.082$				
Fraction of Strain at Which Lower Head Failure Occurs FSLHF								
Scaling Factor for Candling Heat Transfer Coefficients SFCHTC								
Fraction of Un-oxidized Cladding Thickness Initiating T. M. Weakening (m) MechWeak							$\beta_i = 0.363$	
Debris Quenching Heat Transfer Coefficient to Pool (W/(m*m*K)) [4] DebrisHT				$\beta_i = 0.238$ $\beta_{1,4} = -0.871$	$\beta_i = -0.187$	$\beta_i = -0.52$ $\beta_{4,5} = 0.632$		$\beta_i = -0.185$
Debris Falling Velocity (m/s) DFV	$\beta_i = -0.199$							
Minimum Debris Porosity minPorosity								
Time At Temperature - Effective Failure Temperature (K) [5] TaT			$\beta_i = 0.4$		$\beta_i = 0.513$	$\beta_i = -0.039$ $\beta_{4,5} = 0.632$		
Decay Heat Integrated to 10 hours (J) DCH	$\beta_i = -0.46715$		$\beta_i = -0.234$		$\beta_i = -0.151$			

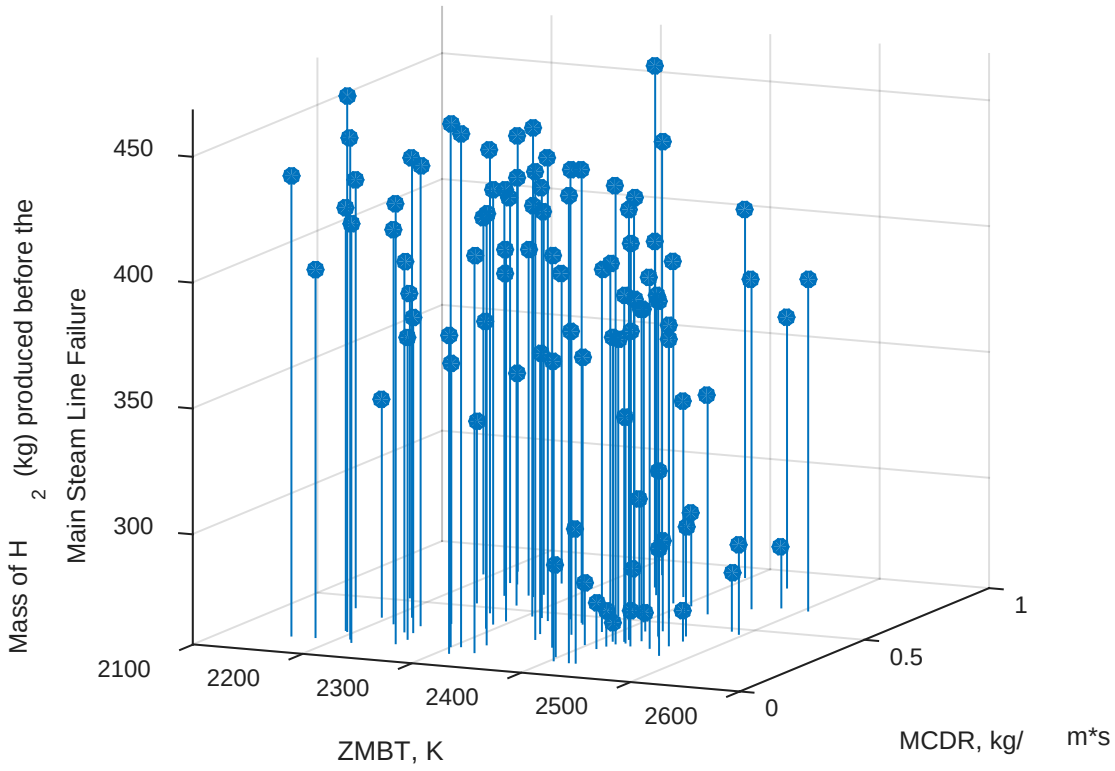

Figure 6.5 – Linear Interaction Between Molten Clad Drainage Rate (kg/(m*s)) {*MCDR*} and Molten Zircaloy Breakthrough Temperature (K) {*MZBT*} at the Time of Main Steam Line Failure for Cumulative Hydrogen Production.

DebrisHT jumps to the second most frequently regressed parameter by exhibiting a negative coefficient for hydrogen production at the time of lower core plate failure, in addition to preexisting regressions for main steam line, lower plenum dryout and end of simulation. A negative trend is slightly noticeable in the raw untransformed data shown in Figure 6.6, but it is difficult to determine if this trend is physical or a function of the inherent variability introduced with the rank transformation.

DebrisHT also shows interaction effects with *RSDR* at main steam line failure and *TaT* at lower plenum dry-out. From Figure 6.7, it is possible that the negative trend is actually an artifact of the sequence variability between main steam line failure and first fuel failure. Future studies of this accident should perform additional order-dependent regressions on main steam line failure and first fuel failure. Figure 6.8 shows the raw data for *DebrisHT* and *TaT* at lower plenum dryout. The rank regression indicates a weak positive relationship between the two variables, but a visual examination of the data does not confirm this relationship.

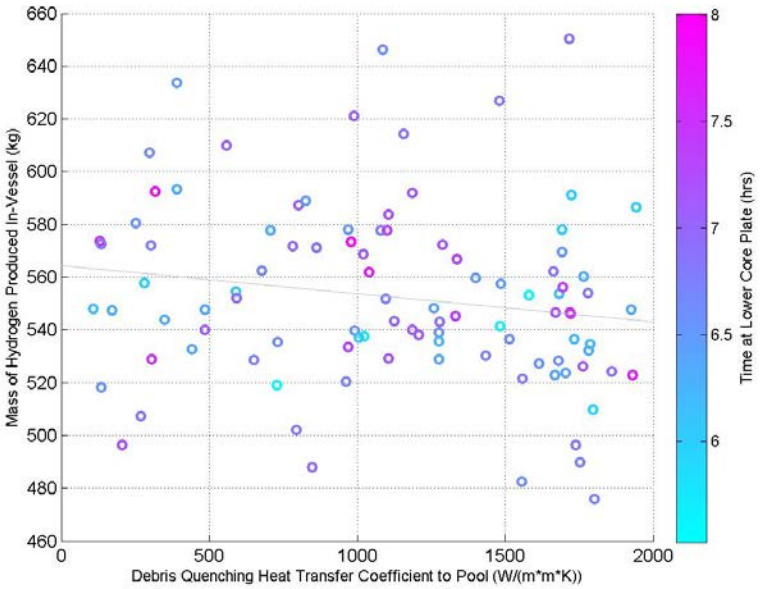

Figure 6.6 – *DebrisHT* Scatterplot of Hydrogen Produced by Lower Core Plate Failure

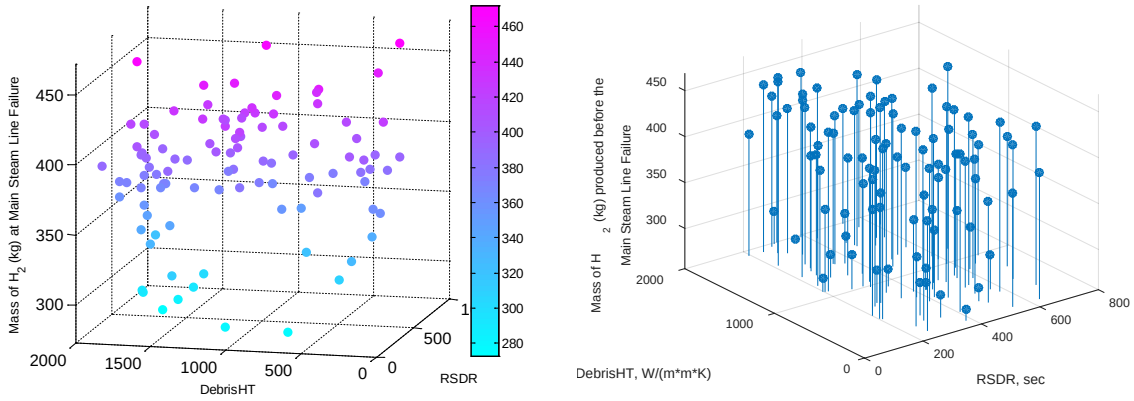

Figure 6.7 – Linear Interaction Debris Quenching Heat Transfer (W/m^{2}K) {*DebrisHT*} and Radial Solid Debris Relocation Time Constant (s) {*RSDR*} at the Time of Main Steam Line Failure for Cumulative Hydrogen Production. [13]

[13] The color scale reproduces the z-axis for clarity.

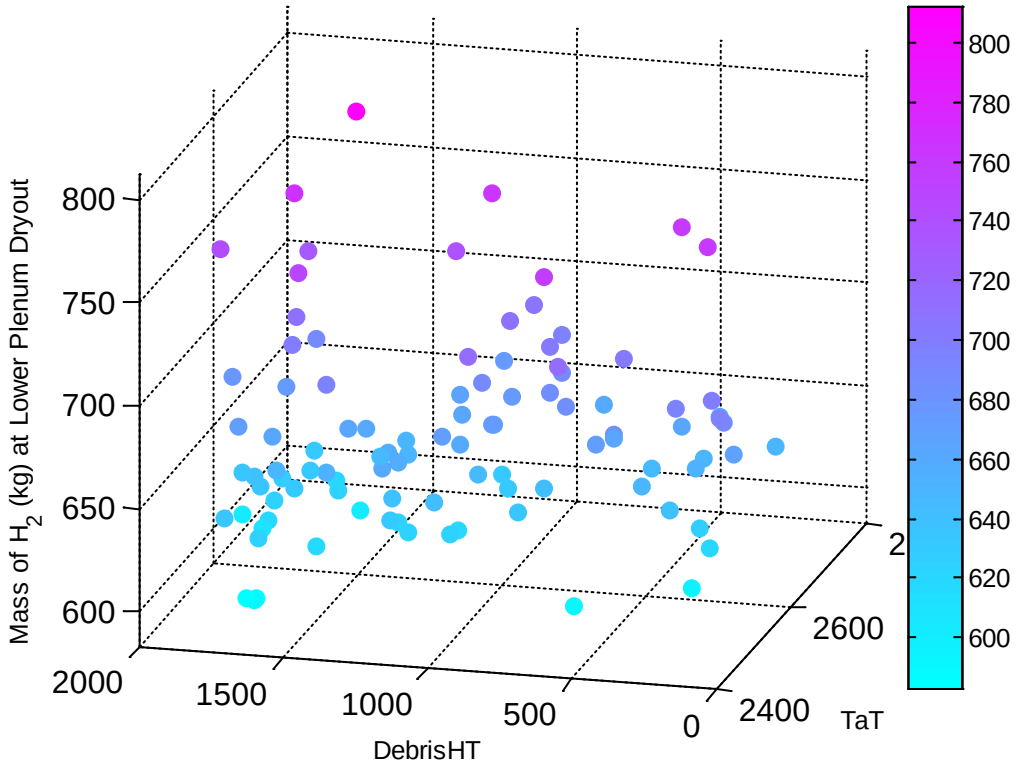

Figure 6.8 – Linear Interaction Debris Quenching Heat Transfer (W/m^{2}K) {*DebrisHT*} and Effective Fuel Failure Temperature (K) {*TaT*} at the Time of Lower Plenum Dryout for Cumulative Hydrogen Production. The color scale reproduces the z-axis for clarity.

In order to promote additional clarity regarding the regression results presented in the hydrogen dependency table, model summary tables at main steam line failure, lower plenum dryout, and lower head failure are shown in Table 6.14, Table 6.15, and Table 6.16. Note that statistically insignificant first order interactions were included to support statistically significant interaction terms for Table 6.14 and Table 6.15, with the *DebrisHT:TaT* term being only marginally significant itself. Thus, the *TaT* effects are suspect.

Table 6.14 – Model Summary Table for Cumulative Hydrogen Production at Main Steam Line Failure

Event	Parameters	Estimate	SE	tStat	pValue
Main Steam Line *[n=100]*	*Intercept*	1.045	0.142	7.36	7e-11
	RSDR	0.174	0.164	1.06	0.292
	MZBT	-0.867	0.162	-5.35	6e-07
	MCDR	-0.727	0.156	1.06	0.00001
	DebrisHT	*0.238*	*0.18*	*1.32*	*0.19*
	RSDR:DebrisHT	-0.871	0.305	-2.86	0.005
	MZBT:MCDR	1.082	0.273	3.96	0.0001
Note: see dependency table for regression fit statistics					

Table 6.15 – Model Summary Table for Cumulative Hydrogen Production at Lower Plenum Dryout

Event	Parameters	Estimate	SE	tStat	pValue
Lower Plenum Dry-out *[n=100]*	*Intercept*	0.284	0.108	2.63	0.01
	MZBT	0.669	0.073	9.17	9e-15
	DebrisHT	-0.52	0.167	-3.11	0.002
	TaT	*-0.039*	*0.183*	*-0.21*	*0.832*
	DebrisHT:TaT	0.632	0.316	2.00	0.048
Note: see dependency table for regression fit statistics					

Table 6.16 – Model Summary Table for Cumulative Hydrogen Production at Lower Head Failure

Event	Parameters	Estimate	SE	tStat	pValue
Lower Head Failure *[n=34]*	*Intercept*	0.08	0.103	0.77	0.445
	MZBT	0.467	0.141	3.30	0.002
	MechWeak	0.363	0.141	2.58	0.015
Note: see dependency table for regression fit statistics					

6.3.3 Fraction of Intact Fuel Mass In-Core

The dependency table for the rank regressions of fractional intact fuel mass in-core is regressed for first fuel failure, main steam line failure, lower core plate failure, lower plenum dryout, lower head failure, and end of simulation. In addition to examining the trends highlighted in the rank regression dependency table (see Table 6.17), it is informative to compare these trends to those highlighted in the raw regressions dependency table (see Table 6.7).

As both of the rank and raw regressions stem from the same sample (i.e., Replicate 1), the relative suitability for regression of each timing FoM should be similar. Indeed, an examination of both dependency tables reveals generally higher fit estimates for later timing FoMs. The rank regressions fit the fraction of intact fuel mass better than the raw regressions and sometimes regress different dependencies.

For example, at the time of first fuel failure, the raw regressions singled out decay heat and molten Zircaloy breakthrough temperature as being important. The rank regressions kept decay heat, and its positive correlation, but dropped the breakthrough temperature in favor of debris falling velocity. In this case, the rank regression emerged with the higher R^2 and the stronger physical explanation; the temperature at which material relocates before fuel failure would potentially lower the intact fuel fraction more than the debris falling velocity keeps fuel intact by removing hot material from the intact fuel.

The rank transformation improves the suitability for regression of fractional intact fuel at main steam line failure. The rank transformation takes the raw regression of effective fuel failure temperature and adds to it an interaction effect with the breakthrough temperature (see Figure 6.9) and maintains the debris falling velocity from the first fuel failure regression.

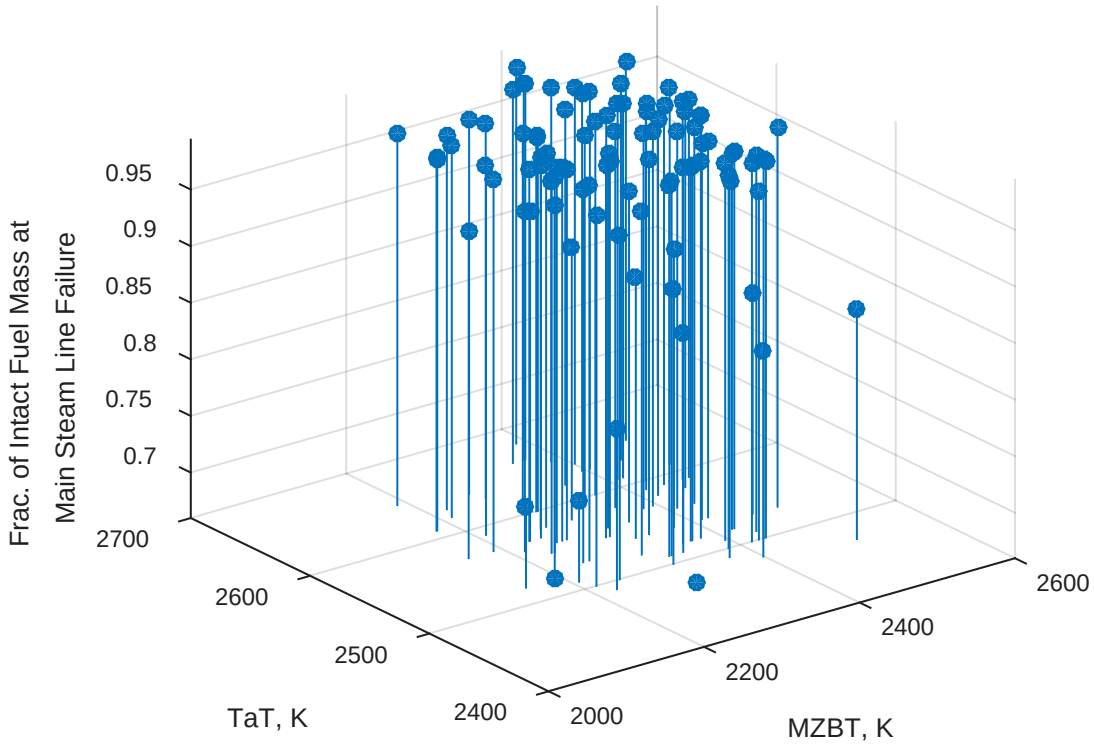

Figure 6.9 – Interaction Term Plot between Molten Zircaloy Breakthrough Temperature (K) {*MZBT*} and Time at Temperature vs Fraction of Intact Fuel Mass at Main Steam Line Failure.

Table 6.17 – Fraction of Intact Fuel Mass, Beginning of Simulation Until t_{FOM}, Rank Data

	First Fuel Failure	Main Steam Line	Lower Core Plate	Lower Plenum Dry-out	Lower Head Failure	End of Simulation
R^2 / R^2_{adj} / F-stat vs. Const./ p-val	.09 / .07 / 4.79 / .01	.4 / .38 / 15.9 / 0	.29 / .26 / 9.69 / 0	.2 / .18 / 11.9 / 0	N/A	.06 / .05 / 5.93 / 0.017
Intercept	0.29	0.47	0.37	0.53	0.51	0.063
Time Constants for Radial (solid) Debris Relocation (s) RSDR						
Time Constants for Radial (liquid) Debris Relocation (s) RLDR						
dT|dz Model, Time Constant for Averaging Flows (s) dTdz_TCAF						
dT|dz Model, Characteristic Coupling Time (s) dTdz_CVH						
dT|dz Model, Relative Weight of Historical Flow (s) dTdz_Smooth						
Molten Zircaloy Break-Through Temperature (K) [1] MZBT		$\beta_i = -0.461$ $\beta_{1,2} = 1.633$	$\beta_i = -0.188$	$\beta_i = -0.35$		
*Molten Cladding (pool) Drainage Rate (kg/(m*s)) MCDR*						
Fraction of Strain at Which Lower Head Failure Occurs FSLHF			$\beta_i = -0.206$			
Scaling Factor for Candling Heat Transfer Coefficients SFCHTC						
Fraction of Un-oxidized Cladding Thickness Initiating T. M. Weakening (m) MechWeak						$\beta_i = 0.148$
*Debris Quenching Heat Transfer Coefficient to Pool (W/(m*m*K)) DebrisHT*						
Debris Falling Velocity (m/s) DFV	$\beta_i = 0.23$	$\beta_i = 0.19$	$\beta_i = 0.088$			
Minimum Debris Porosity minPorosity						
Time At Temperature - Effective Failure Temperature (K) [2] TaT		$\beta_i = -0.456$ $\beta_{1,2} = 1.633$	$\beta_i = 0.12$	$\beta_i = 0.302$		
Decay Heat Integrated to 10 hours (J) DCH	$\beta_i = 0.195$					

For the lower core plate regression, the rank transformation removes the interaction between breakthrough temperature and effective fuel failure temperature while adding fractional strain to induce lower head failure and debris falling velocity. As emphasized in the discussion of Table 6.19, this regression is suspected to have fit inherent variability and thus may not be indicative of population trends.

After lower core plate failure, the benefits derived from conducting a rank regression diminish. The regressions for lower plenum dryout are extremely similar to the raw regressions, adding little to no additional information. At the end of simulation, rank regressions do not resolve the debris quenching heat transfer coefficient found in the raw regression results.

In order to promote additional clarity regarding the rank regression results presented in the fractional intact fuel mass dependency table, model summary tables at main steam line failure, lower core plate failure, and lower plenum dryout are shown in Table 6.18, Table 6.19, and Table 6.20. Note that many of the regression values have marginal significance ($0.1 < pValue < 0.5$) and *FSLHF* in Table 6.19 should not be physically possible because lower head failure is preceded by lower core plate failure. Thus, the applicability of these regressions to samples from the same distribution should be examined before subsequent research decisions are made.

Table 6.18 – Model Summary Table for Fraction of Intact Fuel Mass at Main Steam Line Failure

Event	Parameters	Estimate	SE	tStat	pValue
Main Steam Line *[n=100]*	*Intercept*	0.469	0.126	3.71	0.0003
	MZBT	-0.461	0.196	-2.36	0.020
	DFV	0.19	0.080	2.37	0.020
	TaT	-0.456	0.210	-2.17	0.033
	MZBT:TaT	1.633	0.354	4.62	0.00001
Note: see dependency table for regression fit statistics					

Table 6.19 – Model Summary Table for Fraction of Intact Fuel Mass at Lower Core Plate Failure

Event	***Parameters***	***Estimate***	***SE***	***tStat***	***pValue***
Lower Core Plate [n=100]	Intercept	0.366	0.097	3.77	0.0003
	MZBT	-0.188	0.09	-2.1	0.039
	FSLHF	*-0.206*	*0.088*	*-2.33*	*0.022*
	DFV	0.212	0.088	2.40	0.018
	TaT	0.47	0.11	4.29	0.0004
Note: see dependency table for regression fit statistics					

Table 6.20 – Model Summary Table for Fraction of Intact Fuel Mass at Lower Plenum Dryout

Event	*Parameters*	*Estimate*	*SE*	*tStat*	*pValue*
Lower Plenum	Intercept	0.535	0.083	6.41	5e-09
Dry-out	*MZBT*	-0.35	0.094	-3.73	0.0003
[n=100]	*TaT*	0.302	0.114	2.65	0.009
Note: see dependency table for regression fit statistics					

6.4 Summary of Automated Regression Insights

Key insights from the automated regression analysis are summarized below:

- Whether or not an input parameter is included in a regression model varies over the various timing FoMs. Only a subset of input parameters, such as molten Zircaloy breakthrough temperature, was consistently resolved throughout timing FoMs for a given physical FoM.
- Event timings that occurred during core degradation timings were more easily regressed than early or late phased event timings.
- The mass of material ejected from the lower head was not an effective physical FoM to study with regression analysis due to the single dynamic corresponding timing FoM available for the physical FoM and the relatively small number of samples available for regression because a majority of the replicate realizations did not experience lower head failure.
- Fraction of intact fuel mass occurs in MELCOR in quantized segments due to the system nature of the code. The quantized output data, as opposed to continuous hydrogen data, likely violate key assumptions in the regression analysis. Thus, inference should be done with caution.
- Scatterplots are an important tool for understanding the results of the regression output.

6.5 References

[6.1] U.S. Nuclear Regulatory Commission, State-of-the-Art Reactor Consequence Analyses Project: Uncertainty Analysis of Unmitigated Long-Term Station Blackout of the Peach Bottom Atomic Power Station-Draft Report, NUREG/CR-7155, SAND2012-10702P,Washington, DC, 2012.

7 REGRESSION VALIDATIONS

Regression can be a powerful tool to help analysts understand the impact of uncertainty on the output of computer models. However, the output of these tools, as with all statistical and deterministic techniques, should be analyzed for applicability to the question of interest. This is especially true for results from system representations of severe accidents (e.g. MELCOR). Chapter 7 examines the regression results presented from a selection of physical and timing FoM pairings to determine the accuracy of the regressions produced.

The physical and timing FoM pairings are:

7.1 - Mass of Material Ejected (ME) at Lower Head Failure,

7.2 - Cumulative Hydrogen (H_2) Produced, and

7.3 - Fraction of Intact Fuel Mass .

7.1 Mass of Material Ejected (ME) at Lower Head Failure

This section describes the regressions for the mass of material ejected from the lower head at the time of lower head failure. Ten regression models were created from four samples:

1. Regressions (both rank and raw) trained on the sampled data from Replicate 1,
2. Regressions (both rank and raw) trained on the sampled data from Replicate 2,
3. Regressions (both rank and raw) trained on the sampled data from Replicate 3,
4. Regressions (both rank and raw) trained on the sampled data from the uniform distributions, and
5. Regressions (both rank and raw) trained on the sampled data from Replicate 1 and 2.

Finally, the regressions were applied to the non-training samples to gauge the predictive ability of each regression.

Note that for mass of material ejected from the lower head The regressions were preformed conditional on failure of the lower head. Thus, the discussion of each replicate will begin with a statement of the size of the training data available for regression.

Table 7.1 presents the summary fit statistics for all related regressions conducted for the 1F1 UA. In general, while all fits provide R^2 values under 0.6, Replicate 1 and Replicate 3 seem to have the best R^2 values. Grouping the Replicate 1 and 2 data for regression does not improve upon the regressions fit solely on the Replicate 2 data. The variability of R^2 across the regression samples suggests that the model which minimized the variance of the model-corrected local (sample) variance in the training data found by each of the four regressions may or may not be the ideal model which minimizes the model-corrected global (population) variance. Thus, individually the four regressions may be of limited predictive value.

Table 7.1 – Training Data Fit Comparisons for the 10 Regressions for Mass of Material Ejected from the Lower Head at the Time of Lower Head Failure

Set	*Type*	*n*	*k*	R^2	R^2_{adj}
Rep. 1	Raw	34	3	0.56	0.52
	Rank	34	3	0.62	0.58
Rep. 2	Raw	41	1	0.12	0.10
	Rank	41	1	0.11	0.09
Rep. 3	Raw	43	3	0.41	0.37
	Rank	43	3	0.48	0.45
Rep. U	Raw	42	1	0.28	0.27
	Rank	42	2	0.38	0.35
Rep. 1&2	Raw	75	2	0.13	0.11
	Rank	75	1	0.10	0.09

7.1.1 Replicate 1

Raw linear regression model:

ME ~ 1 + dTdz_CVH + DebrisHT + DFV

Rank linearregression model:

Rank(*ME*) ~ 1 + Rank(dTdz_CVH) + Rank(DebrisHT) + Rank(DFV)

Both meta-models agree regarding the type of regression trends that exist in the Replicate 1 sample, but the rank regression was able to explain more of the variance when compared to the raw regression's ability to explain the variance. The model summary tables for the rank and raw regressions can be found in Table 6.23 and Table 6.24.

Table 7.2 – Model Summary Table for the Raw Regression of Rep. 1 for Mass of Material Ejected from the Lower Head at the Time of Lower Head Failure

	Estimate	*SE*	*tStat*	*pValue*
(Intercept)	1998.7	29340.0	0.1	9.5E-01
dTdz_CVH	8274.1	2681.7	3.1	4.3E-03
DebrisHT	-26.7	5.6	-4.8	4.3E-05
DFV	34160.0	12331.0	2.8	9.5E-03

Table 7.3 – Model Summary Table for the Rank Regression of Rep. 1 for Mass of Material Ejected from the Lower Head at the Time of Lower Head Failure

	Estimate	*SE*	*tStat*	*pValue*
(Intercept)	0.5	0.1	3.8	6.2E-04
dTdz_CVH	0.4	0.1	3.3	2.4E-03
DebrisHT	-0.6	0.1	-5.4	7.3E-06
DFV	0.3	0.1	2.8	8.9E-03

7.1.2 Replicate 2

Raw linear regression model:

$ME \sim 1 + RSDR$

Rank linear regression model:

$\text{Rank}(ME) \sim 1 + \text{Rank}(DFV)$

The linear regression analysis struggled to find linear trends in the Replicate 2 data. The raw regression resolved *RSDR*, and the rank regression resolved *DFV*. *DFV* was regressed from both the rank and the raw regressions from Replicate 1. The model summary tables for the Replicate 2 regressions can be found in Table 7.4 and Table 7.5. Scatterplots for *RSDR* and *DFV* for Replicate 2 can be seen in Figure 7.1. These scatterplots suggest a bifurcated response for a subset of parameter values which explains the low relative fitting estimates.

Table 7.4 – Model Summary Table for the Raw Regression of Rep. 2 for Mass of Material Ejected from the Lower Head at the Time of Lower Head Failure

	Estimate	*SE*	*tStat*	*pValue*
(Intercept)	37903.0	11889.0	3.2	2.8E-03
RSDR	67.1	28.7	2.3	2.5E-02

Table 7.5 – Model Summary Table for the Rank Regression of Rep. 2 for Mass of Material Ejected from the Lower Head at the Time of Lower Head Failure

	Estimate	*SE*	*tStat*	*pValue*
(Intercept)	0.3	0.1	3.9	4.1E-04
DFV	0.3	0.2	2.2	3.5E-02

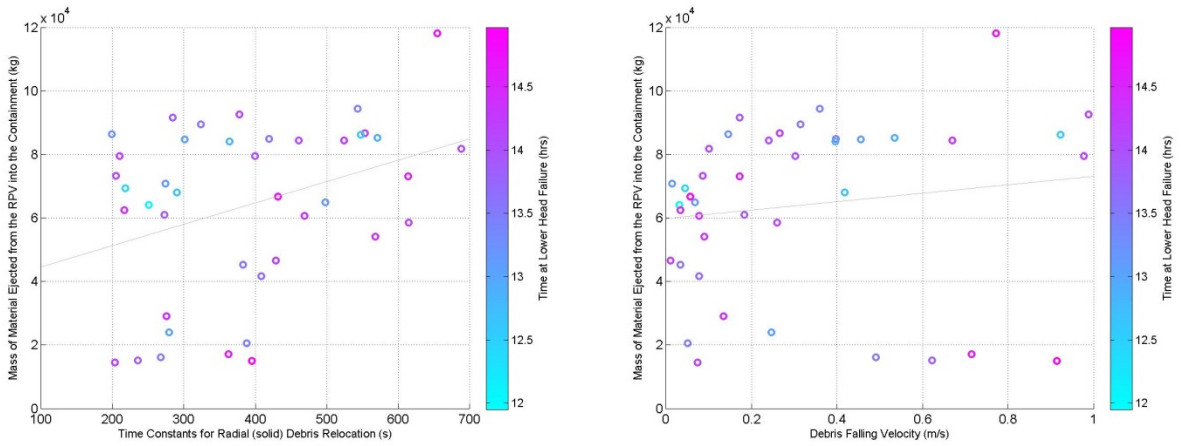

Figure 7.1 – Scatter Plots for *RSDR* and *DFV* from Replicate 2

7.1.3 Replicate 3

Raw linear regression model:

ME ~ 1 + *dTdz_Smooth* + *DFV* + *minPorosity*

Rank linear regression model:

Rank(*ME*) ~ 1 + Rank(*dTdz_Smooth*) + Rank(*DFV*) + Rank(*minPorosity*)

Both meta-models agree regarding the type of regression trends that exist in the Replicate 3 sample, but the rank regression was able to explain more of the variance when compared to the raw regression's ability to explain the variance. Replicate 3 resolved a different *dTdz* model than Replicate 1 and picked *minPorosity* instead of *DebrisHT*. The model summary tables for the rank and raw regressions can be found in Table 7.6 and Table 7.7. Figure 7.2 shows the scatterplots for the resolved terms in Replicate 3.

Table 7.6 – Model Summary Table for the Raw Regression of Rep. 3 for Mass of Material Ejected from the Lower Head at the Time of Lower Head Failure

	Estimate	*SE*	*tStat*	*pValue*
(Intercept)	144070.0	33175.0	4.3	9.7E-05
dTdz_Smooth	-131780.0	52535.0	-2.5	1.6E-02
DFV	41487.0	12228.0	3.4	1.6E-03
minPorosity	-182210.0	56465.0	-3.2	2.5E-03

Table 7.7 – Model Summary Table for the Rank Regression of Rep. 3 for Mass of Material Ejected from the Lower Head at the Time of Lower Head Failure

	Estimate	*SE*	*tStat*	*pValue*
(Intercept)	0.6	0.1	5.9	6.3E-07
dTdz_Smooth	-0.3	0.1	-3.0	5.1E-03
DFV	0.5	0.1	4.1	2.0E-04
minPorosity	-0.4	0.1	-3.4	1.6E-03

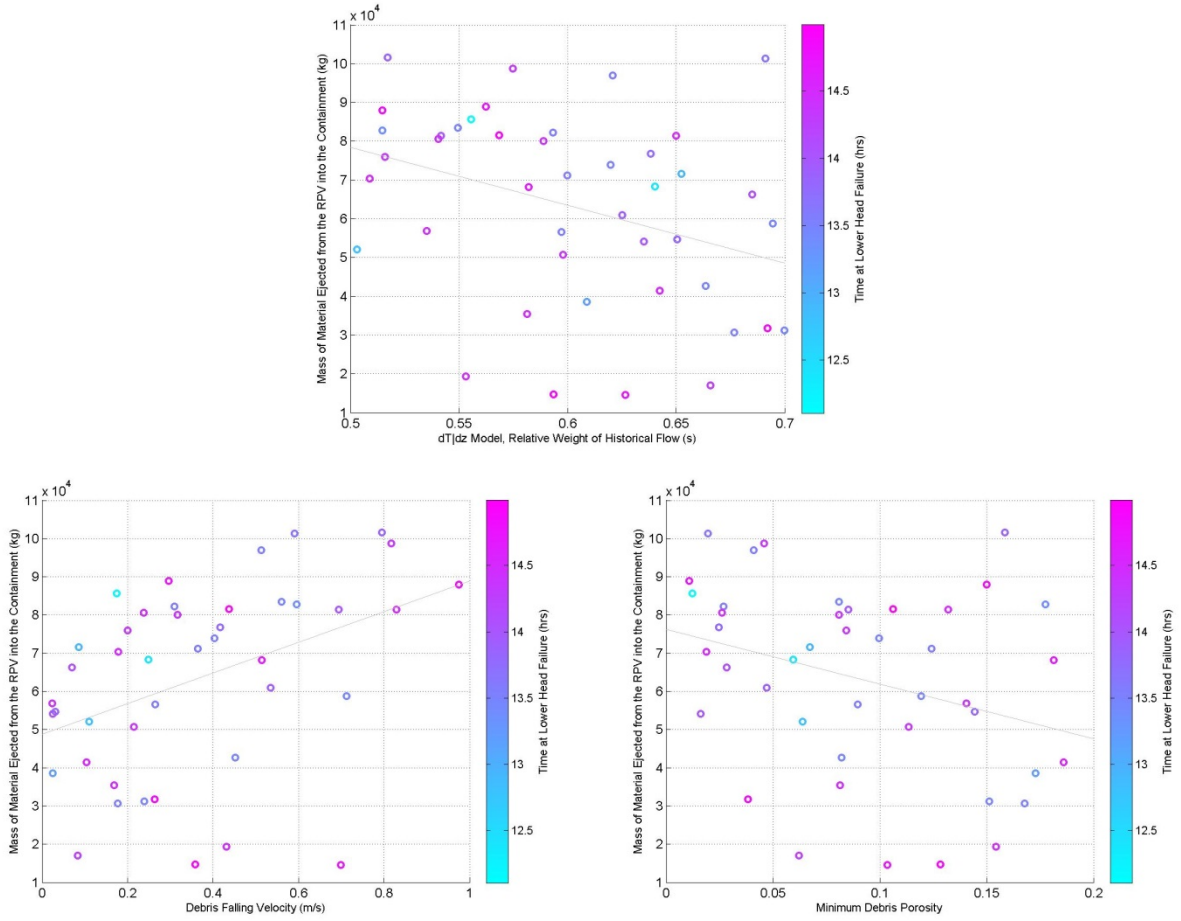

Figure 7.2 – Scatterplots for *minPorosity*, *DFV*, and *dTdZ_Smooth* for Replicate 3

7.1.4 Replicate Uniform

Raw linear regression model:

ME ~ 1 + RSDR

Rank linear regression model:

Rank(ME) ~ 1 + Rank(*RSDR)* + Rank(*DFV)*

Both meta-models agree regarding regression of *RSDR*, but the rank regression also selected *DFV*. The *DFV* is a term that was regressed in all but one of the previous regressions. The rank regression, with its extra predictive term, was able to explain more of the variance when compared to the raw regression's ability to explain the variance. The model summary tables for the rank and raw regressions can be found in Table 7.8 and Table 7.9. Figure 7.3 shows the scatterplots for the resolved terms in Replicate Uniform.

It should be noted that the uniform case puts more probability mass on the tails of the distribution. Thus, theoretically, it sacrifices convergence of central tendencies to better characterize tail behavior.

Table 7.8 – Model Summary Table for the Raw Regression of Rep. U for Mass of Material Ejected from the Lower Head at the Time of Lower Head Failure

	Estimate	*SE*	*tStat*	*pValue*
(Intercept)	23547.0	9716.4	2.4	2.0E-02
RSDR	83.4	20.9	4.0	2.8E-04

Table 7.9 – Model Summary Table for the Rank Regression of Rep. U for Mass of Material Ejected from the Lower Head at the Time of Lower Head Failure

	Estimate	*SE*	*tStat*	*pValue*
(Intercept)	0.1	0.1	1.0	3.0E-01
RSDR	0.4	0.1	3.2	2.4E-03
DFV	0.4	0.1	3.1	3.5E-03

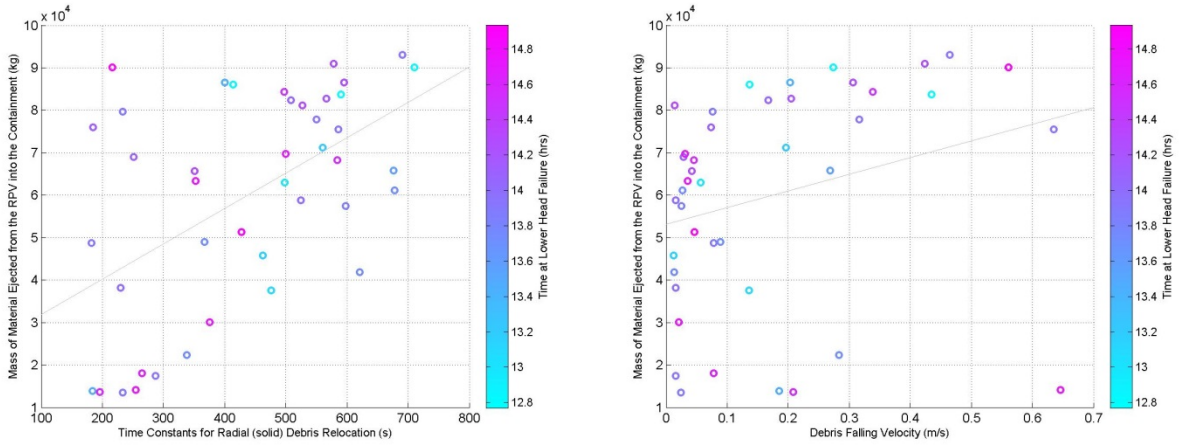

Figure 7.3 – Scatterplots for *RSDR* and *DFV* for Replicate Uniform

7.1.5 Replicate 1 and 2 Pooled

Raw linear regression model:

ME ~ 1 + *RSDR* + *DCH*

Rank linear regression model:

Rank(*ME*) ~ 1 + Rank(*DFV)*

The raw and rank regressions developed two different regression models with approximately the same explanation of variance. The raw regression results include *RSDR* and *DCH* as dependent variables. This is the first regression model prodcued in which decay heat was resolved as significant for lower head failure. The rank regression included *DFV*, which was regressed often in the other samples. It is noteworthy that the Replicate 1 and 2 pooled data reproduced similar trends to Replicate 2, with the addition of *DCH* for the raw regression. The model summary tables for the rank and raw regressions can be found in Table 7.10 and Table 7.11.

Table 7.10 – Model Summary Table for the Raw Regression of Pooled Data from Rep. 1 and 2 for Mass of Material Ejected from the Lower Head at the Time of Lower Head Failure

	Estimate	*SE*	*tStat*	*pValue*
(Intercept)	385010.0	162240.0	2.4	2.0E-02
RSDR	54.7	21.4	2.6	1.3E-02
DCH	-3.5E-06	1.7E-06	-2.1	3.9E-02

Table 7.11 – Model Summary Table for the Raw Regression of Pooled Data from Rep. 1 and 2 for Mass of Material Ejected from the Lower Head at the Time of Lower Head Failure

	Estimate	*SE*	*tStat*	*pValue*
(Intercept)	0.3	0.1	5.4	8.9E-07
DFV	0.3	0.1	2.8	6.3E-03

7.1.6 Comparisons

Table 7.12 and Table 7.13 present the $R^2_{predict}$ and $R^2_{training}$ for the raw and rank regressions of the samples from the MELCOR estimates of mass of material ejected from the lower head at the time of lower head failure. As can be seen, the two replicates with the highest fraction of variance explained, Replicates 1 and 3, seem to be primarily fit to inherent variability. These regressions increase the predictive variance when compared to the sample variance. This is consistent for both the rank and the raw regressions. Replicate 2 has the most constant predictive ability in both rank and raw forms while the pooled data is fairly predictive with raw data but

struggles with rank transformed data. For raw data the three replicates were difficult to predict, but developed meta-models which could predict the Replicate U.

There are three key conclusions which can be drawn from these tables:

1. RSDR seems to be the dominate parameter in producing a predictive relationship. Regressions that predicted this term as the primary component of the regression model were able to reduce the variance in new samples, especially under rank transformation.
2. Regressions for mass ejected from the lower head have low predictive values and are subject to regressing inherent variability, potentially due to either the reduced sample size or the nature of the parameter.
3. Variability in training R^2 values between samples is a potential warning sign for the creation of unstable predictive models. The relatively poor predictive performance of the raw Rep12 regression indicates that the sample size does not significantly improve predictive results for this data set. Increasing sample size appeared to improve the rank regression results more than the raw regression results.

Table 7.12 – Comparison of Predictive Ability of Raw Regressions for Mass of Material Ejected from the Lower Head at the Time of Lower Head Failure

	Rep1	*Rep2*	*Rep3*	*RepU*	*Rep12*
Rep1	0.56	0.005	-0.18	-0.25	0.13
Rep2	-0.83	0.12	-0.16	0.05	0.13
Rep3	-0.36	-0.03	0.41	-0.09	0.004
RepU	-0.70	0.21	-0.24	0.28	0.13
$\overline{R^2_{pred}}$	-0.63	0.06	-0.19	-0.10	0.07
R^2_{adj}	0.52	0.10	0.37	0.27	0.11

Table 7.13 – Comparison of Predictive Ability of Rank Regressions for Mass of Material Ejected from the Lower Head at the Time of Lower Head Failure

	Rep1	*Rep2*	*Rep3*	*RepU*	*Rep12*
Rep1	0.62	0.11	-0.11	0.001	0.10
Rep2	-0.79	0.11	-0.06	0.14	0.10
Rep3	-0.55	0.22	0.49	0.24	0.21
RepU	-0.65	0.21	-0.03	0.38	0.21
$\overline{R^2_{pred}}$	-0.66	0.18	-0.07	0.13	0.21
R^2_{adj}	0.58	0.09	0.45	0.35	0.09

7.2 Cumulative Hydrogen (H_2) Produced at Lower Plenum Dryout

This section describes the regressions for the cumulative hydrogen production at the time of lower plenum dry-out. Ten regression models were created from four samples:

1. Regressions (both rank and raw) trained on the sampled data from Replicate 1,
2. Regressions (both rank and raw) trained on the sampled data from Replicate 2,
3. Regressions (both rank and raw) trained on the sampled data from Replicate 3,
4. Regressions (both rank and raw) trained on the sampled data from the uniform distributions, and
5. Regressions (both rank and raw) trained on the sampled data from Replicate 1 and 2.

Finally, the regressions were applied to the non-training samples to gauge the predictive ability of each regression.

Table 7.14 presents the summary fit statistics for all related regressions conducted for the 1F1 UA. In general, while all fits perform poorly, Replicate 1 and Replicate 3 seem to have the best R^2 values. Grouping Replicate 1 and 2 does not improve the overall fit from Replicate 2.

Table 7.14 – Training Data Fit Comparisons for the 10 Regressions for Cumulative Hydrogen Production at the Time of Lower Plenum Dry-out

Set	*Type*	*n*	*k*	R^2	R^2_{adj}
Rep. 1	Raw	100	4	0.49	0.46
	Rank	100	4	0.52	0.50
Rep. 2	Raw	98	2	0.40	0.39
	Rank	98	1	0.38	0.37
Rep. 3	Raw	100	2	0.34	0.33
	Rank	100	2	0.38	0.36
Rep. U	Raw	100	3	0.45	0.43
	Rank	100	2	0.41	0.40
Rep. 12	Raw	198	3	0.41	0.40
	Rank	198	3	0.44	0.43

7.2.1 Replicate 1

Raw linear regression model:

$H_2 \sim 1 + MZBT + DebrisHT*TaT$

Rank linear regression model:

$\text{Rank}(H_2) \sim 1 + \text{Rank}(MZBT) + \text{Rank}(DebrisHT)* \text{Rank}(TaT)$

Both meta-models agree regarding the type of regression trends that exist in the Replicate 1 sample, but the rank regression was able to explain (marginally) more of the variance when compared to the raw regression's ability to explain the variance. The model summary tables for the rank and raw regressions can be found in Table 7.15 and Table 7.16. For both regressions, *TaT* is an insignificant variable which is only included to support the interaction term *DebrisHT:TaT*, which itself is only marginally significant. Future work may involve examining the predictive ability of this meta-model with and without the interaction term.

Table 7.15 – Model Summary Table for the Raw Regression of Rep. 1 for Cumulative Hydrogen Production at the Time of Lower Plenum Dryout

	Estimate	*SE*	*tStat*	*pValue*
(Intercept)	158.4	411.2	0.4	0.7
MZBT	0.31	0.04	8.79	6.4E-14
DebrisHT	-0.68	0.32	-2.10	3.8E-2
TaT	-0.08	0.16	-0.51	0.61
DebrisHT:TaT	2.6E-4	1.3E-04	2.07	0.042

Table 7.16 – Model Summary Table for the Rank Regression of Rep. 1 for Cumulative Hydrogen Production at the Time of Lower Plenum Dryout

	Estimate	*SE*	*tStat*	*pValue*
(Intercept)	0.28	0.11	2.63	0.01
MZBT	0.67	0.07	9.17	9.9E-15
DebrisHT	-0.52	0.17	-3.11	2.4E-03
TaT	-0.04	0.18	-0.21	0.83
DebrisHT:TaT	0.63	0.32	2.00	0.05

7.2.2 Replicate 2

Raw linear regression model:

$H_2 \sim 1 + dTdz\_CVH + MZBT$

Rank linear regression model:

$\text{Rank}(H_2) \sim 1 + \text{Rank}(MZBT)$

Both meta-models agree regarding the dependency on *MZBT* in the Replicate 2 sample, but the raw regression also resolves the characteristic coupling time within the *dTdz* model. This meta-model is marginally significant (e.g., pValue between 0.01 and 0.05), but its addition does allow the raw regression to explain slightly more of the variance than the rank regression. The model

summary tables for the rank and raw regressions can be found in Table 7.17 and Table 7.18. The scatterplots for *dTdz_CVH* and the *MZBT* can be seen in Figure 7.4.

Table 7.17 – Model Summary Table for the Raw Regression of Rep. 2 for Cumulative Hydrogen Production at the Time of Lower Plenum Dryout

	Estimate	*SE*	*tStat*	*pValue*
(Intercept)	-179	107.11	-1.67	0.10
dTdz_CVH	8.2	3.47	2.36	0.021
MZBT	0.33	0.04	7.71	1.2E-11

Table 7.18 – Model Summary Table for the Rank Regression of Rep. 2 for Cumulative Hydrogen Production at the Time of Lower Plenum Dryout

	Estimate	*SE*	*tStat*	*pValue*
(Intercept)	0.2	0.05	3.87	2.0E-04
MZBT	0.62	0.08	7.59	2.1E-11

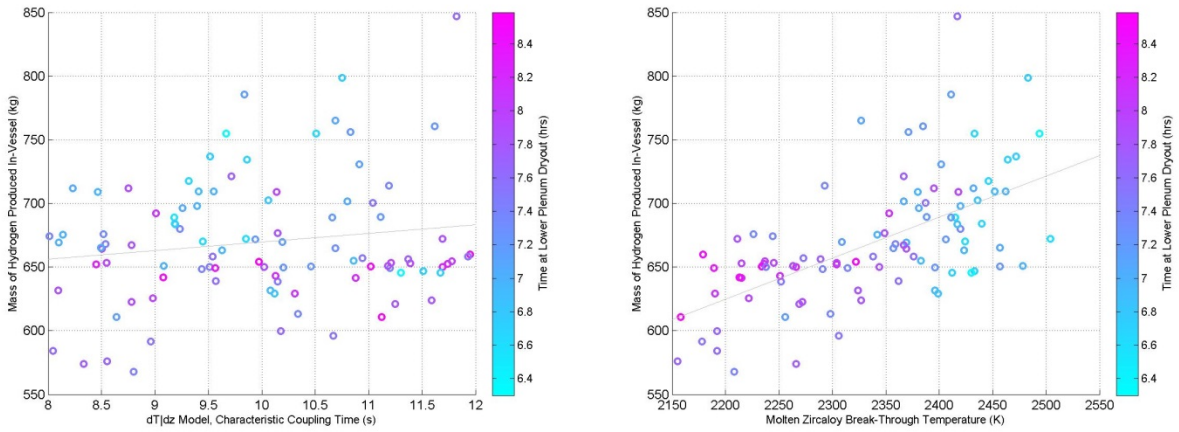

Figure 7.4 – Scatterplots for *dTdz_CVH* and *MZBT* for Replicate 2

7.2.3 Replicate 3

Raw linear regression model:

$H_2 \sim 1 + dTdz\_CVH + MZBT$

Raw linear regression model:

$\text{Rank}(H_2) \sim 1 + \text{Rank}(\text{dTdz\_}CVH) + \text{Rank}(MZBT)$

Both meta-models agree regarding the type of regression trends that exist in the Replicate 3 sample, but the rank regression was able to explain (marginally) more of the variance when compared to the raw regression's ability to explain the variance. The model summary tables for the rank and raw regressions can be found in Table 7.19 and Table 7.20. The scatterplots for *dTdz_CVH* and *MZBT* can be seen in Figure 7.5.

Table 7.19 – Model Summary Table for the Raw Regression of Rep. 3 for Cumulative Hydrogen Production at the Time of Lower Plenum Dryout

	Estimate	*SE*	*tStat*	*pValue*
(Intercept)	-188	123.73	-1.52	0.13
dTdz_CVH	8.4	4.10	2.06	0.042
MZBT	0.33	0.05	6.96	4.0E-10

Table 7.20 – Model Summary Table for the Rank Regression of Rep. 3 for Cumulative Hydrogen Production at the Time of Lower Plenum Dryout

	Estimate	*SE*	*tStat*	*pValue*
(Intercept)	0.1	0.07	1.17	0.24
dTdz_CVH	0.22	0.08	2.66	0.009
MZBT	0.63	0.08	7.48	3.3E-11

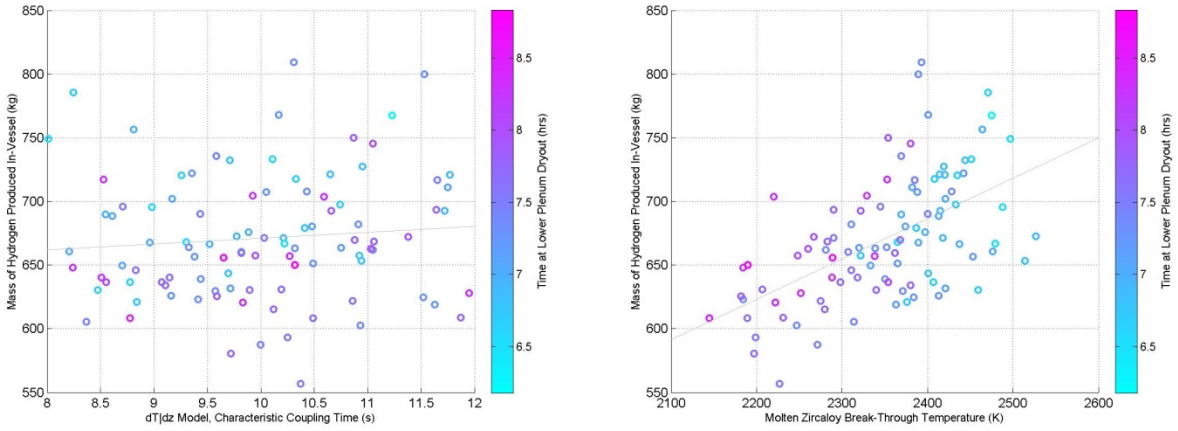

Figure 7.5 – Scatterplots for *dTdz_CVH* and *MZBT* for Replicate 3.

7.2.4 Replicate Uniform

Raw linear regression model:

$H_2 \sim 1 + MZBT + MechWeak + DebrisHT$

Rank linear regression model:

$\text{Rank}(H_2) \sim 1 + \text{Rank}(MZBT) + \text{Rank}(MechWeak)$

Both meta-models agree regarding the dependency on *MZBT* and *MechWeak* in the Replicate Uniform sample, but the raw regression also resolves the *DebrisHT* coefficient. With the extra term, the raw regression was able to explain a higher percentage of the raw training data variance than the rank regression was able to explain of its variance. The model summary tables for the rank and raw regressions can be found in Table 7.6 and Table 7.7. The scatterplots for *MZBT*, *MechWeak*, and *DebrisHT* can be seen in Figure 7.8 and Figure 7.9.

Figure 7.6 – Model Summary Table for the Raw Regression of Rep. Uniform for Cumulative Hydrogen Production at the Time of Lower Plenum Dryout

	Estimate	*SE*	*tStat*	*pValue*
(Intercept)	15.9	89.06	0.18	0.86
MZBT	0.29	0.04	7.94	3.8E-12
MechWeak	-38386	16372.00	-2.34	0.021
DebrisHT	0.02	0.01	2.47	0.015

Figure 7.7 – Model Summary Table for the Raw Regression of Rep. Uniform for Cumulative Hydrogen Production at the Time of Lower Plenum Dryout

	Estimate	*SE*	*tStat*	*pValue*
(Intercept)	0.3	0.06	4.23	5.3E-05
MZBT	0.59	0.08	7.67	1.3E-11
MechWeak	-0.16	0.08	-2.10	0.038

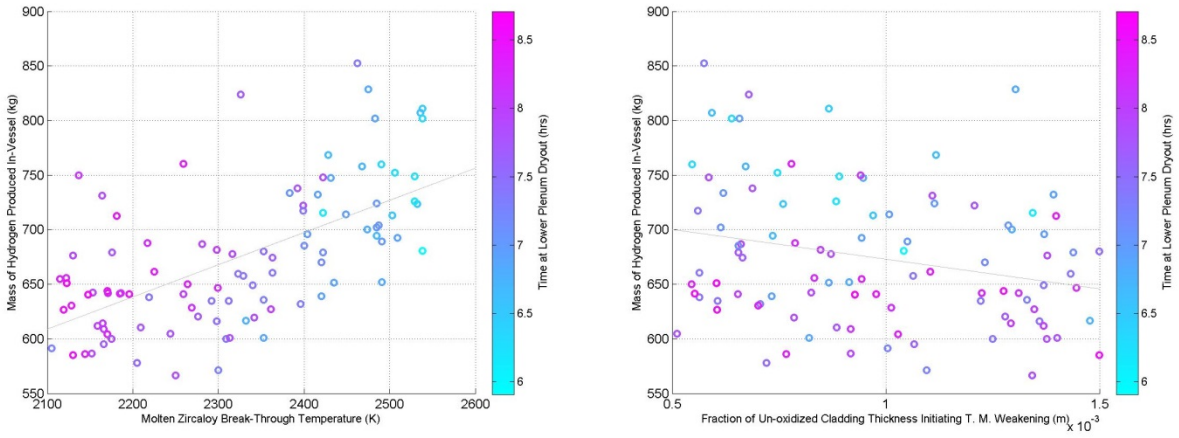

Figure 7.8 – Scatterplots for *MZBT* and *MechWeak* for Replicate Uniform

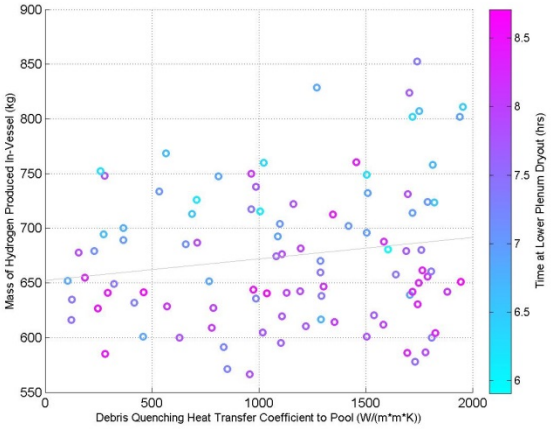

Figure 7.9 – Scatterplots for *DebrisHT* for Replicate Uniform

7.2.5 Replicate 1 and 2 Pooled

Raw linear regression model:

$H_2 \sim 1 + dTdz\_TCAF + MZBT + TaT$

Rank linear regression model:

$\text{Rank}(H_2) \sim 1 + \text{Rank}(MZBT) + \text{Rank}(TaT) + \text{Rank}(DCH)$

Both meta-models agree regarding the dependency on *MZBT* and *TaT* in the pooled Replicate 1 and 2 sample, but the raw regression also resolves the *dTdz_TCAF* coefficient while the rank regression also resolved *DCH*. With these differing fits, the rank regression had an overall better R^2 value over the training data. The model summary tables for the rank and raw regressions can be found in Table 7.21 and Table 7.22.

Table 7.21 – Model Summary Table for the Raw Regression of Pooled Rep. 1&2 for Cumulative Hydrogen Production at the Time of Lower Plenum Dryout

	Estimate	*SE*	*tStat*	*pValue*
(Intercept)	-588	157.74	-3.73	2.5E-4
dTdz_TCAF	1008	482.44	2.09	0.04
MZBT	0.30	0.03	10.90	6.7E-22
TaT	0.17	0.05	3.34	1.0E-3

Table 7.22 – Model Summary Table for the Raw Regression of Pooled Rep. 1&2 for Cumulative Hydrogen Production at the Time of Lower Plenum Dryout

	Estimate	*SE*	*tStat*	*pValue*
(Intercept)	-0.02	0.06	-0.39	0.70
MZBT	0.67	0.06	12.01	3.3E-25
TaT	0.23	0.07	3.50	5.7E-04
DCH	0.12	0.05	2.22	0.028

7.2.6 Comparisons

As was mentioned previously, the range of R^2 fits to the training data was reduced significantly for cumulative hydrogen production when compared to mass ejected from the lower head. The fruits of the higher fit stability throughout the samples are indicative of an overall greater predictive ability of the regression models. The comparison of rank and raw regression predictive ability can be seen in Table 7.23 and Table 7.24.

Table 7.23 – Comparison of Predictive Ability of Raw Regressions for Cumulative Hydrogen Production at the Time of Lower Plenum Dryout

	Rep1	*Rep2*	*Rep3*	*RepU*	*Rep12*
Rep1	0.48	0.30	0.31	0.01	0.41
Rep2	0.27	0.40	0.40	0.23	0.41
Rep3	0.30	0.34	0.34	0.19	0.29
RepU	0.26	0.37	0.36	0.45	0.36
$\overline{R^2_{pred}}$	0.27	0.34	0.36	0.14	0.32
R^2_{adj}	0.46	0.39	0.33	0.43	0.40

Additional notes on Raw Regressions in Table 7.23

Replicates 1 and U had the highest R^2 but lowest predictive ability, especially for raw regressions. Replicate U experienced consistent predictive R^2 of all meta-models (~0.01). Interestingly, Replicate U had a dramatically increased predictive ability for its rank regression. It is possible that the higher probability concentration in the tails does well at predicting general placement with small data sets, but breaks down when trends are set using raw data.

Replicates 2, 3, and 12 had lower initial R^2 but better predictive capability than Replicate 1 and U. Replicate 12's predictive ability for Replicate 3 was worse than either Replicate 1 or 2 separately, but did a better job at predicting Replicate U. Across the board, *dTdz_CVH* & *MZBT* seem to be the reliability predictive terms. Doubling the sample size did not seem to dramatically improve the predictive nature of the regression models.

Table 7.24 – Comparison of Predictive Ability of Rank Regressions for Cumulative Hydrogen Production at the Time of Lower Plenum Dryout

	Rep1	*Rep2*	*Rep3*	*RepU*	*Rep12*
Rep1	0.52	0.40	0.36	0.37	0.44
Rep2	0.24	0.38	0.36	0.34	0.44
Rep3	0.31	0.34	0.38	0.30	0.30
RepU	0.25	0.39	0.39	0.41	0.35
$\overline{R^2_{pred}}$	0.27	0.37	0.37	0.34	0.32
R^2_{adj}	0.50	0.37	0.36	0.40	0.43

Additional notes on rank regressions in Table 7.24

Replicates 1, U, and 12 had the highest R^2 but lowest predictive ability. In general, the predictive nature of the rank regressions improved when compared to the raw regressions. Replicate 1 regressions experienced consistent low predictability across the replicates. Replicate U regressions experienced varying predictability, but it is consistently higher than the corresponding raw regression results. Replicate 12 had a higher R^2 than Replicate 2 but slightly lower predictive capability. Conversely, Replicate 12 had a lower R^2 than Rep1 but had a higher predictive capability.

Replicate 2 and 3 had low initial R^2 but higher predictive ability. Interestingly, Replicates 2 and 3 showed a better ability to explain the variance in the testing sample than the variance in the training data in multiple cases. As with the raw regressions, *dTdz_CVH* , and *MZBT* seem to be the reliability predictive terms.

7.3 Fraction of Intact Fuel Mass (FIFM) at Lower Core Plate Failure

This section describes the regressions for the intact fuel fraction at the time of lower core plate failure. Ten regression models were created from four samples:

1. Regressions (both rank and raw) trained on the sampled data from Replicate 1,
2. Regressions (both rank and raw) trained on the sampled data from Replicate 2,
3. Regressions (both rank and raw) trained on the sampled data from Replicate 3,
4. Regressions (both rank and raw) trained on the sampled data from the uniform distributions, and
5. Regressions (both rank and raw) trained on the sampled data from Replicate 1 and 2.

Finally, the regressions are applied to the non-training samples to gauge the predictive ability of each regression.

Overall R^2 estimates for intact fuel mass are higher and more stable than mass of material ejected in the lower head but lower and less stable than cumulative hydrogen production.

Table 7.25 – Training Data Fit Comparisons for the 10 Regressions for Intact Fraction of Fuel Mass at the Time of Lower Core Plate Failure

Set	*Type*	*n*	*k*	R^2	R^2_{adj}	F_{stat}
Rep. 1	Raw	100	3	0.31	0.29	14.2
	Rank	100	4	0.29	0.26	9.7
Rep. 2	Raw	98	7	0.53	0.49	14.6
	Rank	98	4	0.42	0.39	16.8
Rep. 3	Raw	100	2	0.24	0.23	15.4
	Rank	100	2	0.23	0.22	14.7
Rep. U	Raw	100	2	0.4	0.38	30.7
	Rank	100	2	0.35	0.34	26.5
Rep. 1&2	Raw	198	5	0.39	0.37	24.5
	Rank	198	2	0.23	0.22	14.7

7.3.1 Replicate 1

Raw linear regression model:

FIFM ~ 1 + *MZBT***TaT*

Rank linear regression model:

Rank(*FIFM*) ~ 1 + Rank(*MZBT)* + Rank(*FSLHF*) + Rank(*DFV*) + Rank(*TaT)*

Both meta-models agree regarding the dependency on *MZBT* and *TaT* in the Replicate 2 sample, but the rank regression also resolves the *FSLHF* and *DFV* coefficients. Even with the extra terms in the rank regression, the raw regression was able to explain a higher percentage of the raw training data variance than the rank regression was able to explain of its variance. The regression on *FSLHF* is likely a statistical anomaly because the fraction of strain before lower head failure should have no impact on FoMs before lower head failure occurs. The model summary tables for the rank and raw regressions can be found in Table 7.26 and Table 7.27. The scatterplots for *MZBT, FSLHF, DFV,* and *TaT* are in Figure 7.10 and Figure 7.11. The 3-D scatter plot for *MZBT* and *TaT* was shown in Figure 6.4. The linear trends are significantly more visible in *MZBT, TaT* and *DFV* than in *FSLHF*.

Table 7.26 – Model Summary Table for the Raw Regression of Rep. 1 for Intact Fuel Mass at the Time of Lower Core Plate Failure

	Estimate	*SE*	*tStat*	*pValue*
(Intercept)	16.95	8.32	2.04	0.04
MZBT	-0.01	3.5E-03	-2.13	0.04
TaT	-0.01	3.2E-03	-1.90	0.06
MZBT:TaT	2.8E-06	1.4E-06	2.04	0.04

Table 7.27 – Model Summary Table for the Raw Regression of Rep. 1 for Intact Fuel Mass at the Time of Lower Core Plate Failure

	Estimate	*SE*	*tStat*	*pValue*
(Intercept)	0.37	0.10	3.77	2.9E-04
MZBT	-0.19	0.09	-2.10	0.04
FSLHF	-0.21	0.09	-2.33	0.02
DFV	0.21	0.09	2.40	0.02
TaT	0.47	0.11	4.29	0.00

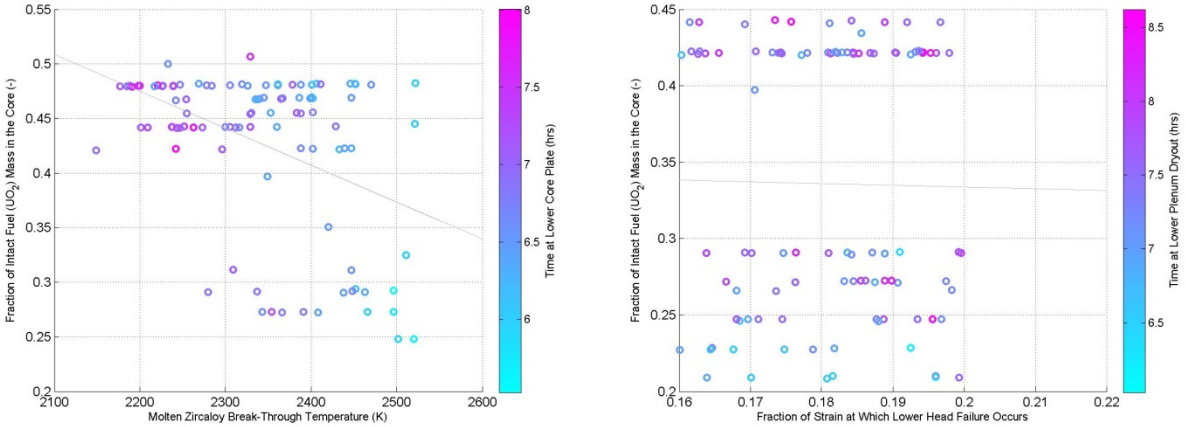

Figure 7.10 – Scatterplots for *MZBT* and *FSLHF* for Replicate 1

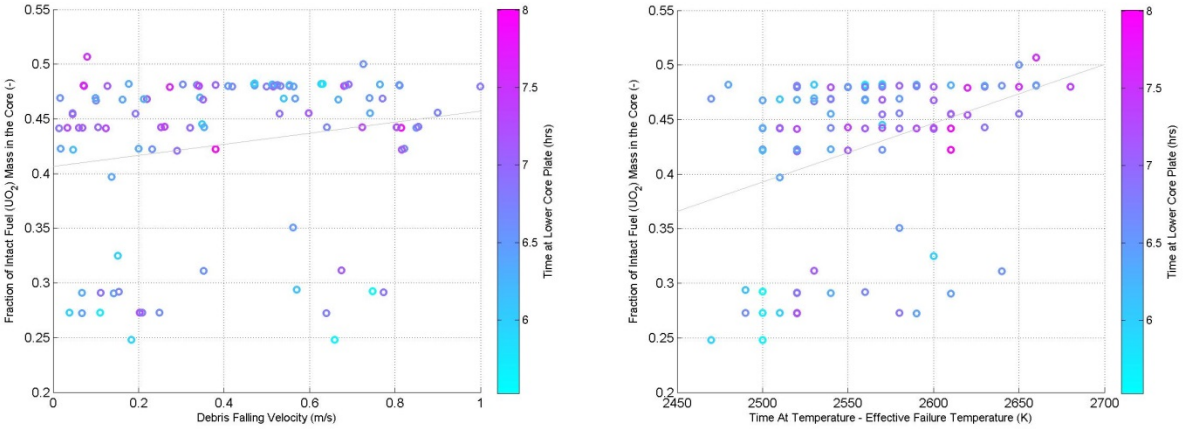

Figure 7.11 – Scatterplots for *DFV* and *TaT* for Replicate 1

7.3.2 Replicate 2

Raw linear regression model:

$$FIFM \sim 1 + TaT + DCH + MZBT*DFV + MCDR*DFV$$

Rank linear regression model:

$$\text{Rank}(FIFM) \sim 1 + \text{Rank}(TaT) + \text{Rank}(MZBT)* \text{Rank}(DFV)$$

Both meta-models agree regarding the dependency on *MZBT* and *TaT* in the Replicate 2 sample, but the rank regression also resolves the *FSLHF* and *DFV* coefficients. The model summary tables for the rank and raw regressions can be found in Table 7.28 and Table 7.29. The scatterplots for *MZBT*, *DCH*, and *TaT* are in Figure 7.12. 3-D plots for *MZBT:DFV* and *MCDR:DFV* are shown in Figure 7.13 and Figure 7.14.

Table 7.28 – Model Summary Table for the Raw Regression of Rep. 2 for Intact Fuel Mass at the Time of Lower Core Plate Failure

	Estimate	*SE*	*tStat*	*pValue*
(Intercept)	-0.36	0.58	-0.62	0.54
MZBT	-6.4E-4	1.2E-4	-5.57	2.6E-07
MCDR	-0.15	0.05	-2.91	4.6E-03
DFV	-1.23	0.54	-2.27	0.03
TaT	6.1E-04	1.2E-04	5.02	2.6E-06
DCH	7.6E-12	3.7E-12	2.05	0.04
MZBT:DFV	5.3E-04	2.3E-04	2.30	0.02
MCDR:DFV	0.21	0.10	2.09	0.04

Table 7.29 – Model Summary Table for the Rank Regression of Rep. 2 for Intact Fuel Mass at the Time of Lower Core Plate Failure

	Estimate	*SE*	*tStat*	*pValue*
(Intercept)	0.47	0.10	4.86	4.8E-06
MZBT	-0.73	0.16	-4.53	1.7E-05
DFV	-0.07	0.16	-0.46	6.5E-01
TaT	0.54	0.10	5.43	4.5E-07
MZBT:DFV	0.65	0.27	2.43	0.02

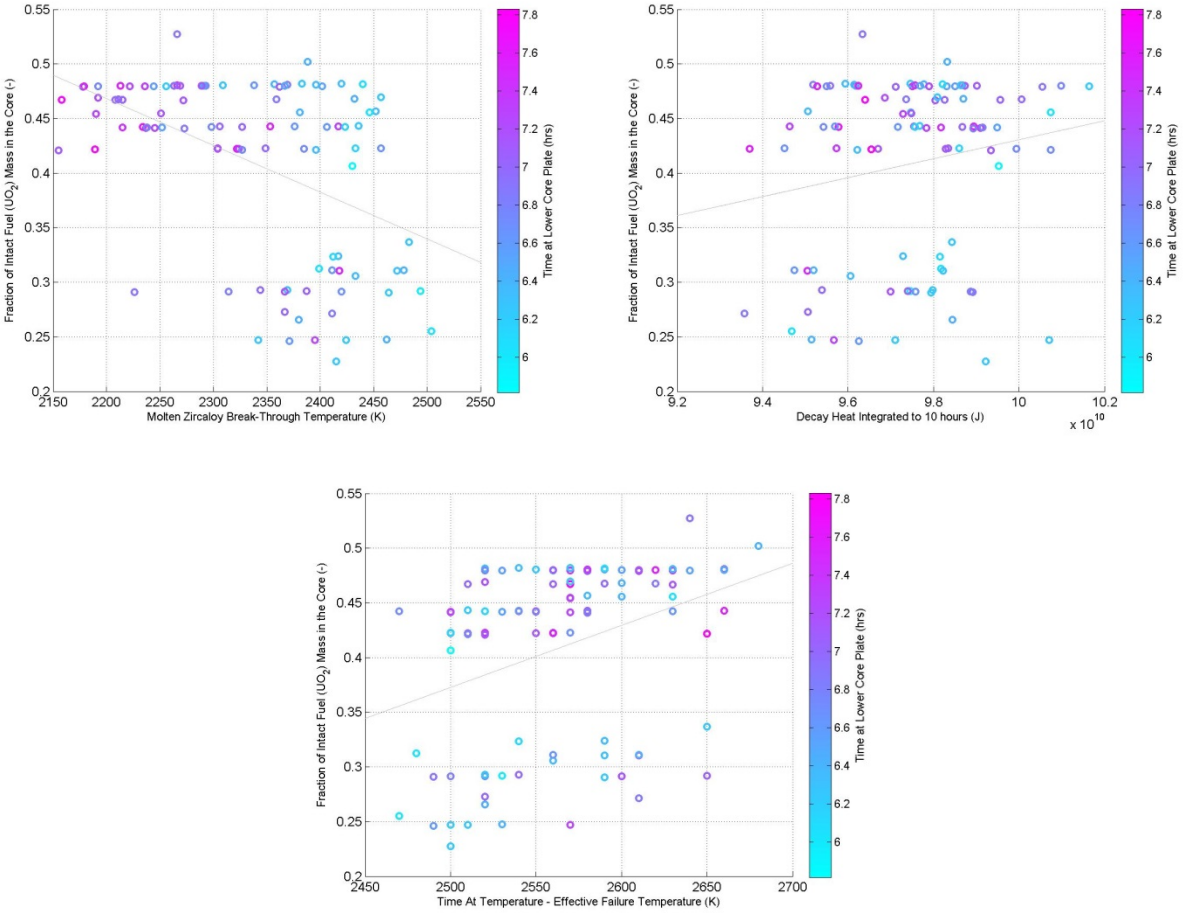

Figure 7.12 – Scatterplots for *MZBT*, *DCH*, and *TaT* for Replicate 2

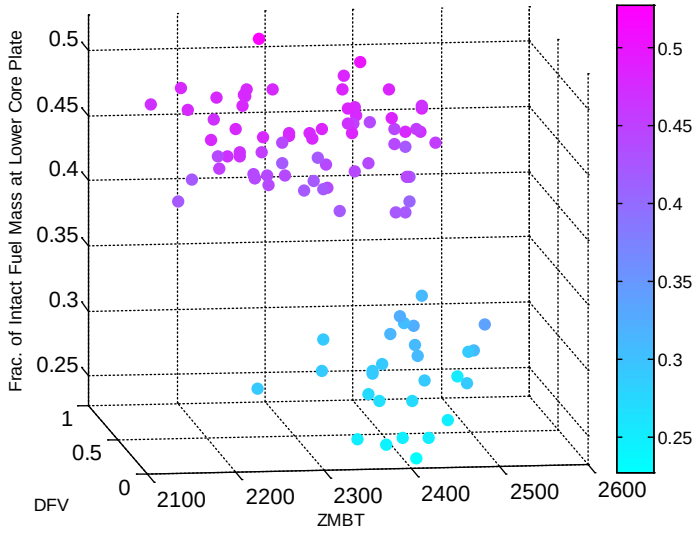

Figure 7.13 – Scatterplot of *MZBT* and *DFV* for Replicate 2

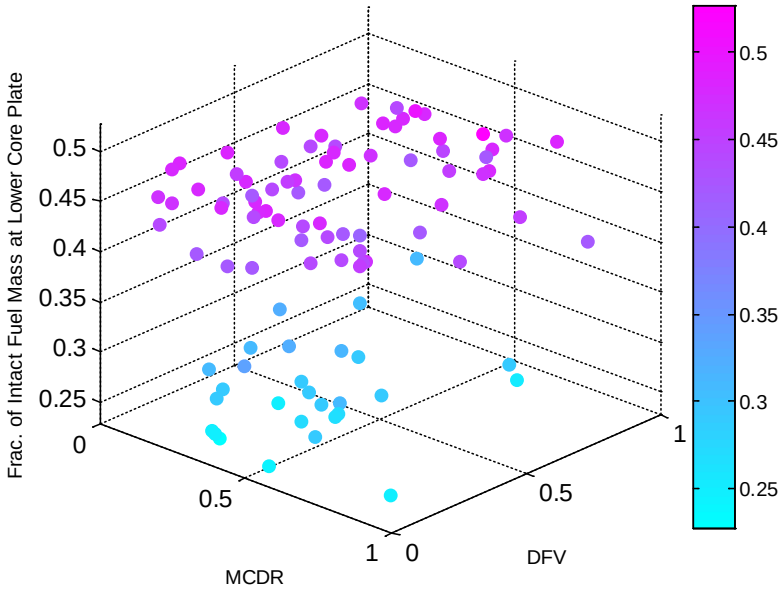

Figure 7.14 – Scatterplot of *MCDR* and *DFV* for Replicate 2

7.3.3 Replicate 3

Raw linear regression model:

$FIFM \sim 1 + MZBT + TaT$

Rank linear regression model:

$\text{Rank}(FIFM) \sim 1 + \text{Rank}(MZBT) + \text{Rank}(TaT)$

Both meta-models agree regarding the dependency on *MZBT* and *TaT* in the Replicate 3 sample. The rank regression did marginally better at resolving the variance in the sample data. The model summary tables for the rank and raw regressions can be found in Table 7.30 and Table 7.31.

Table 7.30 – Model Summary Table for the Raw Regression of Rep. 3 for Intact Fuel Mass at the Time of Lower Core Plate Failure

	Estimate	*SE*	*tStat*	*pValue*
(Intercept)	-0.10	0.46	-0.21	0.84
MZBT	-3.0E-04	8.3E-05	-3.66	4.2E-04
TaT	4.8E-04	1.4E-04	3.29	1.4E-03

Table 7.31 – Model Summary Table for the Rank Regression of Rep. 3 for Intact Fuel Mass at the Time of Lower Core Plate Failure

	Estimate	*SE*	*tStat*	*pValue*
(Intercept)	0.42	0.08	5.00	2.5E-06
MZBT	-0.26	0.09	-2.81	0.01
TaT	0.44	0.11	3.96	1.4E-04

7.3.4 Replicate Uniform

Raw linear regression model:

$FIFM \sim 1 + MZBT + TaT$

Rank linear regression model:

$\text{Rank}(FIFM) \sim 1 + \text{Rank}(MZBT) + \text{Rank}(TaT)$

Both meta-models agree regarding the dependency on *MZBT* and *TaT* in the Replicate 3 sample. The raw regression did marginally better at resolving the variance in the sample data. The model summary tables for the rank and raw regressions can be found in Table 7.32 and Table 7.33.

Table 7.32 – Model Summary Table for the Raw Regression of Rep. Uniform for Intact Fuel Mass at the Time of Lower Core Plate Failure

	Estimate	*SE*	*tStat*	*pValue*
(Intercept)	0.33	0.37	0.89	0.38
MZBT	-3.5E-04	4.9E-05	-7.12	1.9E-10
TaT	3.5E-04	1.3E-04	2.64	0.01

Table 7.33– Model Summary Table for the Rank Regression of Rep. Uniform for Intact Fuel Mass at the Time of Lower Core Plate Failure

	Estimate	*SE*	*tStat*	*pValue*
(Intercept)	0.55	0.08	7.28	8.8E-11
MZBT	-0.47	0.08	-5.65	1.6E-07
TaT	0.39	0.10	3.79	2.6E-04

7.3.5 Replicate 1 and 2 Pooled

Raw linear regression model:

FIFM ~ 1 + *TaT* + *DCH* + *MZBT***DFV*

Rank linear regression model:

Rank(FIFM) ~ 1 + Rank(*minPorosity*) + Rank(*TaT*) + Rank(*MZBT*)* Rank(*DFV*

Both meta-models agree regarding the dependency on *MZBT* and *TaT* in the Replicate 3 sample. The raw regression model also included *DCH* and an interaction between *DFV* and *MZBT*. The rank regression also included *minPorosity* and *TaT*. The raw regression did better at explaining the variance in the sample data. The model summary tables for the rank and raw regressions can be found in Table 7.34 and Table 7.34.

Table 7.34 – Model Summary Table for the Raw Regression of the Pooled Rep. 1+2 data for Intact Fuel Mass at the Time of Lower Core Plate Failure

	Estimate	*SE*	*tStat*	*pValue*
(Intercept)	-0.21	0.43	-0.49	0.62
MZBT	-5.2E-04	0.00	-6.11	5.5E-09
DFV	-0.81	0.41	-1.96	0.05
TaT	4.9E-04	0.00	5.44	1.6E-07
DCH	5.7E-12	0.00	2.13	0.03
MZBT:DFV	3.8E-04	0.00	2.13	0.03

Table 7.35 – Model Summary Table for the Rank Regression of the Pooled Rep. 1+2 data for Intact Fuel Mass at the Time of Lower Core Plate Failure

	Estimate	*SE*	*tStat*	*pValue*
(Intercept)	0.36	0.08	4.28	3.0E-05
MZBT	-0.55	0.12	-4.57	8.5E-06
DFV	-0.04	0.12	-0.30	0.76
minPorosity	0.13	0.06	2.16	0.03
TaT	0.49	0.07	6.69	2.4E-10
MZBT:DFV	0.53	0.21	2.54	0.01

7.3.6 Comparison

As was mentioned previously, the range of R^2 fits to the training data fell in between those calculated for mass ejected from the lower head and cumulative hydrogen production;, both in terms of average R^2 and stability of R^2 between samples. The comparison of rank and raw regression predictive ability can be seen in Table 7.36 and Table 7.37.

Table 7.36 – Comparison of Predictive Ability of Raw Regressions for Intact Fuel Mass at the Time of Lower Plate Failure

	Rep1	*Rep2*	*Rep3*	*RepU*	*Rep12*
Rep1	0.31	0.16	0.25	0.19	0.39
Rep2	0.25	0.53	0.32	0.32	0.39
Rep3	0.23	0.02	0.24	0.23	0.19
RepU	0.34	-1.53	0.38	0.39	0.37
$\overline{R^2_{pred}}$	0.27	-0.45	0.32	0.25	0.28
R^2_{adj}	0.29	0.50	0.23	0.38	0.37

Table 7.37 – Comparison of Predictive Ability of Raw Regressions for Intact Fuel Mass at the Time of Lower Plate Failure

	Rep1	*Rep2*	*Rep3*	*RepU*	*Rep12*
Rep1	0.29	0.21	0.21	0.14	0.34
Rep2	0.32	0.42	0.30	0.30	0.34
Rep3	0.17	0.20	0.23	0.20	0.26
RepU	0.19	0.29	0.32	0.35	0.27
$\overline{R^2_{pred}}$	0.23	0.23	0.28	0.21	0.27
R^2_{adj}	0.26	0.39	0.22	0.34	0.33

Replicate 2 had the most consistency in terms of the meta-model's fit to data and ability of other models to explain more of the variance in the data, but the predictive models from Replicate 2 were unreliable, especially for the raw data. The meta-model predicted from Replicate 3 had the lowest R^2 over the training data but consistently had the best predictive merit. *MZBT* and *TaT* were consistently resolved across the samples and were the only parameters resolved in Replicate 3.

8 MELCOR OUTPUT STABILITY

While the focus of the statistical analysis in this report revolves around the results Replicate 1, the authors would be remiss if some attention was not paid to the perturbation cases. Because there is no physical meaning to the values varied in the three perturbation cases, no regressions were conducted on the perturbation results. Instead, scatterplots and cumulative distributions were used to identify statistical trends in the FoMs.

As a reminder, the three perturbation cases are as follows:

P1. The small input perturbations can generally be interpreted as small[14] (essentially insignificant) variations in all uncertain MELCOR inputs except the time at temperature and decay heat tables.
P2. The dt_{max} perturbation varies the maximum time step that the code can take. It should be noted that this is not the exact time step the code takes during the simulation, which can change as needed by the code. MELCOR may reduce the system time step to overcome various issues (e.g. convergence, solver errors, engineering tolerances), and each MELCOR package (CVH/FL, COR, etc.) may use distinct time step schemes as necessary. Nonetheless, the code/system-level time step is a key user input.
P3. The flow path shuffle perturbation changes the flow path order used to solve matrix solutions in MELCOR at each time step.

8.1 Scatter Plots

This section presents scatterplots for hydrogen produced at a given timing FoM vs the hydrogen produced at the end of the simulation (EoS hydrogen) for each perturbation. Note that all samples follow the same accident progression:

1. Control Rod Failure (not plotted due to the small variability at this timing FoM),
2. Channel Box Failure,
3. Main Steam Line Failure,
4. First Fuel Failure,
5. Lower Core Plate Failure,
6. Lower Plenum Dryout, and
7. Lower Core Plate Failure (optional and not plotted).

For comparison to the perturbation cases, the same five FoMs are plotted for Replicate 1 in Figure 8.1.

8.1.1 P1 – Small Input Perturbation

A selection of hydrogen generation scatterplots from P1 is shown in Figure 8.2. At channel box failure, the variance of EoS hydrogen production as a function of hydrogen produced by channel box failure is fairly constant, but the amount of hydrogen produced seems to be a strong function of channel box failure time, which itself is fairly tight. While trends from fuel collapse are difficult to discern, hydrogen produced at main steam line failure seems to be a strong function of the main steam line failure time. Alternatively, end of simulation hydrogen is a weak function of main steam line failure time, likely due to loss of precision caused by core degradation

[14] Technically, these variations were elicited by forming a uniform distribution around the sampled values for the median-like cases, with the upper and lower bounds of the uniform distribution taken as ±0.5% of the nominal value.

approximations. Fuel failure seems to be a non-precise process, but the same trends exhibited for main steam line failure return for lower core plate failure and lower plenum dryout. The only exception for these last two timing FoMs is that late failures seem to have a reversed trend, where extremely late lower plenum dryout times can occur with lower overall hydrogen levels.

8.1.2 P2 – dt_{max} Perturbation

The dt_{max} perturbation study is interesting as a single ordinate parameter is varied to elicit output changes. If the code were numerically convergent in the traditional sense, one would expect that reduced dt_{max} would correlate to a numerically truer answer. Of course, this is not the case because dt_{max} does not have a one-to-one correlation with the time step taken during discrete events (e.g., due to MELCOR's algorithms, a higher dt_{max} might yield a smaller dt during core degradation than a lower dt_{max}) and because the if-then-else statements used to change geometry in MELCOR are, by definition, not time step convergent. Ad-hoc "engineering tolerances" are implemented in certain sub-models in the code, such as the molten material candling process, that attempt to smooth or remove gross time step dependencies. However, these work-arounds do not completely resolve the issue. Thus, in addition to the hydrogen variability plots, plots of timing FoMs vs dt_{max} for hydrogen production are also presented.

8.1.2.1 Hydrogen Variation Plots

A selection of hydrogen generation scatterplots from P2 is shown in Figure 8.3. The first clustering of results appears to occur with main steam line failure, where both a low and high cluster of hydrogen production levels are reached at the time of main steam line failure. While the distributions of these clusters vary dramatically, a positive correlation between hydrogen at the time of main steam line failure and end of simulation is noticeable. This trend is not as observable in Replicate 1. The range of hydrogen production at first fuel failure is reduced because all dt_{max} occur with main steam line failure occurring well before first fuel collapse. This reduced range continues with lower core plate failure but by lower plenum dryout the dt_{max} variance in hydrogen production has surpassed Replicate 1, primarily due to 3 outliers past 825 kg of H_2. As with P1, main steam line failure, lower core plate failure, and lower plenum dryout all show a roughly positive correlation between failure time and hydrogen levels. The same extremely high failure time negative correlation is also noted (see Section 8.1.1).

8.1.2.2 dt_{max} Dependencies

A selection of max time step sensitivity scatterplots from P2 is shown in Figure 8.4. No dt_{max} dependency is seen, especially for later timing FoMs, and the inherent variability seems to be constant as a function of dt_{max}.

8.1.3 P3 – Flow path Shuffle Perturbation

A selection of hydrogen generation scatterplots from P3 is shown in Figure 8.5. The results from P3 may best be described as a higher variance version of P2, with most of the same trends in the output results visible.

8.1.4 Overall takeaways from the Perturbation Scatterplots

The distribution of hydrogen generation (and thus oxidation) early in the simulation has very little impact on the hydrogen generated at the end of the simulation for all perturbation cases, although mild trends were seen for the time step perturbation study. When the timing FoMs were examined as a function of time step, variance was fairly constant as a function of dt_{max} except for

near the lower end of dt_{max}, near 0.01s, where the variance counter-intuitively starts to increase. This increase in variance at low dt_{max} might be caused by forcing the code to take smaller time steps than the discrete core degradation models were designed for supporting; the lumped-parameter, thermal-hydraulic formulations in MELCOR, and its explicit coupling to the MELCOR other packages, may also have numerical trouble with very small time steps. The system-level physics models in MELCOR were originally geared towards resolving gross, macroscopic changes over rather large time steps.

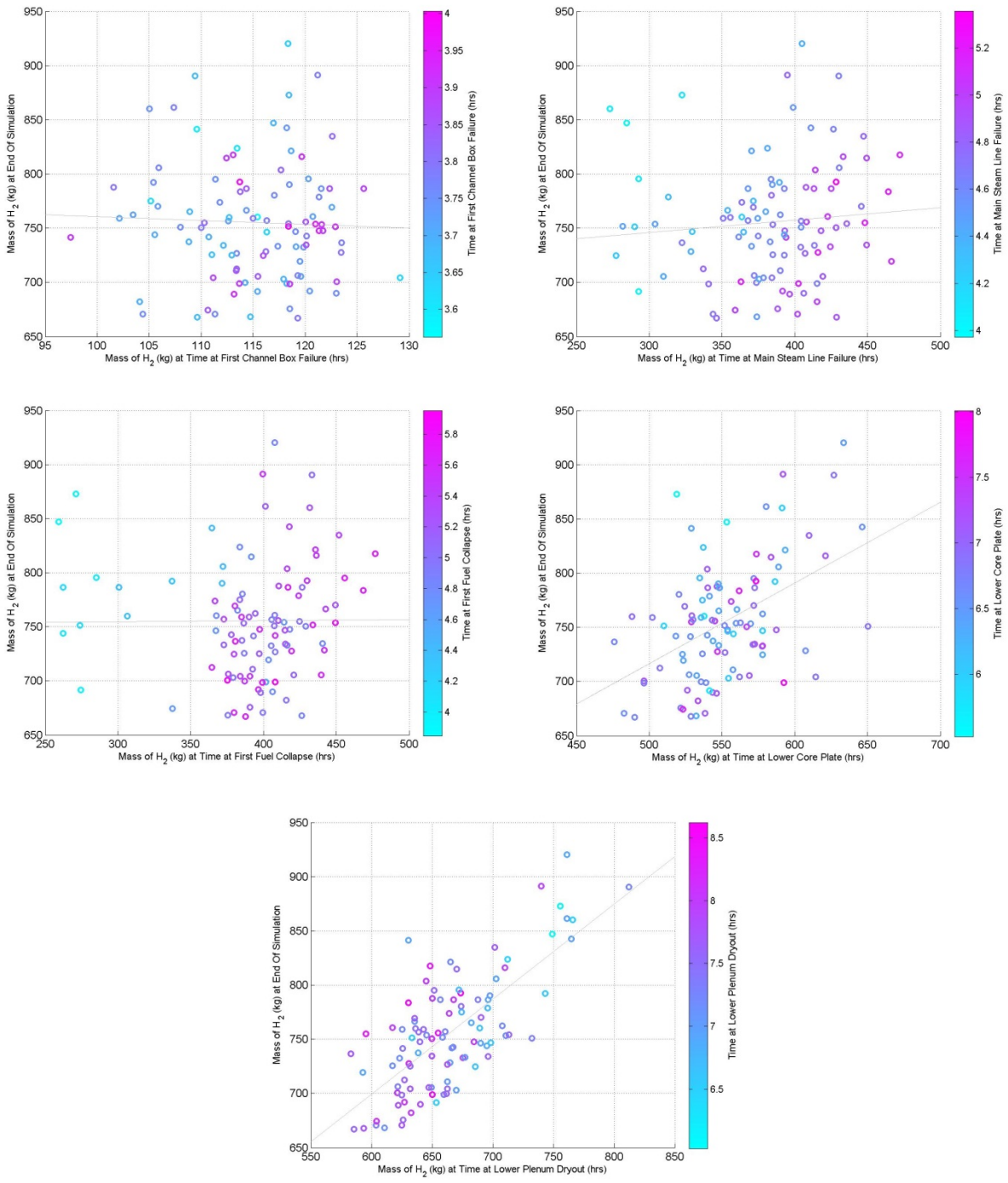

Figure 8.1- Replicate 1 H2 at Timing FoM vs H2 at EoS.

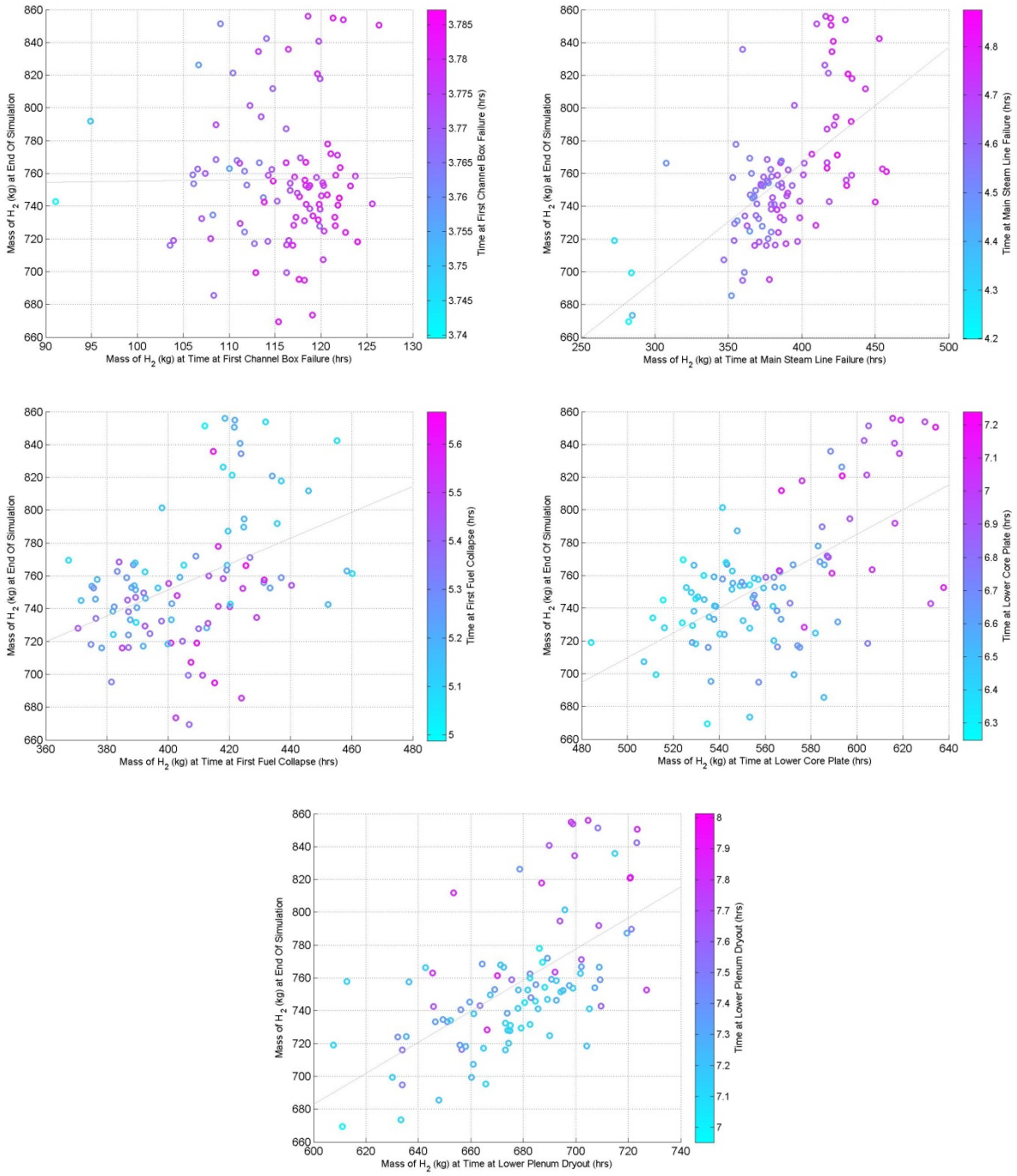

Figure 8.2- P1 H2 at Timing FoM vs H2 at EoS.

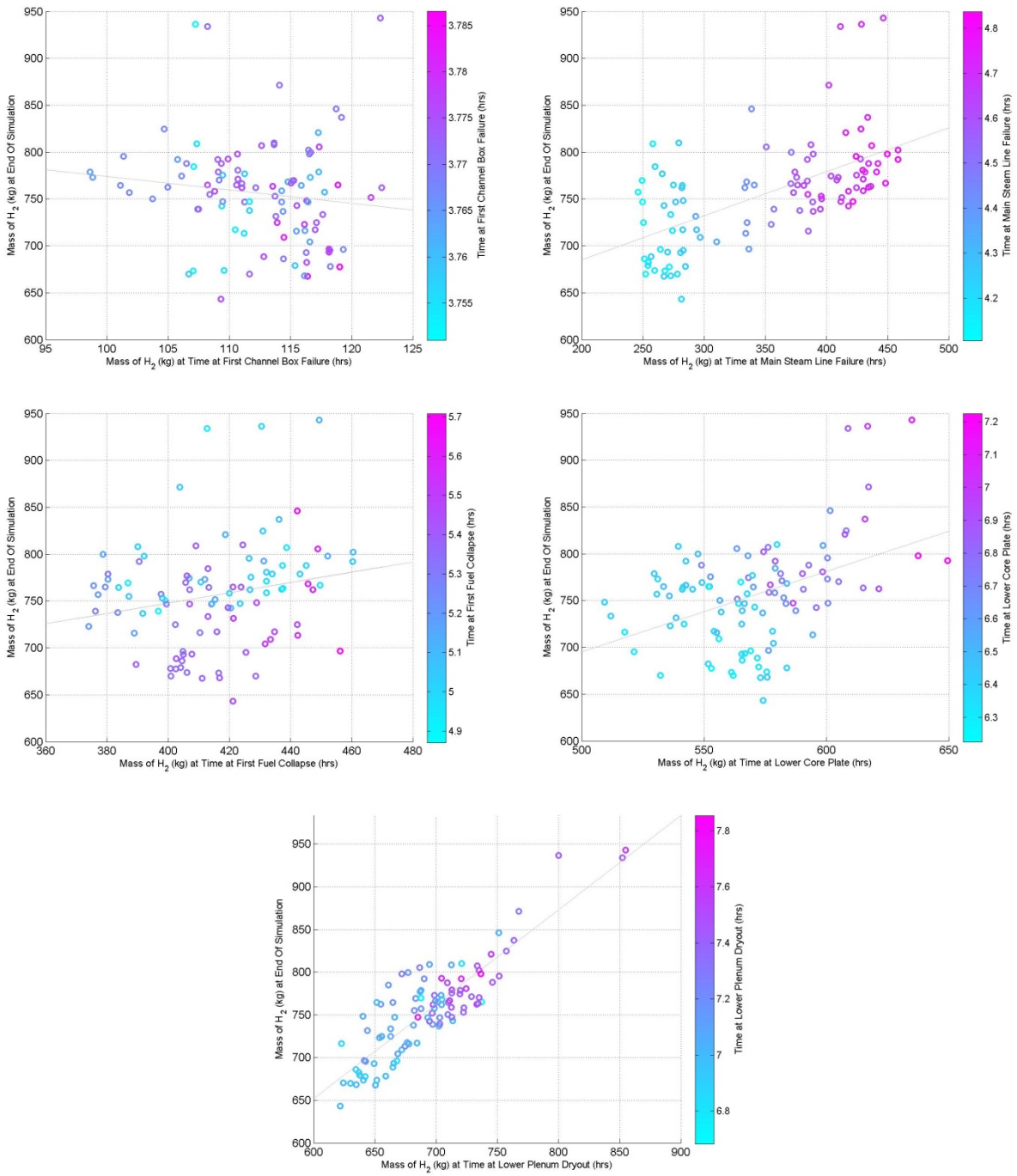

Figure 8.3 – P2 H2 at Timing FoM vs H2 at EoS.

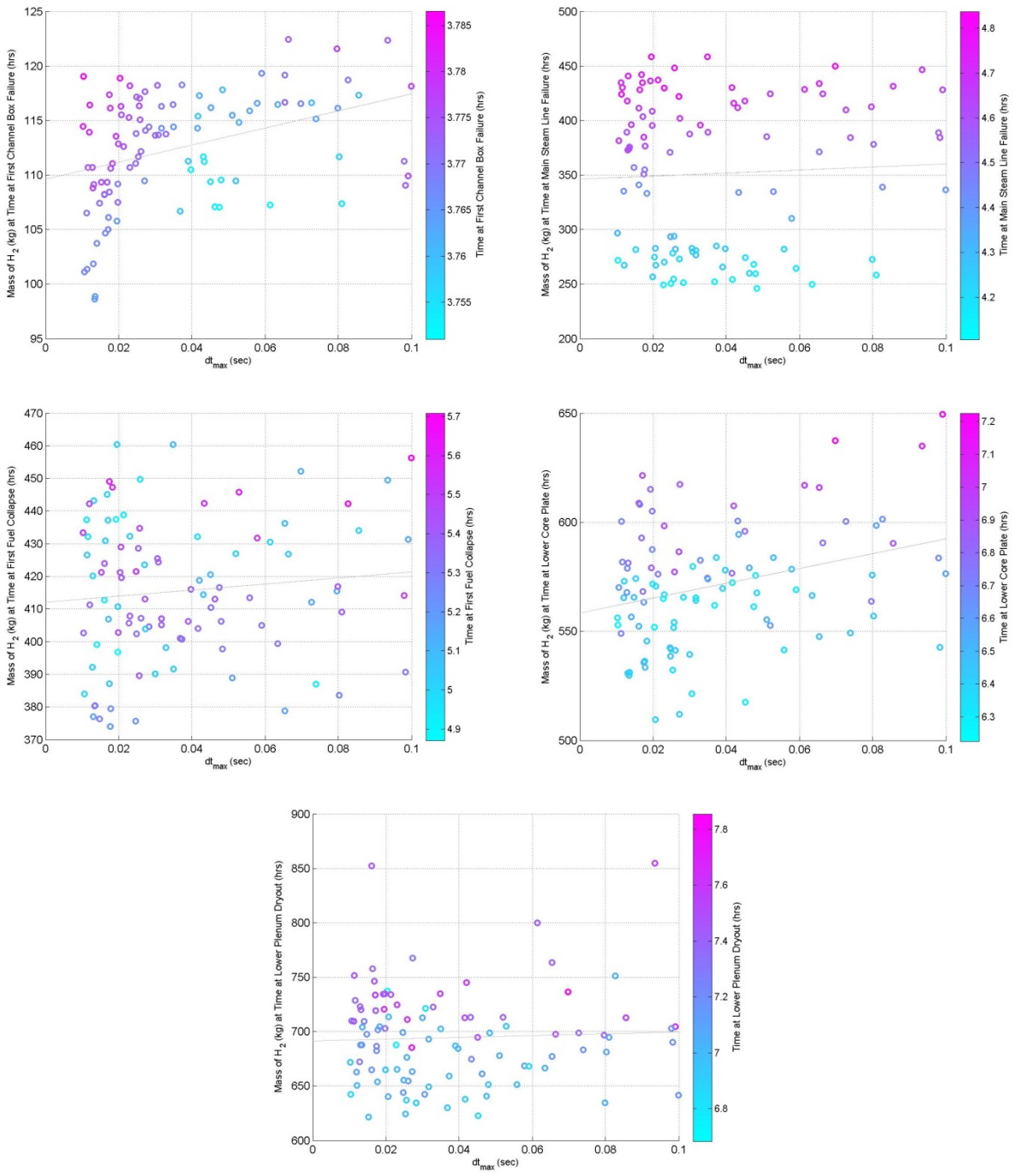

Figure 8.4 – P2 dtmax vs H2 at Timing FoM

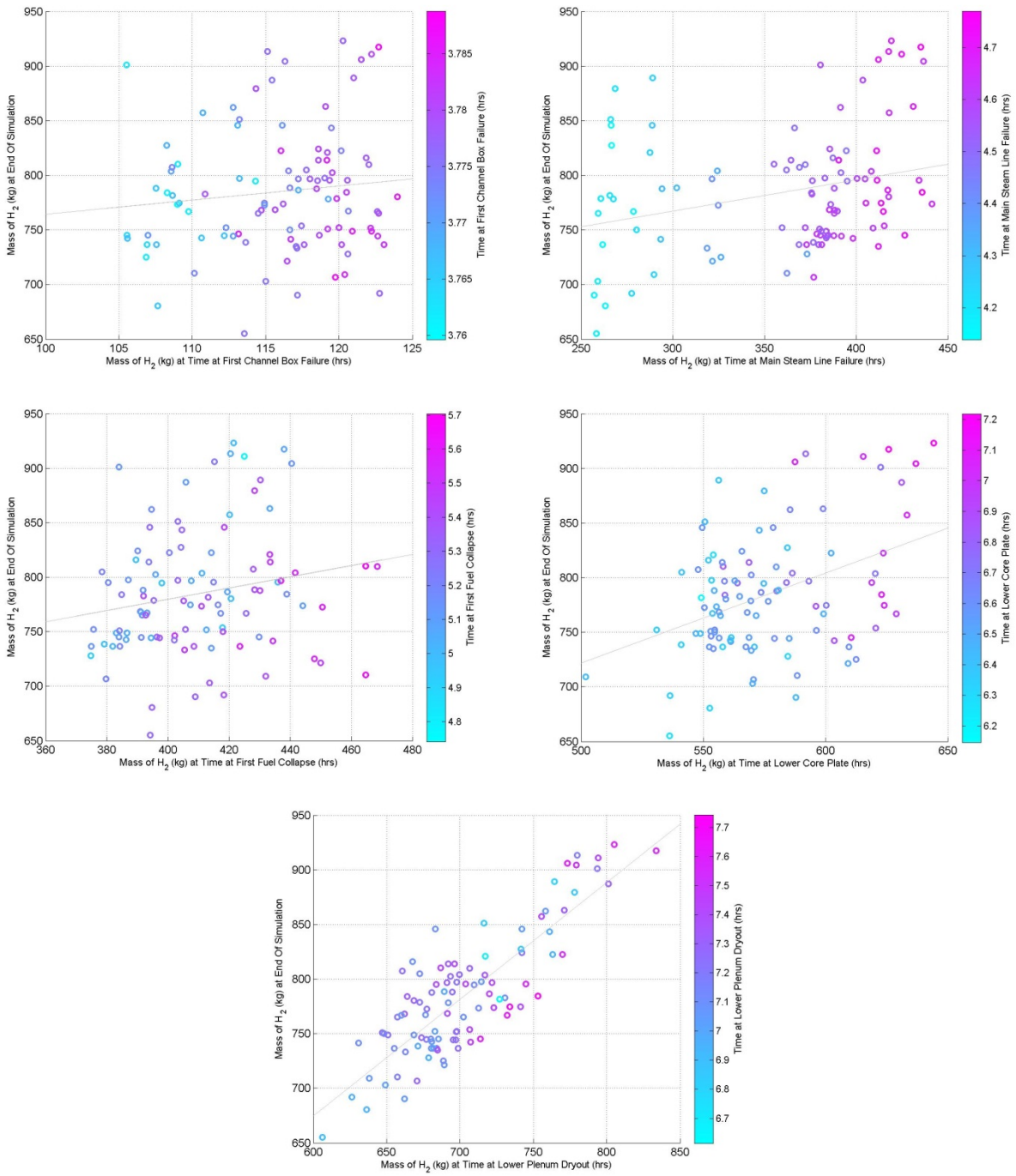

Figure 8.5 – P3 H2 at Timing FoM vs H2 at EoS.

8.2 Cumulative Distribution Functions

The cumulative distributions for Replicate 1, P1, P2 and P3 are shown in Figure 8.6, Figure 8.7, and Figure 8.8. Light dotted lines on the distributions for P1, P2, and P3 indicate the median-like values, selected as realization 13 of Replicate 1, which provides the basis for the input parameters which inform these perturbations.

Figure 8.6 presents the cumulative distributions for event timings. As can be seen, the timing variability is reduced for all events. Even though realization 13 does not experience lower head failure, between 10% and 35% of perturbation simulations resulted lower head failure.

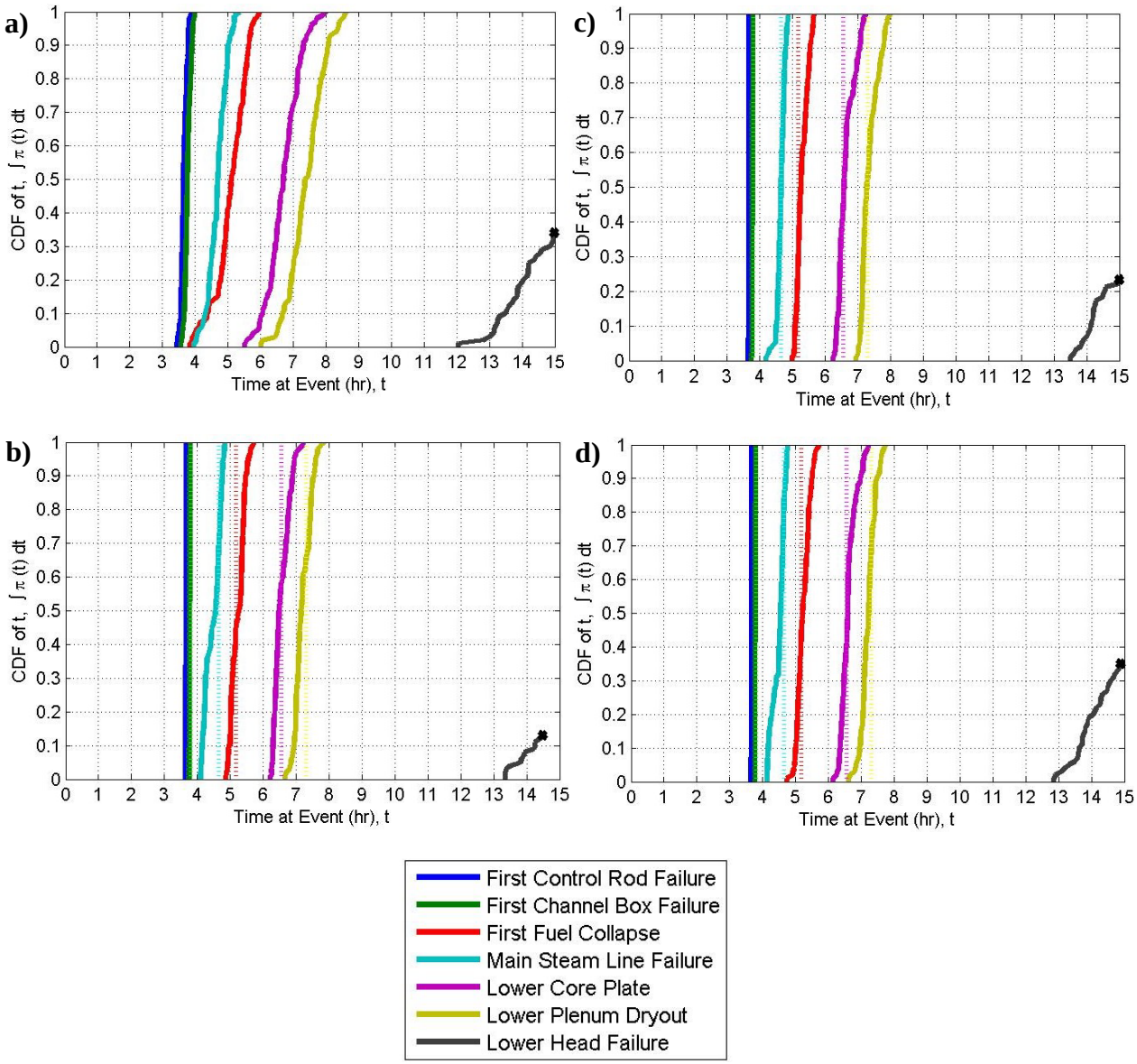

Figure 8.6 – Event Timing Cumulative Distribution Functions: Top Left – Replicate 1, Top Right – P1, Bottom Left – P2, Bottom Right – P3

Figure 8.7 presents the cumulative distributions for in vessel hydrogen production. In each case, main steam line failure exhibits a low hydrogen production cluster at ~250kg and a high hydrogen production cluster at ~400kg. The span of hydrogen production results is narrower early but grows consistent with Replicate 1 toward the end of the simulation. Additionally, the realization 13 hydrogen value coincides with the centroid of the early distributions but tends toward the upper tail of the perturbation distributions late in the accident. Each perturbation continues the trend in Replicate 1of hydrogen production at lower core plate failure spanning the entire hydrogen production at end of simulation.

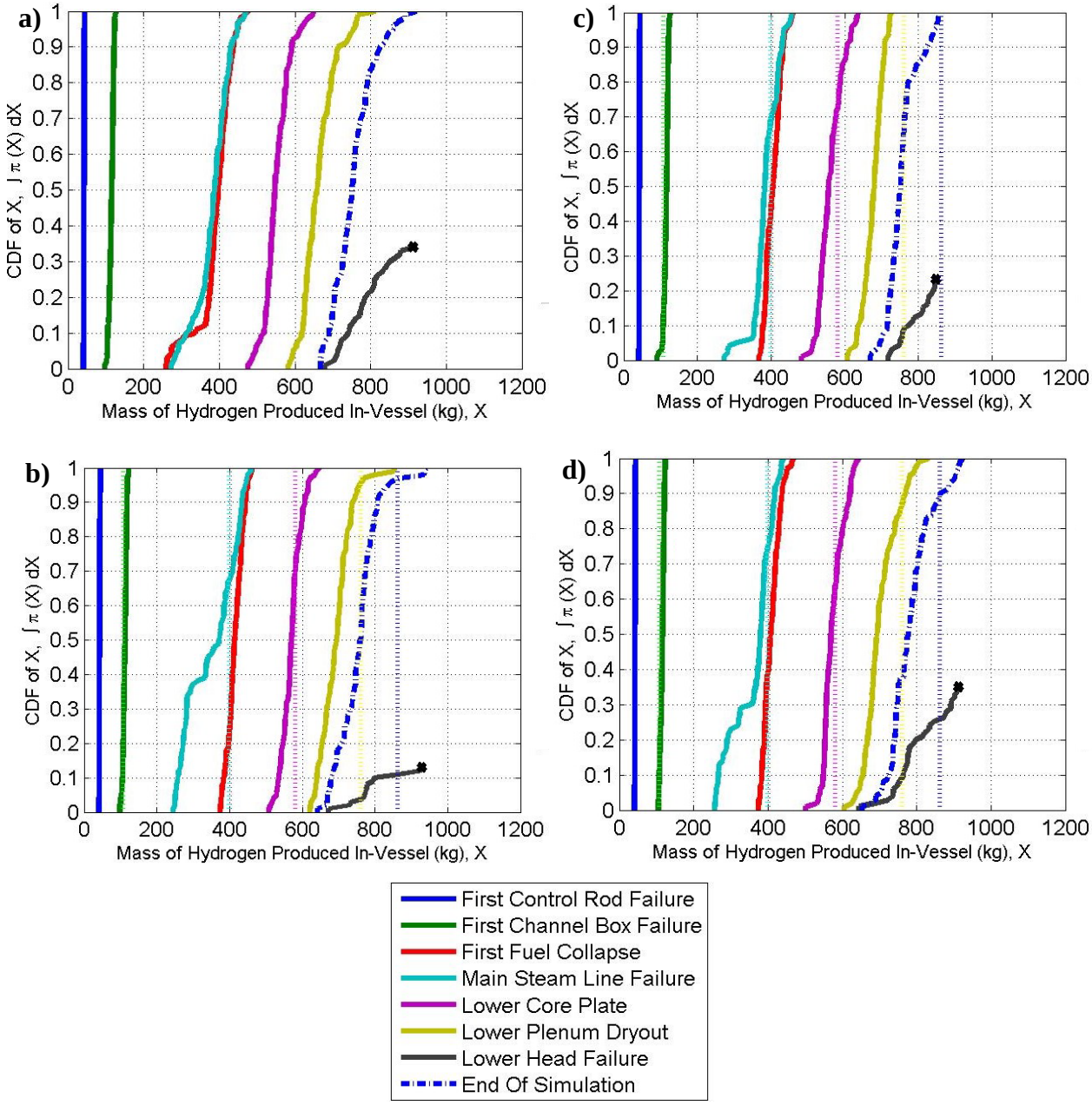

Figure 8.7 – Hydrogen Production Cumulative Distribution Functions: Top Left – Replicate 1, Top Right – P1, Bottom Left – P2, Bottom Right – P3

Figure 8.8 presents the cumulative distributions for fraction of intact fuel mass. Because main steam line failure occurs before first fuel failure in realization 13, the fraction of intact fuel at main steam line failure is ~1.0 for all perturbations. Replicate 1 and the three perturbations all have potential ring failure discretization in the lower core plate failure and lower plenum dryout curves. In general, it is interesting how similar the intact fuel mass curves are between Replicate 1 and the three perturbation cases at each timing FoM. Potentially, the sampled parameters for this UA had minimal effect on the core degradation progression pathway.

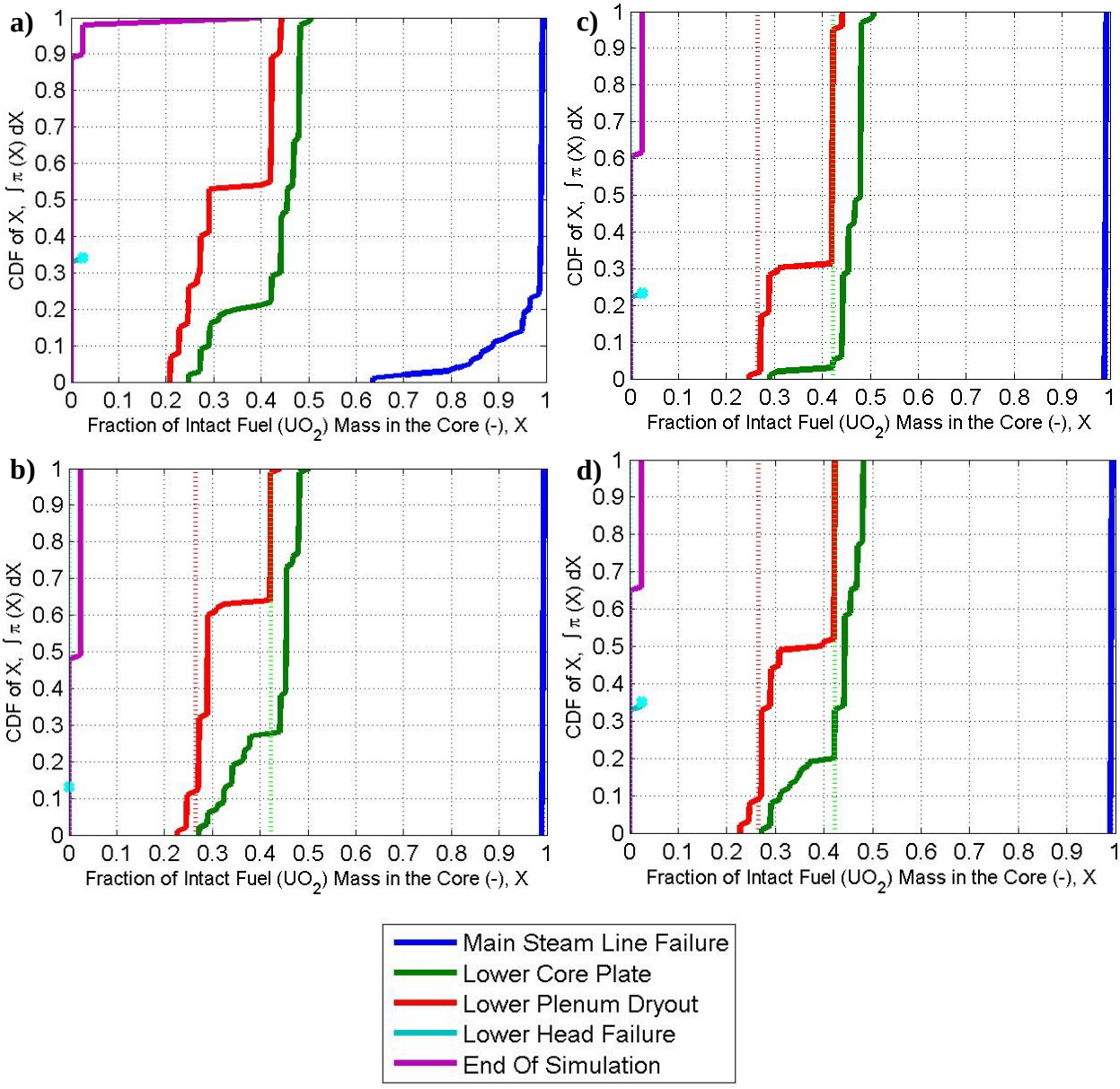

Figure 8.8 – Intact Fuel Mass Cumulative Distribution Functions: Top Left – Replicate 1, Top Right – P1, Bottom Left – P2, Bottom Right – P3

8.3 Summary of MELCOR Output Stability Insights

MELCOR results are stable early in the accident sequence before non-linear and semi-mechanistic core degradation and relocation models are allowed to reduce output stability. All three perturbation methods appear to exhibit the same influence on the distribution of output FoMs. Changes in time step throughout the core degradation models are predicted to have the most direct impact on the progression of core degradation. Small changes in input parameters, changes in the maximum allowable time step, and changes in the flow path arrangement all have the potential to impact the time step taken during core degradation.

P2 (maximum time step) shows that late stage variability in hydrogen production appears to exhibit a constant variance with only a minimum trend in the mean as a function of maximum time step above 0.02 seconds. This implies that the impact of maximum time step stability on MELCOR outputs can be approximated by taking small samples around a nominal (e.g. 0.1 to 0.2 s for large LWR models) maximum time step. This insight can be extremely important when the impacts of MELCOR stability need to be assessed but constraints prevent consistently varying the maximum time step over orders of magnitude.

9 SUMMARY AND CONCLUSIONS

The Volume II of the 1F1 UA explored how common statistical techniques can be utilized to gain insights into severe accident modeling using system codes such as MELCOR. This chapter summarizes the key insights from this report.

9.1 General Accident Insights

The 1F1 UA suggests that water injection at 15 hours would likely have been expected to successfully quench the rubbilized reactor core without failure of the lower vessel head. While lower head failure was not ruled out by our simulated results, lower head failure was only predicted in approximately 40% of the MELCOR simulations. All simulations that resulted in lower head failure before 15 hours predict that most of the fuel rods (i.e., >98%) are no longer intact in the core region.

9.2 Statistical Analysis Summary

Cumulative distributions of output variables are a useful alternative to simple horsetail plots, especially when non-linear temporal effects are examined. Horsetails do not explicitly tell the analyst when events happen, nor do they indicate potential overlap in events, as occurred in Replicate 1 between main steam line failure and first fuel failure.

Scatter plots are fundamental for understanding an uncertainty analysis, but in general there are too many potential scatter plots that can be created to be very helpful to an analyst. Regression techniques are useful in determining predefined trends (e.g., trends that are linear or can be made linear through transformations) in the data. Once trends are highlighted in the regression analysis, it is advisable to examine the scatterplots of the variables that are identified in the regression analysis to truly verify the existence of the suspected trends.

When employing such techniques, especially on smaller sample sizes, it is important to verify the results against additional samples to determine if the regression is describing the population or a combination of the population and inherent variability in the sample. The regression models where used in this report to 'fit' (i.e., regression or meta-model) to a set of training data (FoMs). These meta-models were subsequently tested with new sampled data to evaluate if the meta-models were able to predict new FoMs generated from same exact model, parameters, and distributions. This new testing data is essentially the same data used to train the original regression models, but use a different random number seed for the parameter sampling.

Linear regression tends to over-fit the MELCOR predicted FoMs, even with high R^2 fits created with low p-value terms. In some cases, these regression models can even explain less of the variance when applied to a new sample of data. When multiple regressions were conducted and varying R^2 estimates were produced, the lower R^2 regressions consistently performed better when applied to new datasets. Due to variability generated from discrete events inherent in severe accident system modeling, a questioning approach is always advised when explaining MELCOR outputs and their variability.

The automated regression results from the 1F1 UA produced some interesting high level results:

Mass Ejected from the Lower Head

The Replicate 1 regression identified the *dT/dz* model's relative weight of historical flows, debris falling velocity, and minimum porosity as potential predictive variables for the mass of material ejected from the lower head at the time of lower head failure. After comparing

these results to those from other replicates, none of these three variables were predictive in nature. Instead, radial debris relocation time constant was the only term that consistently described a fraction of the variance associated with this FoM. See section 6.4.4 for more information.

In general, regressions for mass ejected from the lower head have low predictive ability and are subject to regressing inherent variability, potentially due to either the reduced sample size or the nature of the parameter. The variability in training R^2 values between samples is a potential warning sign for the creation of non-predictive meta-models. If further studies of mass ejected from the lower head were conducted, increasing the sample size does not appear to help the predictive nature of regressions. Additionally, rank regressions appear to do a better job than raw regressions for this FoM.

Cumulative Hydrogen Production in Vessel

Replicate 1 predicted a consistent influence of molten Zircaloy breakthrough temperature on hydrogen production throughout the accident progression. This insight is in rough agreement with previous UAs conducted at SNL [9.1]. Additional variables varied in their inclusion in the rank and raw dependency tables throughout the accident progression, including: radial solid debris relocation time constant, debris falling velocity, time at temperature, and debris quenching heat transfer coefficient.

Replicate regression results were examined further for the time of lower plenum dryout. In general, rank regressions had more consistent, but not necessarily better, predictive ability than raw regressions. While the spread of R^2 from sample to sample was not as wide as was seen with mass ejected from the lower head, the same trend of models with higher R^2 producing lower predictive R^2 was noticed. For predicting hydrogen at lower plenum dryout, the only two terms that were consistently included in highly predictive meta-models were molten Zircaloy breakthrough temperature and the *dT/dz* model's characteristic coupling time.

Intact Fuel Mass Fraction

Replicate 1 predated a consistent influence on molten Zircaloy breakthrough temperature and effective fuel failure temperature on intact fuel mass fraction throughout the accident sequence. As can be seen from the cumulative distributions for intact fuel mass fraction, the core degrades in discrete 2D nodes (i.e. axial levels and rings), causing step changes in response and thus limiting the applicably of linear regression analysis.

Replicate regression results were examined further for the time of lower core plate failure. The same general predictive trends found for intact fuel mass and cumulative hydrogen production were also found for intact fuel mass fraction. For predicting intact fuel mass fraction, molten Zircaloy breakthrough temperature and effective fuel failure temperature were consistently resolved in predictive meta-models.

Additionally, the perturbation results were interesting in that general trends found for FoMs in the main uncertainty analysis, other than fuel failure timing, were also noted in the perturbation cases. A key takeaway from the perturbation analysis is that both before and after core degradation, output FoM variances appear to be a fairly constant function of dt_{max}. Thus, future MELCOR analysis may be able to explore a very small range of dt_{max} values to determine if the desired change in output FoMs is robust to the analyst's selection of dt_{max}.

9.3 High Level Conclusions

Detailed conclusions from the statistical analysis can be found in Section 9. The key takeaways from the statistical analysis are as follows:

The results of the 1F1 analyses demonstrate that MELCOR simulation outputs that occur after discrete events (e.g., valve chatter, core material relocation) experience low numerical precision. Numerical precision can produce variability on the same order as the epistemic uncertainties, thus making direct comparisons of results (e.g., tradeoff studies) difficult to defend. Only inputs which can exhibit enough influence on output FoMs to rise above the inherent precision can be isolated via sensitivity analysis. An example of high influence variables are molten Zircaloy breakthrough temperature and radial solid debris relocation time constant.

In general, only R^2 values less than 0.5, and as low as 0.2 for mass of material ejected from the lower head, were achievable with either linear or rank regressions. Furthermore, when multiple regressions were conducted on different samples of the same FoM, the lower models with lower R^2 on the training data exhibited greater predictive ability on testing data sets. In general, only approximately one third of the 15 sampled variables (i.e., radial debris relocation time constant, molten Zircaloy breakthrough temperature, time at temperature relationship for fuel collapse, and the *dT/dz_CVH* numerical parameter) were resolved in regressions that were shown to have predictive ability for the three FoMs examined in detail. Other terms, such as debris falling velocity, were potentially predictive but also appeared prominently in regression that demonstrated poor predictive ability.

The magnitude of inherent variability can lead sensitivity analysis techniques (e.g., regressions) to ascribe trends to the inherent variability instead of or in addition to physical trends. Investigations of identified trends through validation exercises on new samples and/or examination of scatterplot results are required to have confidence in the results of more advanced sensitivity analysis techniques. For example, during validation of the intact fuel fraction at the time of lower core plate failure, cladding thickness corresponding to mechanical weakening and dT/dz model parameters were only regressed in regression models which presented poor predictive ability. Thus, these terms were likely fitted to inherent variability in the samples and not actually indicative of the trends in the sampled population.

Linear regressions can be useful when interpreting UA results, but care must be taken not to conflate major event discontinuities. For example, regressions at 15 hours into the accident when water injection begins performed poorly because 30-40% of the simulations had experienced lower head failure and the remainder of the simulations still had all core material contained in the lower head. Similarly, Replicates 1, 2, 3, and Uniform all experienced approximately 10-20% of the simulations where fuel rods started to collapse before the main steam line failed. Scatterplots showed that outputs for time of first fuel failure and main steam line failure experienced bifurcations which subsequently impeded the regressions. Isolating these sequence variations should greatly increase the suitability for regression of the output data at these timing FoMs.

Physical FoMs are not the only FoMs affected by the MELCOR output inherent variability. Event timing (i.e., timing FoMs) was also affected. While the perturbation study did not vary pre-vessel failure timing FoMs by over an hour $\left(\frac{\Delta t_i}{\bar{t}_i} \leq 15\%\right)$, the timing of vessel failure is extremely uncertain. For example, the 1F1 UA simulations were ended at 15 hours due to the initiation of water injection at that time. During the first 15 hours, the three perturbations studies

predicted anywhere from 15-35% of the simulations would result in lower head failure, with the earliest lower head failure time of approximately 12.9 hours. The realization from which the perturbations were conducted did not predict lower head failure. The magnitude of variability regarding the occurrence of lower head failure before operator action epitomizes the necessity of conducting a full and rigorous uncertainty analysis when evaluating the effectiveness of human intervention to prevent major bifurcation points during accident progression in MELCOR.

9.4 Future Analysis

As with any study, many approaches for analysis were outside the scope and/or budget of the project. This section describes analysis techniques which were unable to be included in the Fukushima UA but which may be considered for inclusion in future analyses.

9.4.1 Improvements in the Molten Zircaloy Breakthrough Temperature

As described in Section 2.2.1, S/Q simulation data from two erosion and one stress-induced failure pathway were used to update the Peach Bottom prior distribution and create a beta distribution for use in the Fukushima UA. While optimally the MELCOR eutectics model would operate efficiently and predict the breakthrough temperature mechanistically, the probabilistic meta-modeling approach may still be improved.

Instead of using both failure pathways to update the same beta distribution, each failure pathway could have its own distribution;, starting with the same Peach Bottom inspired prior distribution and updated with the appropriate failure data. If each distribution is sampled separately, breakthrough would occur at the lower sampled temperature.

9.4.2 Regress on Event Timing

In addition to regressing on physical FoMs, regressions on the timing FoMs themselves may be insightful. Care must be taken for early timing FoMs as low variability in failure timings can lead (and has led) to infinite loops in the stepwise regression algorithm if inclusion and exclusion terms are not selected appropriately.

9.4.3 Advanced Regression Techniques

The Peach Bottom UA used the following three regression techniques to parse the UA output: rank regressions, recursive partitioning and spline regression. Even though the Fukushima UA does not have the main steam line vs safety relief valve failure bifurcation that was seen in the Peach Bottom UA, recursive partitioning and spline regressions may still yield insightful results [9.1][9.2]. When using either the automated techniques used in this report or the automated techniques used in the Peach Bottom UA, care must be taken to avoid their limitations, such as over fitting, which decreases the predictive strength of the meta-model [9.3]. Human examination of either (or both) of the following concepts are important:

- Assumptions of the regression techniques are not (severely) violated and/or
- Insights gained from the training sample are applicable to the greater population of potential results.

Though regression model assumptions are difficult to validate, the extent to which the assumptions are violated affects the likelihood that the model will produce a reliable explanation

of system variance. A meta-model that violates the assumptions of the regression technique employed can still provide insight, but inference based upon the model should be done with care.

9.4.4 Sample Size Study

While the hydrogen and intact fuel fraction regressions did not improve dramatically when Replicate 1 and 2 were combined, improvement was seen for mass of material ejected from the lower head. A more comprehensive sensitivity study should be conducted on the impact of sample size on regression quality. These studies can be conducted by:

- Running more simulations per sample until regression convergence occurs,
- Conducting bootstrap regressions on 70% of Rep 1-3 and examining the consistency of produced meta-models, and
- Employing the Top Down Coefficient of Concordance (TDCC) on regression outputs from the above two methods to quantify convergence [9.4].

9.4.5 Precondition Regressions

Regressions which demonstrate predictive behavior often include terms that were not initially regressed in that sample. Preconditioning the stepwise regression for each sample with a handful of predictive terms may increase the regression stability between samples. The stepwise regression can remove these preconditioned terms if they turn out not to be supported by the data, but preconditioning may force the regression to a global minimal error instead of a local minimal error solution.

9.4.6 Update Dependency Tables After Validation Exercise

The dependency tables presented in this report were constructed from Replicate 1. The validation effort showed that regressions on Replicate 1 were not often descriptive of population trends. Validation efforts should be conducted for each combination of timing and physical FoMs and the dependency tables should be updated with only trends that were descriptive of the population, not the sample.

9.4.7 Examine Other Physical FoMs

In general, FoMs such as iodine and cesium release dominate the risk to the public from a reactor meltdown. Thus, examinations of these FoMs would be informative to some decision-makers. The phenomenology important to the production, release, and transport of radionuclides may be different than the phenomenology that is important to hydrogen production, core integrity, and/or material ejected from the lower lead.

9.4.8 Run Regressions Conditional on Sequence Variations

While the Fukushima UA did not experience the dramatic sequence bifurcations found in the Peach Bottom UA, some sequence variably was experienced regarding the order of main steam line and fuel failure, as well as if the lower head failed. These sequence variations can be studied, and their impacts on other timing FoMs, can be studied in more detail.

9.4.9 Explore Additional Sequence Variability

The 1F1 UA focused solely on system depressurization through main steam line failure. Other explanations for primary system depressurization, such as SRV failure, should be explored in follow-on analyses. Some example sequence variability may include:

- Accident progression after emergency core injection; specifically focusing on injection rates/timings
- Various modes of containment leakage; containment venting.
- Various treatments of reactor building explosion and assumed leak paths for radionuclides to the enviornment.
- Significantly different burnup and decay heat level (e.g. scram near BOC, EOC etc.).

9.4.10 Study the Marginal Distributions of Scatterplots

The Fukushima UA employed simple scatter plots to visually examine output data for trends. These scatterplots can also be viewed with the marginal distributions of both the X and Y variables. Once these marginal distributions are calculated, additional statistical checks can be conducted against both distributions to check for trends. An example scatterplot with marginal histograms from the P1 cases is found in Figure 9.1.

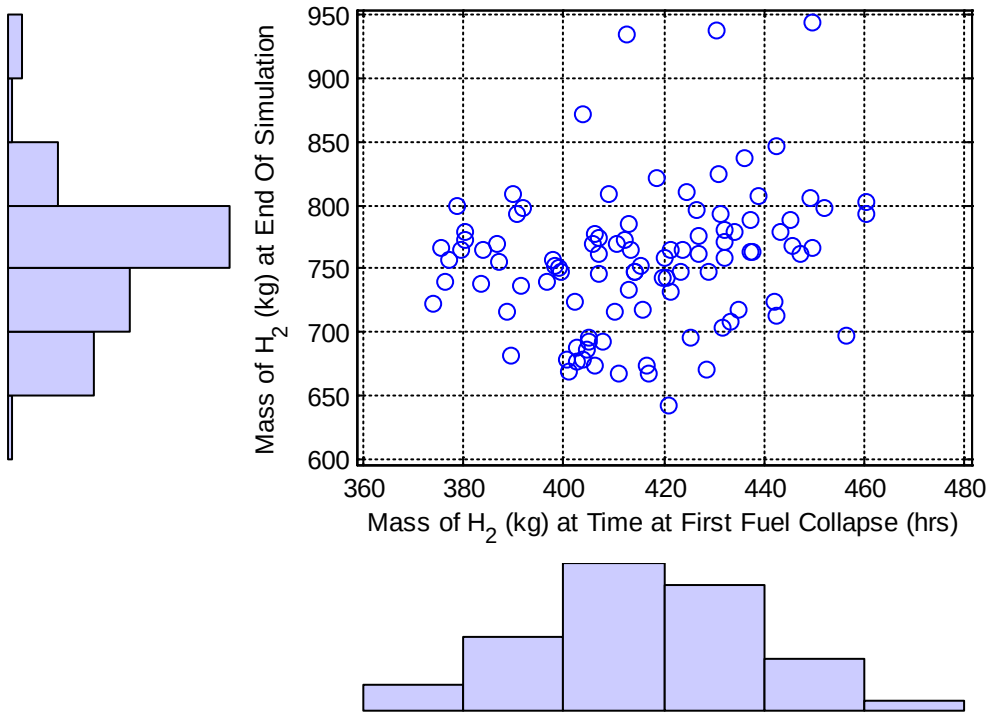

Figure 9.1 – Example Marginal Histogram Scatterplot from P1

9.5 References

[9.1] U.S. Nuclear Regulatory Commission, State-of-the-Art Reactor Consequence Analyses Project: Uncertainty Analysis of Unmitigated Long-Term Station Blackout of the Peach Bottom Atomic Power Station-Draft Report, NUREG/CR-7155, SAND2012-10702P,Washington, DC, 2012.

[9.2] J. C. Helton, F. J. Davis, J. D. Johnson, “A comparison of uncertainty and sensitivity analysis results obtained with random and Latin hypercube sampling,” *Reliability Engineering and System Safety*, **89**, pg. 305-330, 2005.

[9.3] JW Lee, SH Um,JB Lee,J Mun, H. Cho, "Scoring and staging systems using cox linear regression modeling and recursive partitioning," *Methods of information in medicine*, **45** (1), 37–43, 2006.

[9.4] C. B. Storlie, L. P. Swiler, J. C. Helton, C. J. Sallaberry, “Implementation and evaluation of nonparametric regression procedures for sensitivity analysis of computational demanding models,” *Reliability Engineering and System Safety*, **94**, pg. 1735-1763, 2009.

APPENDIX A: 1F1 TIME HISTORIES FROM 1F1 UA VOLUME I

The time histories from Replicate 1 and the Perturbation are reproduced below from Volume 1 of the 1F1 UA for convenience. Blue lines represent individual realizations, the red line represents the median of blue realizations, and the green line is the "median-like" realization (i.e., Realization 13 of Replicate 1) used as the base realization for the perturbation analysis.

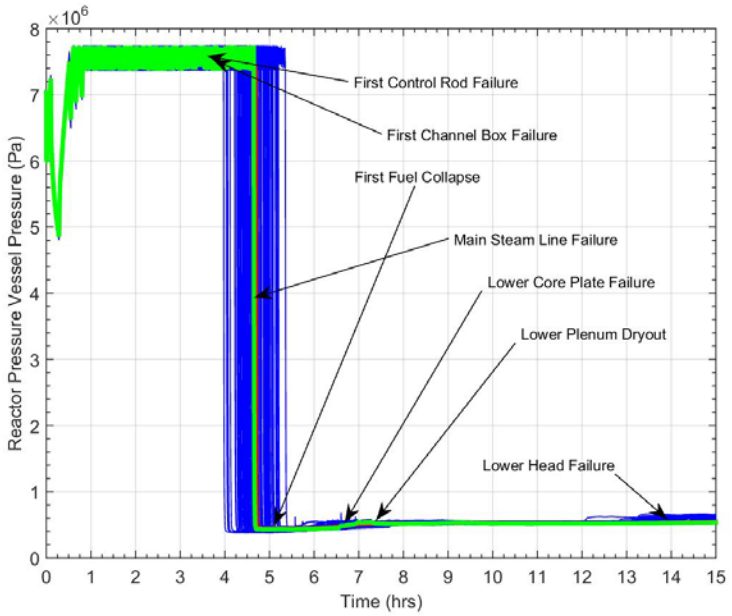

Figure A.1. Reactor Pressure Vessel Pressure (Replicate 1).

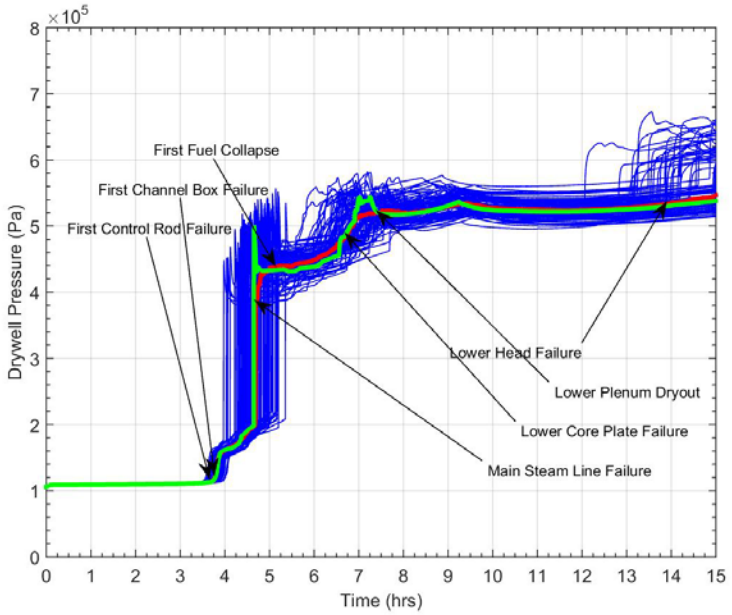

Figure A.2. Dry Well Pressure (Replicate 1).

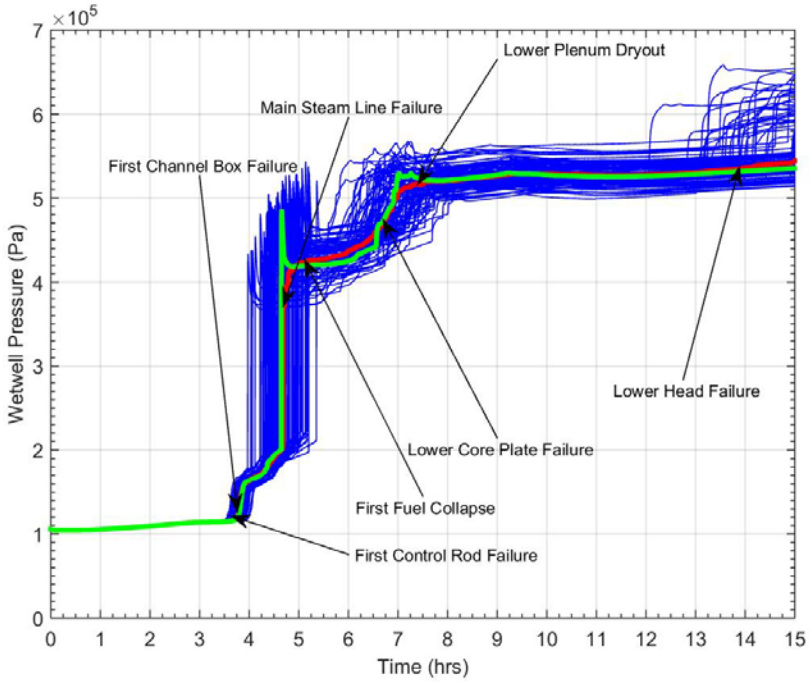

Figure A.3. Wet Well Pressure (Replicate 1).

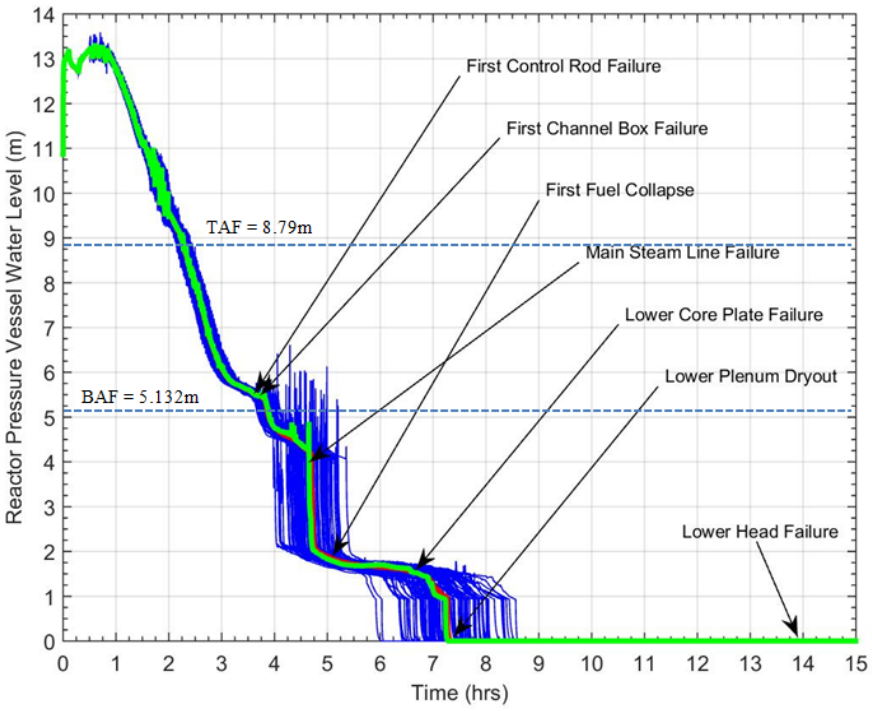

Figure A.4. Reactor Pressure Vessel Water Level (Replicate 1).

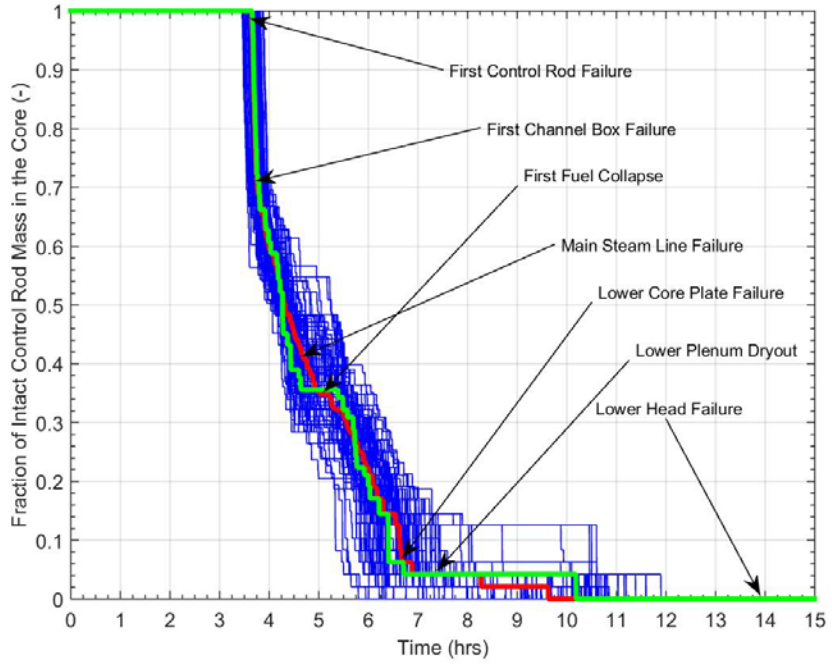

Figure A.5. Fraction of Intact C Rod Mass in the Core (Replicate 1).

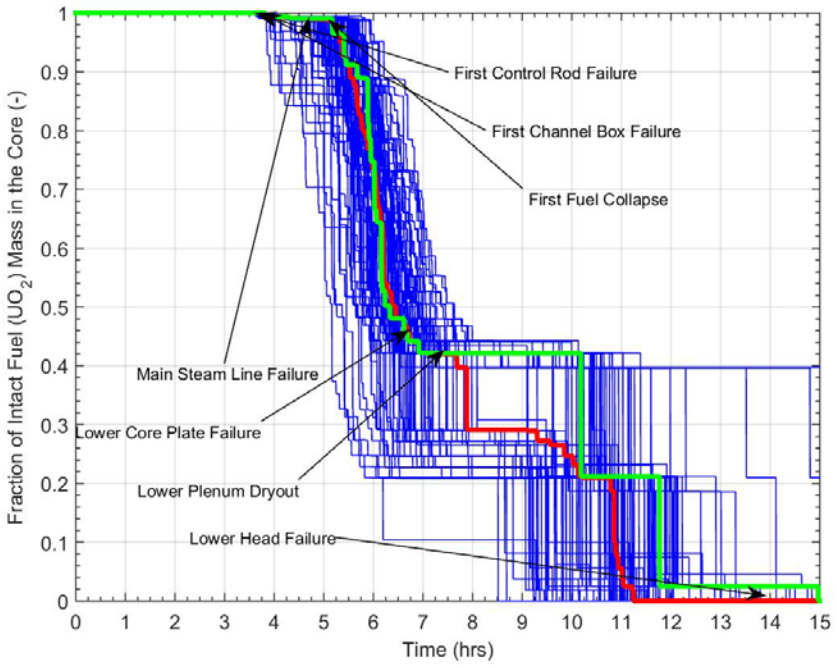

Figure A.6. Fraction of Intact Fuel Mass in the Core (Replicate 1).

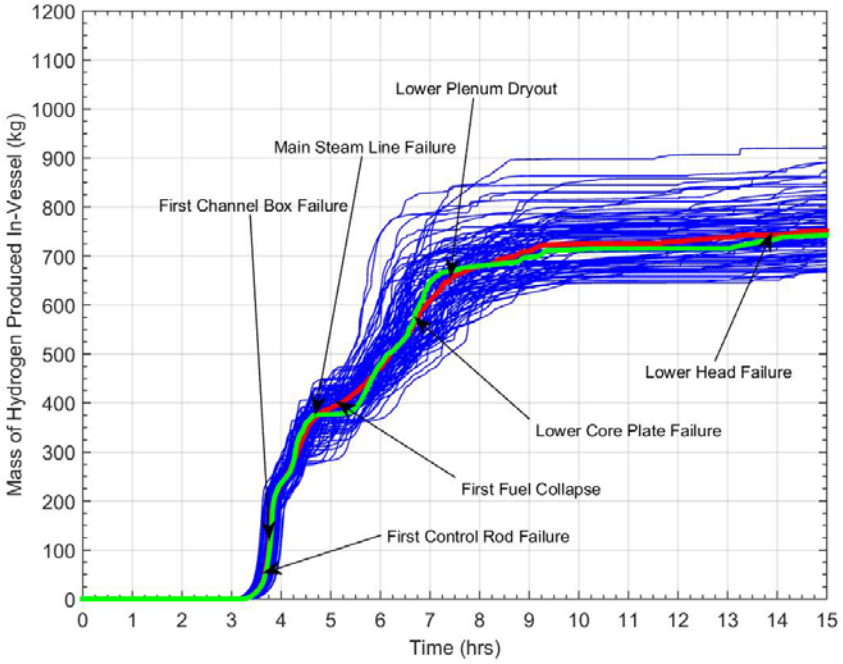

Figure A.7. Mass of Hydrogen Produced from In-Vessel Reactions (Replicate 1).

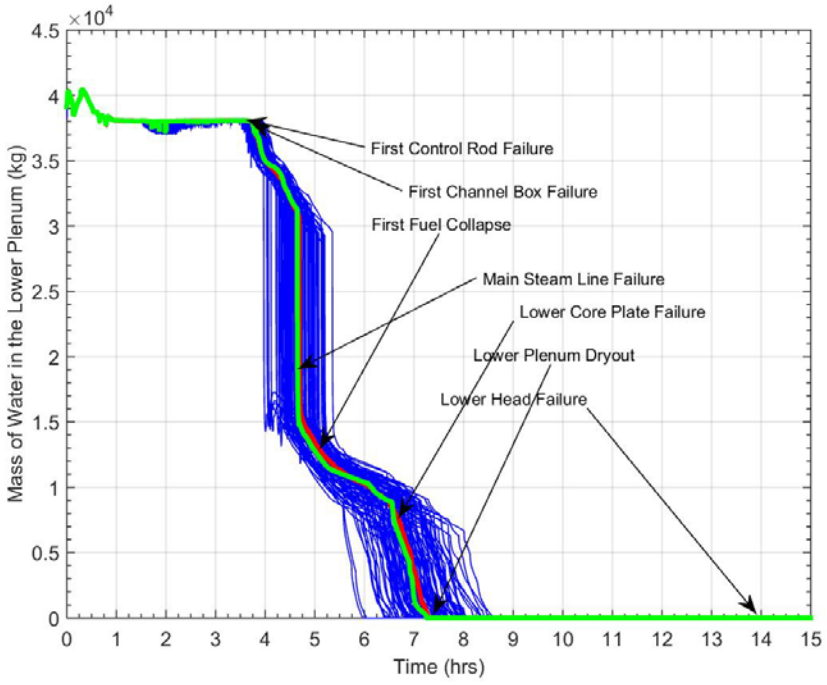

Figure A.8. Water Mass in the Lower Plenum (Replicate 1).

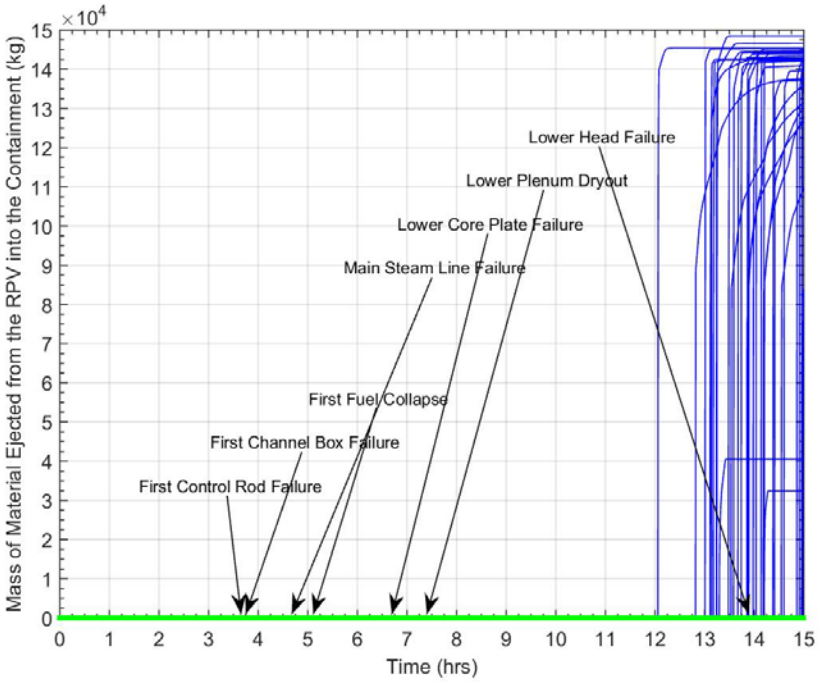

Figure A.9. Mass of Core Material Ejected to the Dry Well (Replicate 1).

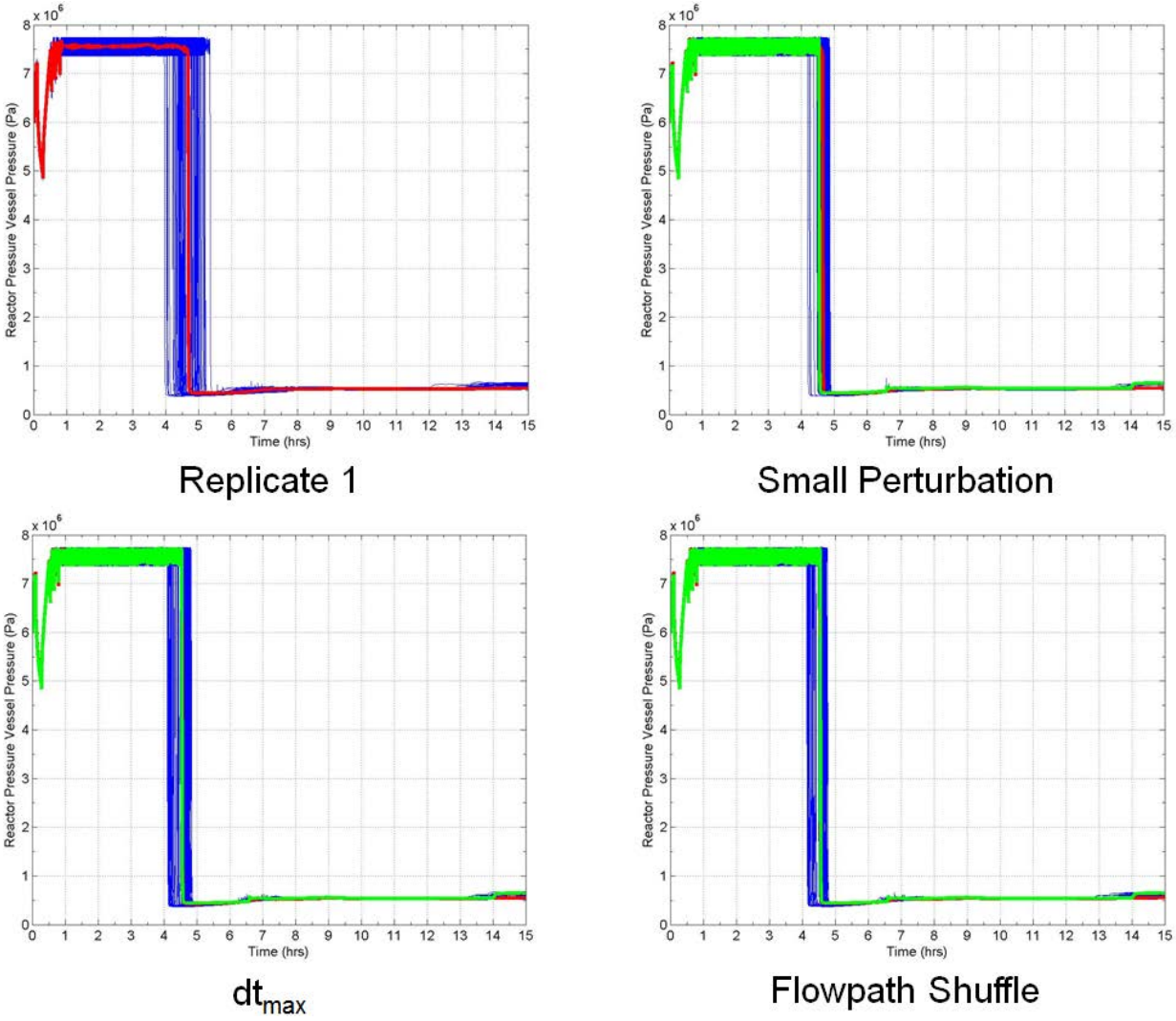

Figure A.10. Comparison of Perturbation Analyses and Replicate 1 Results (RPV Pressure).

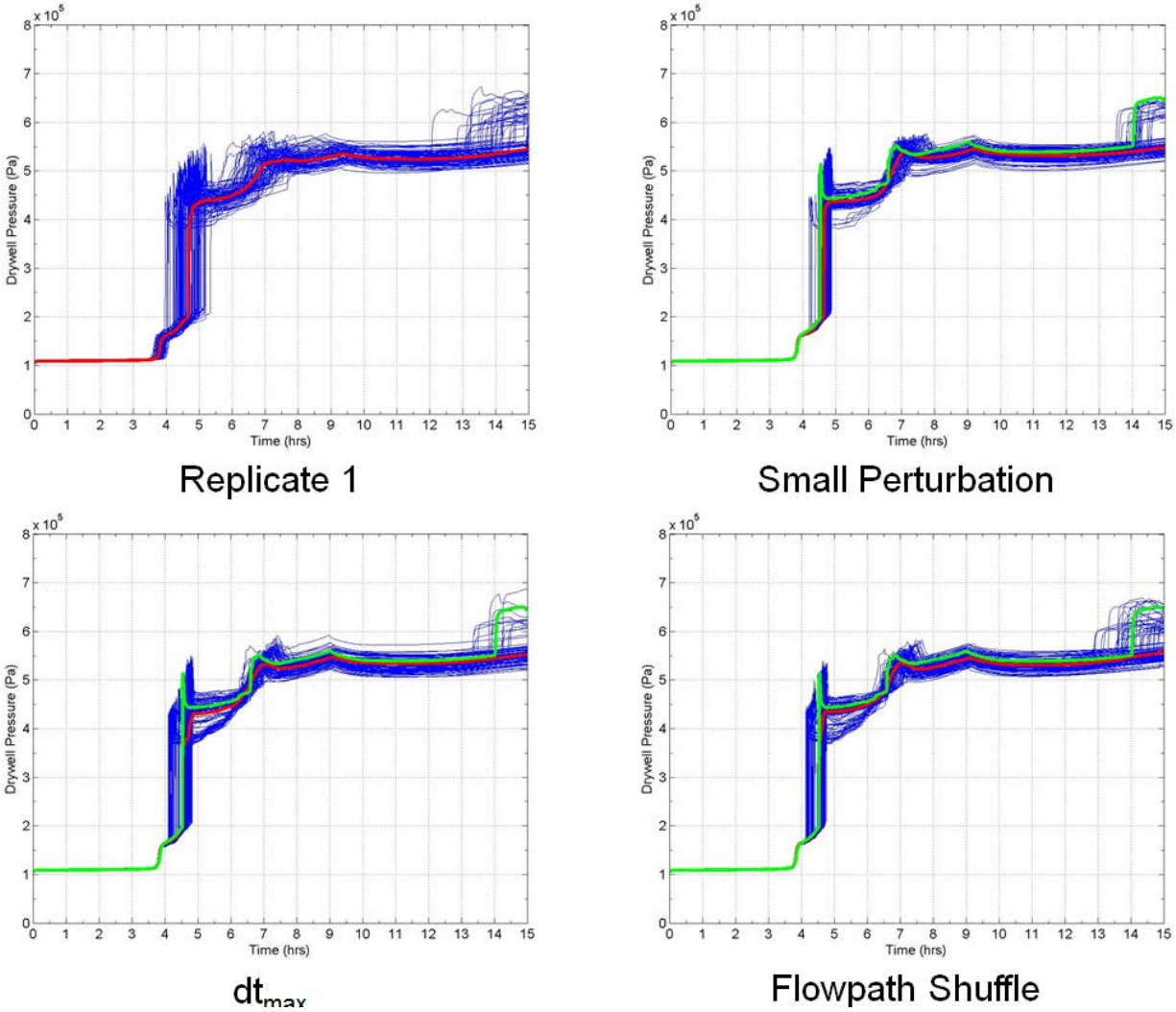

Figure A.11. Comparison of Perturbation Analyses and Replicate 1 Results (Drywell Pressure).

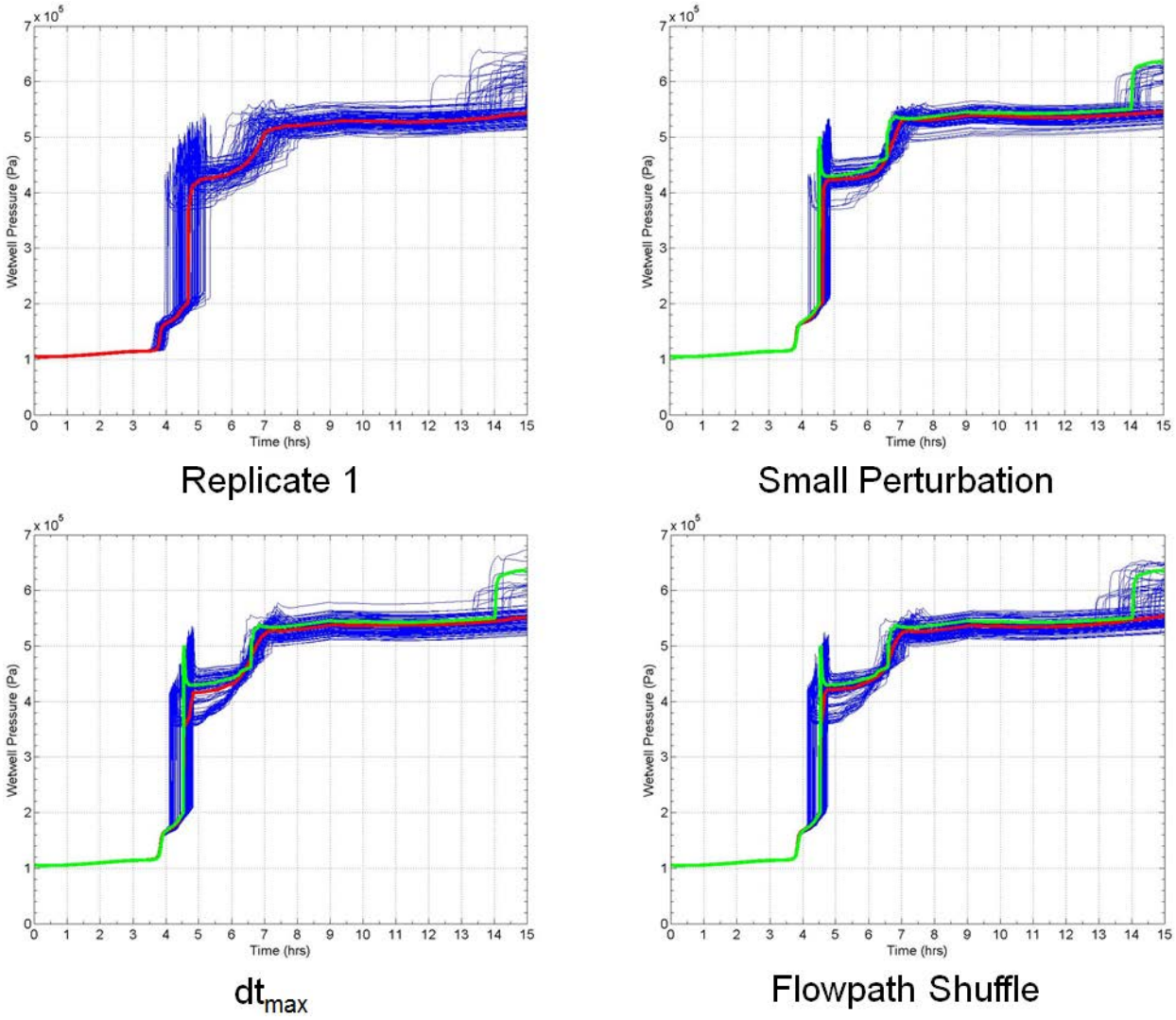

Figure A.12. Comparison of Perturbation Analyses and Replicate 1 Results (Wetwell Pressure).

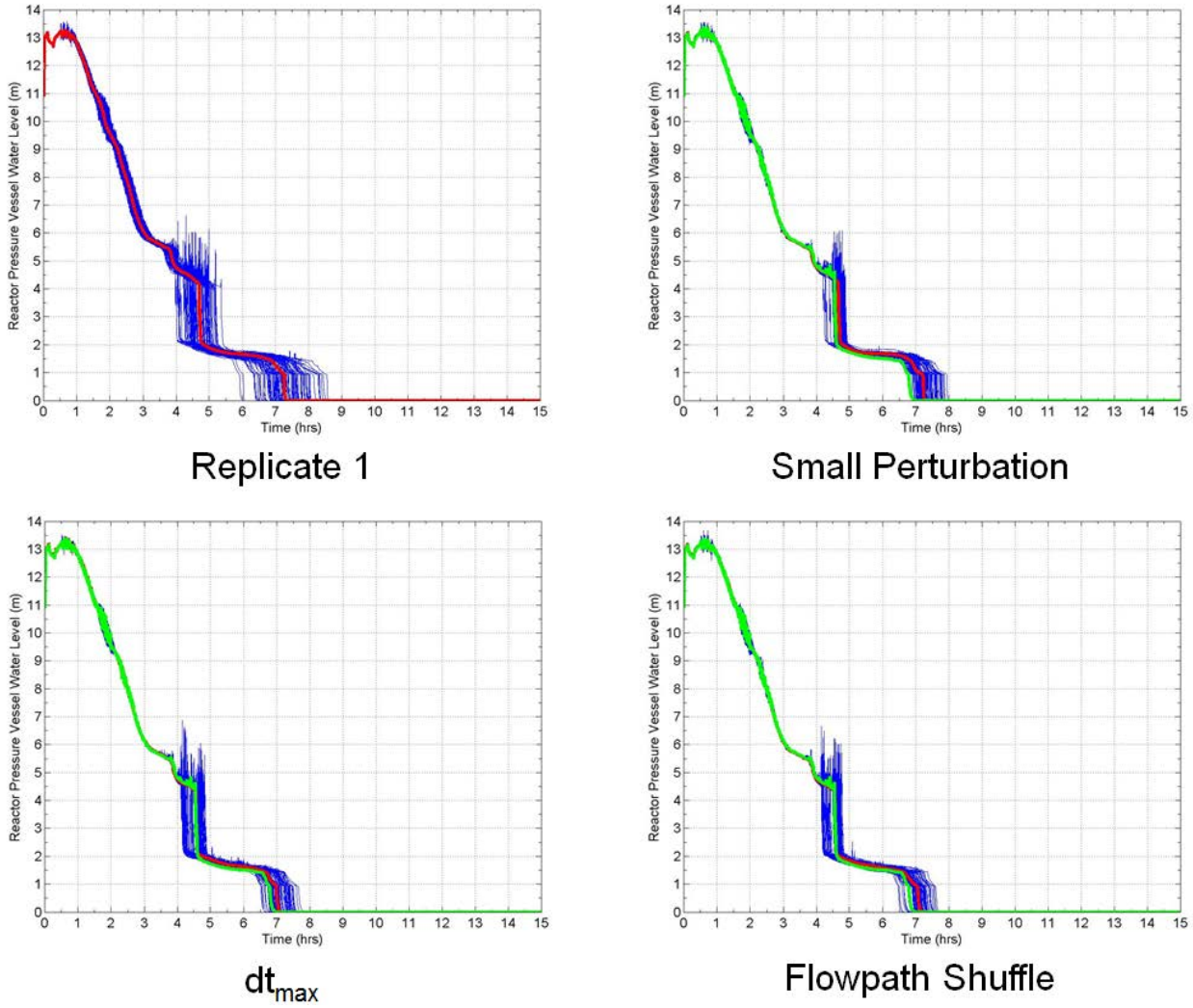

Figure A.13. Comparison of Perturbation Analyses and Replicate 1 Results (Reactor Pressure Vessel Water Level).

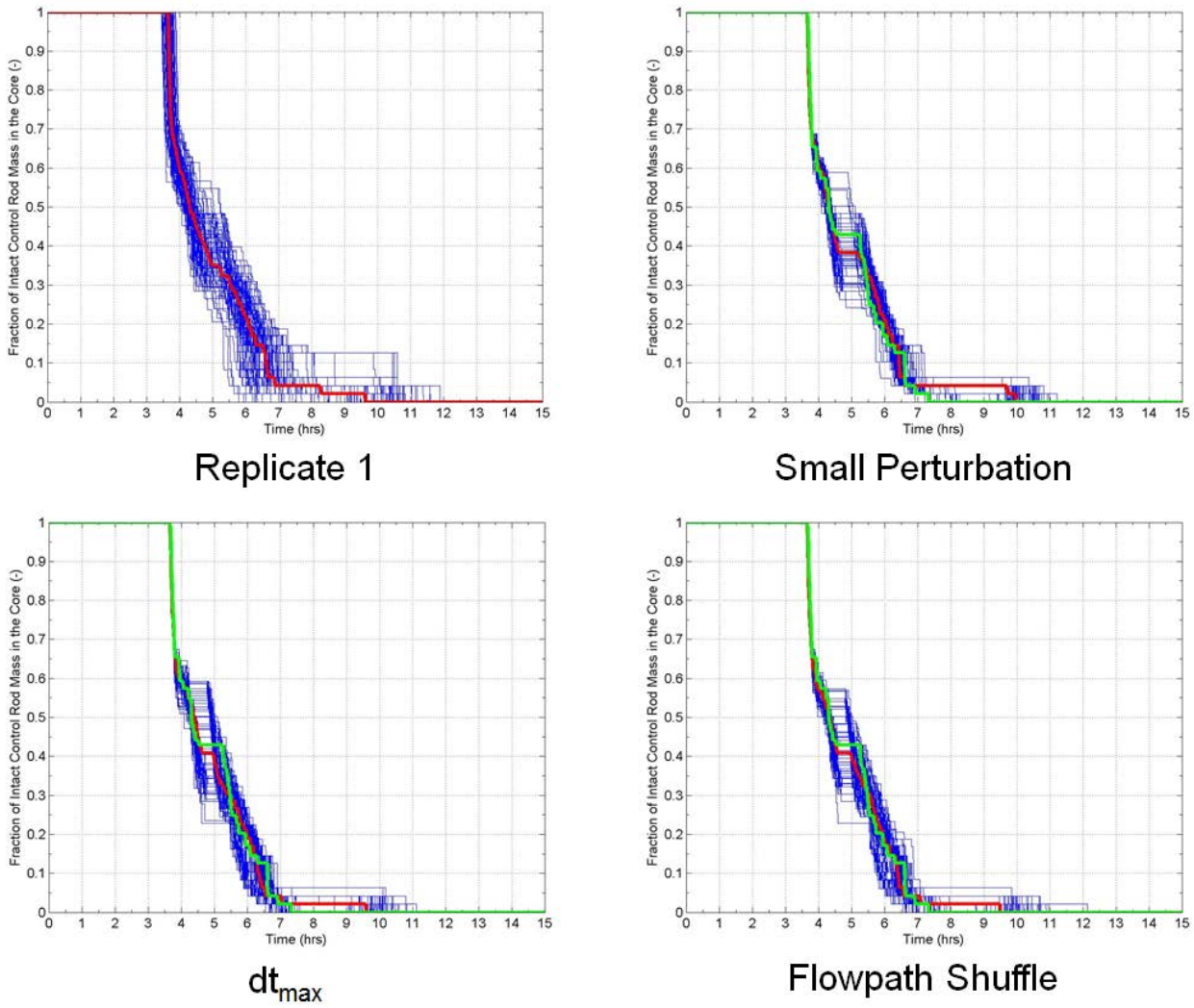

Figure A.14. Comparison of Perturbation Analyses and Replicate 1 Results (Fraction of Intact Control Blade Mass).

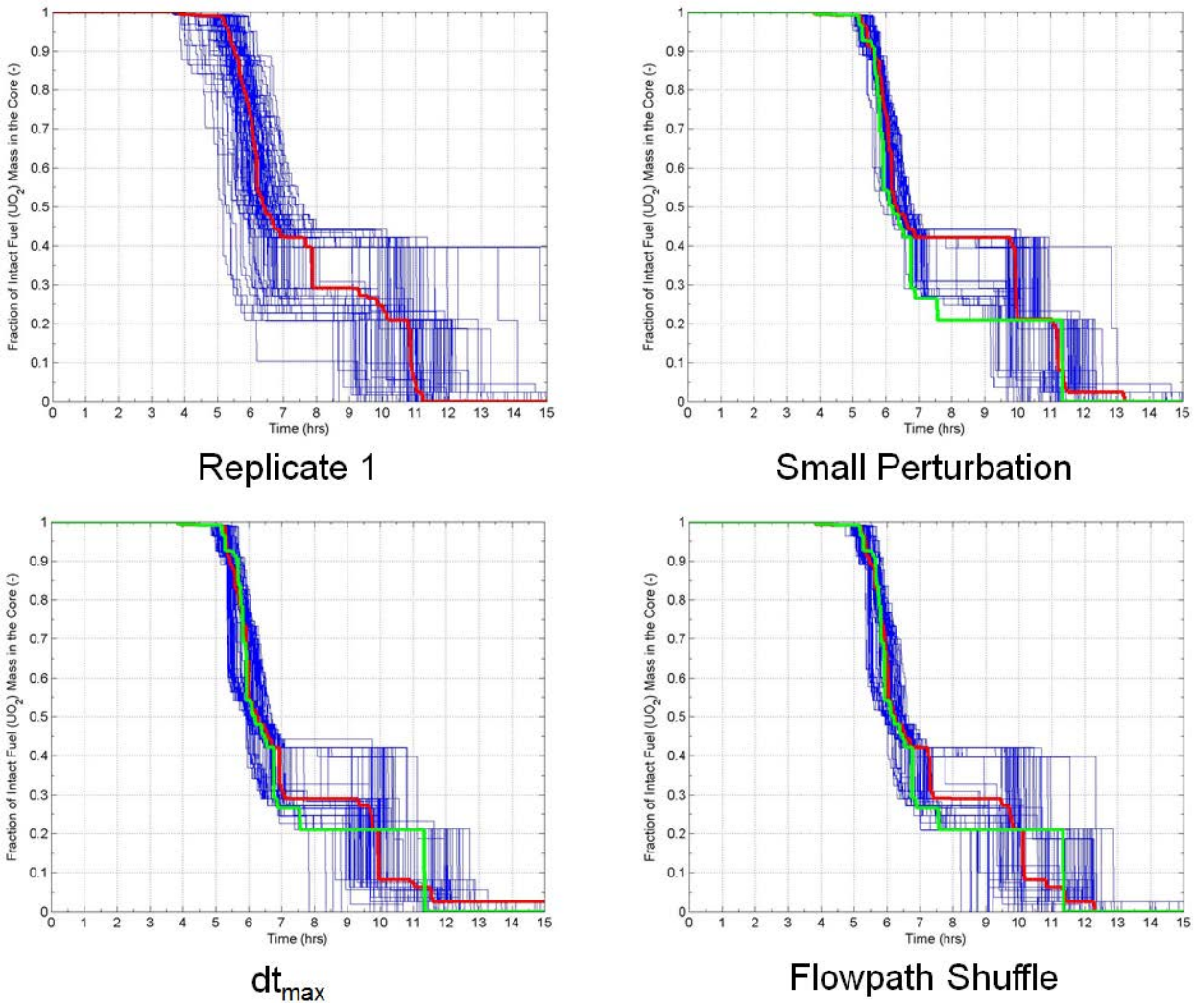

Figure A.15. Comparison of Perturbation Analyses and Replicate 1 Results (Fraction of Intact Fuel Mass).

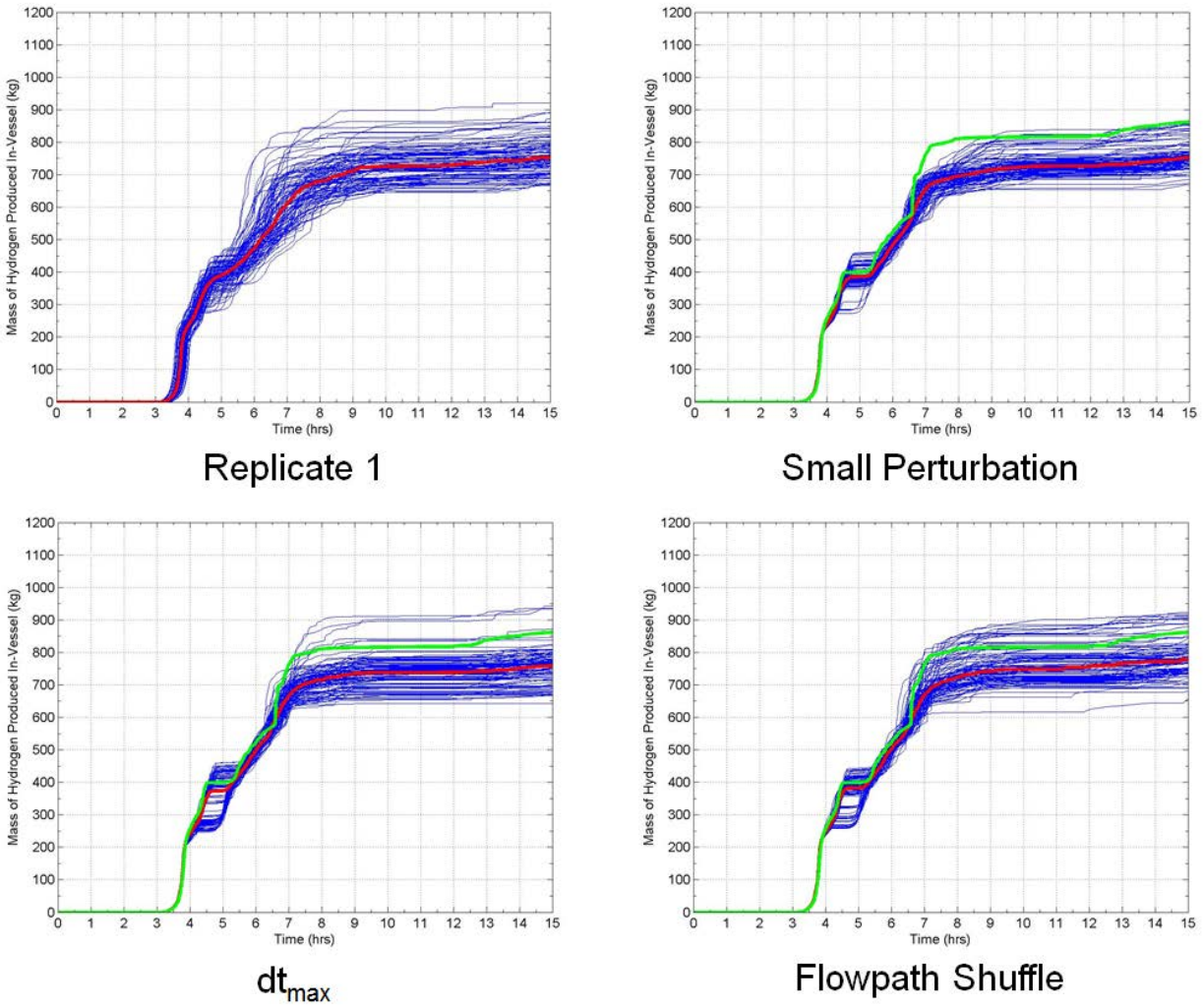

Figure A.16. Comparison of Perturbation Analyses and Replicate 1 Results (Mass of Hydrogen Produced In-Vessel).

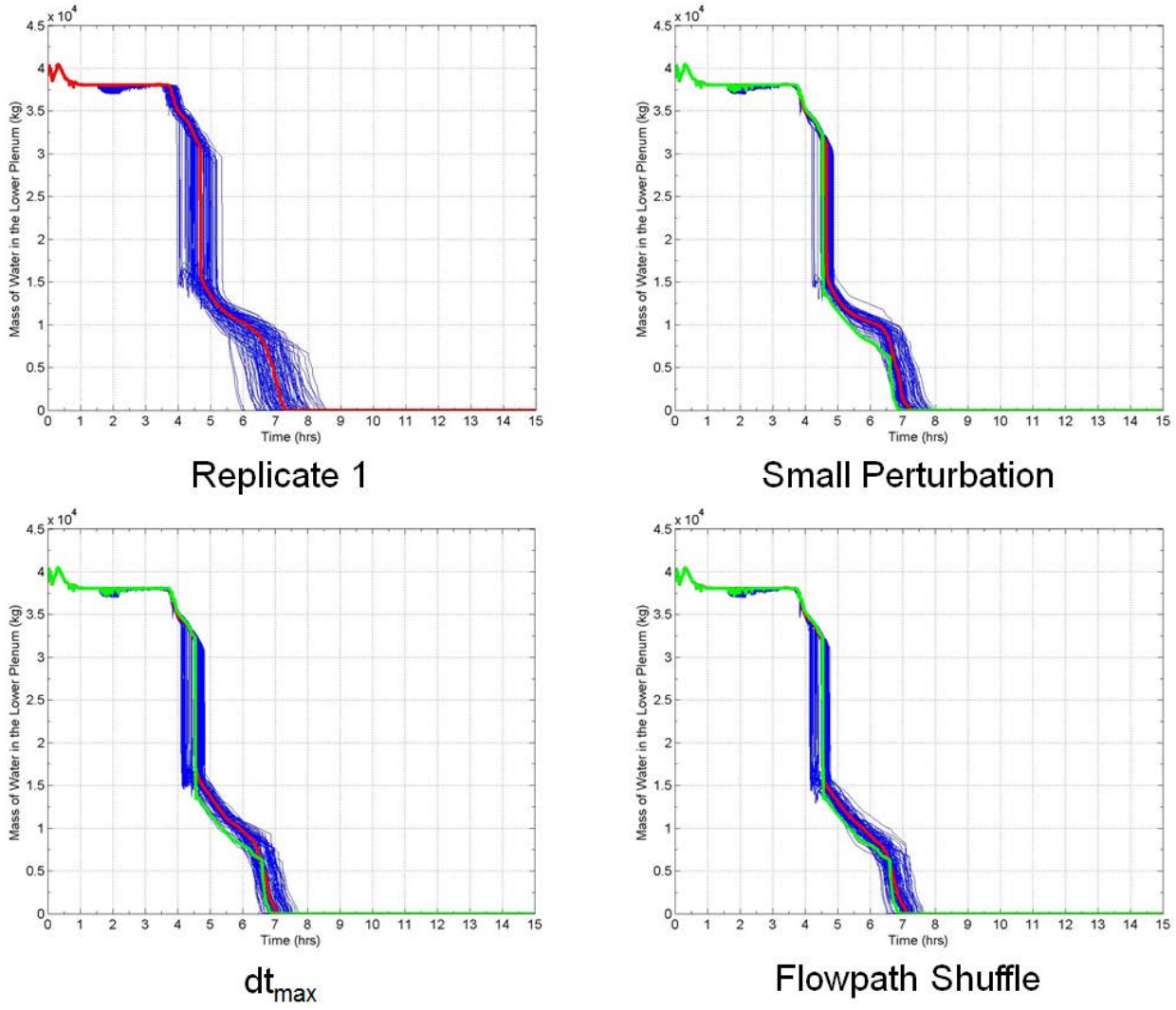

Figure A.17. Comparison of Perturbation Analyses and Replicate 1 Results (Mass of Water in the Lower Plenum).

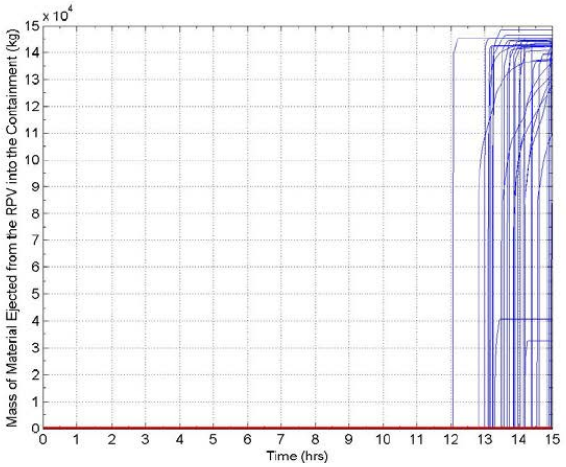

Replicate 1

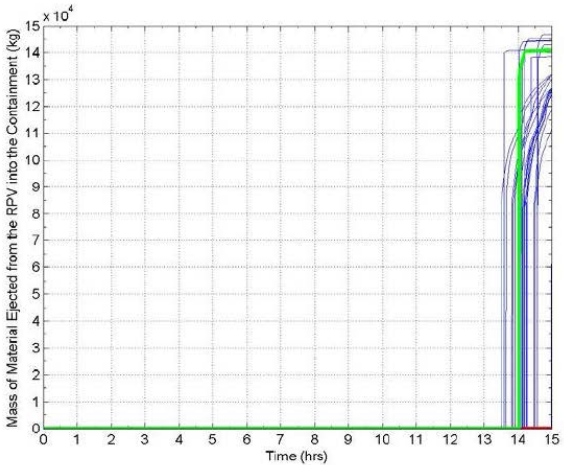

Small Perturbation

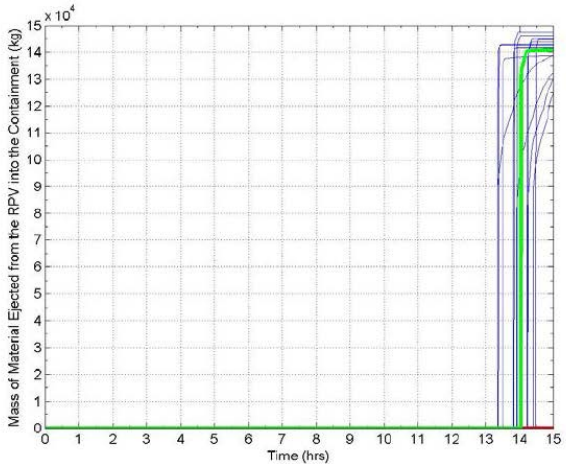

dt_{max}

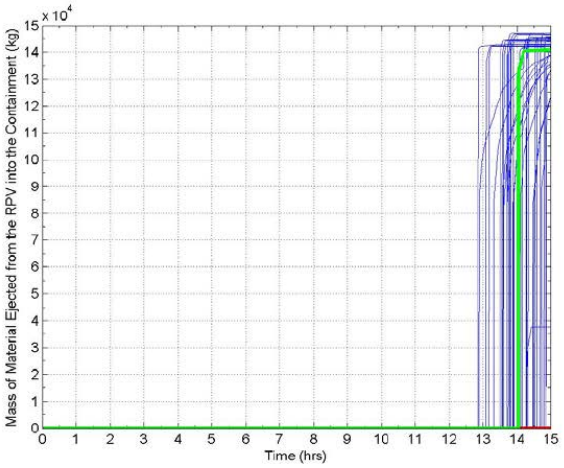

Flowpath Shuffle

Figure A.18. Comparison of Perturbation Analyses and Replicate 1 Results (Mass of Material Ejected).

APPENDIX B: DEPENDENCY TABLES

This appendix contains conditional dependency tables from raw and rank regression of the hydrogen and intact fuel mass fraction physical FoMs. For conditional dependency tables, instead of regressing to the vector **Y**, regressions are conducted on **Y'** which is defined as $\mathbf{Y-Y_i}$, where $\mathbf{Y_i}$ is the physical value from which the timing FoM is being regressed.

Table B.1, B.2 and B.3 show the R^2_{adj} fit statistics for in vessel hydrogen production and intact fuel mass fraction for various timing FoMs conditional on other timing FoMs. The highest R^2_{adj} regressions identified in these tables are examined in more detail in Sections A.1 and A.2 to determine if these conditional dependency tables can provide insight not discernable from the full dependency tables. No conditional dependency tables were able to be regressed for rank intact fuel mass fraction.

Table B.1 – Conditional Regression Fit Statistics for Raw Cumulative In-Vessel Hydrogen Production

Timing FoM	**First Channel Box**	**First Fuel Failure**	**Main Steam Line**	**Lower Core Plate**	**Lower Plenum Dry-out**	**Lower Head Failure**	**End of Simulation**	Averaged R^2
First Control Rod Failure	N/A	0.179	0.126	0.507	0.426	0.231	0.15	0.27
First Channel Box		0.175	0.115	0.504	0.417	0.38	0.151	0.29
First Fuel Failure			0.14	0.395	0.38	0.23	0.21	0.27
Main Steam Line				0.47	0.462	0.522	0.316	0.44
Lower Core Plate					0.17	0.178	N/A	0.17
Lower Plenum Dry-out						N/A	0.0799	0.08

Table B.2 – Conditional Regression Fit Statistics for Rank Cumulative In-Vessel Hydrogen Production

Timing FoM	**First Channel Box**	**First Fuel Failure**	**Main Steam Line**	**Lower Core Plate**	**Lower Plenum Dry-out**	**Lower Head Failure**	**End of Simulation**	Averaged R^2
First Control Rod Failure	N/A	0.2	0.395	0.484	0.483	0.362	N/A	0.38
First Channel Box		0.325	0.398	0.49	0.475	0.626	N/A	0.46
First Fuel Failure			0.0652	0.351	0.334	0.366	N/A	0.28
Main Steam Line				0.505	0.441	0.647	N/A	0.53
Lower Core Plate					0.124	0.496	N/A	0.31
Lower Plenum Dry-out						0.185	N/A	0.19

Table B.3 – Conditional Regression Fit Statistics for Raw Intact Fuel Mass Fraction

Timing FoM	**First Channel Box**	**First Fuel Failure**	**Main Steam Line**	**Lower Core Plate**	**Lower Plenum Dry-out**	**Lower Head Failure**	**End of Simulation**	Averaged R^2
First Control Rod Failure	N/A	N/A	0.176	0.262	0.137	N/A	N/A	0.19
First Channel Box		N/A	0.176	0.262	0.137	N/A	N/A	0.19
First Fuel Failure			N/A	0.275	0.102	N/A	N/A	0.19
Main Steam Line				0.082	0.06	N/A	N/A	0.07
Lower Core Plate					N/A	N/A	0.169	0.17
Lower Plenum Dry-out						N/A	0.09	0.09

B.1 Conditional Cumulative Hydrogen Production

Table B.4 presents the conditional dependency table for raw cumulative hydrogen production from first control rod failure. Only *MZBT* and *RSDR* were regressed, and in general the regression results are worse than the main dependency table. *MZBT* was regressed for every subsequent timing FoM, just as in the main dependency table.

Table B.5 presents the conditional dependency table for rank cumulative hydrogen production from first control rod failure. Only *MZBT* and *TaT* were regressed, and in general the regression results were worse than those summarized in the main dependency table.

B.2 Conditional Intact Fuel Mass Fraction

Table B.6 presents the conditional dependency table for intact fuel mass fraction from first control rod failure. Only *MZBT* and *TaT* were regressed, and in general the regression results are worse than the main dependency table.

B.3 Preliminary Conditional Dependency Table Conclusions

It was hypothesized that breaking the regression results into smaller segments would identify additional linear relationships between input variables and output FoMs. From the tables in Appendix A, the smaller time segments seem to reduce the suitability for regression of the output vectors. Indeed, while regressing to various timing FoMs shows promise, regressing between timing FoMs does not show as much opportunity for severe accident insight.

Table B.4 – Conditional Raw Cumulative Hydrogen Production Table from Main Steam Line Failure

	Lower Core Plate	Lower Plenum Dry-out	Lower Head Failure	End of Simulation
R^2 / R^2_{adj} / F-stat vs. Const./ p-val	.48 / .47 / 88.9 / 0	.47 / .46 / 85.9 / 0	.55 / .52 / 19 / 0	.32 / .32 / 46.7 / 0
Intercept	-643	-810	-886	-574
Time Constants for Radial (solid) Debris Relocation (s)			[44, 108, 169]	
Time Constants for Radial (liquid) Debris Relocation (s)				
dT|dz Model, Time Constant for Averaging Flows (s)				
dT|dz Model, Characteristic Coupling Time (s)				
dT|dz Model, Relative Weight of Historical Flow (s)				
Molten Zircaloy Break-Through Temperature (K)	[745, 813, 874]	[1000, 1091, 1174]	[1073, 1171, 1259]	[868, 947, 1019]
*Molten Cladding (pool) Drainage Rate (kg/(m*s))*				
Fraction of Strain at Which Lower Head Failure Occurs				
Scaling Factor for Candling Heat Transfer Coefficients				
Fraction of Un-oxidized Cladding Thickness Initiating T. M. Weakening (m)				
*Debris Quenching Heat Transfer Coefficient to Pool (W/(m*m*K))*				
Debris Falling Velocity (m/s)				
Minimum Debris Porosity				
Time At Temperature - Effective Failure Temperature (K)				
Decay Heat Integrated to 10 hours (J)				

Table B.5 – Conditional Rank Cumulative Hydrogen Production Table from First Channel Box Failure

	First Fuel Failure	Main Steam Line	Lower Core Plate	Lower Plenum Dry-out	Lower Head Failure	End of Simulation
R^2 / R^2_{adj} / F-stat vs. Const./ p-val	N/A	.19 / .18 / 22.2 / 0	.28 / .26 / 18.6 / 0	.15 / .14 / 16.7 / .00009	N/A	N/A
Intercept	0.04	1.36	1.04	-0.17	0.999	0.992
Time Constants for Radial (solid) Debris Relocation (s)						
Time Constants for Radial (liquid) Debris Relocation (s)						
dT|dz Model, Time Constant for Averaging Flows (s)						
dT|dz Model, Characteristic Coupling Time (s)						
dT|dz Model, Relative Weight of Historical Flow (s)						
Molten Zircaloy Break-Through Temperature (K)			[0.66, 0.72, 0.77]	[0.77, 0.84, 0.9]		
*Molten Cladding (pool) Drainage Rate (kg/(m*s))*						
Fraction of Strain at Which Lower Head Failure Occurs						
Scaling Factor for Candling Heat Transfer Coefficients						
Fraction of Un-oxidized Cladding Thickness Initiating T. M. Weakening (m)						
*Debris Quenching Heat Transfer Coefficient to Pool (W/(m*m*K))*						
Debris Falling Velocity (m/s)						
Minimum Debris Porosity						
Time At Temperature - Effective Failure Temperature (K)		[-1.39, -1.33, -1.28]	[-1.23, -1.18, -1.14]			
Decay Heat Integrated to 10 hours (J)						

Table B.6 – Conditional Intact Fuel Mass Table from First Control Rod Failure

	First Fuel Failure	Main Steam Line	Lower Core Plate	Lower Plenum Dry-out	Lower Head Failure	End of Simulation
R^2 / R^2_{adj} / F-stat vs. Const./ p-val	N/A	.19 / .18 / 22.2 / 0	.28 / .26 / 18.6 / 0	.15 / .14 / 16.7 / .00009	N/A	N/A
Intercept	0.04	1.36	1.04	-0.17	0.999	0.992
Time Constants for Radial (solid) Debris Relocation (s)						
Time Constants for Radial (liquid) Debris Relocation (s)						
dT|dz Model, Time Constant for Averaging Flows (s)						
dT|dz Model, Characteristic Coupling Time (s)						
dT|dz Model, Relative Weight of Historical Flow (s)						
Molten Zircaloy Break-Through Temperature (K)			[0.66, 0.72, 0.77]	[0.77, 0.84, 0.9]		
*Molten Cladding (pool) Drainage Rate (kg/(m*s))*						
Fraction of Strain at Which Lower Head Failure Occurs						
Scaling Factor for Candling Heat Transfer Coefficients						
Fraction of Un-oxidized Cladding Thickness Initiating T. M. Weakening (m)						
*Debris Quenching Heat Transfer Coefficient to Pool (W/(m*m*K))*						
Debris Falling Velocity (m/s)						
Minimum Debris Porosity						
Time At Temperature - Effective Failure Temperature (K)		[-1.39, -1.33, -1.28]	[-1.23, -1.18, -1.14]			
Decay Heat Integrated to 10 hours (J)						

APPENDIX C: REPLICATE AND PERTURBATION DEFINITIONS

Appendix C reproduces descriptive tables (Table C.1 and C.2) regarding the replicates and perturbation analysis from Volume I of the 1F1 UA. Please see Volume I of the 1F1 UA for a more detailed discussion.

Table C.1 – List of MELCOR Cases

case type	id	# rlz	description
Replicates	w-1f1-rep1	100	Replicate 1; base case for statistical analysis
	w-1f1-rep2	100	Replicate 2
	w-1f1-rep3	100	Replicate 3
	w-1f1-rep1u	100	Replicate 1; rerun with uniform distributions
perturbations	w-1f1-p01	100	"median-like" realization rerun with small perturbations of its sampled values (see Table C.2)
	w-1f1-p02	100	"median-like" realization rerun with with DTMAX sampled from a log-uniform distribution (LB = 0.01 s, UB = 0.1 s)
	w-1f1-p03	100	"median-like" realization rerun with the model's flow path input randomly reordered

Table C.2 – Small Perturbation Distributions Based on Rlz13 Sampled Values.

parameter	nomenclature	uniform distribution
time constants for radial (solid) debris relocation	SC1020_1	L.B. = 4.3004E+02 Rlz13 = 4.3220E+02 U.B. = 4.3436E+02
time constants for radial (liquid) debris relocation	SC1020_2	L.B. = 6.5580E+01 Rlz13 = 6.5910E+01 6.6240E+01
dT/dz model, time constant for averaging flows	SC1030_2	L.B. = 9.1232E-02 Rlz13 = 9.1690E-02 U.B. = 9.2148E-02
dT/dz model, characteristic time for coupling dT/dz temperatures to average CVH volume temperature when dT/dz model is active	SC1030_4	L.B. = 8.8286E+00 Rlz13 = 8.8730E+00 U.B. = 8.9174E+00
dT/dz model, maximum relative weight of old flow in smoothing algorithm involving time constant for averaging flows	SC1030_5	L.B. = 5.6377E-01 Rlz13 = 5.6660E-01 U.B. = 5.6943E-01
molten zircaloy melt break-through temperature	SC1131_2	L.B. = 2.3492E+03 Rlz13 = 2.3610E+03 U.B. = 2.3728E+03
molten cladding (pool) drainage rate	SC1141_2	L.B. = 3.4367E-01 Rlz13 = 3.4540E-01 U.B. = 3.4713E-01
fraction of strain at which lower head failure occurs	SC1601_4	L.B. = 1.7313E-01 Rlz13 = 1.7400E-01 U.B. = 1.7487E-01
scaling factor for candling heat transfer coefficients	cor_cht_hfzrXX	L.B. = 1.0826E+00 Rlz13 = 1.0880E+00 U.B. = 1.0934E+00
fraction of un-oxidized cladding thickness at which thermal-mechanical weakening of oxidized cladding begins	cor_rod_2	L.B. = 1.3094E-03 Rlz13 = 1.3160E-03 U.B. = 1.3226E-03
debris quenching heat transfer coefficient to pool	cor_lp_2	L.B. = 9.8654E+02 Rlz13 = 9.9150E+02 U.B. = 9.9646E+02
debris falling velocity	cor_lp_4	L.B. = 4.6894E-01 Rlz13 = 4.7130E-01 U.B. = 4.7366E-01
minimum debris porosity (Lipinski dryout model); SC1244(1) min. porosity used in flow blockage Ergun pressure drop equation; SC4413(5) min. hydrodynamic volume fraction; SC4414(1) minimum porosity to be used in calculating the flow resistance in the flow blockage model; SC1505(1) minimum porosity to be used in calculating the area for heat transfer to fluid; SC1505(2)	minpordp	L.B. = 8.9968E-02 Rlz13 = 9.0420E-02 U.B. = 9.0872E-02

DISTRIBUTION

External Distribution (electronic copy)

1 Michael L. Corradini
DOE-NE-72 Reactor Safety Technologies Program Manager
143 Engineering Research Building
1500 Engineering Drive
Madison, WI 53706

1 Richard A. Reister
U.S. Department of Energy (DOE-NE-72)
Federal Programs Manager
Germantown, MD

1 Kathryn A. McCarthy
DOE-NE-72 Director, Light Water Reactor Sustainability Technical Integration Office
Idaho National Laboratory
Idaho Falls, ID

1 US Department of Energy
Attn: Damian Peko
NE-72
1991 Germantown Road
Germantown, MD 20874

Internal Distribution (electronic copy)

1	MS0748	Dusty Brooks	6231
1	MS0748	Matthew Denman	6231
1	MS0748	Jeff Cardoni	6232
1	MS0748	Randall Gauntt	6232
1	MS0748	Don Kalinich	6232
1	MS0748	Doug Osborn	6232
1	MS0899	Technical Library	9536


Sandia National Laboratories